Design and development of a near-field thermophotovoltaic conversion device

Christophe Lucchesi

N° d'ordre NNT : 2020LYSEI053

THÈSE de DOCTORAT DE L'UNIVERSITÉ de LYON

opérée au sein de
L'Institut National des Sciences Appliquées de Lyon

École Doctorale N° ED 162
Mécanique, Énergétique, Génie Civil, Acoustique

Spécialité : Thermique et Énergétique

Soutenue publiquement le 15/07/2020, par :

Christophe LUCCHESI

Design and development of a near-field thermophotovoltaic conversion device

---

Devant le jury composé de :

KITTEL Achim	Professeur	Universität Oldenburg	Rapporteur
MARTI VEGA Antonio	Professeur	UPM, Madrid	Rapporteur
DELMAS Agnès	Maitre de conférences	INSA de Lyon	Examinatrice
DE WILDE Yannick	Directeur de recherches	Institut Langevin, Paris	Examinateur
GUILLEMOLES Jean-François	Directeur de recherches	IPVF, Palaiseau	Examinateur
KAMINSKI-CACHOPO Anne	Professeur	Grenoble INP - Phelma	Examinatrice
VAILLON Rodolphe	Directeur de recherches	IES, Montpellier	Directeur de thèse
CHAPUIS Pierre-Olivier	Chargé de recherche	CETHIL, Lyon	Co-directeur de thèse
PEREZ Jean-Philippe	Maitre de conférences	IES, Montpellier	Membre invité

Département FEDORA – INSA Lyon - Ecoles Doctorales – Quinquennal 2016-2020

SIGLE	ECOLE DOCTORALE	NOM ET COORDONNEES DU RESPONSABLE
CHIMIE	**CHIMIE DE LYON** **http://www.edchimie-lyon.fr** Sec. : Renée EL MELHEM Bât. Blaise PASCAL, 3e étage **secretariat@edchimie-lyon.fr** INSA : R. GOURDON	**M. Stéphane DANIELE** Institut de recherches sur la catalyse et l'environnement de Lyon IRCELYON-UMR 5256 Équipe CDFA 2 Avenue Albert EINSTEIN 69 626 Villeurbanne CEDEX **directeur@edchimie-lyon.fr**
E.E.A.	**ÉLECTRONIQUE, ÉLECTROTECHNIQUE, AUTOMATIQUE** **http://edeea.ec-lyon.fr** Sec. : M.C. HAVGOUDOUKIAN **ecole-doctorale.eea@ec-lyon.fr**	**M. Gérard SCORLETTI** École Centrale de Lyon 36 Avenue Guy DE COLLONGUE 69 134 Écully Tél : 04.72.18.60.97 Fax 04.78.43.37.17 **gerard.scorletti@ec-lyon.fr**
E2M2	**ÉVOLUTION, ÉCOSYSTÈME, MICROBIOLOGIE, MODÉLISATION** **http://e2m2.universite-lyon.fr** Sec. : Sylvie ROBERJOT Bât. Atrium, UCB Lyon 1 Tél : 04.72.44.83.62 INSA : H. CHARLES **secretariat.e2m2@univ-lyon1.fr**	**M. Philippe NORMAND** UMR 5557 Lab. d'Ecologie Microbienne Université Claude Bernard Lyon 1 Bâtiment Mendel 43, boulevard du 11 Novembre 1918 69 622 Villeurbanne CEDEX **philippe.normand@univ-lyon1.fr**
EDISS	**INTERDISCIPLINAIRE SCIENCES-SANTÉ** **http://www.ediss-lyon.fr** Sec. : Sylvie ROBERJOT Bât. Atrium, UCB Lyon 1 Tél : 04.72.44.83.62 INSA : M. LAGARDE **secretariat.ediss@univ-lyon1.fr**	**Mme Sylvie RICARD-BLUM** Institut de Chimie et Biochimie Moléculaires et Supramoléculaires (ICBMS) - UMR 5246 CNRS - Université Lyon 1 Bâtiment Curien - 3ème étage Nord 43 Boulevard du 11 novembre 1918 69622 Villeurbanne Cedex Tel : +33(0)4 72 44 82 32 **sylvie.ricard-blum@univ-lyon1.fr**
INFOMATHS	**INFORMATIQUE ET MATHÉMATIQUES** **http://edinfomaths.universite-lyon.fr** Sec. : Renée EL MELHEM Bât. Blaise PASCAL, 3e étage Tél : 04.72.43.80.46 **infomaths@univ-lyon1.fr**	**M. Hamamache KHEDDOUCI** Bât. Nautibus 43, Boulevard du 11 novembre 1918 69 622 Villeurbanne Cedex France Tel : 04.72.44.83.69 **hamamache.kheddouci@univ-lyon1.fr**
Matériaux	**MATÉRIAUX DE LYON** **http://ed34.universite-lyon.fr** Sec. : Stéphanie CAUVIN Tél : 04.72.43.71.70 Bât. Direction **ed.materiaux@insa-lyon.fr**	**M. Jean-Yves BUFFIÈRE** INSA de Lyon MATEIS - Bât. Saint-Exupéry 7 Avenue Jean CAPELLE 69 621 Villeurbanne CEDEX Tél : 04.72.43.71.70 Fax : 04.72.43.85.28 **jean-yves.buffiere@insa-lyon.fr**
MEGA	**MÉCANIQUE, ÉNERGÉTIQUE, GÉNIE CIVIL, ACOUSTIQUE** **http://edmega.universite-lyon.fr** Sec. : Stéphanie CAUVIN Tél : 04.72.43.71.70 Bât. Direction **mega@insa-lyon.fr**	**M. Jocelyn BONJOUR** INSA de Lyon Laboratoire CETHIL Bâtiment Sadi-Carnot 9, rue de la Physique 69 621 Villeurbanne CEDEX **jocelyn.bonjour@insa-lyon.fr**
ScSo	**ScSo*** **http://ed483.univ-lyon2.fr** Sec. : Véronique GUICHARD INSA : J.Y. TOUSSAINT Tél : 04.78.69.72.76 **veronique.cervantes@univ-lyon2.fr**	**M. Christian MONTES** Université Lyon 2 86 Rue Pasteur 69 365 Lyon CEDEX 07 **christian.montes@univ-lyon2.fr**

*ScSo : Histoire, Géographie, Aménagement, Urbanisme, Archéologie, Science politique, Sociologie, Anthropologie

Acknowledgements

Avant toutes choses j'aimerais remercier les membres du jury. En premier lieu Yannick De Wilde en tant que président, ainsi que Achim Kittel et Antonio Marti qui ont accepté la lourde tâche d'être rapporteurs. Agnès Delmas, Anne Kaminski et Jean-François Guillemoles pour avoir été examinateurs de ce travail. Bien que les conditions de la soutenance aient été très particulières, les discussions scientifiques qui ont débouché de nos échanges ont été fortement enrichissantes, diversifiées et fructueuses.

Un grand merci aux collègues de l'IES à Montpellier : Dilek, Jean-Philippe, Thierry et Éric. J'ai toujours pris un grand plaisir à travailler avec vous. Vous avez très largement contribué à la réussite de notre projet, je vous souhaite à tous beaucoup de réussite dans la poursuite de votre carrière !

À présent je tiens à remercier tout particulièrement mes directeurs de thèse, à savoir Rodolphe Vaillon et Olivier Chapuis dit « POC », pour m'avoir si bien encadré durant mes trois années et plus de thèse. Le skype du mardi est devenu un rendez-vous incontournable qui a donné naissance à de nombreuses questions et discussions scientifiques très instructives ! J'ai également beaucoup apprécié de vous côtoyer hors du laboratoire, qu'il s'agisse de partager un logement dans un chalet en Laponie (ou un container en Arizona), à l'occasion de diners, d'apéros, ~~de déménagements~~, et lors de conférences scientifiques pour lesquelles vous m'avez fait confiance pour présenter nos résultats. Je vous souhaite à vous deux tous le meilleur pour la suite : que vos projets scientifiques et personnels prennent vie !

J'aimerais maintenant remercier chaleureusement les membres du groupe MiNT du CETHIL qui m'ont accueilli à bras ouverts dans leur équipe ! Merci aux permanents : Séverine Gomès, Olivier Merchiers, Kostas et Stéphane Lefevre, avec lesquels j'ai eu l'occasion de partager des moments d'échanges scientifiques mais également des moments conviviaux lors de nos sorties et repas de groupes (si on allait au Gros Cailloux la prochaine fois ? :p). Merci également aux stagiaires, doctorants et post-doctorants de MiNT avec lesquels j'ai discuté et travaillé : Afaf, Ali, Ahmed, Axel, Georges, Mateo, Mathieu, et Paul M. Un merci spécial à David qui m'a enseigné son savoir expérimental ! Et enfin, je tiens à saluer tout particulièrement Paul D. et Éloïse avec qui j'ai également passé de super moments au labo, pendant le travail (la destruction de sondes SThM notamment) ou les pauses café, et hors du labo lors de diverses sorties et apéros !

Un merci à mes camarades de cantine CNRS : Anthony, Cédric, Hervé, Loïc G., Pierrick et Serge. Les discussions, qui restent à la cantine selon la formule consacrée, y ont toujours été très intéressantes et fort bien animées.

Je tiens également à remercier les membres de l'atelier, Christophe, Nicolas et Xavier, ainsi que les membres du secrétariat, Edwige, Élisa, Florence, Marilyne, Meriem, Sophie et Silas pour leur aide très appréciée. Une dédicace spéciale à Nazaré, dont on attend toujours l'invitation pour un karaoké !

Je voudrais à présent remercier tous les doctorants et post-doctorants que je n'ai pas encore cités et que j'ai eu la chance de croiser durant mon séjour au labo ! Merci à Bilal, Damien, Gabriele, Ghady, Khriscia, Loïc F., Martin, Nicolas, Samuel, Sophie et Thibaut. Un merci également aux

petits nouveaux : Adrien, Félix, Teddy et Julie S. Petite dédicace à Seb, Jean (et ses parents) chez et avec qui j'ai passé un super week-end dans les caves à vin de Bourgogne. Merci à Janett de m'avoir ~~forc..~~ invité à l'accompagner au salon du chiot !

Enfin je voudrais dédier quelques lignes à ma co-bureau (ou « co-bubu » d'après elle), à savoir Julie D. Merci d'avoir débarqué sans prévenir pour t'installer dans mon bureau où j'étais tranquillement tout seul. À défaut d'avoir pu m'apprendre les couleurs, tu as été à mes côtés (à gauche, à droite ou en face selon la configuration des bureaux) durant la majeure partie de ma présence au labo ! J'ai apprécié les carrés de chocolat que tu as pu m'offrir à l'heure du goûter. Je te dois bien le livre de recettes de mes pâtisseries que tu m'as commandé !

Voilà, je crois que j'ai remercié tout le monde, je ne vois pas qui j'aurais pu oublier… Je vais donc conclure en disant que…AH ! Un instant ! On me dit dans l'oreillette que j'ai oublié une personne !... En vérité je n'ai pas vraiment d'oreillettes mais la personne suivante aime bien les blagues donc je voulais lui rendre hommage… Bref ! Je tiens donc à adresser des remerciements tout particuliers à Mathilde pour sa bonne humeur constante et qui a grandement contribué à élever la pause-café au rang de moment immanquable de la journée ! Merci pour tout, et surtout d'avoir été à mes côtés durant la rédaction de ce manuscrit et notamment pendant la période de confinement ! On finira le remix de la chanson des enfoirés un jour ;) « Moi je *dois* rester là, à côté de toi ! ».

Pour terminer (sortez les mouchoirs), une pensée pour mon chat qui a partagé les trois quarts de ma vie et qui, j'en suis sûr, aurait beaucoup apprécié ce manuscrit en tant que support pour y faire la sieste !
Et enfin, maintenant que je pense n'avoir oublié personne, un grand merci à ma famille ! Vous pouvez venir à Lyon quand vous voulez !

Abstracts

Français

Une cellule thermophotovoltaïque (TPV) convertit l'énergie de photons émis par des corps chauds en énergie électrique. Lorsque la distance séparant deux corps rayonnants devient inférieure à la longueur d'onde caractéristique du rayonnement thermique (~10 µm à température ambiante, ~2,3 µm vers 1000°C), le transfert de chaleur radiatif peut s'accroître de plusieurs ordres de grandeur grâce à la contribution des ondes évanescentes. Cette propriété a un intérêt pour la récupération d'énergie en promettant une augmentation de la puissance électrique générée par une cellule TPV lorsqu'elle est placée en champ proche d'un émetteur thermique radiatif. Dans le but de vérifier cette prédiction, cette thèse a consisté à développer un banc expérimental de mesures TPV en champ proche. Le dispositif est basé sur un montage de microscopie thermique avec actuateurs piézo-électriques (SThM). L'émetteur est une sphère micrométrique de graphite attachée sur un levier SThM chauffé de manière thermorésistive jusqu'à 1200 K et la cellule TPV en antimoniure d'indium (InSb), qui ne peut fonctionner au-delà de 100 K, est placée sur le doigt froid d'un cryostat. Le flux radiatif en champ proche transféré par l'émetteur peut être mesuré indépendamment de la puissance électrique générée par la cellule. La preuve expérimentale de l'accroissement de la densité de puissance électrique générée en champ proche, par rapport à la prédiction de la théorie macroscopique du rayonnement, a été apportée avec un facteur jusqu'à 6. L'étude de différents paramètres a permis d'atteindre des puissances TPV de 7.5 $kW.m^{-2}$ et des rendements de conversion mesurés de ~20 %. Des expériences de transfert radiatif en champ proche dans diverses configurations (matériaux, géométries, températures) ont également été menées. La puissance radiative transférée en champ proche suit des lois de puissance très différentes de celles du champ lointain. Ces résultats démontrent expérimentalement l'intérêt applicatif des effets de champ proche pour le rayonnement thermique.

English

Thermophotovoltaic (TPV) cells convert the energy of photons emitted by hot bodies into electrical energy. When the distance between two radiating bodies becomes smaller than the characteristic wavelength of thermal radiation (~ 10 µm at room temperature and ~ 2.3 µm near 1000 °C), radiative heat transfer can be enhanced by several orders of magnitude due to the contribution of evanescent waves. This property has an interest for energy harvesting because it should increase the electrical power generated by a TPV cell located in the near field of a radiative thermal emitter. With the aim of confirming this prediction, this thesis consisted in the development of an experimental setup for performing near-field TPV measurements. The setup is based on a scanning thermal microscopy (SThM) design involving piezoelectric actuators. The emitter is a microsphere made of graphite and glued on a SThM cantilever heated by Joule effect up to 1200 K and the TPV cell made of indium antimonide (InSb), which cannot operate above 100 K, is placed on the cold finger of a cryostat. Near-field radiative heat flux transferred from the emitter is measured independently from the electrical power generated by the cell. A study of different parameters provided the experimental proof of the near-field enhancement of the electrical power density generated in the near field by a factor up to 6 compared with the prediction based on the macroscale theory of thermal radiation. Output electrical power densities reach 7.5 $kW.m^{-2}$ and conversion efficiencies ~20 %. In addition, near-field radiative heat transfer experiments were performed in various configurations (materials, geometries and temperatures). The near-field radiative power follows power laws different from those of the far field. These results highlight the interest of near-field effects on radiative heat transfer for applications.

Outline

Nomenclature and abbreviations

Nomenclature

Symbol	Name	Unit
A	Area	m^2
AA	Active area diameter	m
c	Velocity of light	$m.s^{-1}$
d	Distance	m
d_{min}	Minimum emitter-sample distance	m
$\tilde{d}(r)$	Sphere-plane distance at the local sphere radius	m
D	Diameter	m
D_n	Diffusion coefficient of electrons	$m^2.s^{-1}$
D_p	Diffusion coefficient of holes	$m^2.s^{-1}$
e	Electron charge	C
err_T	Systematic error on temperature determination	
$err_T^{T_{Rmax}}$	Systematic error on T_{Rmax} determination	
$err_T{}^{Calib}$	Systematic error on temperature determination from calibration	
E	Energy	eV
E_C	Maximum energy of the conduction band	eV
EF	Enhancement factor	
E_g	Energy bandgap	eV
E_V	Maximum energy of the valence band	eV
f_l	Strength of oscillator l	
FF	Fill factor	
$F_{c\to env}$	Cell-environment view factor	
$F_{c\to s}$	Cell-sphere view factor	
$F_{s\to d}$	Sphere-disc view factor	
g	Gain	
$G_{Blackbody}^{T=300K}$	Blackbody conductance at 300 K	$W.K^{-1}$
G_{BB}	Blackbody radiative conductance	$W.m^{-2}.K^{-1}$
G_{fit}	Fitting conductance	$W.K^{-1}$
G_{FF}	Far-field radiative thermal conductance	$W.K^{-1}$

G_{NF}	Measured near-field radiative thermal conductance	$W.K^{-1}$
G_{pp}	Plane-plane radiative thermal conductance	$W.K^{-1}$
G_{sp}	Sphere-plane radiative thermal conductance	$W.K^{-1}$
G_{sp}^{evan}	Calculated sphere-plane evanescent radiative thermal conductance	$W.K^{-1}$
G_{tot}	Total emitter radiative thermal conductance	$W.K^{-1}$
$G_{TPV,max}$	Electrical power generated by the cell normalized by the temperature difference between the emitter and the cell	$W.m^{-2}.K^{-1}$
h	Planck's constant	J.s
$\hbar$	Reduced Planck's constant	J.s
I	Electrical current	A
I_{heat}	Current of the Wheatstone bridge	A
I_L	Photogenerated current	A
I_{Pmax}	Current at the maximum electrical power generated by a PV cell	A
I_{ref}	Emitter current at the largest distance	A
I_{TPV}^{ref}	Current of a reference I-V curve	A
IRR	Incorporation rate ratio	
I_{SC}	Short-circuit current	A
I_0	Reverse saturation current (or dark current)	A
J_n	Electron current density	$A.m^{-2}$
J_p	Holes current density	$A.m^{-2}$
k	Fitting coefficient for temperature calculation in *R(T)* calibration curve	$K.W^{-1}$
k_0	Wavevector	m^{-1}
$k_{\parallel}$	Parallel component of the wavevector	m^{-1}
$k_{\perp}$	Perpendicular component of the wavevector	m^{-1}
k_B	Blotzmann's constant	$m^2.kg.s^{-2}.K^{-1}$
K	Kubelka-Munk's absorption coefficient	
l	Oscillator in Drude-Lorentz model	
L	Number of oscillators in Drude-Lorentz model	
$L_{x,y}$	x and y dimensions of a rectangle planar emitter	m
m_0	Electron mass in vacuum	kg
m_e^*	Electrons effective mass	kg
m_h^*	Holes effective mass	kg

n	Real part of the refractive index	
$n(z)$	Density of free electrons at the position z	cm^{-3}
$n_{\Delta\omega}$	Number of rays in the frequency interval $\Delta\omega$	
n_f	Ideality factor	
n_{FF}	Exponent of the temperature power law in the far field	
n_i	Intrinsic carrier concentration	cm^{-3}
n_p	Number of emitted rays	
n_0	Electron concentration at equilibrium	cm^{-3}
N	Number of averaged curves	
N_A	Acceptor concentration	cm^{-3}
N_c	Effective density of states in the conduction band	cm^{-3}
N_D	Donor concentration	cm^{-3}
N_e	Electrons concentration	cm^{-3}
N_h	Holes concentration	cm^{-3}
N_v	Effective density of states in the valence band	cm^{-3}
p_0	Hole concentration at equilibrium	cm^{-3}
$p(z)$	Density of holes at the position z	cm^{-3}
P	Electrical power	W
P_i	Emitted power carried by the ray i	W
P_{max}	Maximum electrical power generated by a PV cell	W
P_{sp}^{evan}	Sphere-plane evanescent power	W
P_0	Power of the incident beam	W
P_{PV}	Electrical power generated by a PV cell	W
P_{TPV}	Electrical power generated by a TPV cell	W
$P_{TPV,max}$	Maximum electrical power generated by a TPV cell	W
$P_{TPV,max}^{vf}$	View factor prediction of the electrical power generated by a TPV cell	W
$P_{TPV,max}^{NF}$	Near-field electrical power generated by a TPV cell	W
P_R	Power of the reflected beam	W
q	Spectral hemispherical radiative heat flux	$W.m^{-2}.(rad.s^{-1})^{-1}$
q^{BB}	Blackbody spectral hemispherical radiative heat flux	$W.m^{-2}.(rad.s^{-1})^{-1}$ or $W.m^{-2}.m^{-1}$
q^{evan}	Evanescent contribution of the spectral hemispherical radiative heat flux	$W.m^{-2}.(rad.s^{-1})^{-1}$

q_{ij}	Spectral hemispherical radiative heat flux emitted by medium i and absorbed by j	$W.m^{-2}.(rad.s^{-1})^{-1}$
$q_{evan}^{frustrated}$	Frustrated modes contribution on the hemispherical radiative heat flux	$W.m^{-2}$
$q_{evan}^{surface}$	Surface modes contribution on the hemispherical radiative heat flux	$W.m^{-2}$
q_{sp}^{evan}	Sphere-plane hemispherical radiative heat flux, evanescent wave contribution	$W.m^{-2}$
q_{tot}^{BB}	Total hemispherical radiative heat flux emitted by a blackbody	$W.m^{-2}$
q^{prop}	Propagative contribution of the spectral hemispherical radiative heat flux	$W.m^{-2}.(rad.s^{-1})^{-1}$
q_{ω}^{n}	Spectral hemispherical radiative heat flux at the point *n*	$W.m^{-2}.(rad.s^{-1})^{-1}$
Q_{env}	Radiative power from the environment	W
Q_{FF}	Far-field radiative power	W
Q^{MC}	Radiative heat flux calculated using Monte Carlo method	W
Q_{NF}	Measured near-field radiative power	W
Q_{rad}	Radiative power	W
Q_{sp}^{evan}	Calculated sphere-plane evanescent flux	W
Q^{VF}	Radiative heat flux considering the view factor evolution	W
r	Local sphere radius	m
re_{ω}	Reflectivity at the frequency ω	
$r_{ij}^{TE,TM}$	Fresnel's reflection coefficient at the interface between media *i* and *j*, for *TE* or *TM* polarization	
R	Electrical resistance	Ω
$Re_{n}^{S,D}$	Number of rays reflected on the sphere (S) or the disc (D) for the *n*-th time	
R_1	Adjustable electrical resistance 1	Ω
R_2	Adjustable electrical resistance 2	Ω
$R_{In,Sb}$	Indium or antimony growth rate	$ML.s^{-1}$
R_C	Radius of curvature	m
R_{cell}	TPV cell radius	m
R_{disc}	Disc radius	m
$R_{emitter}$	Emitter electrical resistance	Ω
R_{max}	Maximum resistance of *R(T)* calibration curve	Ω
R_{RMS}	Root-mean-square roughness	m
R_S	Resistance at maximum emitter sensitivity	Ω

R_{sphere}	Sphere radius	m
R_V	Variable programmable electrical resistance	Ω
R_∞	Reflectivity of an opaque sphere	
st	Semi-transparency coefficient	
S	Surface	m^2
S_{sphere}	Surface of a sphere	m^2
S_{cell}	Surface of a the active area of a TPV cell	m^2
S_c	Kubelka-Munk's scattering coefficient	
t_S	Thickness of the InSb cell substrate	m
T	Temperature	K
T_{amb}	Ambient temperature	K
T_{cell}	Temperature of the cell	K
$TC1$	Thermocouple temperature 1	°C
$TC2$	Thermocouple temperature 2	°C
$T_{emitter}$	Temperature of the emitter	K
T_{env}	Environment temperature	K
$T_{hot,cold}$	Temperature of hot and cold reservoirs	K
Tr	Transmission coefficient for *TE*-polarized waves	
T_{ref}	Emitter temperature at the largest distance	K
T_{Rmax}	Temperature at maximum *R(T)* resistance	K
T_S	Temperature at maximum emitter sensitivity	K
$T_{substrate}$	Substrate temperature	K
T_{Wien}	Temperature of a blackbody with the maximum emissivity corresponding to λ_{Wien}	K
T_ω	Transmittance at the frequency ω	
V	Voltage	V
V_{AB}	Unbalance of Wheatstone bridge	V
V_{heat}	Wheatstone bridge voltage	V
V_{OC}	Open-circuit voltage	V
V_{Pmax}	Voltage at the maximum electrical power generated by a PV cell	V
z	z-piezoelectric actuator displacement	m
z_{max}	Maximum emitter displacement reached at the contact point	m

α	Temperature coefficient	K^{-1}
α_e	Fitting parameter	$eV.K^{-1}$
β	Fitting parameter	K
δG_{NF}	Near-field radiative conductance uncertainty	$W.K^{-1}$
δI	Uncertainty of the emitter current	A
δI_{heat}	Uncertainty of the Wheststone bridge current	A
δQ_{NF}	Near-field radiative power uncertainty	W
$\delta\alpha$	Uncertainty of the thermal coefficient	K^{-1}
$\delta\Delta I$	Uncertainty of the emitter current variation	A
$\delta\Delta\theta$	Uncertainty of the variation of temperature elevation	K
δR	Electrical resistance noise	Ω
δT	Thermal noise	K
δx	Displacement of the reflected laser on the photodiode	m
δz	Topography of the sample measured with AFM	m
ΔG	Thermal conductance difference	$W.K^{-1}$
ΔI	Electrical current difference	A
ΔP	Electrical power difference	W
ΔR	Electrical resistance difference	Ω
ΔT	Temperature difference	K
ΔT_{max}	Maximum temperature difference	K
$\Delta\theta$	Variation of temperature elevation	K
$\Delta\omega$	Frequency interval	$rad.s^{-1}$
ϵ	Emissivity	
$\epsilon_{SiO_2}^{bulk}$	Emissivity of bulk silica	
ε	Permittivity	
ε'	Real part of the dielectric function	
ε''	Imaginary part of the dielectric function	
ε_0	Permittivity of vacuum	
ε_∞	Permittivity when the frequency tends to infinity	
ε_{bl}	Permittivity accounting for contributions by transitions across the band gap and lattice vibrations	
η_{TPV}	Thermophotovoltaic conversion efficiency	%

η_{TPV}^{NF}	Near-field thermophotovoltaic conversion efficiency	%
Γ_D	Drude model damping frequency	s^{-1}
Γ_l	Damping frequency of oscillator l	s^{-1}
η_{max}	Maximum energy conversion efficiency of a heat engine	
κ	Extinction coefficient	
κ_ω	Extinction index	
λ	Wavelength	m
λ_{Chr}	Christiansen's wavelength	m
λ_{gap}	Bandgap wavelength	m
λ_{Wien}	Wien's wavelength	m
μ_n	Mobility of electrons	$m^2.V^{-1}.s^{-1}$
μ_p	Mobility of holes	$m^2.V^{-1}.s^{-1}$
θ	Temperature elevation	K
θ_{ref}	Temperature elevation at the largest distance	K
σ	Stefan-Boltzmann's constant	$W.m^{-2}.K^{-4}$
τ_{e}	Electrons scattering time	s
τ_{h}	Holes scattering time	s
ω	Angular frequency	$rad.s^{-1}$
ω_l	Resonance frequency of oscillator l	$rad.s^{-1}$
ω_p	Plasma frequency	$rad.s^{-1}$
ω_{Wien}	Wien's angular frequency	$rad.s^{-1}$

Abbreviations

Symbol	Name
AFM	Atomic force microscopy
EQE	External quantum efficiency
I-V	Current-voltage
MBE	Molecular beam epitaxy
LHe	Liquid helium
NFRHT	Near-field radiative heat transfer
NF-TPV	Near-field thermophotovoltaics
PV	Photovoltaics

SThM	Scanning thermal microscopy
STM	Scanning tunneling microscopy
STPV	Solar thermophotovoltaics
TE	Transverse electric
TEG	Thermoelectric generator
TM	Transverse magnetic
TPV	Thermophotovoltaics
Im	Imaginary part

List of figures

List of tables

General introduction

The energy consumption across the world increases while the dependence on resources such as coal, gas or oil responsible for the CO_2 generation is gradually reduced. Therefore, new solutions of energy harvesting are requested in order to reduce our dependence on fossil resources. For instance, the energy flow chart released by the Lawrence Livermore National Laboratory[1] shows that renewable energies represented only 11 % of the total energy consumption in the United States in 2019. A remarkable part of 67.5 % of the energy produced across the country was lost as heat and was rejected into the environment. Such an alarming fact leads to the conclusion that waste heat recovery appears critical in order to increase the share of renewable energies. Therefore, it should be achieved by designing and fabricating efficient thermal energy conversion devices.
Thermal energy harvesting can be accomplished by using numerous methods aiming at recovering heat or converting it into mechanical work or electrical energy[2], depending on the temperature of the heat source[3]. Usually, heat sources are classified as low-grade (T < 230 °C), medium-grade (T = 230-650 °C) and high-grade (T > 650 °C). For instance, high- and medium-grade waste heat can be harvested using devices based on thermodynamic cycles, such as Stirling engines, which have been suggested to be the most efficient[4]. For low-temperature heat sources[5], an alternative is to use devices based on the Kalina cycle featuring two fluids and allowing to achieve thermal energy conversion efficiencies comparable to those of a Rankine cycle[6]. These processes do not generate electrical energy, but a mechanical work instead, that can be used directly or further converted into electricity. In addition, they require usually bulky mechanical components which can be noisy. Direct conversion of heat into electrical power can be achieved by solid-state devices with pyroelectric, thermoelastic, thermomagnetic or thermionic properties. The first three devices require temperature fluctuations of the heat source in order to operate, and need respectively either an alternative electric field, stress or magnetic field. They are based on either ferroelectric materials (pyroelectric and thermomagnetic devices) or shape memory alloys (thermoelastic devices). Thermionic devices take advantage of the temperature-induced emission of an electron from a hot electrode to a cooler one. They need a vacuum environment and are suited to high temperature aplications[7]. In addition to these four devices, thermoelectric generators (TEGs) are another solution which require only a temperature difference between a hot and a cold body to operate and generate electrical power. They are based on semiconductor materials exhibiting the Seebeck effect[8]. The practical use of TEGs makes thermoelectric energy harvesting the most popular technology for direct heat-to-electricity conversion. All these solid-state devices have a very low maintenance cost but they are usually exhibiting low efficiencies[2] of the order of 10 % or below.
Another way of directly recovering thermal energy into electrical energy is to use photovoltaic cells for converting infrared thermal radiation emitted by hot sources into electrical power. Such cells differ from conventional solar cells as they require low-energy bandgap semiconductor materials in order to convert low-energy infrared thermal photons. Such cells are referred to as thermophotovoltaic (TPV) cells[9,10]. TPV conversion devices with a hot body temperature above ~1000 °C are comparable with TEGs near 730 °C in terms of generated electrical density and are superior in terms of efficiency[8]. Below ~730 °C, TPV devices are significantly inferior to TEGs because of their poor performances regarding the electrical power density and efficiency. Therefore, the performances of TPV devices must be enhanced in order to compete with TEGs for harvesting low- and medium-grade heat. This can be achieved by tailoring the emission spectrum of the heat source in order to maximize the conversion efficiency and the electrical power generated

by the cell. Such a method can be applied using selective thermal radiative emitters in order to provide a better spectral matching between the emission spectrum and the absorption properties of the cell[11–13]. Another technique consists in using the properties of radiative heat transfer at the nanoscale, when the emitter is located in the close proximity of the TPV cell.

Physics of radiative heat transfer at the nanoscale is very different from that at the macroscale. The classical theory of thermal radiation fails to describe radiative heat transfer when the distance separating two bodies is smaller than the characteristic wavelength of thermal radiation[14] (~ 10 µm at room temperature and ~2.3 µm near 1000 °C). The range corresponding to such distances is referred to as the near-field regime, while the far-field regime corresponds to the macroscale theory. In the near field, the emission spectrum of the heat source is modified in terms of spectral distribution of the radiative power and in terms of amplitude. A new path for thermal radiation emerges due to the contribution of the evanescent waves. Their contribution was theoretically predicted and experimentally confirmed to enhance the thermal radiative power exchanged between two bodies in the near field by up to several orders of magnitude compared with the far field[14–17]. As a consequence, the idea of coupling a TPV cell with a thermal infrared emitter in the near field should lead to a significant rise of the electrical power density generated by the cell[18,19]. The experimental proof of concept of a near-field thermophotovoltaic (NF-TPV) device has been performed only very recently[20–22] but with very low electrical power densities and estimated conversion efficiencies. In this work, we aim at building an experimental setup in order to demonstrate the near-field enhancement of the electrical power density generated by a TPV cell with substantial power densities and high measured conversion efficiencies. A major advance compared with the state-of-the-art experimental devices is that the cell is designed and fabricated for near-field thermophotovoltaics. In addition, the thermal emitter material was selected in order to enhance as much as possible the electrical power generated by the cell in the near field. These characteristics should lead to the building of a demonstration device exhibiting performances comparable to those of thermoelectric generators with an output electrical power density of the order of 1 $W.cm^{-2}$. This work should pave the way for efficient heat-to-electricity energy conversion using thermal radiation harvesting from high and medium-grade heat sources. With the aim of providing a better understanding of radiative heat transfer at the nanoscale for TPV applications, this work has two major objectives reported in two parts. First, the temperature and material dependence of near-field radiative heat transfer is studied for various pairs of materials with large temperature differences of hundreds of kelvins. Second, the experimental demonstration of the enhancement of the electrical power generated by a TPV cell in the near field is performed. The objectives are addressed in six chapters.

In the first chapter, a critical analysis of the near-field radiative heat transfer experiments published in the literature is performed. Key parameters such as temperature and geometry are studied, and a classification of experimental works aims to highlight interesting domains to be considered experimentally.

In the second chapter, near-field radiative heat transfer is approached theoretically. The aim is to assess the material and temperature dependencies of near-field radiative heat transfer, which are expected to be very different from that observed in the far field. These peculiar expected behaviors are investigated for various pairs of materials that will be tested later on during the experimental study. The second goal of this chapter is to find an emitter material to be coupled with a TPV cell in the near field, in order to maximize the electrical power generated by the cell. Calculation tools are specifically developed for this purpose.

The third chapter reports on one major objective of this work being the design, development and characterization of an experimental setup for performing near-field radiative heat transfer and NF-

TPV experiments. The notable original feature of the setup is an integrated cryogenic cooling system needed for studying the physics of NF-TPV. The setup allows a hot thermal emitter to be brought at the closest possible distance of a substrate using piezoelectric positioners in a vacuum chamber while measuring the variations of radiative conductance between the two bodies. The review of the state of the art reported in the first chapter is considered in order to build an experimental setup with comparable or even better performances in terms of measurement accuracy and minimum distance. For instance, thermal emitters with a spherical shape allowing small emitter-sample distances of a few nanometers and no parallelization issue are fabricated based on scanning thermal microscopy (SThM) electrically resistive probes. The enhancement of the radiative conductance is assessed from the decrease of the emitter temperature as the distance with the substrate is lowered, while TPV measurements can be performed simultaneously.

The fourth chapter reports on the results of the near-field radiative conductance measurements. The aim is to study the temperature and material dependence of radiative heat transfer by performing measurements with different pairs of emitter and substrate materials, selected during the theoretical study presented in Chapter II. Large temperature differences up to 900 K are investigated establishing a significant advance of the state of the art. The aim of studying such high temperature differences is to provide a better knowledge of near-field radiative heat transfer in a temperature range suitable for energy harvesting applications. The temperature dependence of the near-field radiative conductance is observed for each pair of materials by measuring the exponent of the temperature power law of the near-field radiative power. Some experiments are performed with the substrate cooled down to 77 K.

In the fifth chapter, several ways for improving the design of NF-TPV experiments are analyzed, so that devices could compete with thermoelectric generators in terms of efficiency and generated electrical power density. An analysis of the state of the art referring to experimental TPV and NF-TPV conversion devices is performed. Advanced details are provided about recent NF-TPV experiments, and characteristics in terms of geometry, materials, temperatures and performances are compared and discussed.

The final chapter reports on an experimental work where a significant enhancement of the electrical power density generated by a TPV cell is observed in the near field compared with the far field. Performances surpassing those previously reported in terms of efficiency and electrical power density are measured, by heating the emitter up to 1100 K and cooling the cell down to 77 K. The electrical power generated by the cell is assessed as a function of the distance with the emitter by measuring current-voltage (I-V) characteristics. The configuration providing the best enhancement of the electrical power density generated by the cell in the near field is obtained by comparing the measurements for TPV cells having different parameters. The substrate thickness and the doping levels were previously determined by a theoretical study while the size of the cells is imposed by the fabrication process.

In the end, future interesting research paths are proposed both for the study of near-field radiative heat transfer and for the improvement of NF-TPV conversion devices.

PART I – NEAR-FIELD RADIATIVE HEAT TRANSFER

Chapter I

Nanoscale radiative heat transfer theory and experiments

I.1 Introduction

Thermal radiation is one of the three main heat transfer mechanisms, the other two being conduction and convection. When temperature of a body is above 0 K, electromagnetic radiation is emitted because of thermally-induced agitation of the electrical charges. For electromagnetic radiation in general, emitted energy depends on temperature and can range from radio waves with meter-scale wavelength to cosmic rays with wavelength less than 10^{-14} m. Most common applications involving thermal radiation occur in the wavelength range from ~ 0.1 µm to 1000 µm, corresponding to the near ultraviolet-visible-infrared region. In this chapter, fundamentals of thermal radiation theory are presented. The macroscale model of thermal radiation between two bodies is first described, also referred to as the incoherent far-field regime. Then, when the distance between two bodies decreases below the characteristic wavelength of thermal radiation, a new path for radiative heat transfer emerges through the evanescent waves. This distance range is called near-field regime. In addition to evanescent waves, wave effects such as interferences due to coherence occur in the transition with the far-field regime. The evanescent wave contribution to radiative heat transfer increases sharply as the distance between two bodies decreases. As a consequence, radiative heat transfer can be enhanced by several orders of magnitude. This enhancement was measured experimentally for different material, temperature and geometry configurations[23–25]. A summary of published experimental works is reported, and a classification is established as a function of various parameters. This classification aims to define state-of-the-art performances, and to highlight most interesting and uninvestigated parameters to study experimentally.

I.2 Macroscale surface-to-surface thermal radiation theory

The macroscale thermal radiation theory describes radiative heat transfer between two bodies in the incoherent far-field regime, where the distance between two bodies is large compared with the characteristic wavelength of thermal radiation. In this case the electromagnetic waves are propagative and incoherent. This means that incoherent waves are emitted from a body and propagate until they are absorbed by a lossy material. The base model for far-field thermal radiation is the definition of the radiative hemispherical heat flux for blackbody radiation and is described next.

I.2.1 Blackbody radiation

In the theory, a blackbody is defined as a perfect emitter and absorber. It has the role of a reference to which real absorbing and emitting materials can be compared. The emissive properties of the blackbody can be expressed using Planck's hemispherical spectral distribution of radiative heat flux[26,27]:

$$q^{BB}(\lambda,T) = \pi \frac{2hc^2}{\lambda^5} \frac{1}{e^{hc/\lambda k_B T} - 1}, \qquad (I.1)$$

$$q^{BB}(\omega,T) = \pi \frac{\hbar\omega^3}{4\pi^3 c^2} \frac{1}{e^{\hbar\omega/k_B T} - 1}. \qquad (I.2)$$

Eq. (I.1) provides the spectral hemispherical radiative heat flux q^{BB} (in W.m^{-2}.m^{-1}), as a function of wavelength λ at a temperature T. The constants c, h and k_B are the velocity of light, the Planck constant and the Boltzmann constant respectively. Note that the directional spectral intensity, in

$W.m^{-2}.m^{-1}.sr^{-1}$, is given by the same equation but without the factor π. Eq. (I.2) gives q^{BB} (in $W.m^{-2}.(rad.s^{-1})^{-1}$) as a function of angular frequency $\omega = \frac{2\pi c}{\lambda}$. In this equation, $\hbar = \frac{h}{2\pi}$ is the reduced Planck constant. Figure I.1 shows the spectral hemispherical emissive power as a function of angular frequency (left) and wavelength (right). The spectral distribution is broad around the frequency or wavelength of the maximum, called ω_{Wien} and λ_{Wien} respectively.

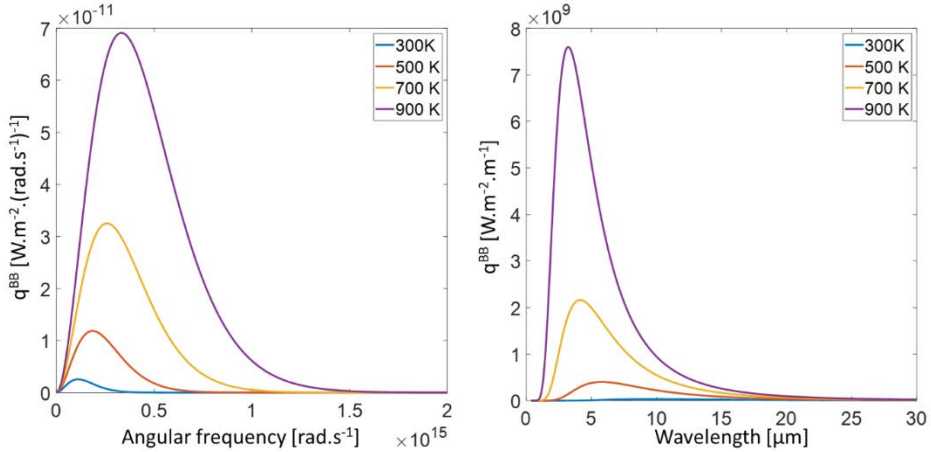

Figure I.1: Hemispherical radiative heat flux as a function of the angular frequency and the wavelength for different temperatures

I.2.2 Wien's law

Wien's law indicates the frequency or the wavelength where the spectral hemispherical radiative heat flux of a blackbody is maximum. This law is obtained by calculating the derivative of Eq. (I.1) and (I.2), as a function of λ or ω. Wien's law can be written as follows:

$$\lambda_{Wien} = \frac{2.898\ 10^{-3}}{T}, \qquad (I.3)$$

$$\omega_{Wien} = 3.697\ 10^{11}\ T, \qquad (I.4)$$

where T is defined in kelvin.

Wien's wavelength as a function of temperature is represented in Figure I.2. At room temperature ($T \sim 300$ K), its value is approximately 10 µm. Above 4000 K, λ_{Wien} is in the visible range of the spectrum corresponding to wavelengths ranging from 400 to 700 nm.

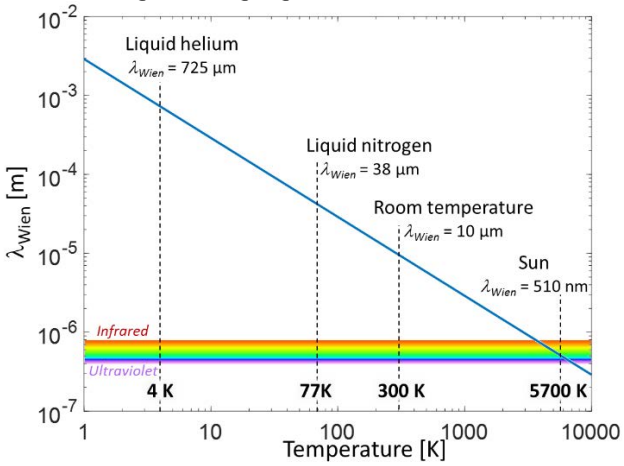

Figure I.2: Wien's wavelength as a function of temperature

I.2.3 Total emitted flux

The total hemispherical radiative heat flux q_{tot}^{BB} (in W.m^{-2}) emitted by a blackbody is obtained by integrating q^{BB} over the entire spectrum. The integrated equation is the Stefan-Boltzmann law:

$$q_{tot}^{BB}(T) = \sigma T^4 , \qquad (I.5)$$

where σ is the Stefan-Boltzmann constant equal to 5.670 10^{-8} W.m^{-2}.K^{-4}. Figure I.3 represents q_{tot}^{BB} as a function of temperature. Blackbody radiation corresponds to the limit of the emitted radiative heat flux reachable by a real material in the far-field regime. The spectral hemispherical emissivity of a real material is described as the ratio of its hemispherical radiative heat flux q divided by the power emitted by a blackbody:

$$\epsilon(\lambda, T) = \frac{q(\lambda, T)}{q^{BB}(\lambda, T)} \qquad (I.6)$$

The emissivity ϵ of a real material can take values ranging from 0 to 1, with the maximum when q is equal to q^{BB}.

To illustrate the emissivity of real materials, Figure I.4 compares the spectral hemispherical emissivity of SiO_2, graphite and aluminum (Al) to that of a blackbody. SiO_2 is a very good thermal emitter in the far field. For instance, the emissivity of SiO_2 is above 0.8 from λ = 2 to 7 µm with a maximum that almost reaches 1. The emission spectra of the three selected materials are very different, with a flat behavior for graphite and Al, and large variations for SiO_2. The example of aluminum shows that the emissivity of metals is very low in the infrared region. For opaque materials, emissivity is equal to absorptivity and the sum of absorptivity and reflectivity is equal to 1. Because metals are very reflective, their emissivity in the infrared region is very low. The dependence of emissivity on wavelength, in the case of SiO_2 for example, can sometimes be beneficial for applications such as selective emitters or absorbers.

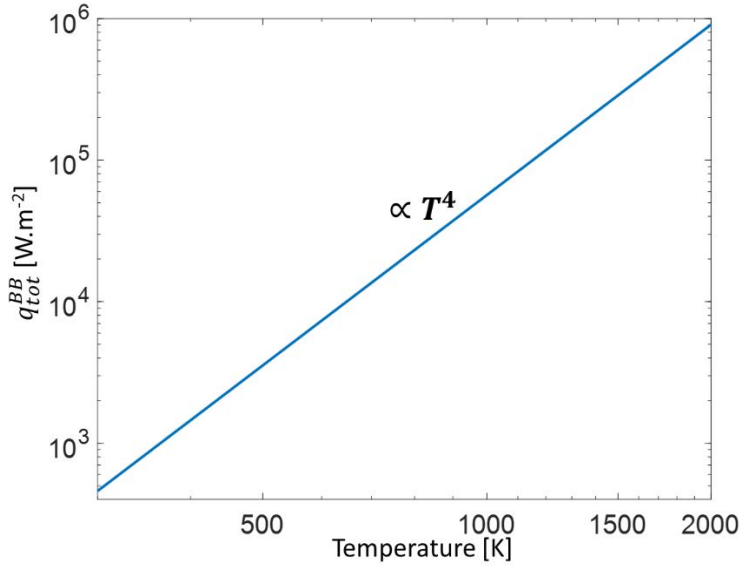

Figure I.3: Total hemispherical radiative heat flux emitted by a blackbody as a function of temperature

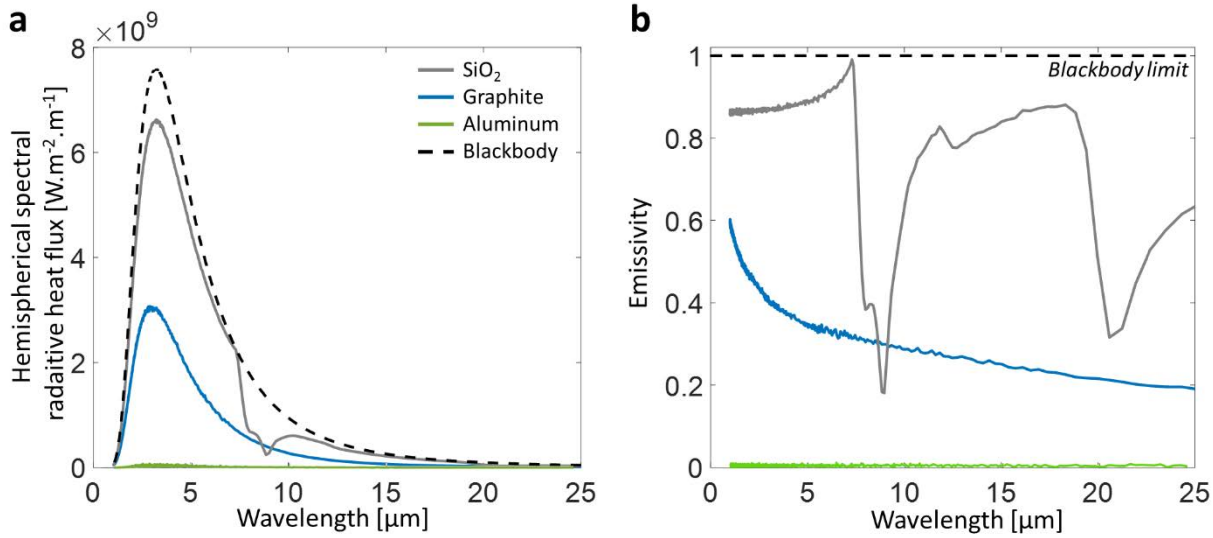

Figure I.4: Hemispherical radiative heat flux (a) and emissivity spectra (b) as a function of wavelength, for the three selected materials compared to those of a blackbody at 900 K

I.3 Near-field radiative heat transfer

In the near-field regime, when the distance between two bodies is approximately lower than λ_{Wien}, the macroscale model for radiative heat transfer is no longer relevant to describe the radiative heat flux. At such distances, propagative waves considered incoherent in the macroscale model, undergo coherency effects such as interferences. Also, evanescent waves contribute to radiative heat transfer simultaneously with propagative waves.

I.3.1 Coherence effects on propagative waves

When two bodies are separated by a distance of the order of λ_{Wien}, coherence effects of thermal radiation occur, causing propagative waves to interfere.

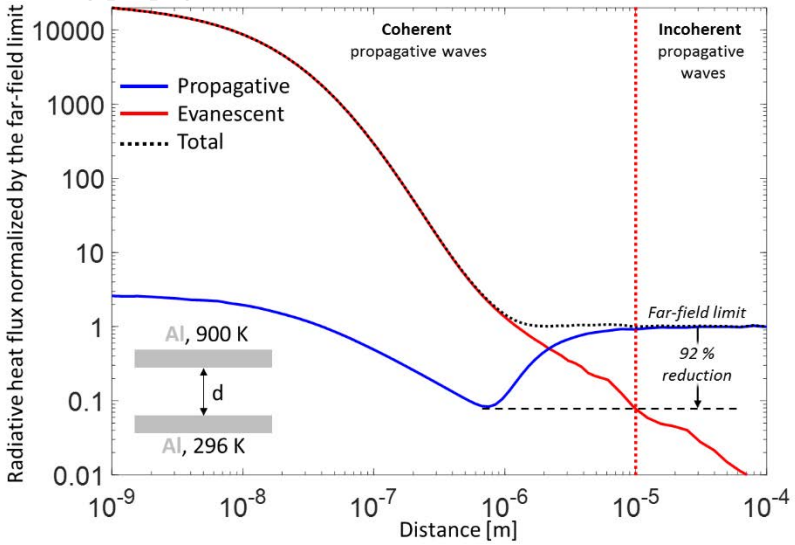

Figure I.5: Propagative and evanescent wave contribution to radiative heat transfer as a function of distance, between a 900 K aluminum semi-infinite plate and a 296 K aluminum semi-infinite plate, normalized by the far-field limit

In the cavity created by the gap distance between the two bodies, propagative waves are reflected, leading to constructive and destructive interferences. Interferences induced by coherence effects can cause lowering of the total exchanged radiative heat flux between the two bodies. This effect is especially strong in the case of highly reflective materials, such as metals[28]. Figure I.5 shows calculated propagative wave contribution to radiative heat transfer between two aluminum plates, respectively at 900 K and room temperature. Calculations were performed using equation (I.7). Data are normalized by the far field limit. For distances above 10 µm, propagative wave contribution to radiative heat transfer is equal to the far-field limit. At lower distances, coherence effects start to appear, leading to a decrease of radiative heat transfer. At d = 700 nm, propagative wave contribution to radiative heat transfer is reduced by 92 % compared to the far field limit. This phenomenon is less important as temperature decreases or for less reflective materials[28]. For materials such as SiO_2, Figure I.6 shows that the reduction of the propagative wave contribution to radiative heat transfer due to coherence effects is only 2%. In addition, this reduction cannot be seen on the total radiative heat flux (sum of the propagative and evanescent wave contributions) due to the contribution of evanescent waves. The increase of radiative heat transfer through evanescent waves overrides the reduction of the contribution of propagative waves caused by coherence effects. Therefore, no reduction of total near-field radiative heat transfer can be measured with low reflective materials such as SiO_2. Experimental works are focusing on enhancement of radiative heat transfer due to evanescent wave contribution.

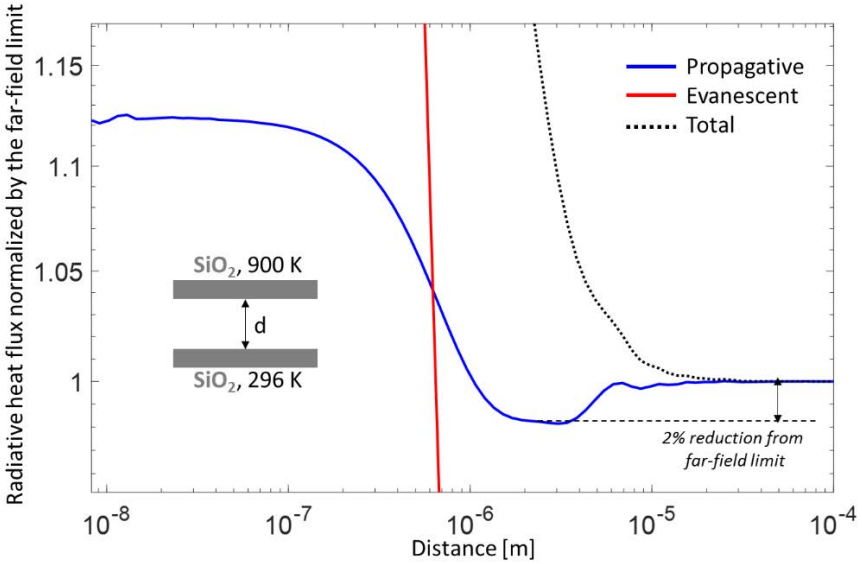

Figure I.6: Propagative and evanescent wave contribution to radiative heat transfer, normalized by the far-field limit, between two SiO_2 semi-infinite plates at 900 K and room temperature

I.3.2 Evanescent waves

Evanescent waves do not propagate away from the emitter surface, but are confined along the emitter surface, at least at one side of the surface[14,29]. The amplitude of this kind of waves decreases exponentially according to the distance from the surface. The distance where the intensity of radiation decreases by a factor 1/e (~37%), corresponding to the penetration depth, is of the order of λ_{Wien}. This explains why radiative heat transfer through evanescent waves only occurs between bodies separated by distances smaller than λ_{Wien}. There are different modes of evanescent waves:

the frustrated and non-frustrated mode (also called surface mode). These two modes come from different phenomena that are described in the following sections.

I.3.2.1 Frustrated modes

The frustrated modes are the result of total internal reflection of propagative waves in the emitting medium. In Figure I.7, when the parallel component of the wavevector $k_{\parallel} < k_0$, (with $k_0 = \omega/c$) the perpendicular component $k_{2\perp}$ is a real number corresponding to the case of a propagative wave. The wave is evanescent when $k_{\parallel} > k_0$, implying that its amplitude is attenuated exponentially above the surface[30]. There is a value of the angle θ_1, called the critical angle θ_c, corresponding to the limit when $k_{\parallel} = k_0$ ($\theta_2 = 90°$). Above this angle, there is total internal reflection in the medium. The frustrated modes are propagative in the medium 1 and evanescent in vacuum.

I.3.2.2 Surface modes

Surface modes are evanescent at both side of the interface. In Figure I.7, these modes correspond to $k_{\parallel} > k_1$, with $k_1 = n_1 k_0 = n_1 \frac{\omega}{c}$ (n_1 being the refractive index of medium 1). Surface mode resonances can result from the coupling between a mechanical oscillation in the structure of the material and the electromagnetic field. In the case of dielectric materials, the phonons are oscillating and the coupling is called surface phonon polariton (SPhP). In a similar way, natural oscillations of the electrons in a metal are called plasmons so the coupling is called surface plasmon-polariton (SPP).

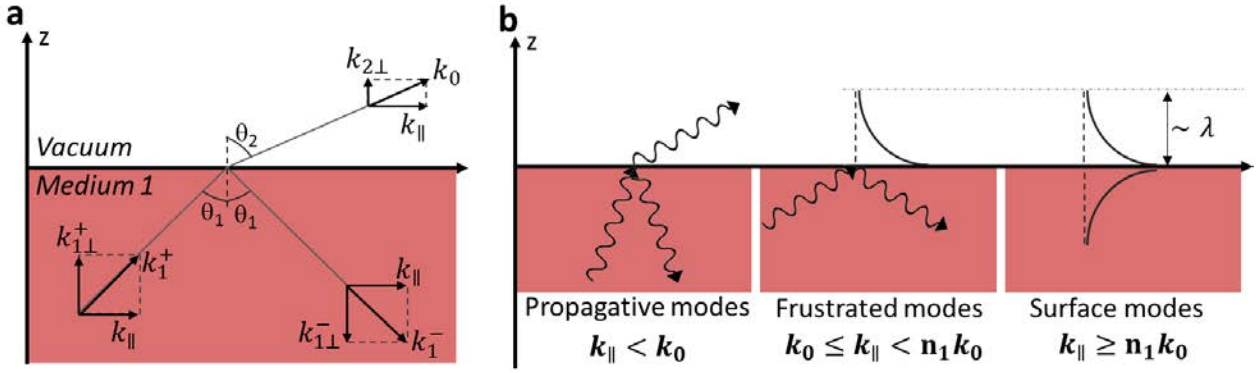

Figure I.7: (a) Schematic of a wave incident at an interface. (b) Different types of propagative and evanescent waves

I.3.3 Near-field radiative heat transfer calculations between two planar and parallel bodies

The first exact theoretical calculations of radiative heat transfer between two planar and parallel bodies in the near field were performed by Polder and Van Hove[14] in 1971. The calculation method is based on the fluctuation-dissipation theorem applied to the thermally fluctuating micro-currents in the medium, constituting the source of the emitted thermal radiation. The exchanged radiative flux is determined from the complex dielectric function $\varepsilon = \varepsilon' + i\varepsilon''$ of the materials[14,31]:

$$q_{13}(d,\omega,T_1) = \frac{\Theta(\omega,T_1)}{4\pi^2}\int_0^{k_\parallel<k_0} k_\parallel \sum_{i=TE,TM} \frac{\left(1-\left|r_{21}^i\right|^2\right)\left(1-\left|r_{23}^i\right|^2\right)}{\left|1-r_{21}^i r_{23}^i e^{2ik_{2\perp}d}\right|^2} dk_\parallel + \frac{\Theta(\omega,T_1)}{\pi^2}\int_{k_\parallel=k_0}^{\infty} k_\parallel e^{-2Im(k_{2\perp})d} \sum_{i=TE,TM} \frac{Im\left(r_{21}^i\right)Im\left(r_{23}^i\right)}{\left|1-r_{21}^i r_{23}^i e^{2ik_{2\perp}d}\right|^2} dk_\parallel , \quad (I.7)$$

$$\Theta(\omega,T) = \frac{\hbar\omega}{e^{\frac{\hbar\omega}{k_B T}}-1}. \quad (I.8)$$

In Eq. (I.7), $q_{13}(d,\omega,T_1)$ is the radiative flux emitted at the frequency ω by the medium *1*, at a temperature T_1 and absorbed by the medium *3* separated by a vacuum gap d corresponding to medium *2* in Figure I.8a. Blue and red parts of the equation correspond respectively to propagative and evanescent waves contributions. The perpendicular component of the wavevector is $k_{2\perp} = \sqrt{\varepsilon k_0^2 - k_\parallel^2}$. The Fresnel reflection coefficients $r_{21,23}^{TE,TM}$ at the interfaces *12* and *23* are accounting for both the transverse magnetic *TM* and transverse electric *TE* polarizations (Figure I.8b) and are defined as

$$r_{21}^{TE} = \frac{k_{2\perp}-k_{1\perp}}{k_{2\perp}+k_{1\perp}}, \quad (I.9)$$

$$r_{21}^{TM} = \frac{k_{2\perp}\varepsilon_1 - k_{1\perp}\varepsilon_2}{k_{2\perp}\varepsilon_1 + k_{1\perp}\varepsilon_1}. \quad (I.10)$$

Eq. (I.8) is the mean energy of a Planck oscillator. The exchanged flux between the two media is the difference between that emitted by *1* and absorbed by *3*, and that emitted by *3* and absorbed by *1*:

$$q(d,\omega,T_1,T_3) = q_{13}(d,\omega,T_1) - q_{31}(d,\omega,T_3). \quad (I.11)$$

Polder and Van Hove reported a sharp enhancement of the exchanged radiative power as the vacuum gap between two bodies decreases. The impact of surface polariton resonances were investigated in other theoretical works[32,33]. They reported several orders of magnitude enhancement of the radiative heat flux between two plates made of silicon carbide (SiC) or silica glass. Contribution of the surface waves is demonstrated to be largely dominant at low distance in the order of 10 nm. Strikingly, heat transfer becomes almost monochromatic with most of the exchanged flux taking place near the wavelength of the surface polariton resonance.

In addition to theoretical analyses, near-field radiative heat transfer between two bodies can be investigated experimentally. The next section gives a review of published experimental works, investigating various geometries and other key parameters, such as temperature and materials.

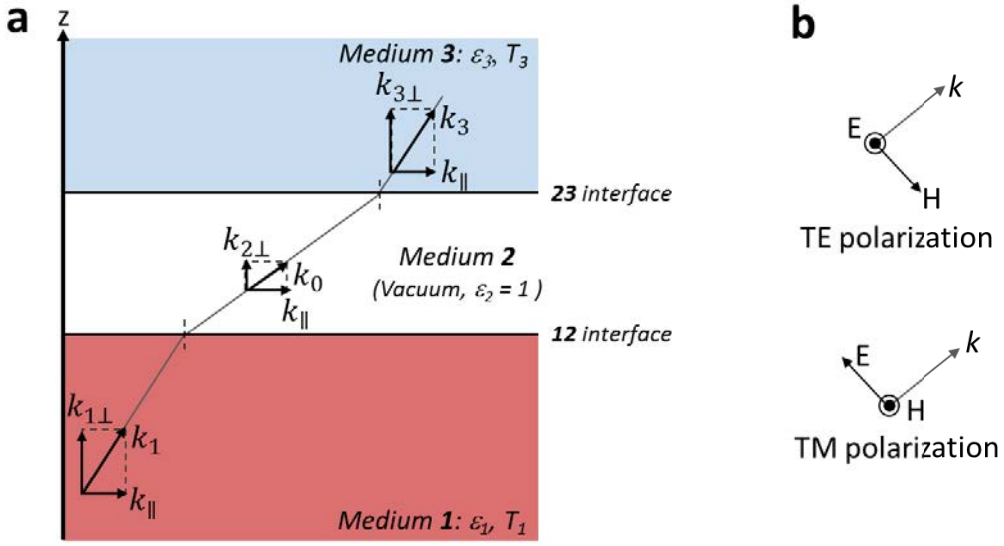

Figure I.8: (a) Configuration of two planar bodies separated by a vacuum gap. (b) Difference between TE and TM polarizations (E and H are the electric and magnetic fields)

I.4 Experimental demonstrations of radiative heat transfer enhancement in the near field

Radiative heat transfer in the near field was well studied experimentally. The first measurement of radiative heat transfer enhancement was performed by Hargreaves[34] in 1969. He measured the exchanged radiative power between two plates made of a 100 nm chromium layer deposited on glass, as a function of the vacuum gap distance between the plates. One of the plates was held at 306 K while measuring the power that had to be supplied to keep the other plate at 323 K. He reported an enhancement factor of ~ 2 of the exchanged radiative power as the gap distance decreased from 5.8 µm to ~ 1 µm. From then on, many experimental proofs of near-field radiative heat transfer enhancement were reported. Various configurations were studied, in terms of temperature differences, materials or geometries[15–17,23–25,34–69]. In next sections, works found in the literature are classified as a function of various parameters. This classification aims to find the global trends and improvement paths for future experiments.

I.4.1 Temperature difference and minimum distance

Figure I.9 reports on experimental published works for different geometries, as a function of the minimum gap distance and the maximum temperature difference between the emitter and the substrate. Uncertainties may exist on values reported from literature, especially on estimated values such as minimum distances, which cannot always be measured directly. Three different types of geometry were considered for experiments. They consist in a planar substrate and an emitter shape being either a plane, a sphere or a tip. In Figure I.9 it appears that the minimum reachable distance is of the order of angströms for the tip-plane geometry, compared with a few nanometers with the sphere-plane and tens of nanometers with the plane-plane geometry.
The sub-micrometer distance range is technically challenging to achieve for the plane-plane geometry because of parallelism issues. As a consequence, sub-micrometer distances for this geometry could be studied only during the last decade. It is interesting to remark that no experimental work was performed with temperature differences between the emitter and the

substrate above 420 K. In the aim of energy conversion applications, large temperature differences are required to maximize thermal energy conversion. The maximum energy conversion efficiency of a heat engine was given by Carnot[70] in 1824 and expressed as the following:

$$\eta_{max} = \frac{\Delta T}{T_{hot}} = 1 - \frac{T_{cold}}{T_{hot}}, \qquad (I.12)$$

where temperatures of the hot and cold reservoirs are labelled T_{hot} and T_{cold}, ΔT being their difference. It appears that the maximum conversion efficiency tends to 1 when $T_{hot} >> T_{cold}$. Large temperature differences also lead to large exchanged radiative power (see Sec. I.3.3, Eq. (I.11)) and, by extension, lead to large generated power from an energy conversion device.

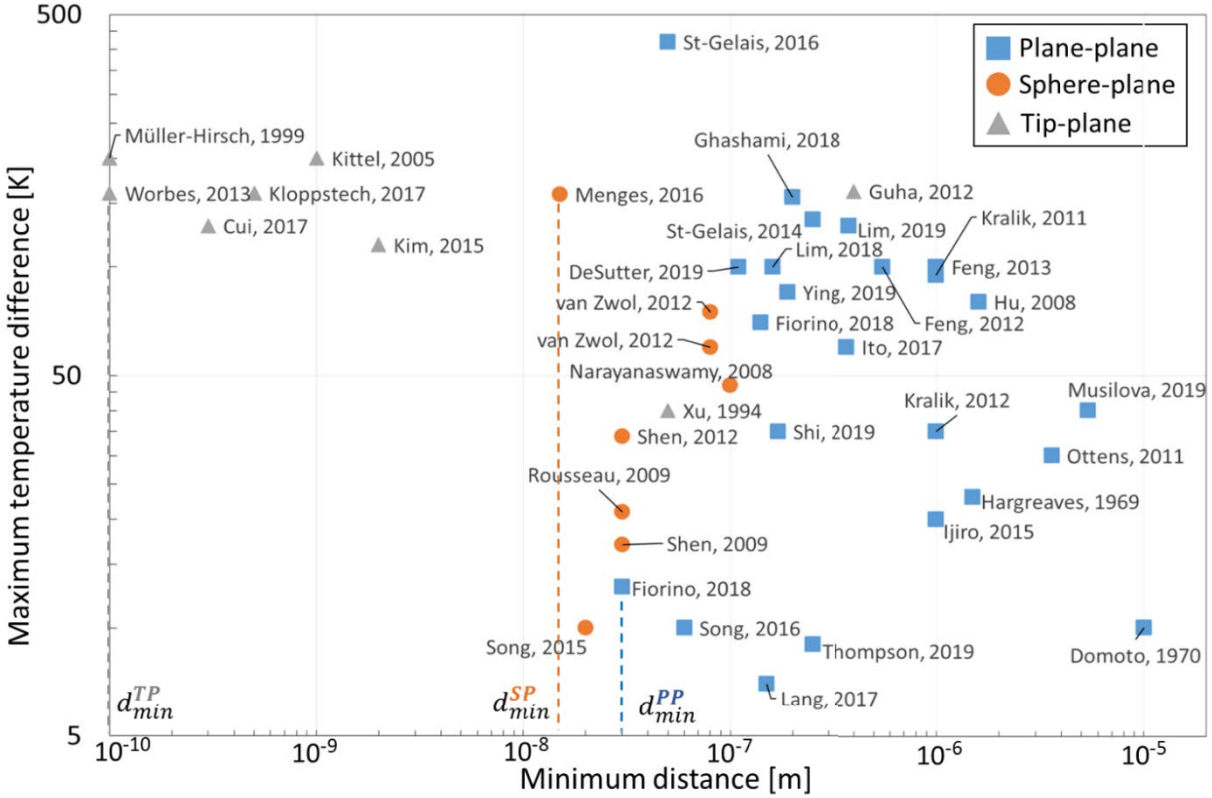

Figure I.9: Experimental demonstrations of near-field radiative heat transfer enhancement as a function of minimum gap distance and maximum temperature difference for various geometries[15–17,23–25,34–69]

I.4.2 Exchange area

It is obvious that the exchanged radiative power between two bodies is related to the exchange area. The exchange area is defined as the projection of the emitter area surface on the substrate (see inset of Figure I.10). If the emitter is larger than the receiver, then the exchange area is that of the receiver. As a consequence, the larger the exchange area the larger the exchanged power. Based on this fact it is interesting to sort the experimental works by their exchange areas. Figure I.10 summarizes the exchange area identified in these works, as a function of the minimum distance for the three different geometries. For the tip, the exchange area A for near-field radiative heat transfer is based on the curvature radius R_C at the apex of the tip. Similarly for the sphere, the exchange area is based on the sphere radius R_{sphere} (see the legend in Figure I.10). In the case of a planar

emitter, the exchange area can be either πR^2 for a disc of radius R, or L_xL_y for a rectangle (L_x and L_y being respectively the length and the width).
In Figure I.10, the relation between the minimum distance d_{min} and the exchange area A is clearly highlighted. The smallest distances are reached by the devices with the smallest exchange area. This is simply due to the fact that it is experimentally challenging to approach a large object to another at small distances. The experimental points can be fitted considering the following power laws: $A = 6.4\ 10^{10} d_{min}^{2.59}$ or $d_{min} = 6.7\ 10^{-5} A^{0.39}$. It might be a loose technological limit.
Three main categories can be extracted from the experimental data and are called here macroscale, microscale and nanoscale devices. Macroscale devices show the largest exchange areas but also the largest minimum reachable distances. This category is constituted only by planar emitters with an exchange area larger than 1 mm^2. Usually, the gap distance between large planes is provided by microstructured spacers. Recently, DeSutter *et al.*[23] used 20 and 30 µm diameter SU-8 3005 epoxy resist micropillars. They could reach vacuum gaps as low as 110 nm between large 5x5 mm^2 planes. Microspheres can also be used as spacers. In the work of Hu *et al.*[39], they used 1 µm diameter polystyrene spheres to create a gap between discs having a diameter of 1.27 cm. In any case, the spacers are made of low thermal conductivity materials in order to minimize heat transfer via conduction. Microscale devices have exchange areas between 1 µm^2 and 1 mm^2. This category is composed of the three emitter geometries and exhibit minimum distances from ~ 10 nanometers to one micron. Minimum distances reached for this category are often limited by surface roughness[40,56]. It can be noted that two tip-plane experiments are in this category. Xu *et al.*[36] used a flattened indium needle as the emitter. The needle was brought into contact with the sample and a force was applied to flatten the tip of the needle and create a flat surface. Thus, this work could also be classified as a plane-plane experiment. In the work of Guha *et al.*[45], they used a tip with a large 15 µm radius of curvature at the apex. This value is much higher than that of the other works dealing with a tip-plane configuration, where curvature radii are less than a micron[17,25,37,48,53,64].

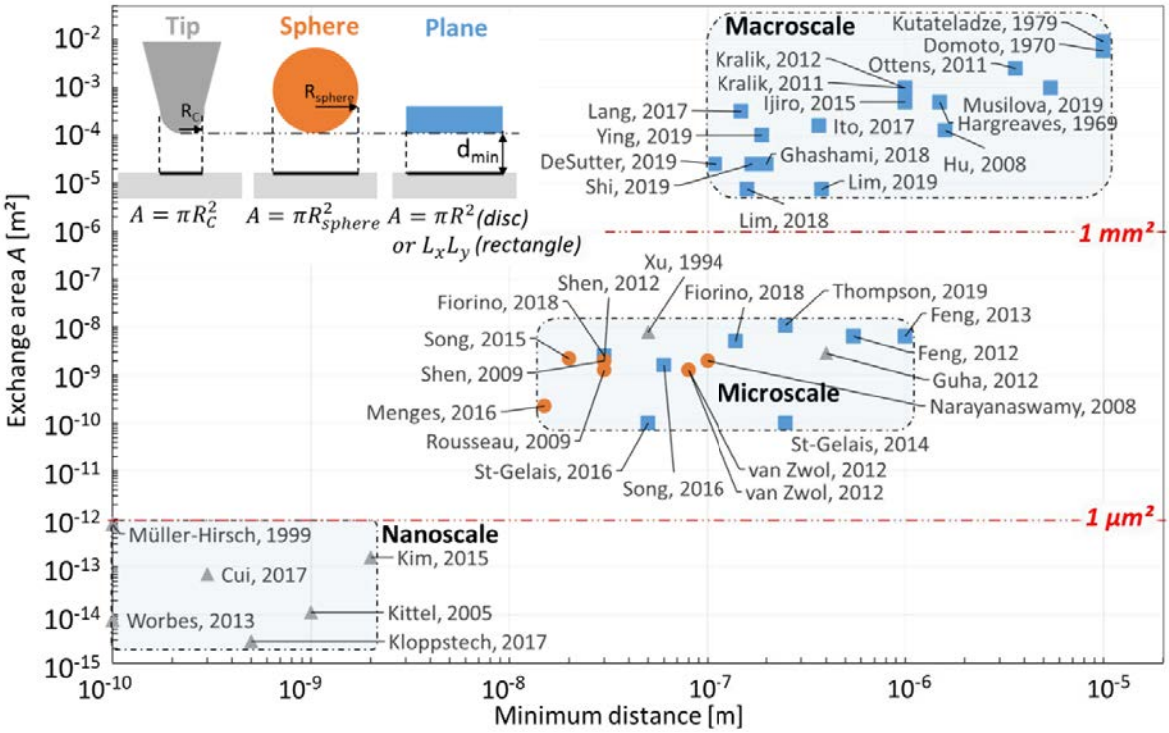

Figure I.10: Experimental works classified by exchange area according to the minimum distance for various geometries

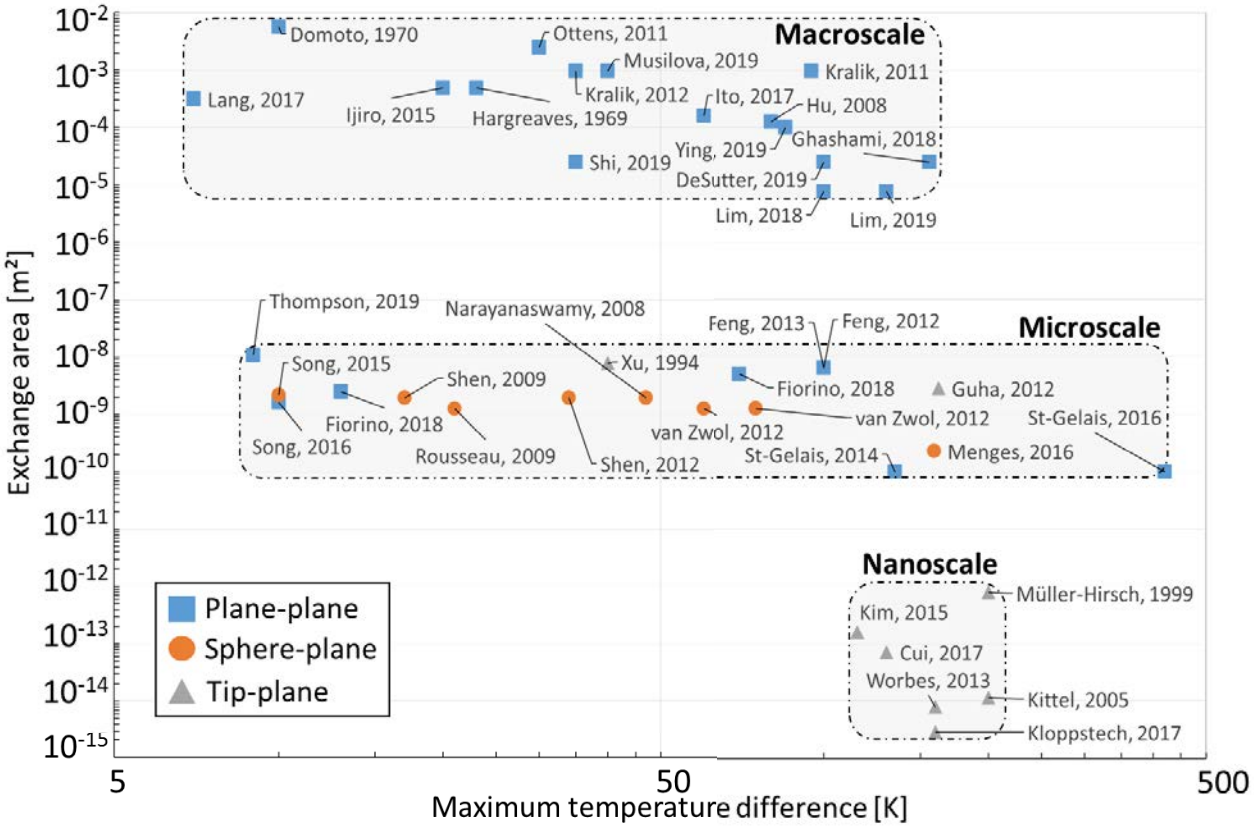

Figure I.11: Experimental works classified by exchange area according to the maximum temperature difference for various geometries

The last category is that of nanoscale devices, which is composed only of tip-plane geometries with exchange areas lower than 1 μm^2. With this category of experimental devices, the extreme near field at a sub-nanometer distance range can be studied. Minimum distances are limited by snap-in and stiction issues. Snap-in is caused by attraction forces bringing the tip at contact with the sample at low distance (see measurements in Figure III.23). Stiction is the static friction that needs to be overcome to move an object located in close proximity to another. In the similar works of Kloppstech *et al*.[25] and Cui *et al*.[53], measurements between a tip and an electrically conductive gold surface were performed in the last 5-7 nm before contact. Kloppstech *et al*. made measurements between a 30 nm radius of curvature tip at room temperature, fabricated with a Au/Pt thermocouple integrated at the apex, and a flat gold surface cooled down to reach ΔT = 160 K. Cui *et al*. chose a larger 150 nm radius of curvature tip with a Au/Cr thermocouple and a heated gold surface so as to reach ΔT = 130 K. In both works, the integrated thermocouple at the apex of the tip was used as a thermometer to measure the temperature increase or decrease of the tip, initially at room temperature, as a function of the gap distance. They reported radiative fluxes significantly higher than predicted. These deviations with theory were not well explained but could be attributed to probe contamination or to other heat transfer mechanisms occurring at low distances.

For microscale and nanoscale devices, the gap distance between the emitter and the substrate is monitored by piezoelectric actuators. Piezoelectric materials can retract or expand when a voltage is applied. This property allows motions with sub-nanometer resolution, which is perfectly suited for near-field radiative heat transfer experiments.

Due to the small exchange area of the nanoscale devices, larger temperature differences are needed in order to increase the signal-to-noise ratio for detecting near-field radiative heat transfer. This is clearly observed in Figure I.11, where the exchange area is represented as a function of the maximum temperature difference. Nanoscale devices were used in experiments studying temperature differences comprised between 100 and 200 K only.

The largest temperature difference of 420 K[49] was studied with a microscale device. The maximum temperature difference for the macroscale devices is 156 K. This lower maximum temperature difference can be explained by the fact that macroscale devices exchange a lot of radiative power due to the large exchange surface. This large thermal flux between the emitter and the substrate can cause the substrate to be significantly heated, leading to substrate cooling and thermomechanical issues such as thermal expansion. In Figure I.12, near-field radiative thermal conductance is represented as a function of exchange area. Near-field conductance, corresponding to the conductance enhancement above the far-field limit, is showed in $W.K^{-1}$ and in $W.m^{-2}.K^{-1}$ when normalized by the exchange area. In the bottom figure, a clear trend appears as expected with an increase of the near-field radiative conductance G as a function of the exchange surface. Conductances from experimental works, with room temperature substrates, follow a $G \propto A^{0.90}$ evolution, close to the $G_{Blackbody}^{T=300K} \propto A^{1}$ evolution calculated between a blackbody at 300 K and a blackbody having a temperature tending to 300 K. The measurements exhibiting the lowest and largest conductances are separated by more than 7 orders of magnitude. Some experimental points are significantly away from the shaded area representing the evolution trend. These deviations can be partly explained by taking the studied materials into account. Most of the experimental works focus on SiO_2. It is a material well suited for near-field radiative heat transfer because it supports surface phonon polaritons resonances (see details in chapter 2).

For a same temperature difference and exchange surface configuration, the measured exchange radiative power can strongly vary as a function of materials. In the literature, a few materials other than SiO_2 were studied. For instance, gold (Au) was investigated in most tip-plane geometry experiments[17,25,53]. Other metals were also investigated. The works of Domoto *et al*.[35] and Kralik *et al*.[43,69] focused on copper (Cu) and tungsten (W) respectively. It is seen in Figure I.12 that the measured conductances for these two metals were several orders of magnitude lower than that from the works involving SiO_2. Other various materials were also studied, such as doped silicon[23,57], sapphire[42] or nitrides (silicon nitride (SiN)[61], niobium nitride (NbN)[60]). The effect of multi-layered materials were explored in the work of Lim *et al*[62]. They measured near-field radiative heat transfer between two planar multi-layer structures, made alternatively of titanium (Ti) and magnesium fluoride (MgF_2). It was demonstrated that near-field thermal radiation could be tuned using surface plasmon polaritons and their interactions at each metal (Ti)/dielectric (MgF_2) interfaces. Another parameter explaining deviations from the global trends for the experiments from Domoto[35], Kittel[17], Kralik[43,69], Kloppstech[25] and Musilova[60] is the substrate at low temperature. So in addition to the effect of the material, cryogenic temperatures may have an impact on the measured near-field radiative conductance.

In Figure I.12a, the conductance is normalized by the exchange area. It appears that all the experimental works involving SiO_2 (shaded area) have measured conductances over 4 orders of magnitudes. It is worth noticing that the sphere-plane experiments all gather in the same zone. This is mainly due to the fact that the sphere diameters that were used are very similar, from 40 to 53 µm[16,40,41,44,47,67,68], with an exception for the work of Menges *et al*.[24] with a 17 µm in diameter sphere. In this last work, they investigated the near-field radiative heat transfer between a SiO_2 sphere and a vanadium dioxide (VO_2) thin film (15 nm thickness) deposited on a titanium dioxide

(TiO_2) substrate. VO_2 is an interesting material because of its transition from an insulating to a metallic state around 46 °C. They used a SThM silicon probe as a heater/sensor to heat the sphere and determine its temperature and dissipated power. They found a factor 2 difference on the near-field radiative conductance comparing the insulating and the metallic state.

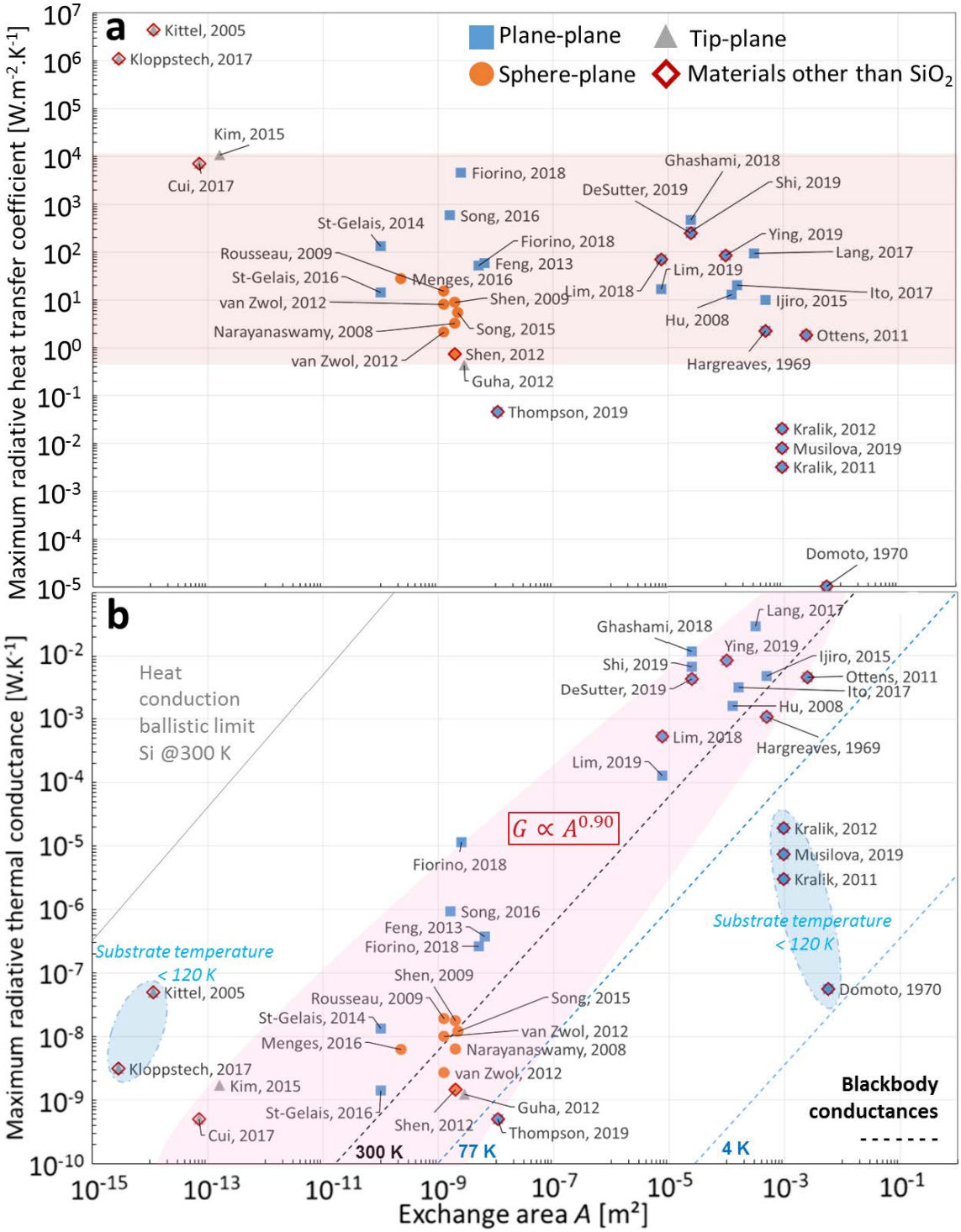

Figure I.12: Maximum radiative heat transfer coefficient (a) and maximum radiative thermal conductance (b) as a function of exchange area for the three geometries. Experimental works involving materials other than SiO_2 are highlighted

This comparison of the experimental works found in the literature tells us that there is space for experiments with the aim to go beyond this state-of-the-art. Large temperature differences over 420 K are still uninvestigated and are required for energy conversion applications. Another emerging field of study is certainly the material dependence of near-field radiative heat transfer. The wide majority of the experimental works used SiO_2, so it could be worth performing experiments with many other materials instead. This is especially true for the sphere-plane geometry for which experimental works only focused on a limited range of materials. A sphere made of a material different than SiO_2 was used only in the work of Shen *et al*.[44] in 2012. They used a 50 µm in diameter glass sphere with a 100 nm thick gold film deposited by sputtering. The skin depth of gold in the wavelength range studied in this work was less than 20 nm, so the near-field radiative transfer measurements could be attributed to a gold surface. They attached the sphere on the tip of a gold-coated silicon nitride AFM cantilever to create a bimaterial effect. This effect induces a bending of the AFM cantilever as a function of temperature because of the difference in thermal expansion coefficient between the two different materials. After calibration, a relation between the bending and the temperature could be deduced and used to determine the temperature as a function of the bending. In this work, heating of the sphere was provided by a 3 mW laser beam at 650 nm wavelength. In this Au-Au experiment, a radiative conductance 4 times smaller than in their previous SiO_2-SiO_2 experiment in 2009[41] was measured with the same technique.

I.4.3 Resolution of the experimental works

The ability to detect radiative conductance and power variations is a key parameter for near-field radiative heat transfer experiments. It was shown previously that the conductance increases accordingly to the exchange area. In Figure I.13a, the near-field radiative conductance resolution δG_{NF} (in $W.K^{-1}$), corresponding to uncertainties of conductance measurements, is represented as a function of both exchange area (left) and conductance (right). The conductance resolution is higher than 1 $\mu W.K^{-1}$ for the macroscale devices. This is due to the large exchange area and the large conductance measured with these setups. The lowest resolutions are found for the microscale and nanoscale experiments with similar values of a few tens of picowatts per kelvin. It seems that, below an exchange area of $\sim 10^{-8}$ m^2, the conductance resolution levels off independently of the exchange area. In Figure I.13a (right figure), δG_{NF} is represented as a function of conductance. With this representation, a clear trend of the conductance resolution appears with $\delta G_{NF} = 0.1 G^{0.98}$. This means that the percent error of the near-field radiative conductance measurements performed in published experimental works is around 10 % and varies proportionally to the conductance. Resolution in terms of radiative power $Q_{NF} = G_{NF}\Delta T$, is provided in Figure I.13b, with the power resolution δQ_{NF} plotted as a function of maximum radiative power. Globally, the same trend appears as that from the conductance resolution curve, with a quasi-linear behavior $\delta Q_{NF} = 0.1 Q_{NF}^{0.98}$. However, the best performances in conductance are not obtained by the same experiments when compared in power. This is explained by the dissimilarities of maximum temperature differences. The temperature difference studied by Kim *et al.*[48] is 115 K, while it is only 9 K for Thompson *et al*.[61]. In terms of radiative conductance resolution, the first experimental work exhibits the best performance, but the second work is the best in terms of power resolution. Therefore, large temperature differences may be useful to enhance conductance resolution.

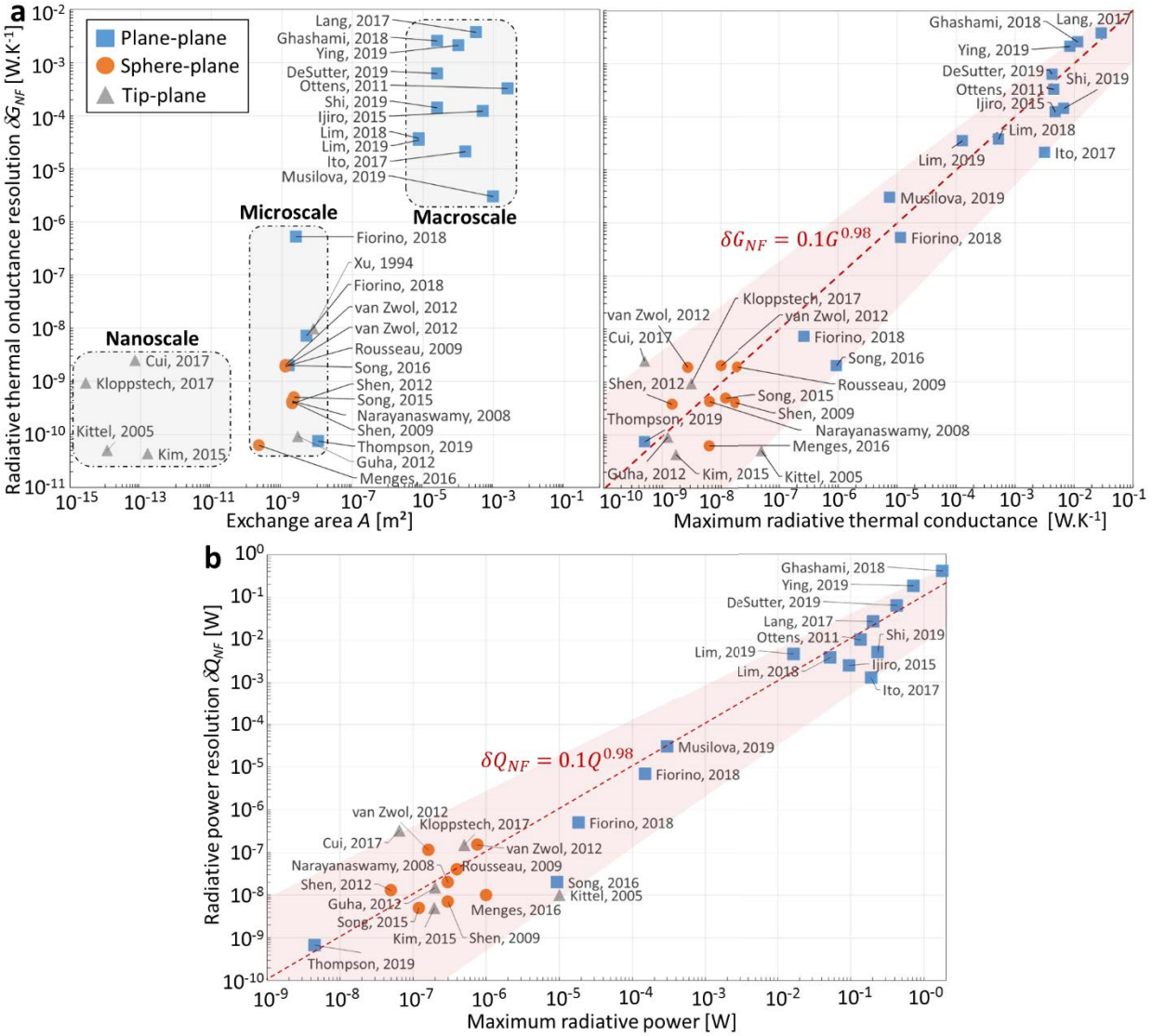

Figure I.13: Near-field radiative conductance (a) and power (b) resolution as a function of the exchange area and conductance and power for the three different geometries

I.5 Conclusions

Thermal radiation of macroscale bodies has been well described since the early 1900s by the blackbody theory. At the nanoscale, radiative heat transfer exhibits major changes in terms of spectral distribution and total power of thermal radiation compared with macroscale thermal radiation. For calculations, optical properties of the emitting bodies represented by the dielectric function are taken into account to calculate emission spectra of real materials, depending on distance from the surface. Different behaviors can appear, in the form of emissivity peaks and drops, at given wavelengths where various effects such as resonances can occur[71]. Since 1970s, after the first exact calculation of near-field radiative heat transfer, many theoretical and experimental works have described and measured the influence of evanescent waves and coherence effects on thermal radiation heat transfer. Measurements between planar surfaces are challenging

because of parallelism issues. Until recently, the sub-micrometer regime could be studied only with sphere-plane or tip-plane geometries where parallelism issues do not exist. These two geometries are great for probing near-field heat transfer at low distances, but the exchange power is low due to the small exchange areas. Various materials and temperature differences were studied in the literature. However, large temperature differences with $\Delta T > 420$ K have not been investigated yet. In the aim of exploiting evanescent waves for thermal energy harvesting, large temperature differences is a key parameter that has to be experimentally studied at the lowest possible distances. A compromise between small reachable distance and large radiative flux leads to perform experiments with a microsphere emitter geometry. In order to compare and complete the state of the art, the experimental study of near-field radiative heat transfer detailed in chapter IV will focus on classical materials, such as SiO_2, and other materials presenting an interest for energy conversion applications (see details in chapter 2). Near-field radiative conductance temperature dependence will be also studied with temperature differences up to 900 K.

Chapter II

Near-field radiative heat transfer calculations

II.1 Introduction

Before experimentally measuring radiative heat transfer in the near field, calculations have to be made in order to determine the expected order of magnitude of heat fluxes. This analysis is also important to determine the best configurations to be tested experimentally. Thus, one of the objectives is the selection of the emitter and receiver materials. The objective is to find an emitter material that enhances as much as possible the exchanged radiative heat flux in the near field when combined with a TPV cell as a receiver, for specific wavelengths where photocurrent generation occurs. This wavelength range corresponds to wavelengths smaller than the gap wavelength of InSb ($\lambda < \lambda_{gap}^{InSb}$), the semiconductor material selected in this work (see Sec. V.4). Calculations of the exchanged radiative power will be performed as a function of emitter-substrate distance, temperature difference, materials and geometry, based on the optical properties of the materials. The system studied in the experiments is simulated by separately calculating the contribution of the propagative and evanescent waves. This is necessary to optimize the dimensions of the emitter and the TPV cell, with the aim of maximizing the enhancement of the photoconversion in the near field. The numerical calculation tools developed here are also useful for studying the temperature and material dependence of near-field radiative heat transfer. With the experimental setup, several pairs of emitter-receiver materials are studied. An objective of this theoretical analysis is to determine the expected near-field behaviors as a function of materials and temperature differences for comparisons with experimental results.

II.2 Plane-plane geometry

The first step of the theoretical study is the calculation of the near-field radiative heat transfer between two semi-infinite planar media separated by a vacuum gap. The results of this study will provide a set of heat flux databases for different configurations of materials and temperatures, as a function of the gap distance between the two plates. These results will be used to estimate the evanescent wave contribution to the exchanged radiative heat flux in the case of the sphere-plane geometry with the proximity flux approximation.

II.2.1 Radiative heat flux calculations

Radiative heat flux calculations are made between two semi-infinite planar media. A schematic of the configuration is given in section I.3.3 (Figure I.8). The emitting and receiving bodies are labelled *1* and *3* and are separated by a vacuum gap labelled *2*. The equation of the spectral radiative flux emitted by *1* and absorbed by *3* is given in Eq. (I.7) . The propagative q_{13}^{prop} and evanescent q_{13}^{evan} contributions of the radiative heat flux can be calculated separately according to

$$q_{13}^{prop}(\omega) = \frac{1}{4\pi^2}\frac{\hbar\omega}{e^{\frac{\hbar\omega}{k_B T}}-1}\int_0^{k_\parallel<k_0} k_\parallel \sum_{i=TE,TM} \frac{\left(1-\left|r_{21}^i\right|^2\right)\left(1-\left|r_{23}^i\right|^2\right)}{\left|1-r_{21}^i r_{23}^i e^{2ik_{2\perp}d}\right|^2} dk_\parallel \,, \qquad (II.1)$$

$$q_{13}^{evan}(\omega) = \frac{1}{\pi^2}\frac{\hbar\omega}{e^{\frac{\hbar\omega}{k_B T}}-1}\int_{k_\parallel=k_0}^{\infty} k_\parallel e^{-2Im(k_{2\perp})d} \sum_{i=TE,TM} \frac{Im\left(r_{21}^i\right)Im\left(r_{23}^i\right)}{\left|1-r_{21}^i r_{23}^i e^{2ik_{2\perp}d}\right|^2} dk_\parallel \,. \qquad (II.2)$$

It is reminded that $\hbar\omega$ is the energy of a photon, $\hbar$ the reduced Planck's constant, k_B is Boltzmann's constant, and $r_{21,23}^{TE,TM}$ the Fresnel reflection coefficients defined in Eq. (I.9) and (I.10). The total

flux $q(d, \omega, T_1, T_3)$ exchanged between the two media is the difference between that emitted by *1* and absorbed by *3*, and that emitted by *3* and absorbed by *1* (equation (II.3)):

$$q(d, \omega, T_1, T_3) = \left(q_{13}^{prop} + q_{13}^{evan}\right) - \left(q_{31}^{prop} + q_{31}^{evan}\right). \quad (II.3)$$

The total flux depends on distance d between the two media, angular frequency ω, and media temperatures T_1 and T_3. It is calculated based on the optical properties of the materials, represented by the complex dielectric function ε.

II.2.2 Optical properties

Dielectric functions of the materials that were used for the calculations come from experimental measurements data reported in the literature or from models. Eq. (II.1) and (II.2) show that the imaginary part of the dielectric function has a large influence on radiative heat transfer. Materials with resonances such as surface phonon polaritons exhibit large peaks in the imaginary part of the dielectric function, thus resulting in an increase of radiative heat flux for the evanescent wave contribution. For near-field thermophotovoltaic applications, such resonances can be valuable to maximize the generated electrical power. The condition is that resonances must occur in the spectral range where photocurrent generation occurs, at wavelength lower than the gap wavelength of the TPV cell material ($\lambda < \lambda_{gap}^{InSb}$). The dielectric functions of the studied materials are presented as a function of wavelength in Figure II.1 .

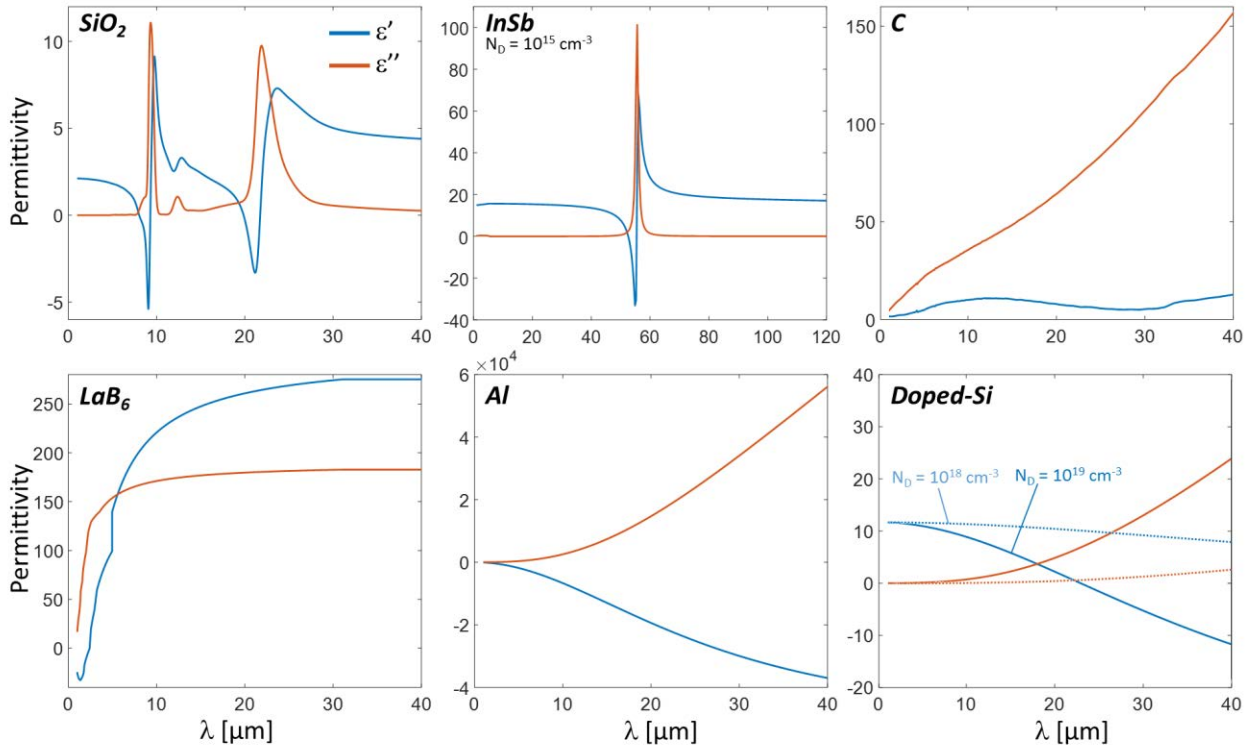

Figure II.1: Real and imaginary parts of the dielectric functions of different materials at room temperature

II.2.2.1 SiO_2

For SiO_2, data come from measurements[72] performed from room temperature up to 1480 K (Figure II.2). This material was chosen for its two infrared resonances, already well-studied experimentally as highlighted in chapter I. The dielectric function exhibits a dependence on temperature with a stronger effect close to the peaks of the imaginary part ε''. Calculations at an intermediate temperature, 730 K for example, were made using interpolated data between the two closest measured temperatures, 672 and 966 K for this example. The three observed peaks on ε'' are caused by the resonances of the atomic bonds. The peaks at 9.0 µm and 12.5 µm correspond respectively to the asymmetric and symmetric stretching vibration of O-Si-O bonds. The third peak near 22 µm is caused by the bending vibrations[73].

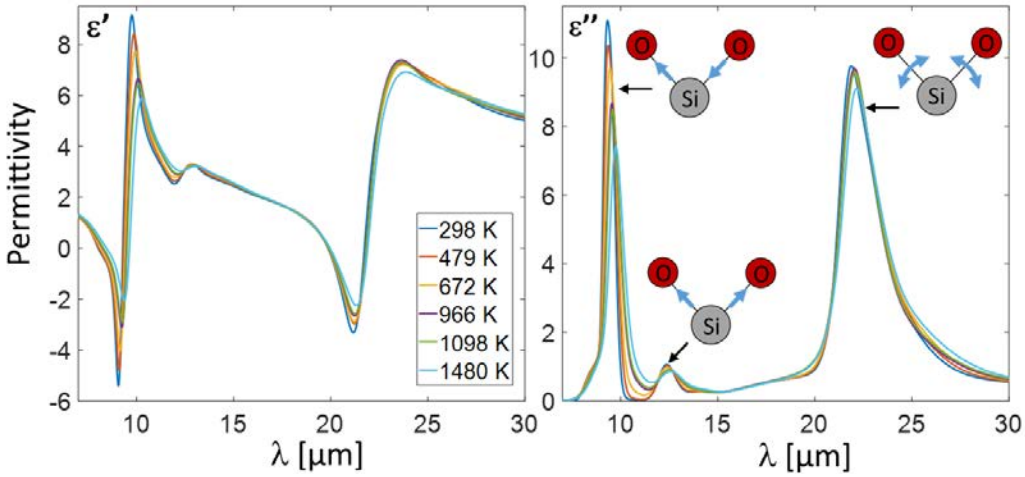

Figure II.2: Real (left) and imaginary (right) part of the dielectric function of SiO_2 as a function of temperature. Sketches on the right graph represent vibrations modes of silica

II.2.2.2 InSb

The dielectric function was calculated using a code developed in this work[74]. The effect of the p- or n-doping level was taken into account, along with the temperature dependence. The gap wavelength of InSb decreases from 7.3 down to 5.3 µm when temperature decreases from room temperature down to 77 K.

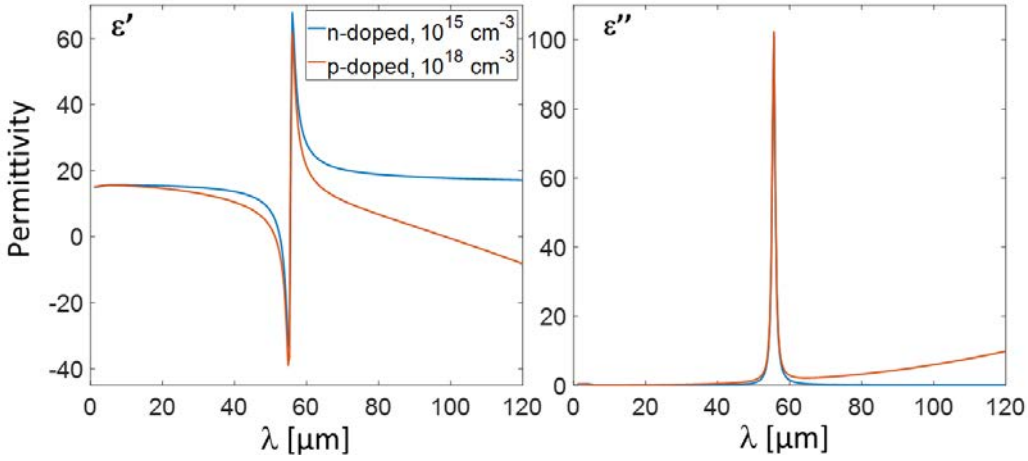

Figure II.3: Dielectric function of InSb at 77 K for two different doping levels

The values presented in Figure II.3 were calculated at 77 K because it corresponds to the chosen working temperature of the InSb TPV cells (see Sec. VI.2.3.1). Because of the free carriers, influence of doping has a significant impact for $\lambda > 20$ µm but will not affect much radiative heat transfer with emitters around 1000 K, where the wavelength of the maximum spectral flux is $\lambda_{Wien} \sim 3$ µm. In the same way, the phonon polariton at $\lambda \sim 55$ µm has a large wavelength compared to λ_{Wien}.

II.2.2.3 Graphite

Data come from measurements found in the literature[75]. This material is interesting for the relatively high imaginary part of its dielectric function at short wavelengths, especially at $\lambda < \lambda_{gap}^{InSb}$ where photocurrent generation occurs.

II.2.2.4 LaB_6

Lanthanum hexaboride (LaB_6) was studied for the same reasons as graphite but in this case, both the real and the imaginary part of the permittivity are high. The data used for the calculations were extracted from curves found in the literature[76,77].

II.2.2.5 Al

Aluminum (Al) was chosen to test the possibility to use metals. The dielectric function was calculated using a Drude-Lorentz model[78] with parameters taken from the literature[79]. The model that was used is described as follows:

$$\varepsilon(\omega) = \varepsilon_\infty - \frac{\omega_p^2}{\omega^2 - i\omega\Gamma_D} + \sum_{l=1}^{L} \frac{f_l \omega_p^2}{\omega_l^2 - \omega^2 + i\omega\Gamma_l}. \qquad (II.4)$$

ε_∞ is the dielectric constant when frequency tends to infinity, ω the angular frequency, ω_p the plasma frequency, ω_l the resonance frequency, Γ_D the damping frequency, f_l and Γ_l the strength and damping frequency of the harmonic oscillator l. The following table lists the different parameters and their respective values[79].

Table II.1: Drude-Lorentz model parameters for aluminum

Parameter	Value(s)
ε_∞	1
ω	$1.884\ 10^{11}$ to $1.884\ 10^{15}$ rad.s-1
ω_p	$2.276\ 10^{16}$ rad.s^{-1}
Γ_D	$7.141\ 10^{13}$ s^{-1}
ω_l	$[0.246, 2.346, 2.747, 5.276]10^{15}$ rad.s^{-1}
f_l	0.227, 0.05, 0.166, 0.03
Γ_l	$[0.506, 0.474, 2.0525, 5.138]10^{15}$ s^{-1}
L	4

II.2.2.6 Doped silicon

The last selected material is doped silicon. It is commonly used and its optical properties can easily be tuned by changing the doping type and level. The dielectric function was calculated using a Drude model taking into account the contribution of electrons, indexed *e*, holes indexed *h*[80]:

$$\varepsilon(\omega) = \varepsilon_{bl} - \frac{{N_e e^2}/{\varepsilon_0 m_e^*}}{\omega^2 - i\,{\omega}/{\tau_e}} + \frac{{N_h e^2}/{\varepsilon_0 m_h^*}}{\omega^2 - i\,{\omega}/{\tau_h}}, \qquad (II.5)$$

where $\varepsilon_{bl} = 11.7$ is the constant permittivity accounting for contributions by transitions across the bandgap and lattice vibrations. The two last terms are Drude models for transitions in the conduction band and valence band respectively. The parameters τ_e and τ_h are electron and hole scattering times, and m_e^* and m_h^* are their effective masses equal to $0.27m_0$ and $0.37m_0$ with m_0 being the electron mass in vacuum. The constants e and ε_0 are the electron charge and the permittivity of vacuum. N_e and N_h are the electron and holes concentrations depending on the dopant concentration N_D (donors) and N_A (acceptors). Depending on the doping type, two equations can be used:

$$N_e = \frac{1}{2}\left[N_D - N_A + \sqrt{(N_D - N_A)^2 + 4n_i^2}\right], \quad N_h = \frac{n_i^2}{N_e}, \qquad (II.6)$$

$$N_h = \frac{1}{2}\left[N_A - N_D + \sqrt{(N_A - N_D)^2 + 4n_i^2}\right], \quad N_e = \frac{n_i^2}{N_h}. \qquad (II.7)$$

Eq. (II.6) corresponds to n-doped silicon ($N_D >> N_A$) and Eq. (II.7) corresponds to p-type silicon ($N_A >> N_D$), with n_i the intrinsic carrier concentration.

II.2.3 Calculations of the flux databases

The objective is to calculate a database of near-field radiative heat fluxes in plane-plane geometry for different emitter-receiver distances. The results will be used as input data in the estimation of the flux for evanescent waves in a sphere-plane configuration. A complete database needs to be calculated for each configuration of temperature and materials, so the computation time has to be reduced as much as possible. It is reasonable to consider a distance range from 1 nm to 100 µm, because at 300 K, λ_{Wien} = 10 µm and the near field is not expected to be contributing at larger distances. A reference database calculation was made using 1200 points (20h computation time) with a logarithmic discretization. The results were used to estimate the flux for evanescent waves between a sphere and a planar substrate with the method described in section II.3.2 (see Eq. (II.8)).

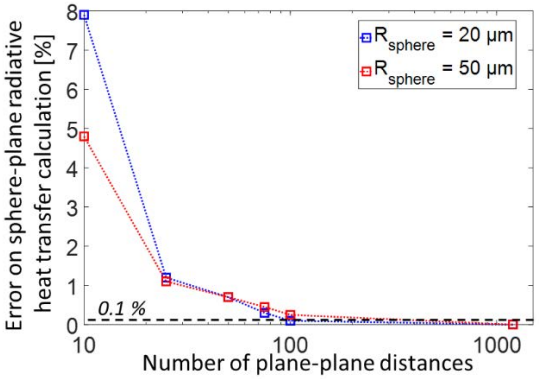

Figure II.4: Study of the computation time optimization for the plane-plane distance discretization

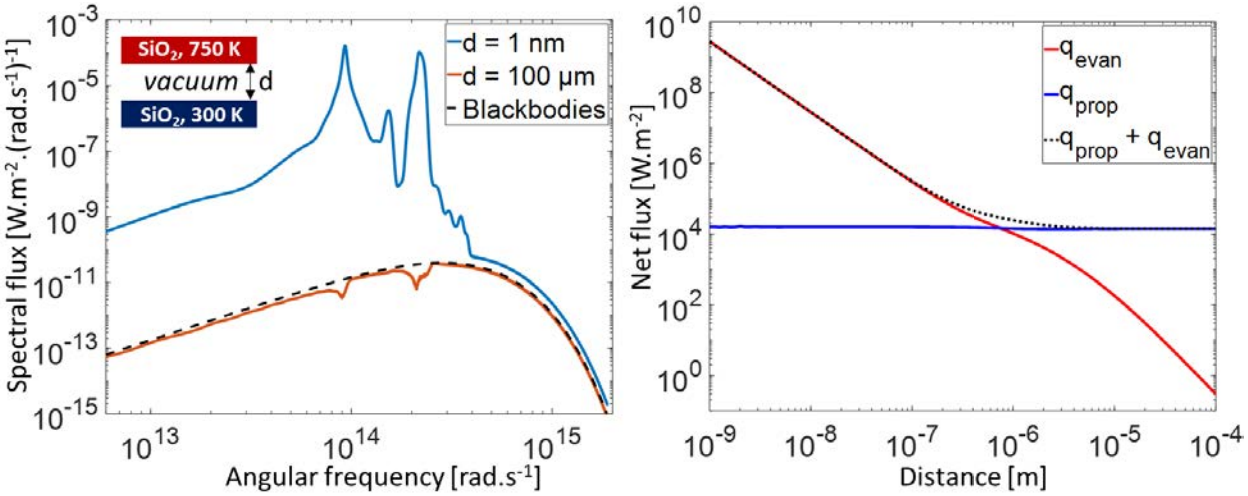

Figure II.5: Spectral and net radiative heat flux for the SiO_2-SiO_2 planar configuration as a function of angular frequency and distance

Different distance discretizations were tested and compared to the reference. A difference of 0.1 % was found with a 100-point logarithmic distance discretization for a sphere with a 20 µm radius (Figure II.4) corresponding to the spheres used in the experiments. The calculation of a full database with 100 distances requires less than 2 hours of computation time. Calculations were made in a large spectral range from 1.88 10^{11} to 1.88 10^{15} rad.s^{-1}, respectively 10000 and 1 µm. Integration of the spectral flux over this frequency range corresponds to more than 99.8 % of the total net flux radiated by a blackbody for a 77 to 1200 K temperature range. The results are presented in Figure II.5. The left plot shows the spectral radiative heat flux of both propagative and evanescent wave contributions according to angular frequency, for two different distances, compared with the flux exchanged between two blackbodies. At d = 100 µm the flux between the SiO_2 plates is close to the one exchanged between the blackbodies but is lower at the phonon polaritons frequencies. This means that SiO_2 is a good infrared emitter in the far field. At the lowest distance of d = 1 nm, the flux is enhanced by several orders of magnitudes with a larger increase at the resonances. The integration over the whole spectral range gives the total net radiative flux (in W.m^{-2}) as a function of distance.

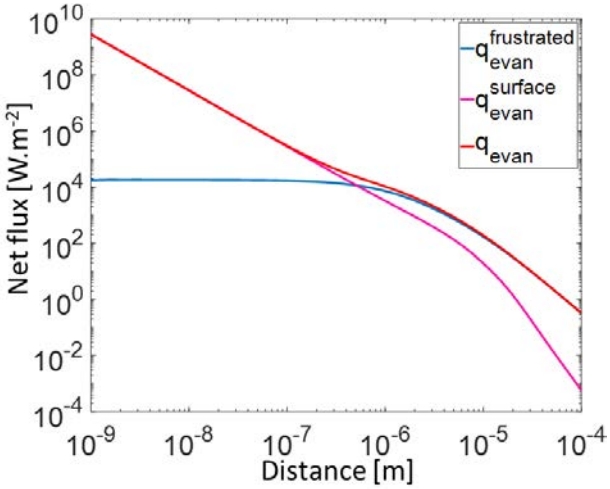

Figure II.6: Contribution of the frustrated and surface modes in the evanescent component of the radiative heat flux.

The right plot of Figure II.5 shows separately the propagative and evanescent wave contributions. It can be seen that q_{prop} is independent on distance, while q_{evan} increases as distance decreases and becomes higher than q_{prop} for $d \sim 1$ µm. The evanescent wave contribution can be decoupled in two parts involving the frustrated modes and the surface modes. The frustrated mode contribution $q_{evan}^{frustrated}$ is calculated by integrating Eq. (II.2) on the $k_{\parallel}$ from k_0 to nk_0, while the surface mode contribution $q_{evan}^{surface}$ results from the integration from nk_0 to ∞. It can be seen in Figure II.6 that the surface mode contribution becomes higher than the frustrated mode contribution for $d < 500$ nm. Also, $q_{evan}^{surface}$ keeps increasing when the distance decreases compared to $q_{evan}^{frustrated}$ which levels off.

Because the frustrated modes are caused by total internal reflection, enhancing radiative heat transfer in the near field by several orders of magnitude requires the presence of surface modes caused by the coupling of thermal photons with the material resonances (surface phonon polariton for example). The transmission coefficient for *TE*-polarized waves at the interface between media *1* and *2* is expressed as $Tr = |r_{21}^{TE}|^2$ and is represented in Figure II.6b as a function of ω and $k_{\parallel}$. The black and green dashed lines indicate $k_{\parallel} = k_0$ and $k_{\parallel} = nk_0$ respectively. The zone on the left of the black curve corresponds to the purely propagative modes while the zone on the right of the green curve corresponds in some cases to the surface modes, the area in-between representing the frustrated modes. It can be seen that there is a spectral domain where $k_0 > nk_0$, corresponding to $n < 1$. This means that, in this case, frustrated modes cannot exist and the flux for evanescent waves comes from the surface wave contribution only. The full calculated database can be visualized in Figure II.8 as a 2D map of the spectral radiative heat flux (in logarithmic scale for clarity) as a function of distance and angular frequency for q_{prop} and q_{evan}. For sphere-plane calculations, only the evanescent component of the database will be used in the proximity flux approximation (PFA, detailed in II.3.2). The propagative component is not well estimated with PFA so another method will be used to estimate this contribution based on a Monte Carlo ray tracing method (see Sec. II.3.3).

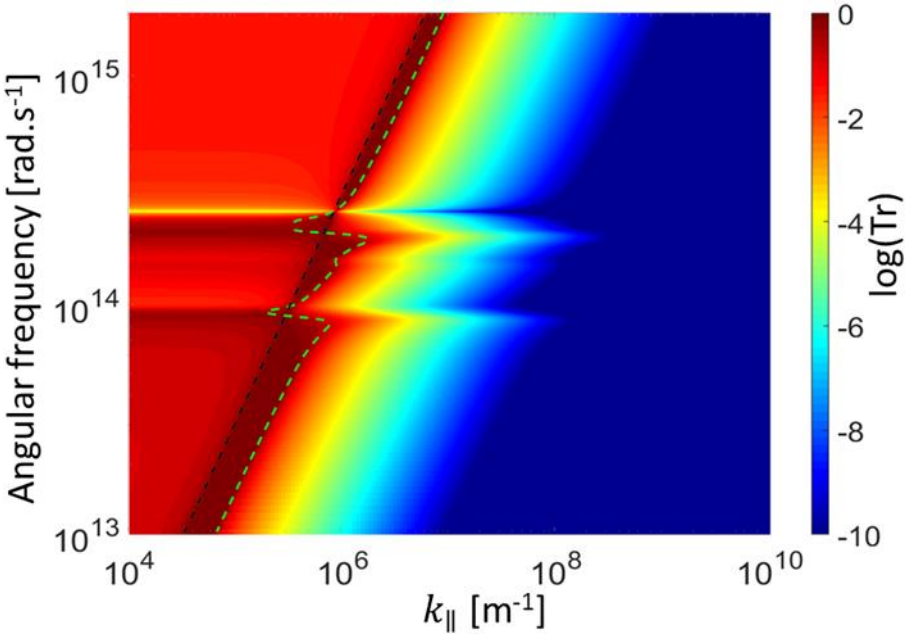

Figure II.7: TE-polarized wave transmission coefficient at the 12 interface as a function of angular frequency and $k_{\parallel}$

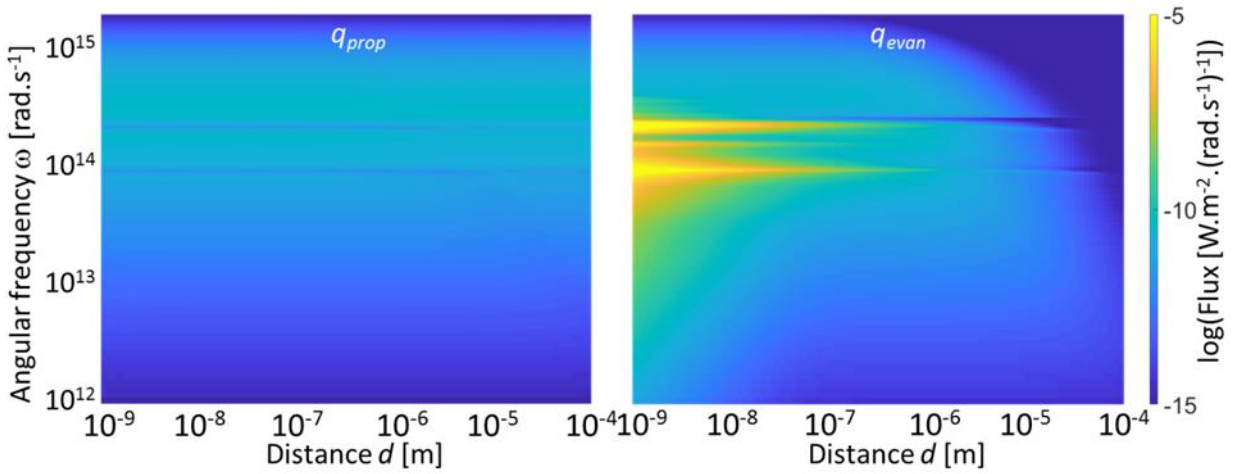

Figure II.8: Spectral radiative heat flux between a SiO_2 planar emitter at 750 K and a SiO_2 planar receiver at 300 K as a function of angular frequency and distance

II.3 Sphere-plane geometry

Calculations of the radiative heat transfer in the near field between a spherical emitter and a finite planar substrate is more complex than for the plane-plane geometry. A finite substrate implies to take into account the thickness and lateral size. The thickness of the substrate can create interference issues while the finite lateral size involves a view factor depending on sphere-plane distance. The problem is divided into two parts. First, the contribution of evanescent waves is estimated using the q_{evan} database previously calculated for the plane-plane geometry and the proximity flux approximation. Then, propagative waves are taken into account using a ray tracing Monte Carlo method. The sum of the two contributions gives the total exchanged radiative heat flux.

II.3.1 Difference between plane-plane and sphere-plane geometry

The plane-plane geometry provides a high exchanged radiative heat flux in the near field. This is due to the higher fraction of the emitter surface in the near field compared to a spherical emitter at the same distance. This difference is schematically represented in Figure II.9 where spherical and planar emitters are placed at the same distance d from a receiver. The distance range where the near-field effect occurs is represented by the colored area. As explained in the previous chapter, this distance range corresponds to $d < \lambda_{Wien}$.

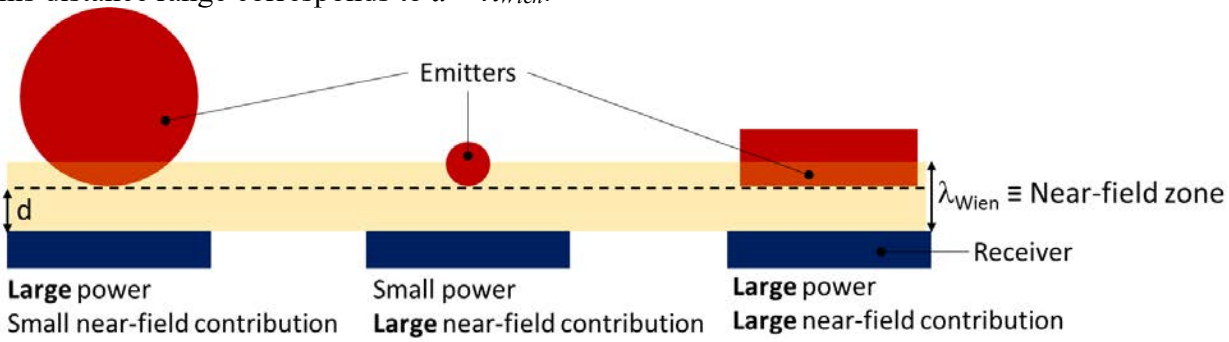

Figure II.9: Exchanged radiative power and near-field contribution differences between spherical and planar emitters

The fraction of the emitter surface that faces the receiver appears more important in the case of a planar emitter compared to the large and small spheres. The small sphere exchanges less power compared to the large one because of the smaller emitting surface, but the fraction of its surface at $d < \lambda_{Wien}$ is more important, meaning a larger near-field relative contribution. Each configuration has its advantages and drawbacks. The drawback of the planar emitter case is that it is experimentally challenging to create a small gap distance with the receiver, due to the need of a very accurate parallelism, and that small emitters might exchange very low power.

II.3.2 Proximity flux approximation

The principle of the proximity flux approximation (PFA), also called Derjaguin approximation[81], is that the spherical shape is approximated as the sum of small planar elements parallel to the planar substrate. The sphere-plane flux or conductance G_{sp} can be calculated by integrating the local plane-plane flux G_{pp} weighted by the local perimeter $2\pi r$ over the half sphere as:

$$G_{sp}(d,T) = \int_0^{R_{sphere}} G_{pp}\left[\tilde{d}(r),T\right] 2\pi r dr \,, \qquad (II.8)$$

$$\tilde{d}(r) = d + R_{sphere} - \sqrt{R_{sphere}^2 - r^2} \,. \qquad (II.9)$$

Here, $\tilde{d}(r)$ is the sphere-plane distance taken at the local sphere radius r, calculated knowing the sphere radius R_{sphere} and the minimum sphere-plane distance d (Figure II.10). For each local radius r, the approximation assumes that heat transfer occurs only between the small planar areas of the sphere and the closest areas on the substrate, with the assumption that the distance dependence of the flux is sharp (*e.g.* $\frac{1}{d^n}$ with n large). This is a reasonable assumption for evanescent waves, but probably wrong for propagative waves that are emitted in all directions. As a consequence, it was necessary to study the two contributions separately.

In addition to the sphere-plane configuration, PFA can be used in order to estimate radiative heat transfer between a tip having a small radius of curvature and a planar substrate. For this configuration, the geometry of the tip consists in a spherical shape located at the apex of a conical part. In the work of Nguyen et al.[82], PFA calculations were performed considering a tip having a radius of curvature of 50 nm and were compared with numerical calculations using the boundary element method. In this case PFA was found to overestimate the radiative heat flux by a factor 2, meaning that PFA might not be accurate for describing near-field radiative heat transfer for sharp objects.

Exactness of PFA calculations depends on the sphere radius and the gap distance with the planar substrate. Otey *et al.*[83] performed numerically exact calculations of radiative heat transfer, between a dielectric sphere and a plate. They compared their results with different approximations, including PFA.

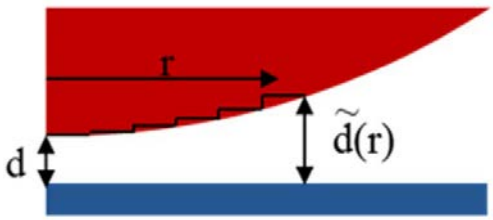

Figure II.10: Schematic of the proximity flux approximation

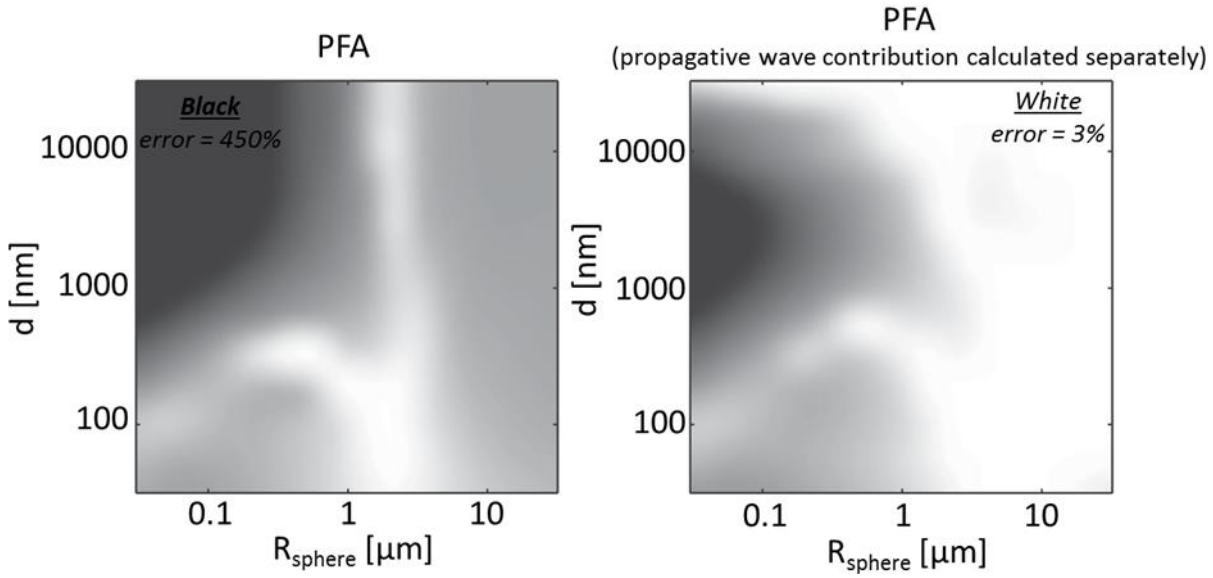

Figure II.11: Diagram of the relative accuracy of PFA to the sphere-plane radiative heat flux. Figures taken from Otey et al.[83].

They concluded that PFA was of practical use when $R_{sphere} >> d$, and if the propagative wave contribution was treated separately. Figure II.11 shows the relative accuracy of PFA compared to exact calculations. If the propagative wave contribution is calculated separately, PFA provides a good approximation of the radiative heat flux for spheres with $R_{spheres} > 10$ µm. In our experiments, spheres with radii of the order of 20 µm are used. Therefore, we chose PFA as the best choice for calculating near-field radiative heat transfer, keeping in mind that this method is an approximation providing results not perfectly equal to exact calculations.

Calculations presented in Figure II.12a,b were made between SiO_2 spheres at 750 K and a SiO_2 semi-infinite planar substrate at 300 K. For the spheres, the evanescent contribution of the radiative flux is obtained as $Q_{sp}^{evan} = G_{sp}^{evan} \Delta T$ with $\Delta T = T_{sphere} - T_{substrate}$. To compare the results with the plane-plane configuration, the flux density was obtained by dividing the evanescent wave contribution of the sphere-plane radiative heat flux by the projected sphere surface on the substrate:

$$q_{sp}^{evan} = \frac{G_{sp}^{evan} \Delta T}{\pi R_{sphere}^2}. \qquad (II.10)$$

Different sphere radii were studied from 50 nm to 50 µm. It can be seen on Figure II.12b that the larger the sphere diameter the larger the exchanged power because of the larger area. Because the proportion of the sphere in the near-field zone is larger for small spheres (Figure II.9), the power enhancement factor between the closest and largest distance is larger for the small spheres. In terms of power per surface unit (Figure II.12c), the trend is inverted with a large flux for small spheres. As the radius decreases, the evolution as a function of distance gets closer to the planar emitter.

For the experiments, the size chosen is $R_{sphere} = 20$ µm. This radius is a compromise between near-field radiative enhancement factor (see section II.4.3) and mechanical limitation of SThM probes where the sphere is attached. These probes do not allow the use of too large, therefore heavy, spheres because it could bend and damage the cantilever. The drawback of using a large sphere is that it implies a smaller expected near-field enhancement compared to a smaller sphere or a planar emitter by several orders of magnitude.

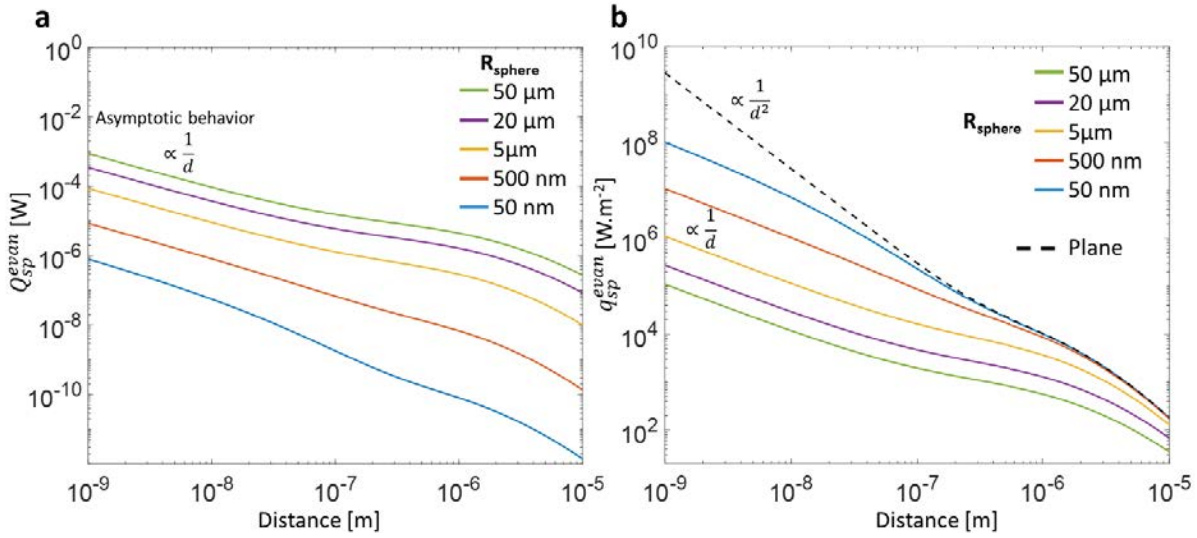

Figure II.12: Sphere-plane near-field radiative heat transfer calculations
(a) PFA calculations as a function of sphere radius. (b) Evanescent wave contribution of the radiative heat flux for different sphere radii compared to a planar emitter

II.3.3 Contribution of the propagative waves

The far-field radiative heat flux was estimated based on two different approaches. Let us note that we did not compute the emission exactly but in the large-sphere approximation, where interference effects are neglected[84]. First, the macroscopic theory of view factors was used by assuming diffuse isotropic surfaces. The substrate geometry here is a finite disc which represents the illuminated area of the TPV cell used in the experiments. The analytic expression of the sphere-disc view factor, depending on the cell and sphere radii R_{disc} and R_{sphere}, and on the sphere-disc distance d, reads as follows[85]:

$$F_{s\to d}(d) = \frac{1}{2}\left(1 - \frac{1}{\sqrt{1+\left(\frac{R_{disc}}{d+R_{sphere}}\right)^2}}\right) \qquad (II.11)$$

Due to the flatness of the surfaces, it could be argued that the surfaces are specular and not diffuse. A second method was implemented, using a Monte Carlo ray tracing numerical approach. The properties of the emitting sphere and the materials of the substrate were considered, such as emissivity and reflectivity, as a function of ω and emission angle. In this method, $n_p = 10^6$ rays are generated with random starting points on the surface of the sphere. Emission angles are generated corresponding to a uniform hemispherical emission, with θ and φ the angles in spherical coordinates (Figure II.13d). θ is randomly generated between 0 and π, following the expression $\theta = 2\sin^{-1}\sqrt{u}$, u being taken from a uniformly distributed set of random numbers in the interval 0 to 1. φ is taken from a uniformly distributed set of random numbers in the interval 0 to 2π. A fraction of the total power emitted by the sphere is attributed to each ray depending on the spectral distribution of radiative heat flux at the emitter temperature. The spectrum is decomposed into 100 frequencies intervals with more rays attributed to frequencies near the maximum emissivity of the blackbody (Figure II.13a).

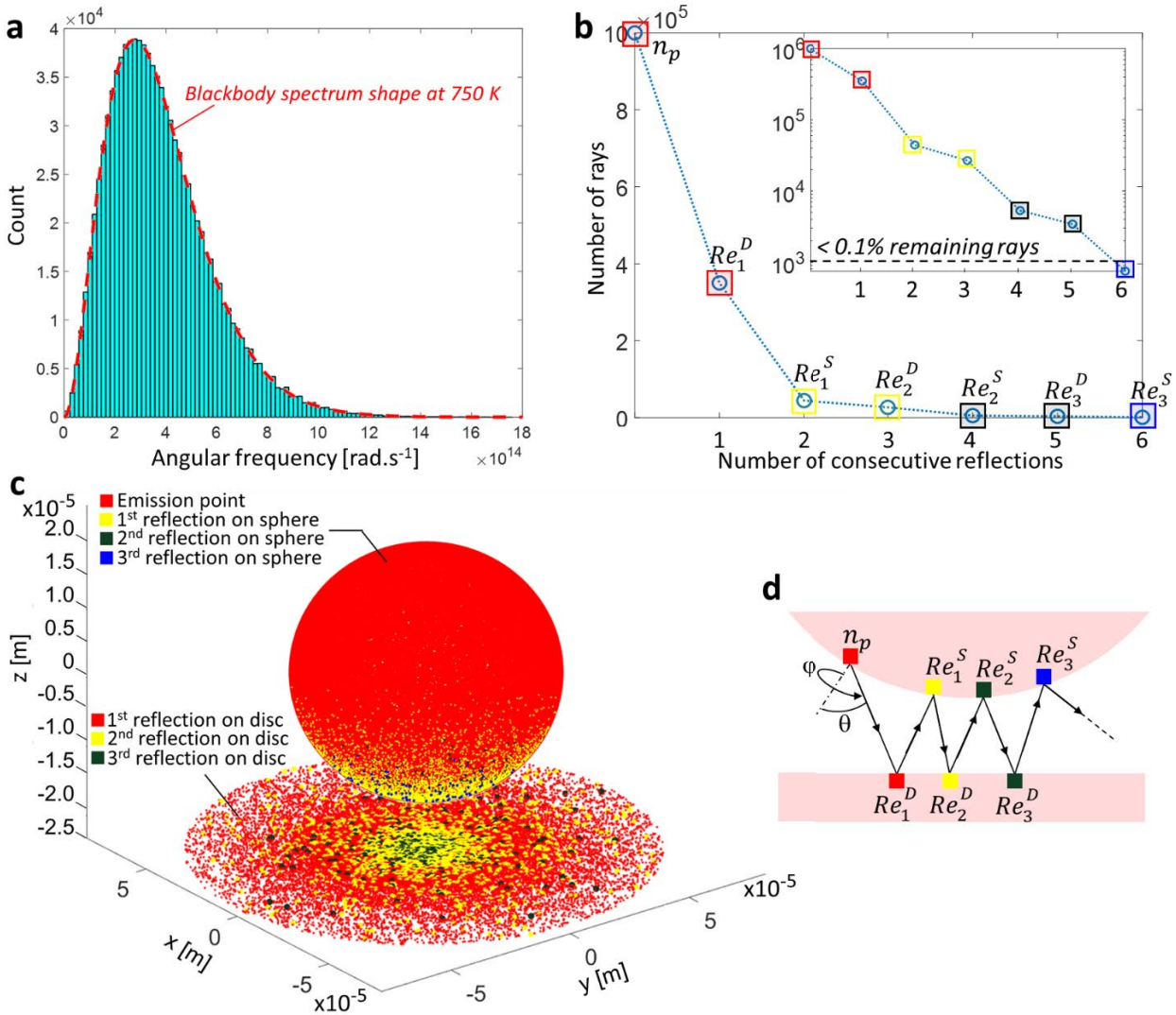

Figure II.13: Monte Carlo calculations
(a) Histogram of the number of emitted ray as a function of their attributed frequency interval. (b) Number of remaining rays as a function of the number of consecutive reflections. (c) 3D plot of a Monte Carlo ray tracing calculations between a 40 µm diameter SiO_2 sphere at 750 K at d = 5 µm from a 160 µm diameter SiO_2 disc at 300 K. (d) Schematic of the consecutive reflections

For each frequency interval $\Delta\omega$, the emitted power $P_i(\Delta\omega)$ carried by a ray i is calculated as follows:

$$P_i(\Delta\omega) = \frac{S.\epsilon_{SiO_2}^{bulk}(\omega,\theta).st(\omega,\theta)}{n_{\Delta\omega}} \int_{\omega}^{\omega+\Delta\omega} q^{BB}(\omega,T)d\omega\,, \qquad (II.12)$$

where S is the area of the whole sphere, $\epsilon_{SiO_2}^{bulk}$ is the emissivity of the bulk material (SiO_2 in this example) at frequency ω and the emission angle θ. $n_{\Delta\omega}$ is the number of rays in the frequency interval $\Delta\omega$, and $q^{BB}(\omega,T)$ is the spectral hemispherical radiative heat flux of the blackbody at a temperature T. st is the semi-transparency coefficient. It is introduced here because of the small diameter of the sphere: the emittance of finite materials may be different from that of bulk materials, because of transparency effects. In a medium, the intensity of electromagnetic waves is

exponentially attenuated following a $\propto e^{-\kappa_\omega x}$ law, κ_ω and x being respectively the extinction index and the distance travelled by the wave in the medium. A semi-transparent medium is described as an environment where the amplitude of an electromagnetic wave does not tend to 0 after travelling through the entire medium. Radiative heat fluxes are modified by volumetric absorption and reinforcement phenomena that must be taken into account to estimate the correct emittance. Details on calculation of *st* are provided in appendix 3.

Once the rays are emitted (from point n_p in Figure II.13d), calculations are made to check if, when coming from the sphere, they are crossing the surface of the disc (point Re_1^D). If so, the trajectory is extended by considering the angle of incidence, and the power lost by the ray (absorbed by the substrate) is calculated using the reflectivity value. If not, the ray is no longer considered in the system.

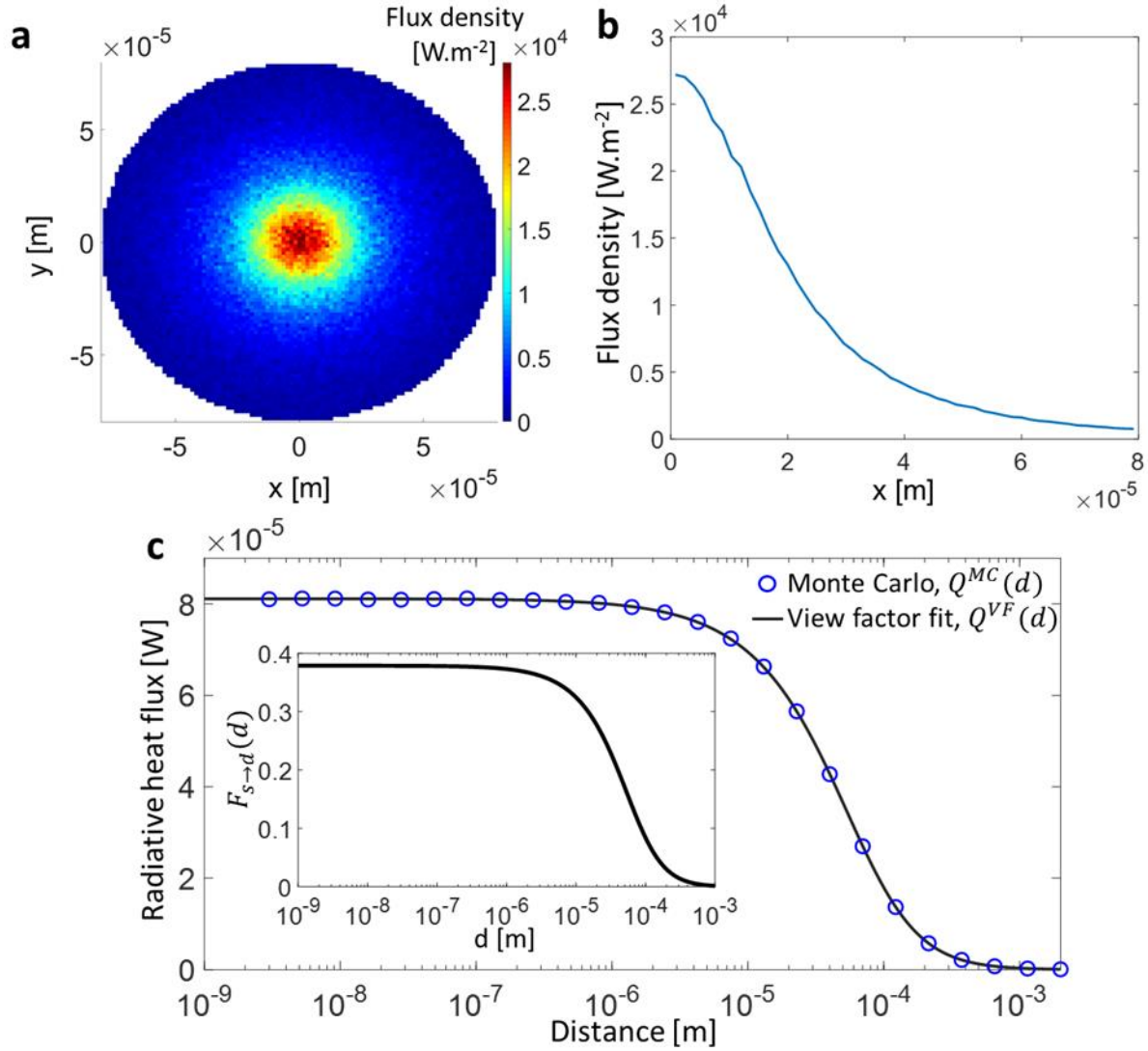

Figure II.14: Radiative heat flux density received by the disc and comparison with analytical view factor. (a) Local radiative power density deposited by a 40 µm SiO_2 sphere at 750 K on a flat SiO_2 semi-infinite disc having a diameter of 160 µm at 300 K, for a distance equal to 5 µm. (b) Radiative power density as a function of disc radius. (c) Evolution of the radiative power calculated using the view factor as a function of distance, compared with the Monte Carlo simulations. The inset shows the view factor as a function of distance

Then it is calculated if the extended trajectory of the reflected ray crosses the surface of the sphere (point Re_1^S). Using the same principle as before, the power loss and the reflected trajectory are calculated. In this method, up to 6 consecutive reflections are considered for the same ray, because it was estimated that the number of rays experiencing more reflections was negligible. In Figure II.13b, the initial number of rays n_p is plotted along with the number of rays that are first reflected on the disc Re_1^D, then on the sphere Re_1^S and so on until a third reflection on the sphere Re_3^S takes place (see the schematic on Figure II.13d). It can be seen that less than 0.1% of the initial rays are remaining after the 6th reflection. A graphical representation of the results of the Monte Carlo method, with only 10^5 initial rays for clarity, is shown in Figure II.13c. The 3D plot represents a SiO_2 spherical emitter at 750 K with a diameter of 40 µm, separated by d = 5 µm from a 160 µm in diameter SiO_2 optically thick disc at 300 K. It can be seen that the flux density received by the disc is higher close to the center. The total flux absorbed by the disc, which may be representative of a TPV cell, is provided by a map of the flux density (Figure II.14a) and a flux density profile integrated as a function of cell radius (Figure II.14b). It is observed in the figures that the power density decays by 50% for a radius of 20 µm. For the TPV experiments, it is then not necessary to use cells with a too large radius as most of the surface would not be much illuminated by the propagative waves coming from the sphere.

The evolution of the radiative heat flux $Q^{MC}(d)$ absorbed by the cell could also be calculated as a function of distance (Figure II.14c). It can be seen that for distances smaller than ~ 3 µm, variations of the flux are relatively small (< 4 %) so most of the measured enhanced radiative conductance is coming from the contribution of the evanescent waves in the near field. The Monte Carlo simulations of the specular bodies considering 10^6 rays were compared with the analytical expression of the diffuse-emission view factor (Eq. (II.11)). For the comparison, the analytical view factor is calculated as a function of sphere-disc distance (inset Figure II.14c). It is then fitted to the Monte Carlo radiative heat flux calculations at d = 5 µm using the following equation:

$$Q^{VF}(d) = \frac{F_{s\to d}(d)}{F_{s\to d}(5\mu\mathrm{m})} Q^{MC}(5\mu\mathrm{m})\,. \qquad (II.13)$$

$Q^{VF}(d)$ is the radiative heat flux as a function of distance considering the view factor evolution, $F_{s\to d}(d)$ is the analytical view factor as a function of distance, $F_{s\to d}(5\ \mu\mathrm{m})$ is the analytical view factor at d = 5 µm, and $Q^{MC}(5\ \mu\mathrm{m})$ is the radiative heat flux calculated with Monte Carlo at d = 5 µm. The very good agreement for all distances between Monte Carlo calculations and $Q^{VF}(d)$ shows that the specularity of the surface is therefore not key to the computation of the exchanged radiative heat flux. Taking into consideration this result and because the Monte Carlo simulations need a significant computational time, the propagating mode contribution of the radiative heat flux is calculated for a single distance (d = 5 µm) using the Monte-Carlo method. The flux as a function of distance is deduced from both $Q^{MC}(5\ \mu\mathrm{m})$ and the analytical view factor using equation (II.13).

In the case of calculations with an InSb TPV cell as the material of the disc, the reflectance of the multilayered structure (see Figure VI.3) was first calculated by electromagnetic means. The transmission function of the propagative waves is calculated as a function of $k_{\parallel}$ (traduced in polar angles) at the top interface of either the cell or a blackbody. The ratio between the transmission function for the cell and that for the blackbody gives the absorptance of the cell. The reflectivity is then *1 – absorptance* and is included in the Monte Carlo approach for the estimation of the propagative wave contribution to radiative heat transfer (Figure II.15). It can be seen in the figure that the reflectance has a behavior close to periodic for $\omega < 5.10^{14}$ rad.s^{-1} due to interferences inside

the multilayer. This explains the larger impact of the substrate thickness on the reflectance than that of the doping level. Details on TPV cell structure are provided in Sec VI.2.

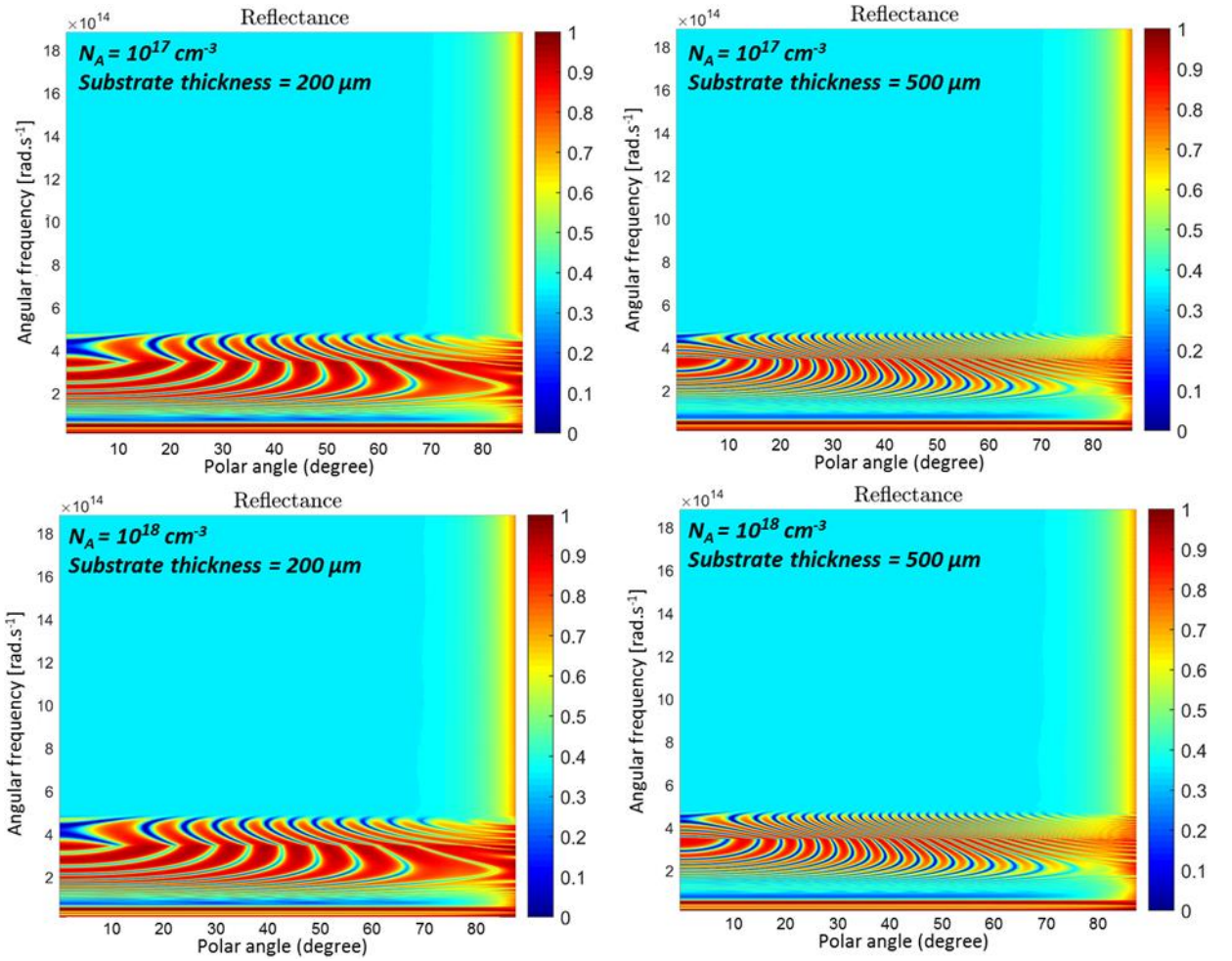

Figure II.15: Reflectance of InSb TPV cells for different p-doping levels and substrate thicknesses

II.4 Parametric study of the materials

The selection of the emitter material is an important step in order to determine which material would be the most efficient to be coupled with a TPV cell in the near field. In addition, it is interesting to determine the expected behavior for different symmetrical and asymmetrical emitter/substrate combinations in order to compare with the experimental results. Temperature dependence of radiative heat transfer in the far field and the near field are also investigated as different behaviors are expected.

II.4.1 Emitter for near-field thermophotovoltaic electrical power enhancement

The objective is to find an emitter material to be coupled with an InSb TPV cell at 77 K, providing the highest radiative heat transfer at $\lambda < \lambda_{gap}^{InSb,77K}$ corresponding to wavelengths useful for photocurrent generation. It is reminded that $\lambda_{gap}^{InSb,77K}$ = 5.3 µm. The optical properties of the studied materials have been reported in section II.2.2. Here, calculations are for planar emitters at

732 K coupled with InSb at 77 K. In Figure II.16a the spectral flux is represented as a function of wavelength. Below the gap wavelength of InSb, graphite appears to be the best material, followed by doped silicon and LaB_6. The worst materials are SiO_2 and aluminum, with spectral fluxes lower by one order of magnitude. It is interesting to note that at the resonance wavelength of InSb (~ 55 µm), doped silicon is better than graphite. To find the best material for photocurrent generation, the radiative flux integrated over all the wavelengths is compared with the flux integrated over $\lambda < \lambda_{gap}^{InSb,77K}$ only (Figure II.16b). Considering the total flux for all the wavelengths, doped silicon provides the best near-field enhancement of radiative heat transfer. But for $\lambda < \lambda_{gap}^{InSb,77K}$ at the lowest distance, graphite is significantly better than doped silicon. At d > 60 nm, doped silicon is slightly better than graphite but tends to level off at the lowest distances. As a result, graphite was chosen with the initial aim of studying the sub-100 nm regime for thermophotovoltaic conversion. The study of the experimental setup (see section III.4.2) concludes that the minimum achievable distance is around 100 nm. Knowing this limitation, doped silicon could provide equivalent or even better performances than graphite as the emitter material. However, the radiative heat flux exchanged at wavelength lower than $\lambda_{gap}^{InSb,77K}$ is larger with a silicon emitter than a graphite one and could induce heating of the cell leading to lower performances. Ideally, a better emitter material would be supporting surface phonon polaritons at wavelengths close to $\lambda_{gap}^{InSb,77K}$, in order to enhance the radiative heat transfer and the electrical power generation in the near field, by several orders of magnitude. We looked for such material but could not find one suitable for the timeframe of this work.

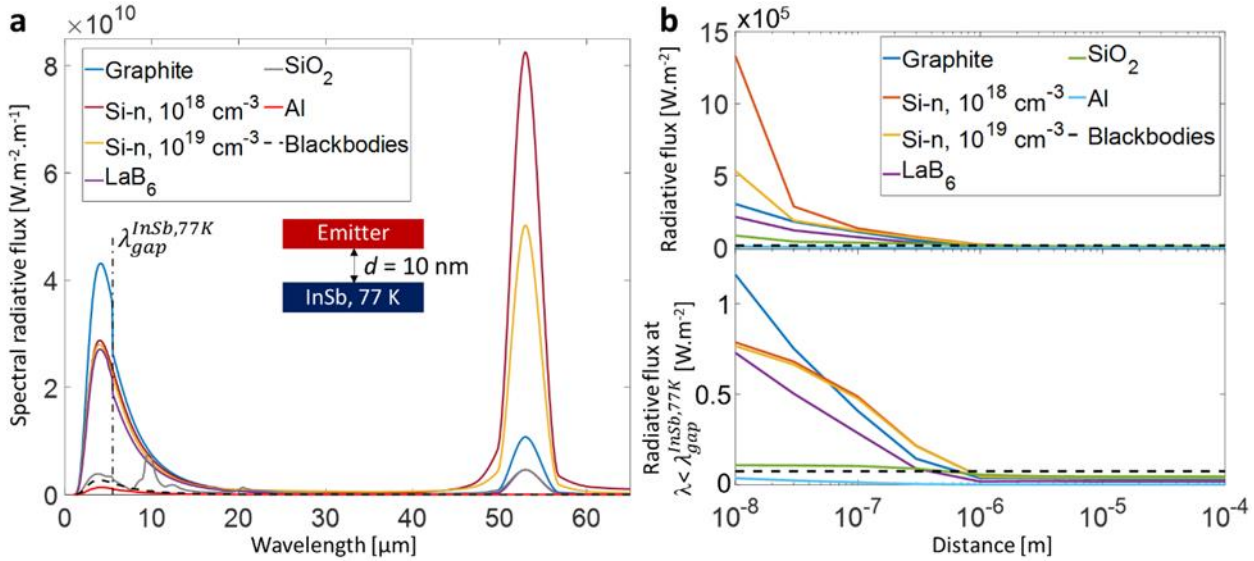

Figure II.16: Selection of the best emitter material for near-field thermophotovoltaic experiments (a) Plane-plane spectral radiative heat flux calculations between different materials at 732 K and InSb at 77 K. (b) Radiative heat flux as a function of distance for the selected materials, integrated over all wavelengths (top) and over $\lambda < \lambda_{gap}$(InSb, 77K) (bottom)

II.4.2 Calculations for different pairs of materials

The experimental setup allows measurements of near-field radiative conductance with either a SiO_2 or a graphite emitter. The studied substrate materials are graphite, SiO_2 and non-intentionally doped InSb. The non-intentionally doped InSb substrate has a residual 10^{15} cm^{-3} n-type doping

concentration. This choice was made so the analysis of symmetrical (the emitter and the receiver are the same material) and asymmetrical configurations was possible. The temperature dependence of the dielectric function was considered for SiO_2 only, the other materials were described with data taken at room temperature.

II.4.2.1 SiO_2 emitter

Calculations of the plane-plane evanescent component of radiative thermal conductance are compared with sphere-plane calculations considering a 40 µm in diameter SiO_2 sphere with an equivalent exchange surface (Eq. (II.10)). Figure II.17 shows the results for the different substrate materials at 300 K, as a function of the emitter temperature from 300 K to 1200 K. As expected, the largest values are obtained for the symmetrical SiO_2-SiO_2 configuration with a planar emitter. There are some differences between the results for the planar and the spherical emitters. First the conductance values are lower with a spherical emitter because of the reasons depicted in Figure II.9. In addition, the spherical shape of the emitter induces a shift in the evolution of the conductance as a function of distance. The rise of conductance at the lowest distances due to the contribution of the surface waves starts at smaller distances for the spherical emitter. It is clearly seen in the case of the graphite substrate: the conductance increases sharply for $d < 100$ nm with the planar emitter, and for $d < 10$ nm with the spherical emitter. This effect is even more noticeable with the InSb substrate where the contribution of surface waves is barely seen with the spherical emitter. As expected, the conductance enhancement as a function of distance for the plane-plane configuration tends to a $1/d^2$ evolution, which is different from that of a sphere-plane configuration where the evolution tends to a $1/d$ law[40].
Evolution of the conductance as a function of emitter temperature is shown at different distances in Figure II.18.

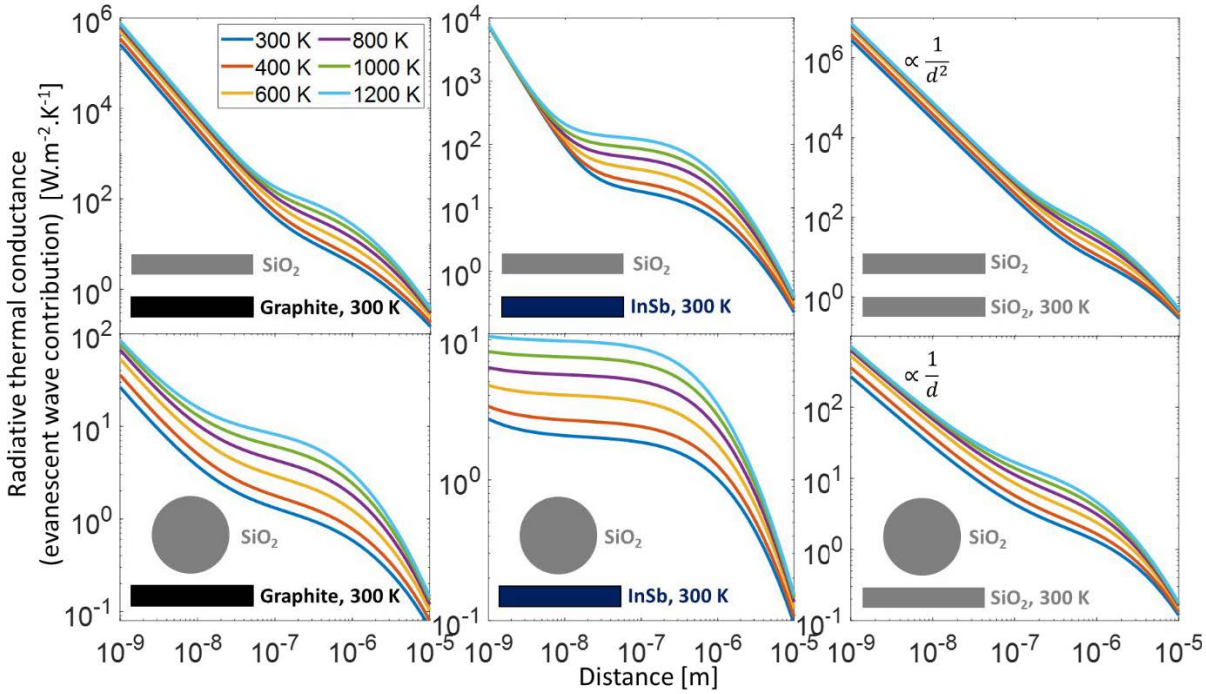

Figure II.17: Evanescent wave contribution to radiative thermal conductance between SiO_2 planar and spherical emitters at different temperatures and planar substrates made of different materials at 300 K

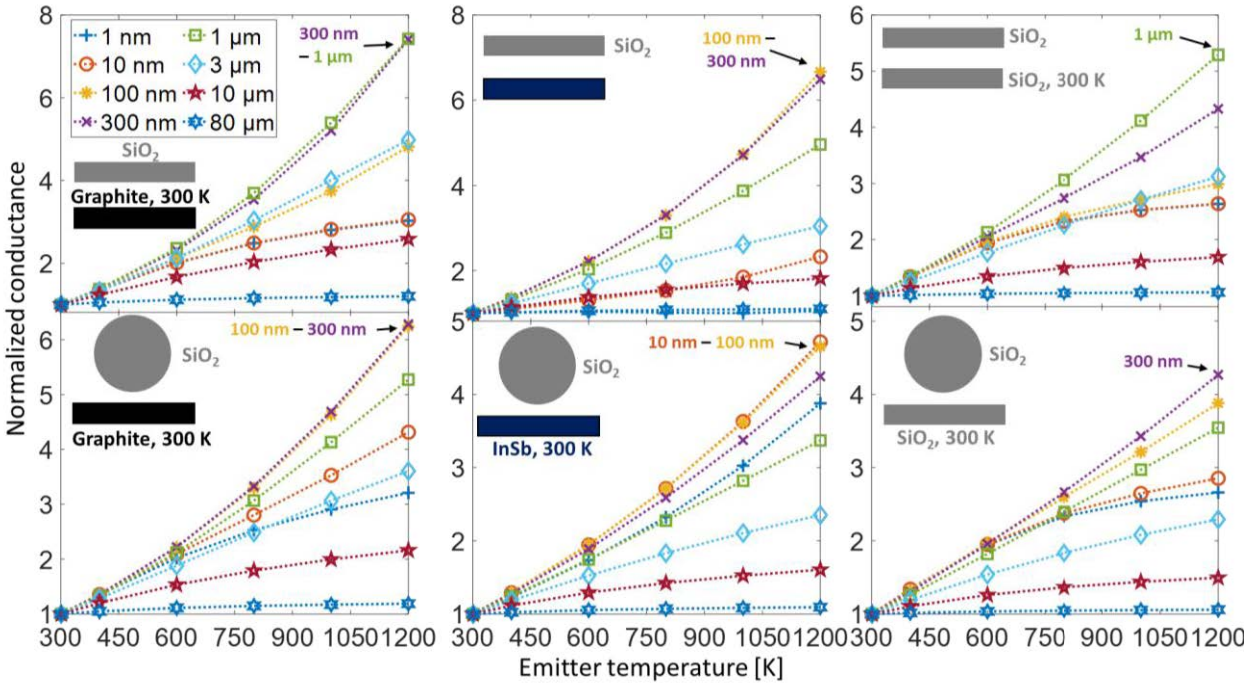

Figure II.18: Evolution of the evanescent wave contribution to radiative conductance as a function of emitter temperature for different distances between a SiO_2 planar and spherical emitters and a planar substrate at 300K made of SiO_2, graphite or InSb

Here the conductance was normalized by that calculated at 300 K to observe the different behaviors. It is observed that the conductance increases at different rates, depending on materials and distance. The greater increase was found with a planar SiO_2 emitter and a graphite substrate at a 300 nm distance. In each configuration, the maximum conductance enhancement is lower with a spherical emitter and is reached for a distance approximately 3 times smaller. Temperature dependence of the near-field radiative conductance can be studied as a function of the distance by plotting the exponent of the power law of the radiative conductance determined using the Stefan-Boltzmann law. The radiative conductance G_{BB} between two blackbodies is expressed as

$$G_{BB} = \sigma \frac{T^4 - T_0^4}{T - T_0}. \qquad (II.14)$$

Here T and T_0 are respectively the hot and cold body temperature and σ the Stefan-Boltzmann constant. In this case the exponent of the temperature power law described in the Eq. (II.14) is equal to 4.

The radiative conductance between two blackbodies is shown in Figure II.19 as a function of the hot body temperature from 300 to 1200 K. The radiative heat flux between two blackbodies is calculated using Planck's law and does not depend on distance between the two bodies. Therefore, the exponent of the power law remains equal to 4 independently from the distance. For real materials, the emission spectrum is modified in the near field at specific frequencies depending on the optical properties of the materials.

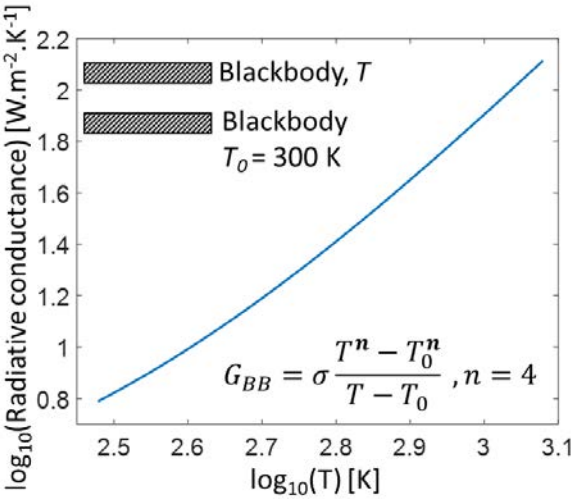

Figure II.19: Radiative conductance between two planar blackbodies as a function of emitter temperature with a receiver at 300 K.

It is shown in Figure II.20 representing the radiative heat flux between a planar body made of SiO_2 at 1200 K and planar bodies at 300 K made either of graphite, InSb or SiO_2. The figure shows the spectra calculated at distances of 100 µm, 1 µm, 100 nm and 10 nm compared to the radiative flux exchanged between two blackbodies. The radiative flux is mainly enhanced at low frequencies but with peaks appearing at the resonance frequencies of the surface polaritons of SiO_2 and InSb. It is reminded that graphite does not support any surface polariton. Because of the differences in spectral distribution of the radiative heat flux as a function of distance and materials, differences in terms of radiative conductance power law may be expected. In order to verify this hypothesis, the radiative conductance as a function of temperature in the 300 to 1200 K range is fitted at each distance by using the expression

$$G_{fit} = C\sigma \frac{T^n - T_0^n}{T - T_0}, \qquad (II.15)$$

with two fitting parameters being *C* the pre-factor and *n* the exponent. This expression is derived from the conductance calculated between two blackbodies (Eq. (II.14)).

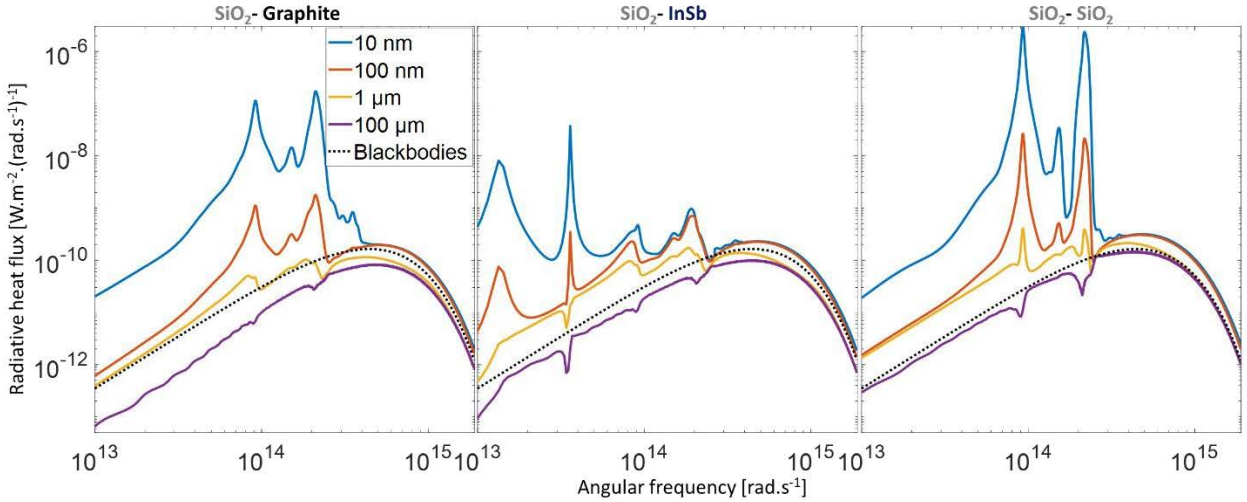

Figure II.20: Radiative heat flux as a function of angular frequency between planar SiO_2 bodies at 1200 K and planar bodies made of either graphite, InSb or SiO_2 at 300 K

The pre-factor is representative of the emissivity properties of the materials, in the far field as well as in the near field and depends on the dielectric functions. It is linked of the radiative conductance enhancement as distance decreases already observed in Figure II.17. The radiative conductance as a function of temperature for the plane-plane configuration between two quasi-blackbody materials having a dielectric function $\varepsilon = 1 + 0.01i$ is shown in Figure II.21a for several distances. The squares represent the complete calculation while the lines are the fit made using Eq. (II.15). The total radiative heat flux is represented in blue while the contribution of evanescent waves in shown in red. The evolution of the radiative conductance is well fitted as a function of distance and temperature using the temperature power law for both contributions. The fit of the radiative conductance at all distances allows to determine the exponent of the temperature power law as a function of distance, represented in Figure II.21b. As expected for this configuration the exponent in the far field reaches $n_{FF} = 4$ and tends to 2 in the near field at the smallest distance because of the contribution of evanescent waves. The transition between the far field and the near field depends on the imaginary part of the dielectric function. This fitting method can be used on calculated data but is also applied to near-field radiative heat transfer measurements presented in Chapter IV. In the following, the exponent of the temperature power law is determined for each pair of materials, considering a plane-plane or sphere-plane configuration.

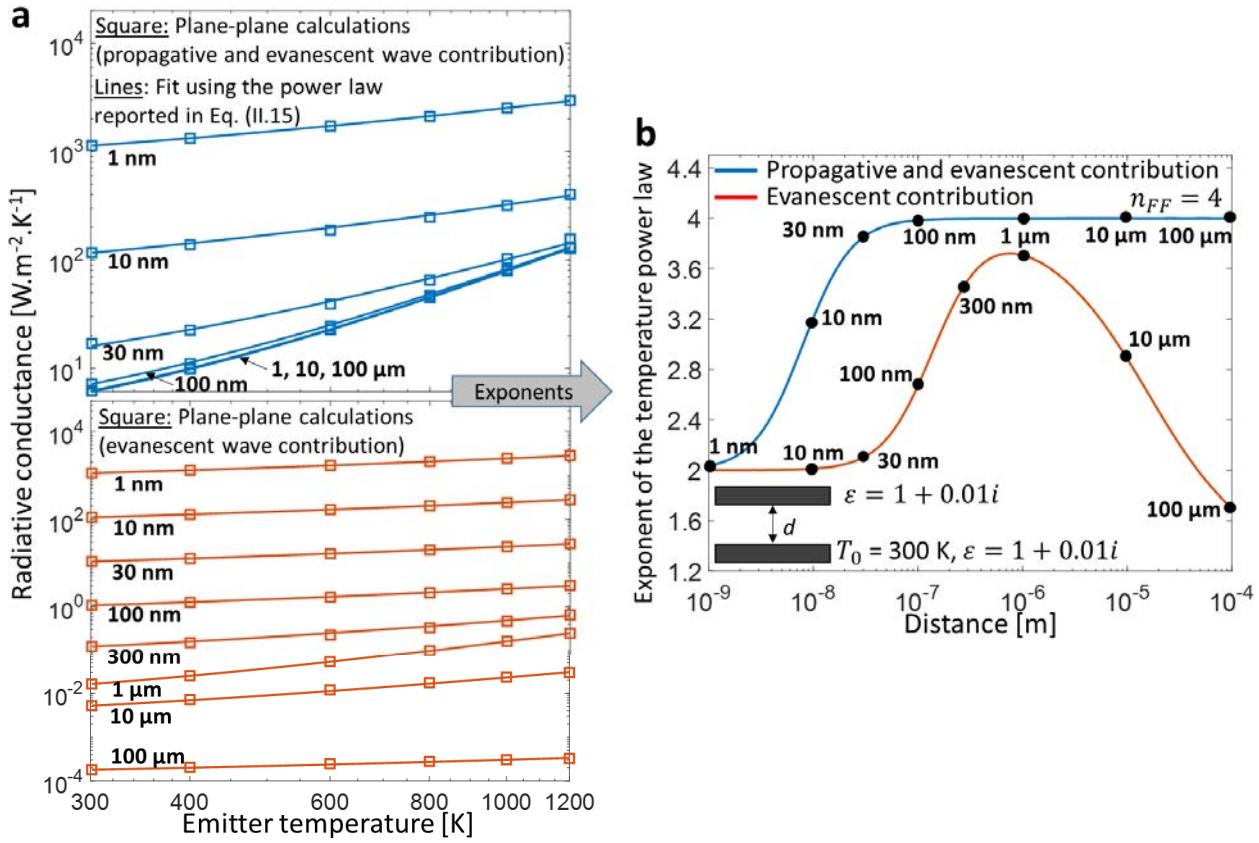

Figure II.21: Method for determining the exponent of the temperature power law.
(a) *Radiative conductance for different distances as a function of emitter temperature between two semi-infinite planar materials having a dielectric function $\varepsilon = 1 + 0.01i$ considering an emitter temperature ranging from 300 to 1200 K. The squares are full calculations of the total radiative heat flux and the evanescent wave contribution only, while the lines result from the fitting with the temperature power law. (b) Exponent of the temperature power law as a function of distance*

The exponent obtained as a function of distance is shown in Figure II.22 for the studied pairs of materials. Four configurations are studied: evanescent contribution and total radiative conductance for the plane-plane and the sphere-plane configuration. Above a distance of 10 µm, the exponent determined considering the total radiative conductance levels off to a value n_{FF} corresponding to the far-field regime. The values of n_{FF} exceed the value of 4 representative of the blackbody because of the shape of the spectra of the radiative heat flux for these materials in the far field (curve at d = 100 µm in Figure II.20). These spectra are lower in amplitude than that between two blackbodies with larger differences at low frequencies meaning a lower emissivity, well seen for the SiO_2-graphite configuration. When temperature increases, the frequency of the maximum radiative heat flux ω_{Wien} is shifted towards high frequencies (from $1.1.10^{14}$ at 300 K to $4.4.10^{14}$ at 1200 K), where the shape of the spectra for the real materials are close to that of the blackbodies. Therefore, the radiative heat flux in the far field for these materials is enhanced at a faster apparent rate than that between two blackbodies, because of the increasing emissivity of the material at high frequencies. The highest impact is found for the SiO_2-graphite configuration with a far-field exponent n_{FF}= 4.30. When the distance decreases, the modification of the emission spectrum induced by the increasing contribution of the evanescent waves to radiative heat transfer has a significant influence on the exponent. Below ~ 10 nm radiative heat transfer occurs mainly through the contribution of the evanescent waves for the plane-plane configuration. Therefore, the exponent of the temperature power law considering the total radiative conductance or only the evanescent contribution tends to the same value for the plane-plane configuration but not necessarily for the sphere-plane configuration. For the sphere-plane configuration, the contribution of propagative waves is calculated with the Monte Carlo method because it is reminded that the proximity approximation is expected to be invalid for considering the propagative wave contribution (see Sec. II.3.2). For the evanescent contribution it is observed that the maximum exponent is shifted at lower distances compared to the plane-plane configuration. Power laws have a similar exponent for both configurations at the lowest and largest distances, except for the SiO_2-InSb case at low distance. For the evanescent wave contribution, it appears that the exponent varies from $n = 1.04$ to $n = 3.10$ depending on distance, materials and geometry. These large variations are interesting because they are different from that of the propagative contribution. They also provide another way of comparison with the experimental measurements.

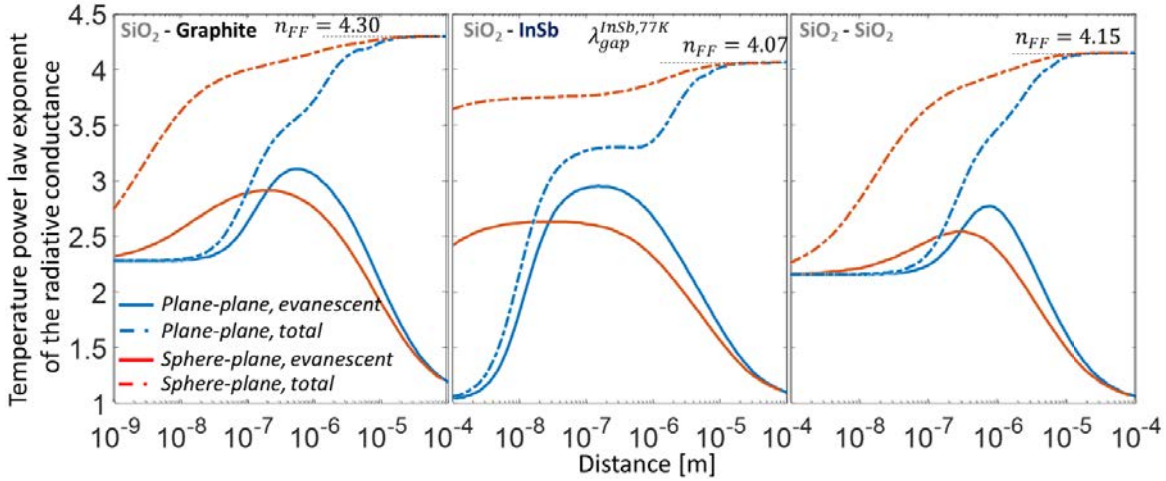

Figure II.22: Exponent of the temperature power law of the radiative conductance as a function of distance between a planar or spherical emitter made of SiO_2 and planar substrates at 300 K made either of graphite, InSb or SiO_2. The temperature dependence of the dielectric function is considered for SiO_2 only, data are taken at 300 K for the other materials.

In order to further understand the behavior as a function of distance of the exponent of the temperature power law, contribution of frustrated and surface modes are plotted separately for the plane-plane configuration (Figure II.23). This configuration was selected over the sphere-plane one because calculations give more reliable results than those from PFA. The proportion of the frustrated mode contribution is also represented as a function of distance. At large distances, evanescent wave contribution to radiative heat transfer is mainly due to frustrated modes. Therefore, the temperature power law of the total evanescent wave contribution to radiative power is that of the frustrated modes. When distance decreases, frustrated mode contribution to total evanescent wave contribution of radiative heat transfer becomes smaller, due to increasing surface mode contribution. At low distances, surface modes dominate the evanescent wave contribution to radiative heat transfer. As a consequence, the temperature power law of the total evanescent wave contribution to radiative power is that of the surface modes.

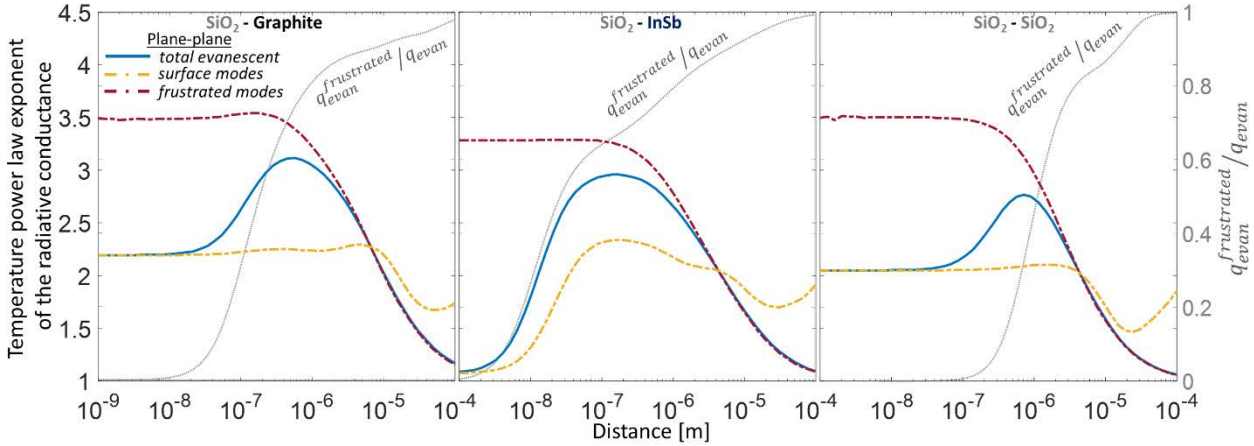

Figure II.23: Temperature power law exponent of the evanescent wave contribution to the exchanged radiative heat flux as a function of distance between a SiO_2 planar emitter from 400 K to 1200 K, and a planar substrate made of SiO_2, graphite or InSb at 300 K

II.4.2.2 Graphite emitter

The same kind of calculations is performed for a graphite emitter. The substrate materials, temperature and the sphere diameter are the same as before. In Figure II.24, it is observed that the highest evanescent thermal conductance values are obtained with the symmetrical graphite-graphite configuration. The graphite-InSb configuration presents a similar behavior to that with the SiO_2 emitter, with a conductance that levels off at low distances. However, conductance values are 3 times larger with a graphite emitter compared to those with a SiO_2 one. This is expected because graphite was estimated to be a better emitter to paired with an InSb substrate, in order to increase radiative heat transfer in the near field (Figure II.16). The graphite-SiO_2 configuration is interesting because it is the inverse of the SiO_2-graphite case studied in the previous section. For these two cases, the calculations give quasi-identical results.

Figure II.25 shows the normalized radiative conductance (evanescent wave contribution) as a function of emitter temperature, for different distances. The greater increase of the radiative conductance with an emitter temperature varying from 300 to 1200 K, of a factor of 13, was found with a planar graphite emitter paired with a planar InSb substrate at d = 100 nm. For the graphite-graphite configuration, the largest enhancement was found at the lowest distance. This configuration is noteworthy because the conductance enhancement rate as a function of temperature is always increasing as distance decreases for the sphere-plane configuration.

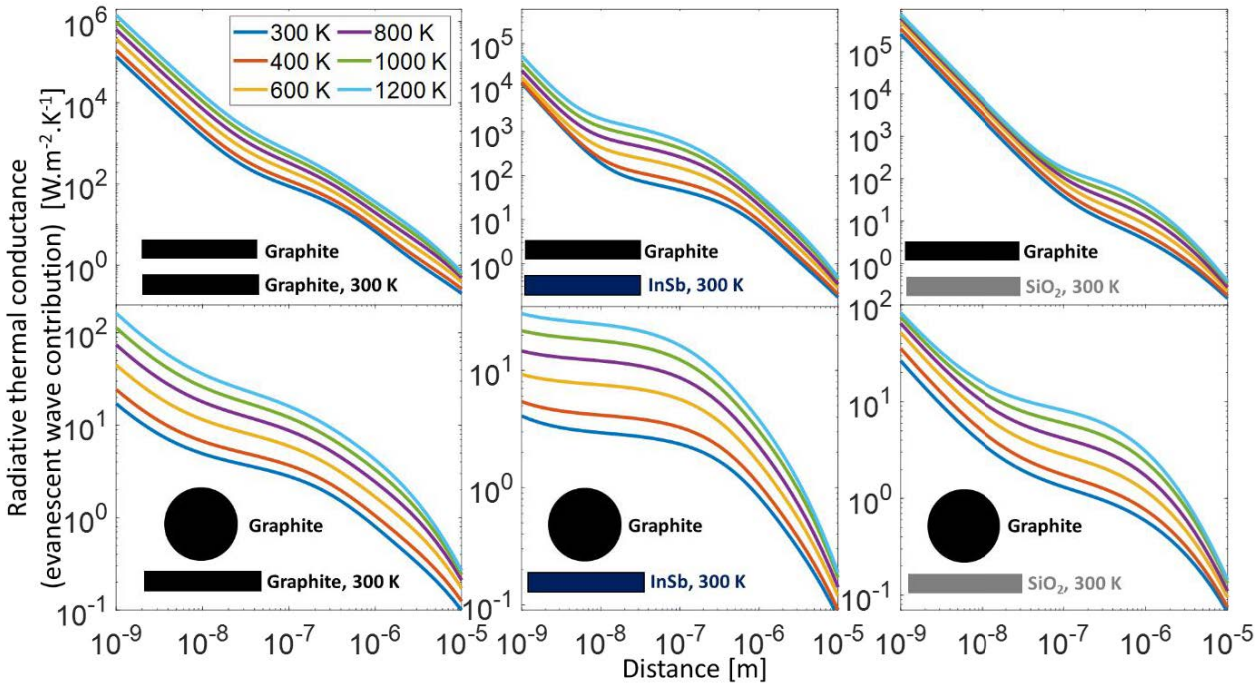

Figure II.24: Evanescent wave contribution of radiative thermal conductance between graphite planar and spherical emitters at different temperatures and planar substrates made of different materials at 300 K

The spectral distribution of radiative heat transfer between a planar graphite emitter at 1200 K and planar substrates made of the different studied materials at 300 K is provided in Figure II.26.

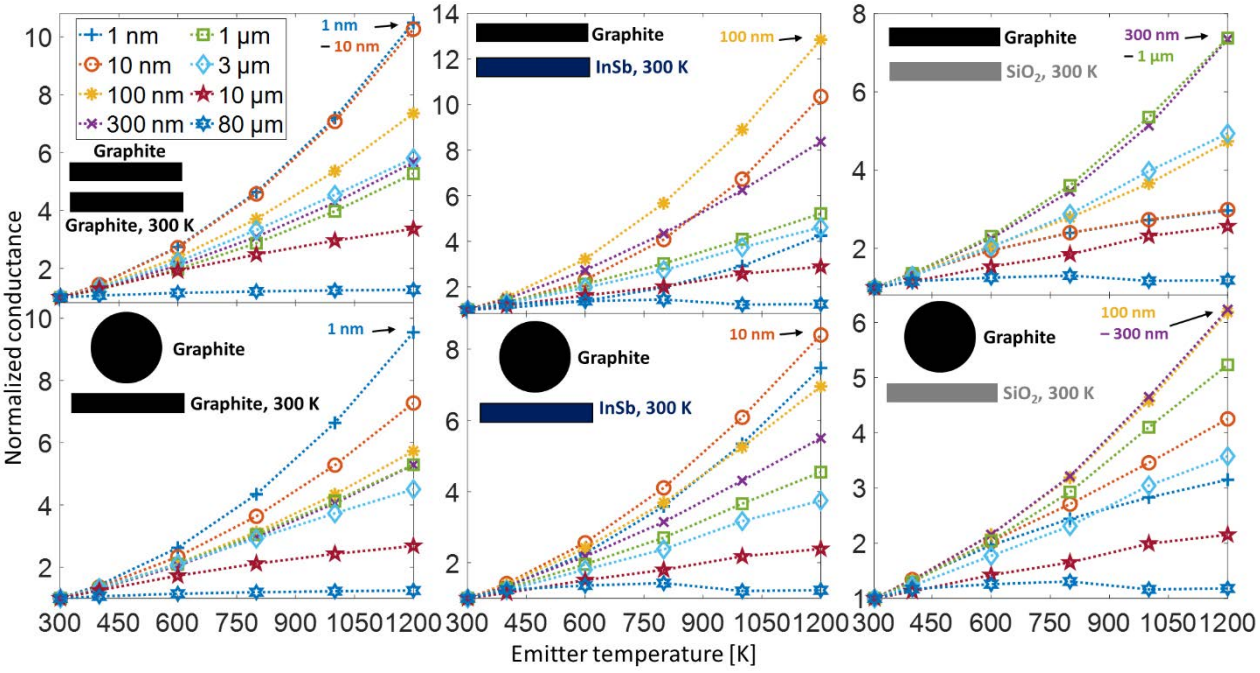

Figure II.25: Evolution of the evanescent wave contribution to radiative conductance as a function of emitter temperature, for different distances between a graphite spherical or planar emitter and a planar substrate at 300K made of SiO_2, graphite or InSb

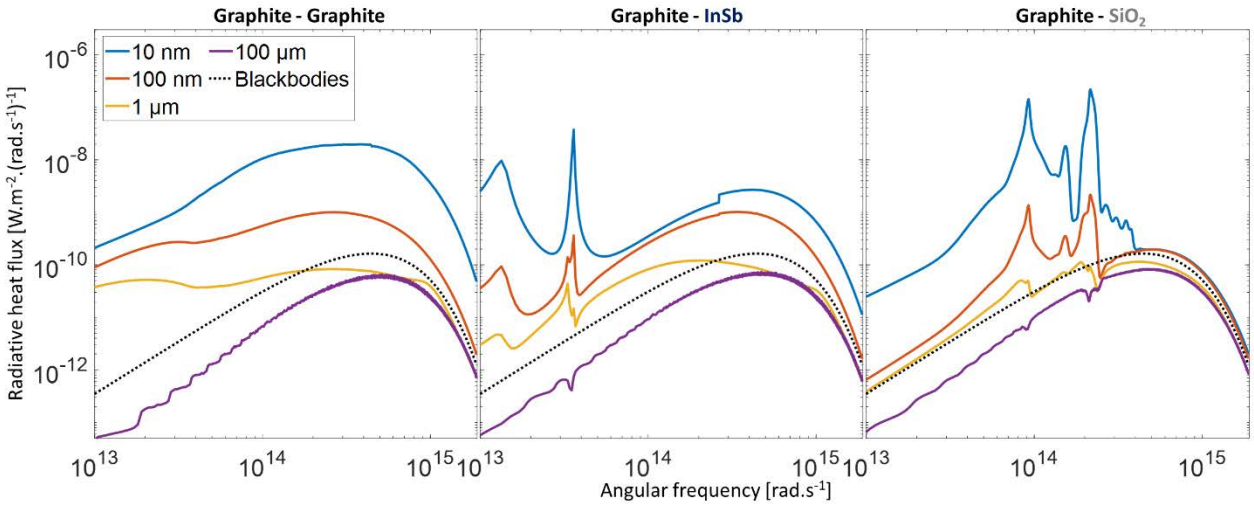

Figure II.26: Radiative heat flux as a function of angular frequency between planar graphite bodies at 1200 K and planar bodies made of either graphite, InSb or SiO_2 at 300 K

For the graphite-graphite configuration, the absence of peak appearing at small distances in the consequence of the lack of surface polariton for graphite. However, radiative heat transfer is observed to be enhanced by almost the same factor not depending on the angular frequency. For the graphite-InSb configuration, radiative heat transfer in the near field is greatly enhanced at low frequencies especially at the resonance frequency of the surface polariton supported by InSb. In addition, the enhancement is still significant at high frequencies. The configuration with a SiO_2 substrate shows a large increase of radiative heat transfer at the resonance frequencies of the SiO_2 surface polaritons, but a small enhancement at high frequencies. The observations for these three configurations may indicate that the exponent of the temperature power law for the evanescent wave contribution is expected to be the highest for the configurations with a graphite substrate due to the largest enhancement of radiative heat transfer at high frequencies.

Similarly to the calculations performed with a SiO_2 emitter, the exponent of the temperature power law of the radiative conductance is calculated as a function of distance and presented in Figure II.27.At a distance of 1 nm and as expected, the graphite-graphite configuration exhibit the largest exponent equal to 3.37, followed by the configuration with an InSb substrate with $n = 2.43$ and then $n = 2.25$ for the graphite-SiO_2 configuration. The emissivity properties of the materials lead to far-field exponents of the radiative conductance temperature power law ranging from 4.18 for the graphite-InSb configuration up to 4.32 for the graphite-graphite one.

For the graphite-InSb configuration, the impact of the surface mode contribution on the exponent of the temperature power law is very large near a distance of 100 nm. The increase of the exponent for the surface mode contribution may be observed by comparing the radiative heat flux spectra (Figure II.26) for distances of 1 µm and 100 nm. It is seen that the radiative heat transfer enhancement calculated between these two distances occurs at a faster rate as the frequency increases.

For the graphite-SiO_2 configuration, the behavior of the exponent as a function of distance for the total evanescent wave contribution is the same as that for the inverse SiO_2-graphite configuration. However, contributions of frustrated and surface modes are different between the two configurations. Surface modes start to contribute significantly (> 10 %) to evanescent waves below 10 µm for the SiO_2-graphite configuration, compared to 400 nm for the graphite-SiO_2 configuration.

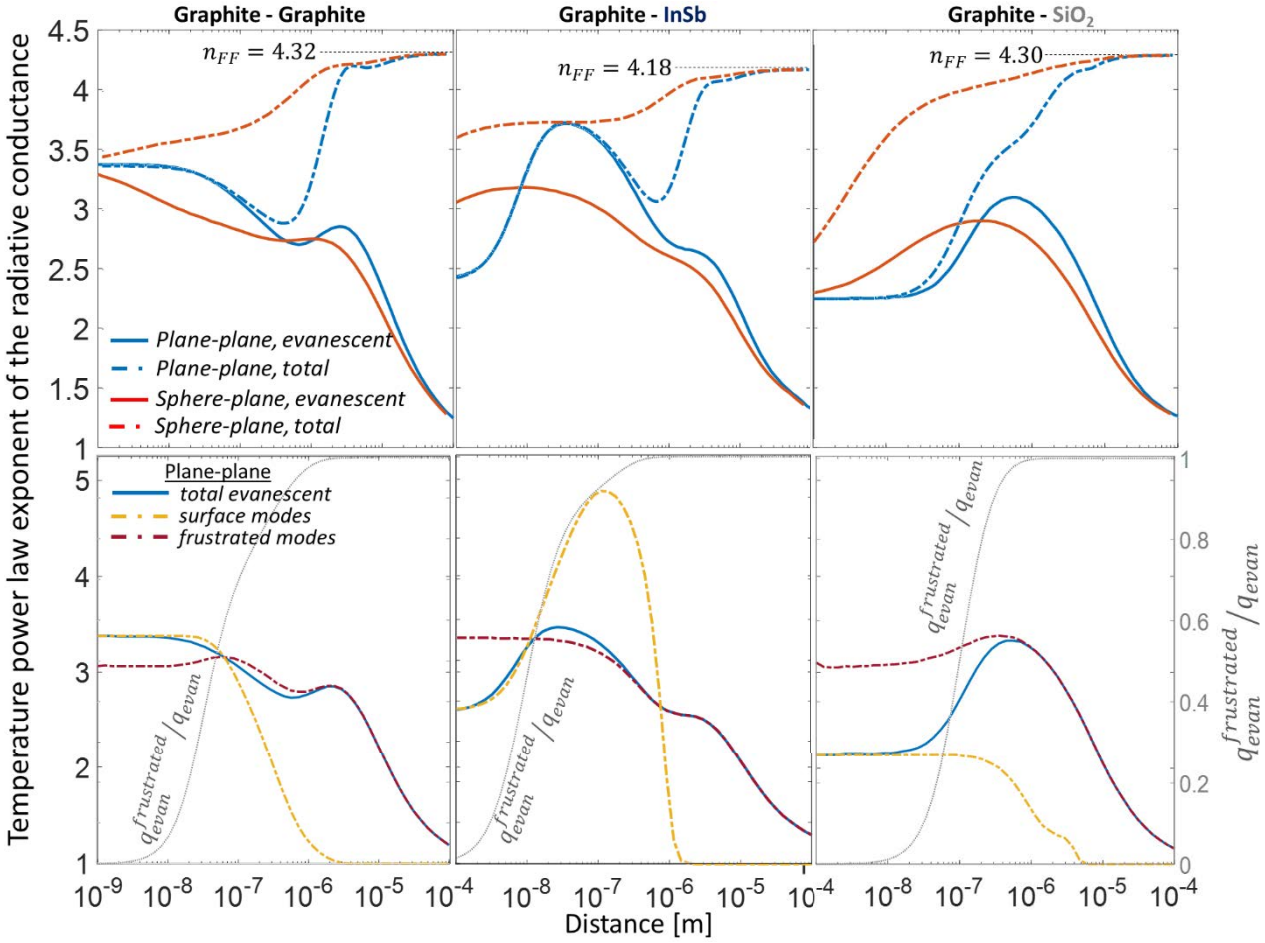

Figure II.27: Temperature power law exponent of the exchanged radiative heat flux as a function of distance between a graphite planar or spherical emitter, from 400 K to 1200 K, and a planar substrate made of SiO_2, graphite or InSb at 300 K. Dielectric functions data are taken at 300 K for all materials.

For a better visualization of the differences between the two configurations, previously calculated data are reported in Figure II.28. The total conductance difference between the two configurations is below 4 %. Differences are attributed to dielectric function data used in the calculations. For SiO_2, the dielectric function depends on temperature, as seen in Figure II.2. Therefore, for the SiO_2-graphite configuration, optical properties of SiO_2 are not constant as a function of temperature, and differs from the graphite-SiO_2 configuration where SiO_2 stays at 300 K. The difference of optical properties for SiO_2, whether it is used as the room temperature substrate or the hot emitter, results in differences of radiative heat transfer. This phenomenon is called thermal rectification, where thermal transport along an axis depends on the sign of the temperature gradient[86]. The largest differences in near-field thermal radiative conductance are found with the emitter at 800 K. At 300 K, optical properties of SiO_2 are the same for both configurations, resulting in an identical radiative conductance. It is also worth noticing that the far-field law exponents are equal to 4.30 for both configurations. Experimentally, thermal rectification measurements[55,87] seem very challenging, because of the near-field radiative conductance difference of a few percent only between the two configurations.

In the next section, a focus is made on the optimal geometrical configuration for near-field thermophotovoltaic experiments. Previously, graphite was determined to be the most appropriate material to be paired with a TPV cell in the near field. Now, geometrical considerations have to be investigated in order to maximize near-field radiative heat transfer with an InSb cell.

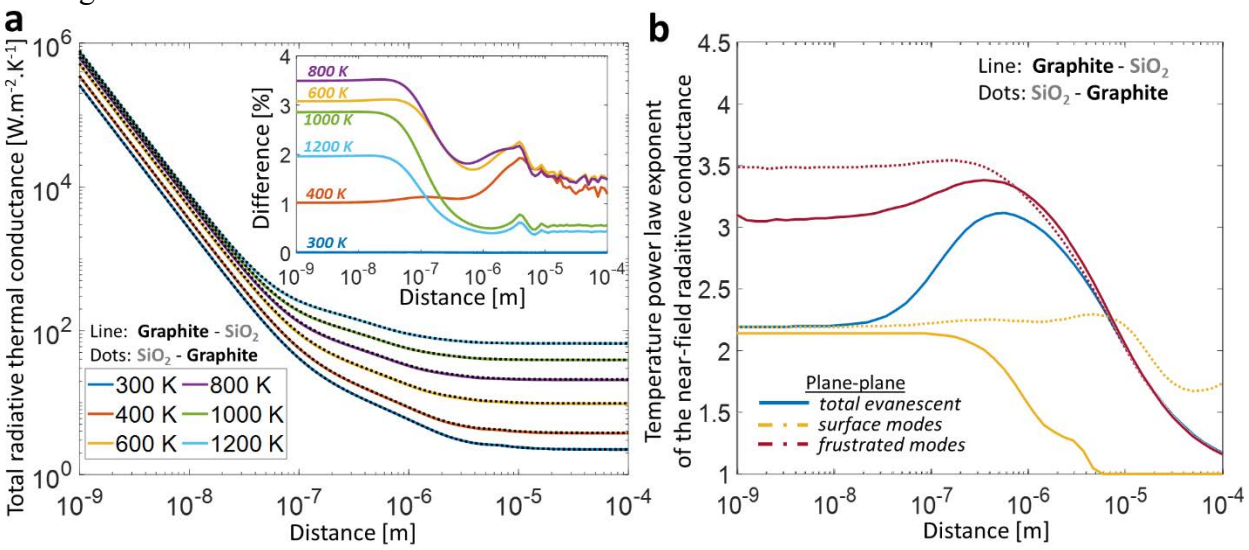

Figure II.28: Comparison between the SiO_2-graphite and the graphite-SiO_2 plane-plane configurations. (a) Total radiative thermal conductance as a function of distance for different temperatures considering the graphite-SiO_2 (lines) and SiO_2-graphite (dots) configurations. (b) Exponent of the temperature power law as a function of distance.

II.4.3 Optimal geometrical configuration for near-field thermophotovoltaics

One of the objectives of this work is to demonstrate a factor 2 enhancement of the TPV generated electrical power in the near field compared to a far-field illumination. This can be achieved by determining the best sphere and TPV cell sizes. First the contribution of the propagative waves was calculated using the Monte Carlo method (see Sec. II.3.3). Then the evanescent contribution was obtained using PFA. The cell radius is taken into account in PFA by integrating only for radii $r < R_{cell}$ (Figure II.10). The sum of the two contributions gives the total exchanged radiative heat flux. The objective is reached when the total exchanged radiative heat flux for $\lambda < \lambda_{gap}^{InSb,77K}$ is more than two times that of the contribution of propagative waves only. To match with the experimental conditions, the emitter is a graphite sphere at 732 K while the InSb cell is at 77 K. The enhancement factor (EF) was calculated at d = 10 nm because it seemed initially to be a reachable distance with the experimental setup. A map of the enhancement factor is shown in Figure II.29a as a function of sphere and cell radii. The maximum cell radius corresponds to the largest active area of the fabricated cells. The dotted line represents the EF = 2 level. The map shows that the highest EF are obtained with small cells and large spheres. In this case (Figure II.29b, top), a large fraction of the propagative waves does not reach the cell due to the view factor. The evanescent contribution is large because of the large radius of curvature of the sphere that locally tends to a flat surface above the cell. If the cell radius is too large (Figure II.29b, bottom) the evanescent contribution of radiative heat flux is almost the same but the propagative contribution is much higher, thus reducing the enhancement factor. On the enhancement factor map, there is an area where R_{sphere} < 3 µm in which EF > 2 even for large cells. In that case, the sphere is smaller than λ_{Wien} so all its surface contributes to the near-field radiative heat transfer, as

explained previously in Figure II.9. Nevertheless, for small sphere radii ($R_{sphere} < \lambda_{Wien}$), validity of the calculation method of the propagative wave contribution to radiative heat transfer is questionable, because of sub-wavelength emissivity issues[84]. Experimentally, it is easier to use relatively large spheres for power detectability. The smallest cell radius available was 10 µm so it was decided to use graphite spheres with $R_{sphere} \geq 17$ µm, corresponding to the $EF = 2$ limit. This limit is a purely radiative parameter. Electrical properties of the TPV cell depend on illumination level and have a high impact on the enhancement factor. A cell under low illumination conditions presents high dark current for a low photogenerated current (see chapter VI for more details). In the end, a high illumination of the cell is expected to maximize the enhancement factor for both the radiative and electrical sides.

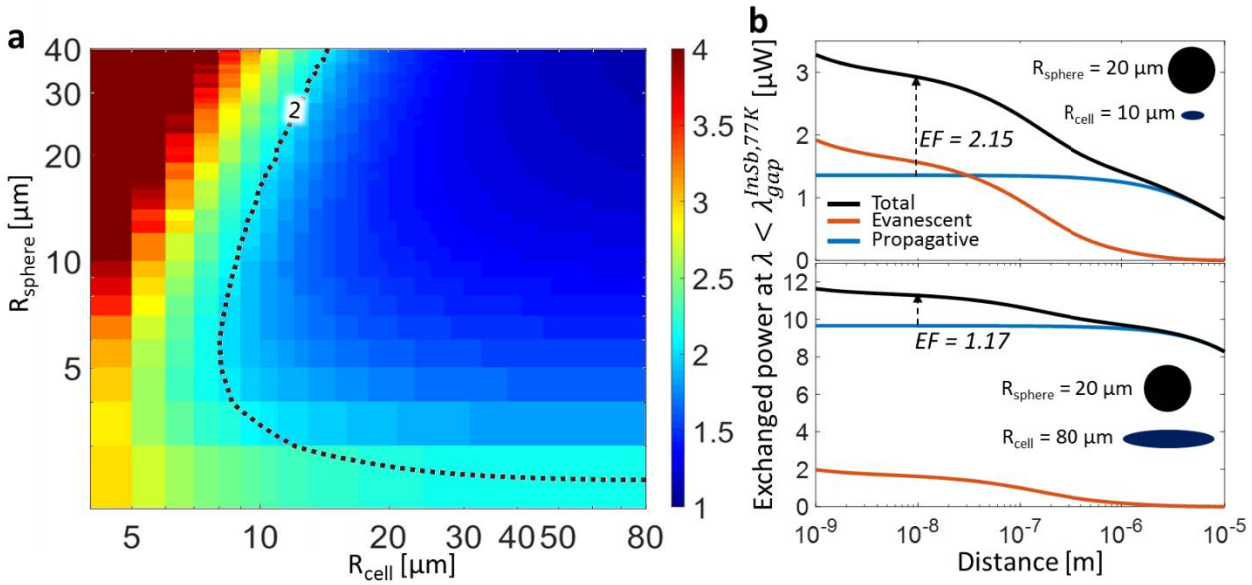

Figure II.29: Optimal geometrical configuration for near-field thermophotovoltaics (a) Enhancement factor as a function of the sphere and cell radii. (b) Evanescent and propagative wave contribution to the exchanged radiative heat flux as a function of distance for two different geometries

II.5 Conclusions

Theoretical study of radiative heat transfer is an essential step for designing the setup and compare the experimental results with that expected by calculations. This work has led to the development of numerical tools for the calculation of radiative heat transfer in the far field as well as in near-field conditions. Based on the optical properties of the emitting and receiving materials, the exchanged power between two objects has been calculated as a function of distance, temperature and geometry. The propagative and evanescent wave contributions have been treated separately using respectively a Monte Carlo ray tracing method and the proximity flux approximation. One of the objectives of this study was the selection of the best emitter material to be paired with an InSb TPV cell in order to increase as much as possible the generated electrical power by the cell in the near field. The real geometry of the system has been considered, with a spherical emitter and a cell in the shape of a disc. Calculations have shown best results with a graphite emitter. Then the sizes of the graphite emitter and the cell have been optimized in order to obtain an $EF > 2$ enhancement factor of the exchanged power useful for photoconversion.

The calculation tools have also been used to calculate the near-field radiative heat transfer between several pairs of emitter-receiver materials. It has been observed that the near-field radiative conductance evolution as a function of distance and temperature is very different from one materials pair to another. The exponent of the temperature power law of the exchanged power in the near field is also different from that in the far field, due to the modification of the emission spectra induced by the contribution of evanescent waves. These interesting theoretical results as a function of materials and temperature will be compared with the near-field radiative heat transfer experiments.

Chapter III

Design and characterization of the experimental setup

III.1 Introduction

Performing near-field radiative heat transfer measurements requires an emitter body that can be heated and brought close to contact at nanometric distances from a receiver. A vacuum environment is needed for avoiding heat transfer via air conduction. Variations of the radiative heat flux between the two objects as a function of the distance can be determined by various methods (see Sec. I.4). Such methods consist in measuring the temperature decrease of the emitter, the temperature increase of the receiver or the power to supply to the emitter (or extract from the receiver) to maintain a given temperature difference. In the case of this work, it was chosen to measure the temperature variations of a spherical emitter being brought close to contact from a fixed substrate. The substrate can be either at room temperature or cooled at cryogenic temperatures down to 10 K. The spherical shape involves for a single emitter a set of vertical distances with the planar receiver and thus reduces the exchanged heat flux compared with a planar emitter. The benefit is that it allows avoiding parallelism issues faced when trying to approach two plates at nanometric distances (see Sec. II.3.1). Building such an experimental setup requires precise electrical resistance-temperature calibration of the thermal emitter. The expected radiative thermal conductance variations are very weak, of the order of 10^{-11}-10^{-8} $W.K^{-1}$. In addition, the study of a few nanometer gap distances between the emitter and the receiver requires an accurate monitoring of the distance. In this chapter, the aim is to build an experimental setup, with performances in terms of maximum temperature, minimum distances and conductance resolution similar or possibly better to other similar works found in the literature (se Sec. I.4). The setup must be designed to be modular because it will be used to perform measurements with different emitter materials, and receivers comprising bulk materials and TPV cells. Fabrication and characterization of the emitter will be described along with the integration of the emitter in the global experimental setup comprising the vacuum system and the electrical measurement instrumentation. A characterization study of the setup will provide key information such as the minimum reachable emitter-sample distance and the accuracy of the near-field thermal radiative conductance measurements. These performances will be compared with other works from literature.

III.2 Fabrication of the thermal emitter

In order to heat up and measure the temperature of micrometric objects, resistive probes of scanning thermal microscopes (SThM) are well suited due to the temperature dependence of their electrical resistance. The resistive part of the probe located near the tip can be heated and by Joule effect up to several hundreds of kelvins while being used as a thermometer at the same time. SThM probes are sub-millimeter devices with micrometric resistive elements, making them easy to bring at a few nanometers close to contact in practice. Commercially available probes usually have heater parts shaped as a few-micrometer tip. The geometry of the tip harshly limits the near-field radiative heat transfer because of the very small exchange surface with the sample. The challenge is therefore to glue a microsphere on the tip of a probe in order to get more surface to exchange near-field radiation with the sample.

III.2.1 Combining a sphere and a SThM probe

A few types of probes are commercially available. For example, the palladium nano-probe (KNT) consists in a silicon nitride (Si_3N_4) cantilever and palladium metallic wire at the apex. It can only be heated up to 140°C.

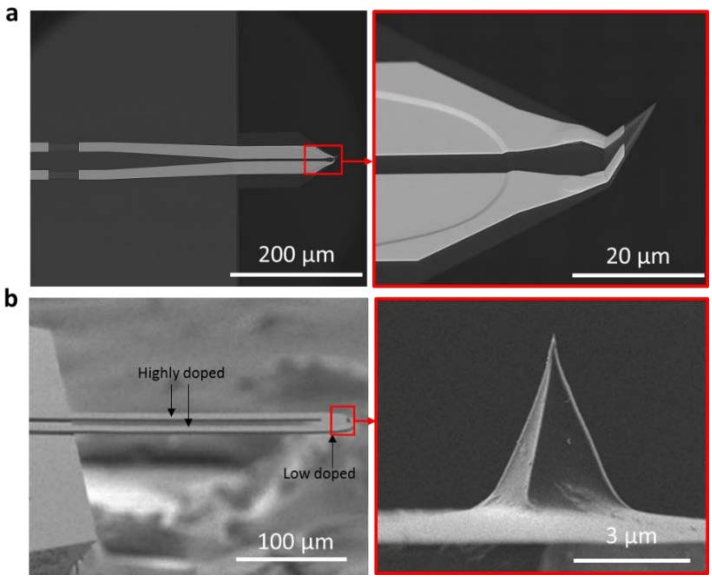

Figure III.1: Images of the different types of SThM probes with zoom on the apex. (a) Palladium probe. (b) Doped silicon probe

In this work, temperatures of several hundreds of degrees are needed in order to maximize the heat transfer, so an alternative choice is the doped silicon probe VITA-HE-NANOTA-200 from Bruker. This probe has a highly doped (N_D = 10^{20} cm^{-3}) cantilever with a low electrical resistance and a low-doped tip (N_D = 10^{16}-10^{17} cm^{-3}) with a high electrical resistance where the majority of the Joule heating occurs (Figure III.1b).
For the experiments, SiO_2 and graphite microspheres are glued on the tip of this kind of probe. The SiO_2 spheres, from Microsphere-Nanosphere Corpuscular Inc., have an expected monodisperse diameter distribution of 40 µm. Graphite spheres, from Goodfellow, are poly-dispersed with diameters ranging from 20 to 50 µm (Figure III.2).

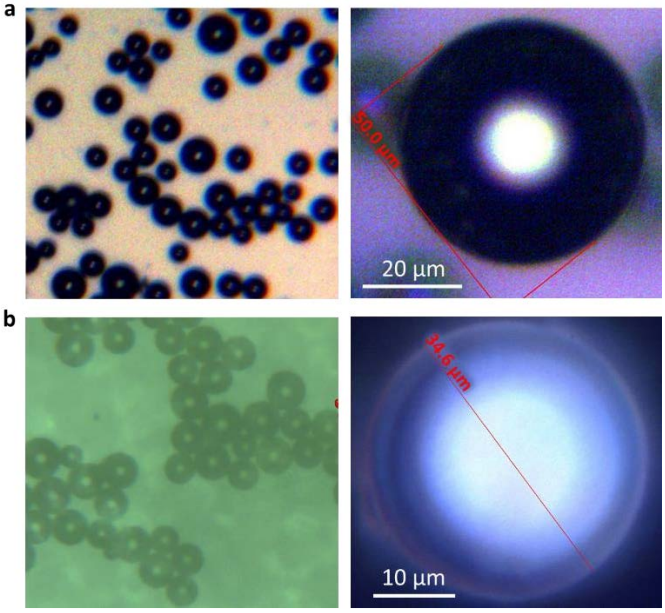

Figure III.2: Optical microscope images of the microspheres. (a) Graphite spheres. (b) SiO_2 spheres

In both cases, an alumina (Al_2O_3) based ceramic adhesive (RESBOND 989F) was used to glue the sphere on the tip of the probe. According to the supplier, this adhesive can withstand temperature up to 1650 °C and is made of 600 nm particle diameter. The small particles make it perfect for gluing micron-sized spheres. First, the spheres are deposited on a glass substrate that is mounted on a 3-axis positioning system. The SiO_2 spheres are dispersed in water, so a drop of the solution is deposited on the substrate then the water is removed with absorbent paper and air drying. The probe is held in a fixed position above the substrate and a Veho VMS-004 microscope camera with x400 magnification is used to visualize the spheres and the probe for precise positioning (Figure III.3). A scan is performed in *xy* directions to find a sphere with the appropriate diameter. The size of the spheres can be estimated by comparing them to the known length of the cantilever of the probe (200 µm). Once the desired sphere is found and the probe placed close to it (1), a drop of adhesive is deposited on the substrate close to the probe. The substrate is then moved to put the tip of the probe inside the adhesive drop (2), then retracted in the other direction to extract the probe with a small amount of adhesive deposited on the tip of the probe (3). The sphere is brought into contact with the adhesive-covered tip during a few seconds (4). The contact is seen by the change of light reflection on the probe due to the bending of the cantilever. The probe is then retracted (5) and moved away (6) to avoid gluing multiple spheres. The adhesive dries at room temperature and at an especially fast rate considering the small quantity that is used. After a few minutes of drying, the emitter (probe-sphere system) is ready to be calibrated. At the end of the process, the exact diameter of the sphere is measured by optical microscopy or by scanning electron microscopy (SEM) (Figure III.4).

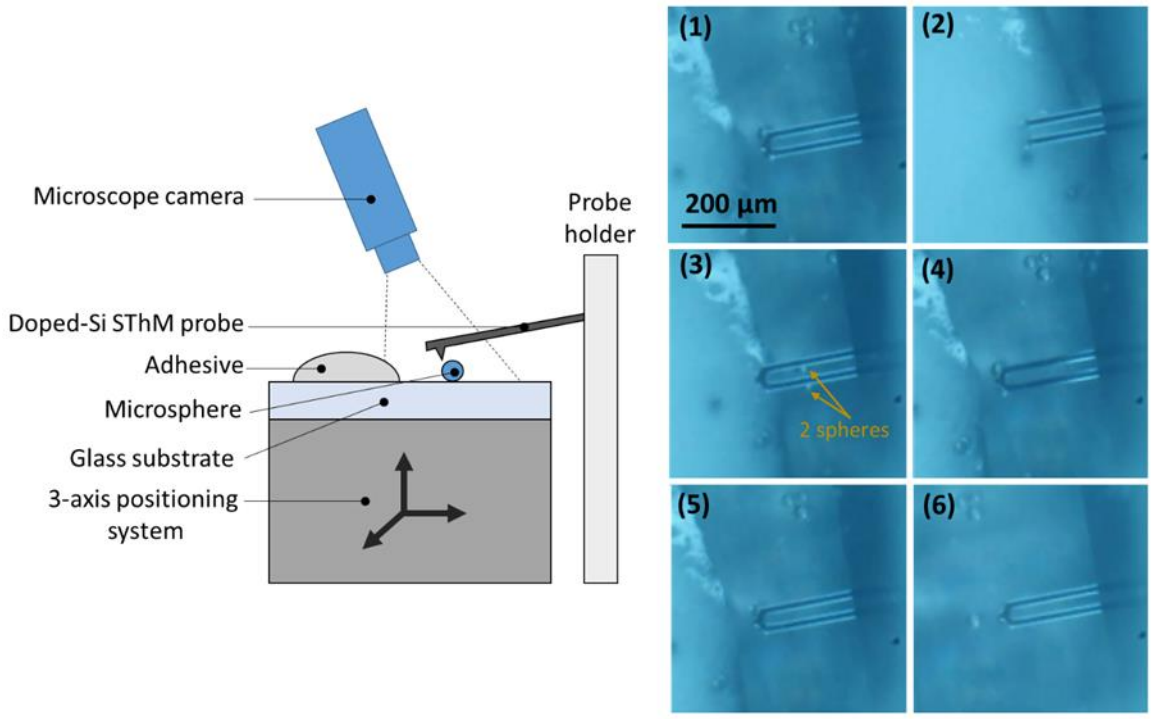

Figure III.3: Procedure for gluing a sphere on the tip of a SThM probe

III.2.2 Calibration process

Once the sphere and the probe are assembled, the next important step is the electrical resistance-temperature calibration of the emitter. During the experiments the temperature of the emitter is

inferred from its electrical resistance so the resistance-temperature *R(T)* curve must be determined. This calibration process is repeated for each emitter because of slight differences during the fabrication process from one probe to another. One part of the process consists in directly measuring the electrical resistance at different temperatures. In the other part, the temperature is deduced from the resistance according to the electrical power measurement.

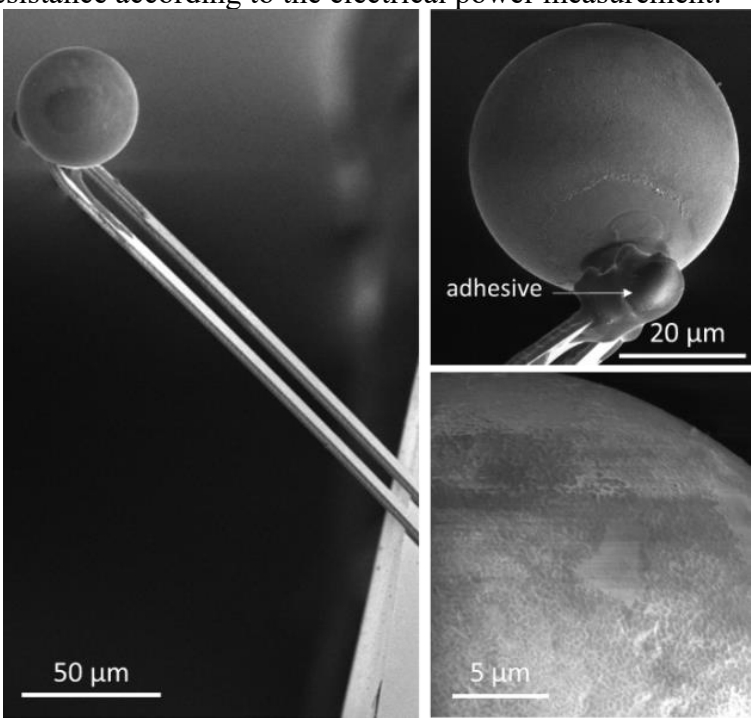

Figure III.4: SEM images of a sphere glued on the tip of a doped-Si SThM probe.

III.2.2.1 Oven calibration measurement

First, the whole system composed of the probe and its half-moon shaped holder is put in an oven typically used for thermocouple calibration (Fluke 9144) (Figure III.5). Because of the half-moon holder, the electrical resistance measurement could only be performed from room temperature up to 140 °C. At higher temperatures, the glue fixing the probe on the half-moon (Figure III.5, left) and other components of the holder start to deteriorate and may damage the probe.

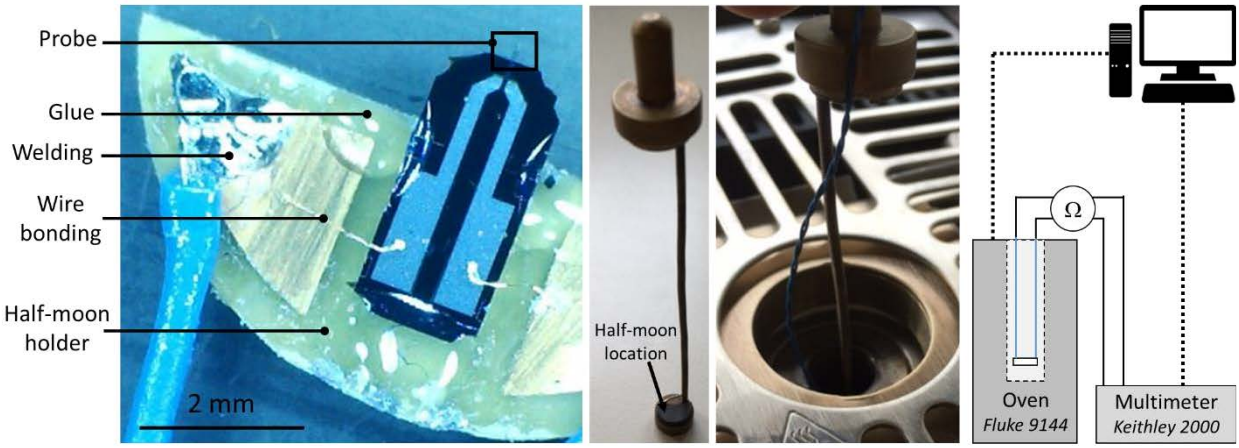

Figure III.5: Setup for the R(T) calibration curve measurement in the oven.

A probe was modified in order to perform electrical resistance measurements in the oven at higher temperatures. The probe was removed from its half-moon holder by melting the glue and breaking the wire bonding. Then the probe was glued on a glass substrate with the same ceramic adhesive as that used for gluing the spheres. The electrical contacts were taken with bare wires connected to the probe with silver paste (inset Figure III.6, left). The modified probe could no longer be used for near-field experiments because it was embedded in ceramic. The only purpose of this probe was to find a fitting law for the *R(T)* curve that could be applied to non-modified probes, in order to determine the resistance-temperature relation for a large temperature range based on non-destructive measurements at $T < 140$ °C. The measurement data of the modified probe show that the electrical resistance reaches a maximum at a temperature T_{Rmax} near 620 K (≈ 350 °C) and then start to decrease. The probe is made of doped silicon, so at a given temperature depending on the doping level, the thermally generated carrier concentration becomes higher than the doping concentration. On the one hand, the resistivity increases with temperature due to the decrease in the majority carrier mobility. On the other hand, the resistivity decreases due to the increase in thermally generated carrier concentration. This second effect becomes dominant for temperatures larger than the point of maximum resistance[88,89]. A quadratic fit of the measured data gives a very good agreement from room temperature up to a temperature close to T_{Rmax}. Therefore, the first part of the calibration process for the non-modified probes consists in measuring the resistance in the oven up to 140 °C with small steps (5 °C, 30 min stabilization time) and then fit the data with a quadratic model. The *R(T)* curve is then known from room temperature up to approximately T_{Rmax}. The second calibration step is needed to determine T_{Rmax} and get the *R(T)* curve for all temperatures.

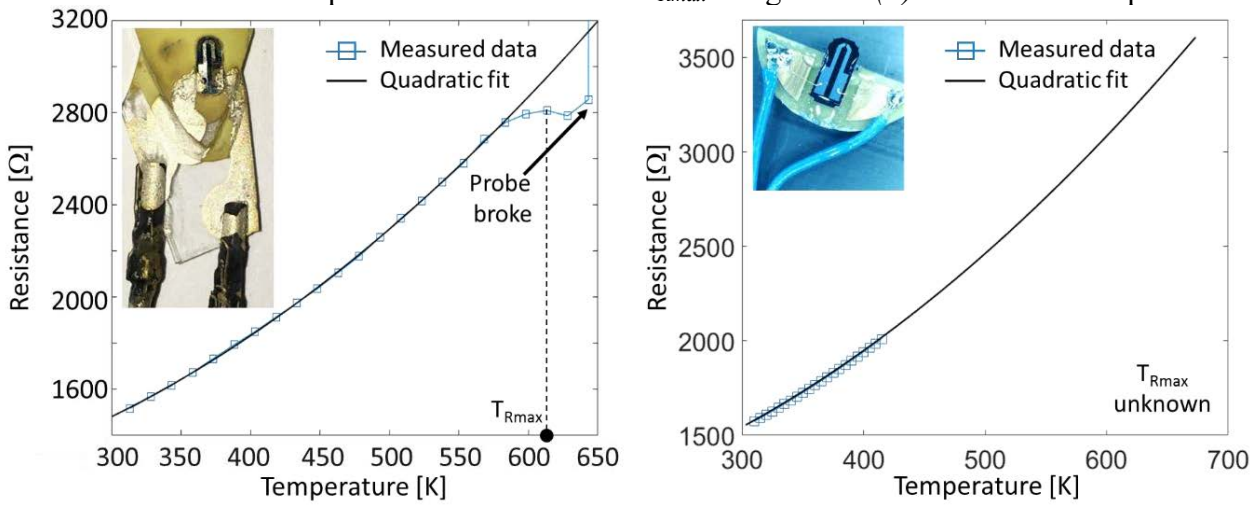

Figure III.6: R(T) curve measured in the oven for the modified (left) and non-modified (right) probe.
The inset in the left figure shows the modified probe.

III.2.2.2 Temperature deduced from electrical power

The second part of the calibration aims to determine the calibration curves for temperatures $T > T_{Rmax}$. Because a direct measurement in not possible, electrical resistances at this temperature range were measured according to the electrical power *P* supplied to the probe (Figure III.7a). The temperature was then deduced from this *R(P)* curve. At $T > T_{Rmax}$, the temperature of the probe due to Joule heating is proportional to the supplied electrical power as $T = kP + T_{amb}$, which is not the case at lower temperatures[88]. A fitting coefficient *k* was applied to the electrical power in order

to calculate the temperature. The coefficient k was adjusted until the curve matches the fit of the oven-measured part of the $R(T)$ curve for $T \approx T_{Rmax}$ (Figure III.7b). The images of the emitter heated by Joule effect in vacuum (Figure III.7c) show that the sphere starts to glow in the visible range of the electromagnetic spectrum at $T > 700$ °C. This proves that the heat coming from the low-doped part of the SThM probe, where the sphere is glued, is well conducted into the sphere. The maximum reachable temperature is 1414 °C (1687 K), which corresponds to the melting point of silicon. Since the evolution of the electrical resistance is not linear as a function of temperature, the sensitivity of the emitter is temperature dependent.

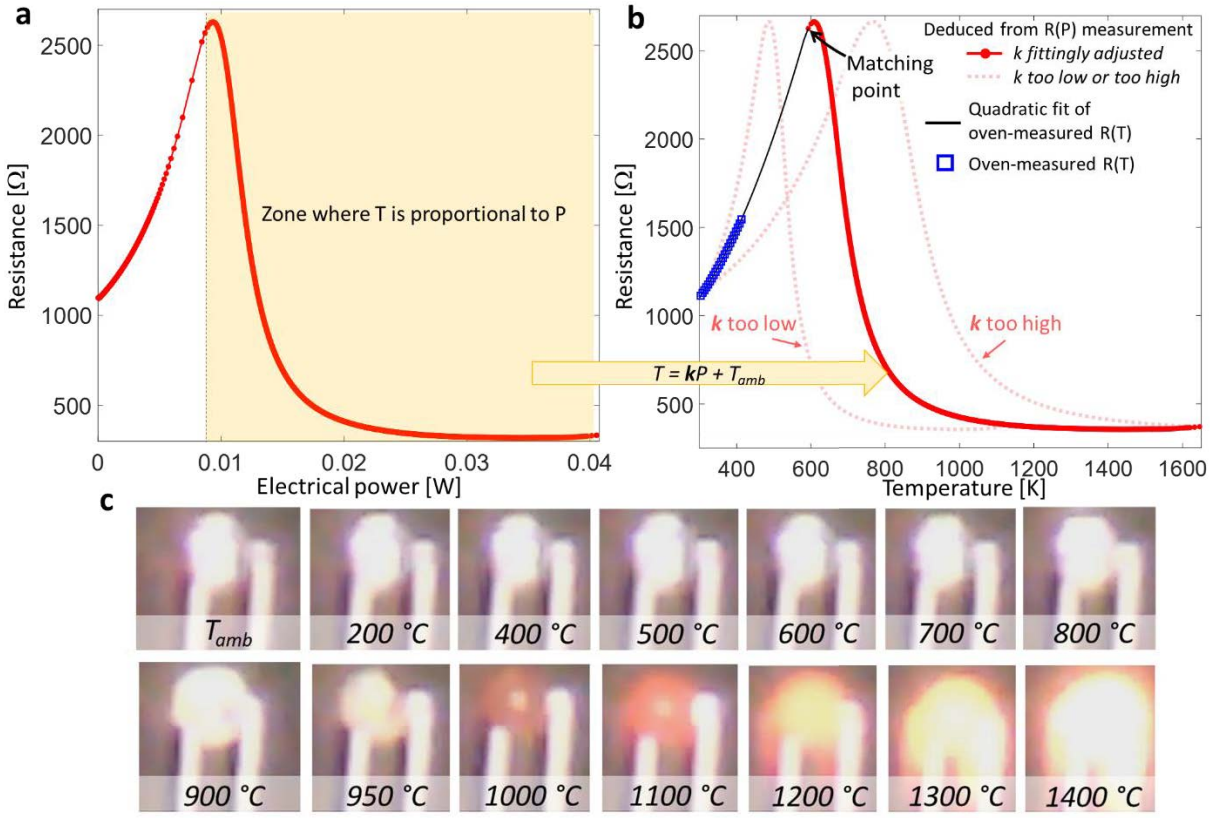

Figure III.7: Calibration curve for the whole temperature range.
(a) R(P) electrical measurement. (b) Reconstructed R(T) calibration curve. (c) Images of a probe with a sphere heated by Joule effect from T_{amb} to 1400 °C.

III.2.3 Temperature coefficient of electrical resistance

The best sensitivity point is found where a small temperature change induces a large electrical resistance variation that can be easily measured experimentally. The temperature coefficient α (in K^{-1}) is used to determine this point and is calculated using the following equation:
Here R and T are respectively the electrical resistance in Ω and the temperature in K. α is positive

$$\alpha = \frac{1}{R}\frac{dR}{dT}. \qquad (III.1)$$

from room temperature up to T_{Rmax} then becomes negative at higher temperatures. Absolute values of α are shown in Figure III.8 in order to determine the temperature T_S where $|\alpha|$ is maximum. This

temperature corresponds to the maximum temperature variation sensitivity of the emitter. For each emitter, T_S has approximately the same value of 732 K (459 °C). At higher temperatures, the temperature variation sensitivity of the emitter decreases and becomes small near 1400 K, where the electrical resistance reaches a stable value as a function of temperature. Heating the emitter beyond this temperature is possible but the temperature deduction would have a high uncertainty. A solution for studying larger temperature differences would be to heat the emitter while measuring the temperature increase of the substrate (instead of the temperature decrease of the emitter) with another device. This way, emitter temperatures up to 1600 K might be reached so temperature differences up to 1300 K might be investigated.

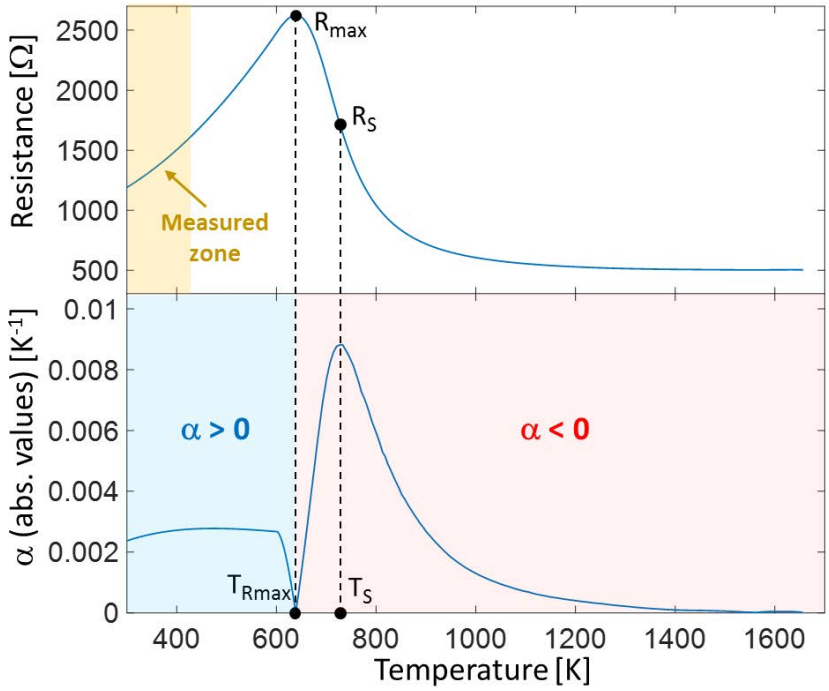

Figure III.8: R(T) curve and temperature coefficient as a function of the emitter temperature

III.2.4 Systematic error from the emitter calibration

The accuracy of the temperature determination is partly driven by the *R(T)* calibration curve, used to infer the temperature from the electrical resistance measurement. As explained in Sec. III.2.2, this curve is actually measured only from room temperature up to 140 °C, then a quadratic fit is applied on the measured data up to a value close to T_{Rmax} = 330-380 °C. It can be seen on Figure III.6 (left) that the fit is valid up to T = 0.95 T_{Rmax}. The rest of the curve, which is measured electrically, is theoretically valid for $T > T_{Rmax}$ only. As a consequence, the *R(T)* curve between 0.95 T_{Rmax} and T_{Rmax} is not accurately determined. The curve for this temperature range is calculated from the electrically measured part. Considering the accuracy of the *R(T)* determination close to T_{Rmax}, the temperature determination using the calibration curve can therefore be considered with a systematic error $err_T^{T_{Rmax}}$ = 5 %.

The different contributions of the low-doped (tip) and highly-doped (cantilever) parts of the emitter on the global electrical resistance have to be considered. The calibration method in the oven set the entire probe at the same temperature. However, only the tip of the probe is heated during the experiments, creating a temperature gradient inside the probe which is different from that during

the calibration. It was demonstrated in the thesis work of Éloïse Guen[90] that this difference in temperature gradient, coupled with the different doping levels inside the probe, leads to a systematic error on temperature determination err_T^{Calib} = 15 %. Considering the two sources of systematic error, the global systematic error on temperature determination is $err_T = err_T^{T_{Rmax}} + err_T^{Calib} \approx 20$ %. It was chosen to sum the uncertainties so it corresponds to the worst-case scenario. This global systematic error leads to uncertainties on the temperature coefficient determination. From equation (III.1), the relative uncertainty on alpha can be expressed as:

$$\frac{\delta\alpha}{\alpha} = \frac{\delta\Delta R}{\Delta R} + \frac{\delta R}{R} + \frac{\delta\Delta T}{\Delta T} = \frac{2\delta R}{\Delta R} + \frac{\delta R}{R} + \frac{err_T \Delta T + 2\delta T}{\Delta T}. \qquad (III.2)$$

The terms δR and δT are respectively the electrical resistance and temperature random noises, measured with the method described in section III.4.3.1. The previous equation tells that the relative uncertainty on α is larger or equal to the systematic error err_T, depending on the random electrical noise.

III.3 Experimental setup

This part describes the experimental setup that was built in order to perform near-field radiative heat transfer and near-field thermophotovoltaic measurements. The vacuum system and electrical circuit will be described along with the cryogenic cooling system. The data acquisition and processing, which is controlled using several Matlab codes as communication interfaces between the computer and all the instruments, will also be detailed.

III.3.1 General design

The main objective of the experiments is to measure the increase of the radiative heat transfer in the near field, at distances of a few micrometers down to a few nanometers, between a spherical emitter and a planar substrate. The substrate is either a bulk material or a TPV cell. To perform such measurements, the temperature drop of a calibrated emitter is measured in vacuum according to the gap distance from the substrate.

III.3.1.1 Vacuum system

The experiments were done inside a vacuum chamber at a pressure of the order of 10^{-6}-10^{-7} mbar in order to avoid heat transfer with the substrate from air conduction (Figure III.9). To reach this pressure range, a primary pump was used to lower the pressure down to ~ 10^{-2} mbar in a few minutes. Then a turbomolecular pump was turned on in series with the primary pump and the pressure dropped down to ~ 10^{-6} mbar after approximately 10 hours. This long time can be explained by the outgassing of some components inside the vacuum chamber and the residual humidity. Because of the small gap distances, the low pressure has to be maintained without any mechanical vibrations. When the lowest pressure was reached, an ion pump was started then both the primary and turbomolecular pumps were turned off and the valve between them was closed. In the end, only the ion pump was working and maintaining the desired vacuum level. This kind of pump allows to obtain lower vacuum, but this is not the goal. The main interest is that its principle is based on trapping gases, therefore no mechanical part induces vibrations.

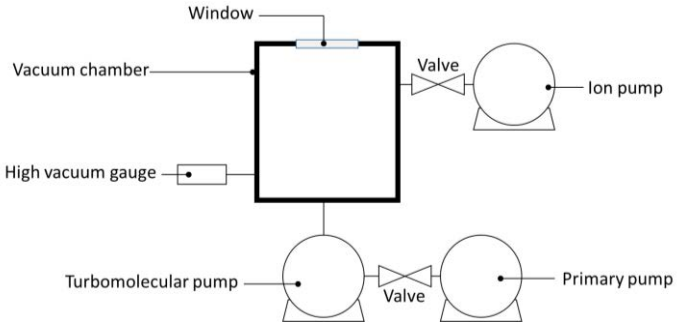

Figure III.9: Schematic of the vacuum system

III.3.1.2 Measurement setup

The general experimental setup is detailed in Figure III.10. The emitter is attached to a 3D-printed holder by a magnetic surface. The holder is made of an electrically insulating polymer (polyactic acid, PLA) to keep the emitter away (4 cm) from the z piezoelectric positioner (Figure III.11c). This distance is needed in order to avoid electrical perturbations coming from the positioner during the measurements. The piezoelectric positioner acts as a capacitor and generates an electrostatic field when a voltage is applied. These perturbations were observed by supplying an electrical current to a resistor, positioned at a distance *d* above the piezoelectric positioner (Figure III.11a). The voltage of the resistor was measured while a 0-100 V voltage ramp was applied to the piezoelectric positioner. Voltage variations of the resistor were observed in coordination with the piezo voltage ramp (Figure III.11b). The amplitude of the resistor voltage variation decreased when the distance increased, and nearly vanished after 28 mm. The z-piezoelectric positioner is an Attocube ANPz51, designed for high vacuum (10^{-8} mbar), with a displacement range of 2.5 mm in slip-stick mode, and 5 µm only with sub-nanometric resolution in fine positioning mode. It is controlled by an Attocube ANC 300 device with an ANM 300 module that allows both slip-stick and fine positioning at the same time. For emitter-sample distances lower than 5 µm, a voltage generator supplies a DC voltage from 0 to 6.667 V to the ANC 300 controller. The voltage is then amplified 15 times to deliver a 0-100 V voltage to the piezoelectric positioner, corresponding to a 0-5 µm displacement range.

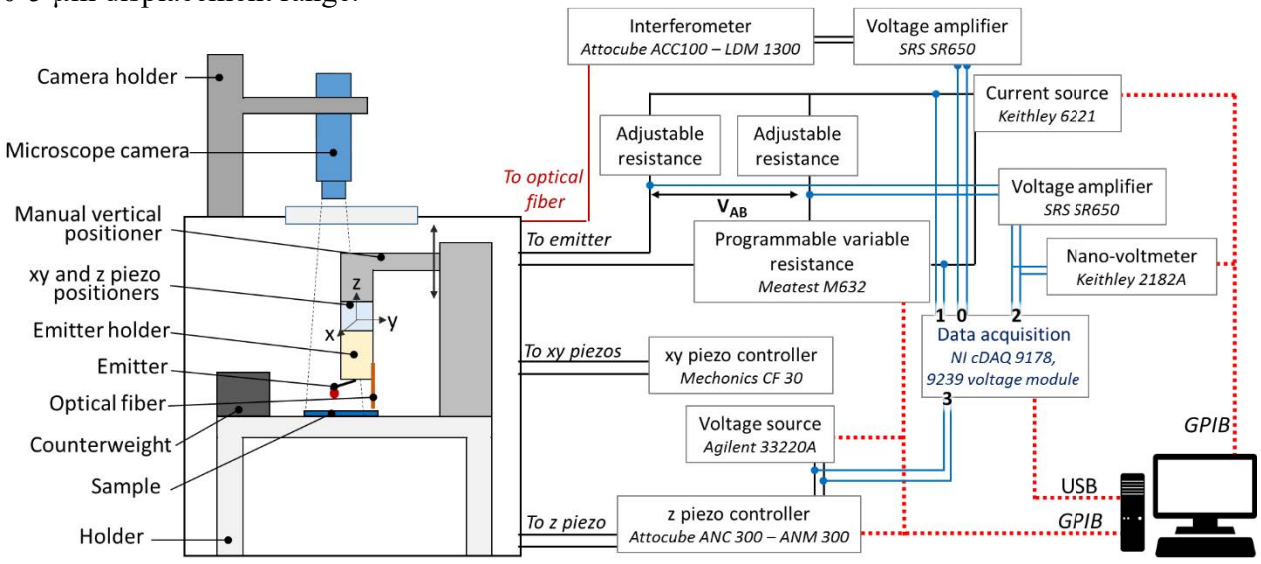

Figure III.10: General sketch of the experimental setup

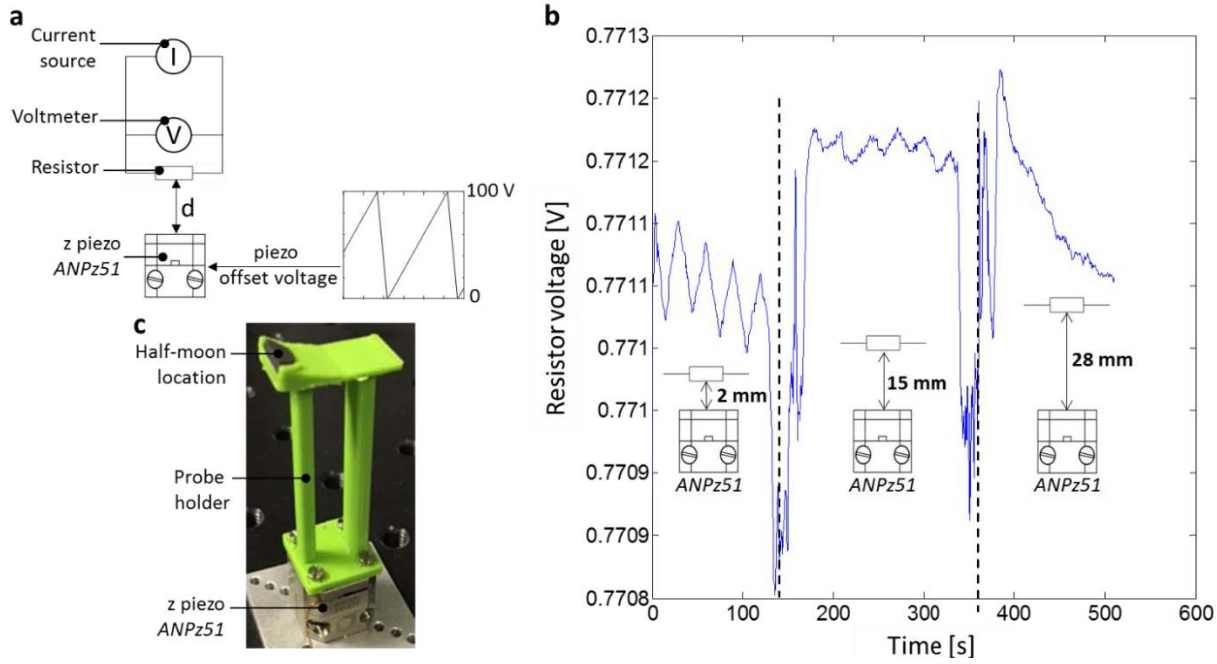

Figure III.11: Electrical perturbations induced by the z piezoelectric positioner. (a) Schematic of the measurements of the electrical perturbations. (b) Resistor voltage as a function of time. (c) 3D printed probe holder

A set of x and y-axis piezoelectric positioners is mounted on top of the z-axis one in order to provide a 3 mm range slip-stick displacement in the xy plane. They are monitored by a Mechonics CF 30 controller. All the previous detailed elements are attached to a manual vertical positioner for coarse positioning above the sample with several centimeters range.

This large distance range is needed in order to easily manipulate the emitter before and after the experiments. This positioner is not remotely controlled so once the vacuum chamber is closed it remains in a fixed position. A long working distance camera (Dino-Lite Edge 3.0 AM73115MTF) placed outside the vacuum chamber is used to visualize the emitter and the sample. This camera provides a 40x optical magnification at a 15 cm distance and a good resolution of 2560x1920 pixels allowing numerical magnification. Finally, an optical fiber for interferometric measurement is placed on the emitter holder. It is useful to measure vibrations between the emitter and the sample, therefore the determination of the distance near the contact is more accurate. The interferometer controller (Attocube ACC 100 with LDM 1300 module) feeds a λ_{laser} =1310 nm laser beam with a 120 µW power through the optical fiber. The laser beam is reflected on the sample surface while the fiber is moving vertically (Figure III.12a), and then the interferometric signal is acquired by the controller and amplified with a 2x gain (Figure III.12b).

The electrical setup for measuring the electrical resistance of the emitter is also depicted in Figure III.10. The emitter acts as an electrical resistance that is part of a Wheatstone bridge, also composed of two manually adjustable resistances and a programmable variable resistance that is remotely controlled. A Keithley 6221 current source is used in this setup. During the experiments, the emitter is heated up at a certain temperature corresponding to a specific value of its electrical resistance inferred from the *R(T)* calibration curve. The temperature is stabilized after 30 to 60 minutes and only a small thermal drift of the order of 10^{-5} K.s^{-1} remains (Figure III.13).

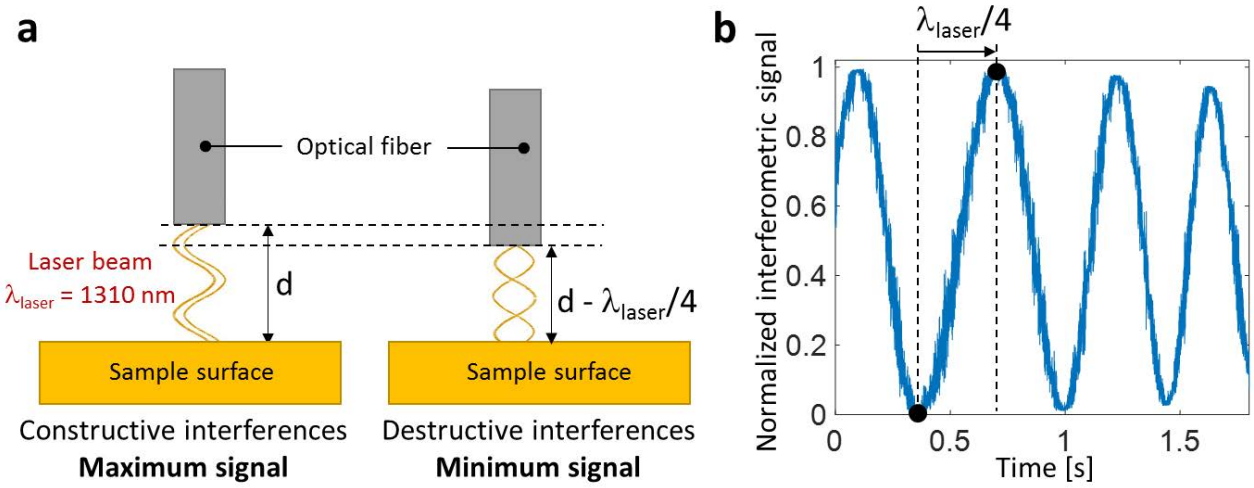

Figure III.12: Interferometric measurement principle.
(a) Sketch of the laser beam coming from the optical fiber and reflected on the sample surface.
(b) Normalized interferometric signal as a function of time while the fiber is moving

The programmable variable resistance value R_V is set to the target resistance value and then the current is adjusted until the bridge is balanced ($V_{AB} = 0$, $R_{emitter} = R_V$) with the emitter out of contact at a distance $d \approx 5$ µm. V_{AB} is amplified with a 100x gain by a voltage amplifier. The value is directly read on a Keithley 2182A nano-voltmeter and acquired by a NI cDAQ 9178 with a 9239 voltage acquisition module. The four ports on the cDAQ, labeled from 0 to 3, are respectively used to acquire at a 2 kHz rate the interferometric signal, the voltage of the Wheatstone bridge V_{heat}, the amplified V_{AB} and the voltage supplied to the controller of the z-piezoelectric positioner. Instruments are connected by a GPIB interface to the computer while the cDAQ is connected via USB. Matlab codes were developed to control all the instruments and acquire the data, using the *Instrument Control* and *Data Acquisition* toolboxes.

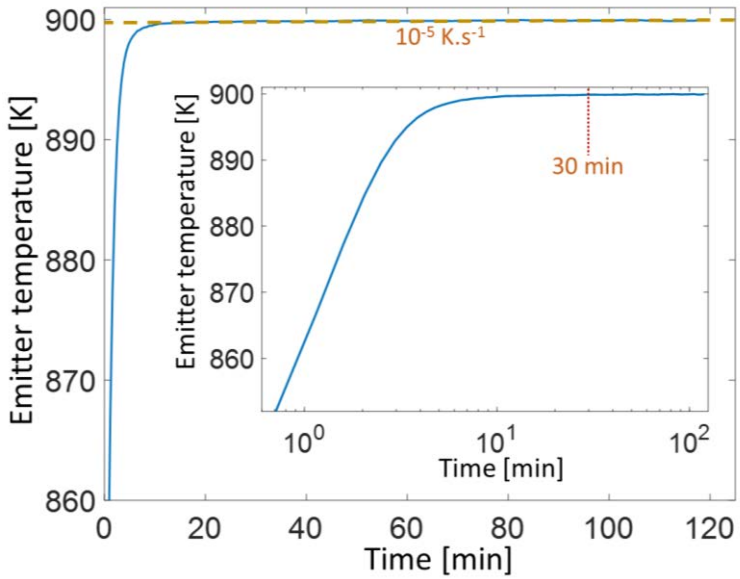

Figure III.13: Transient heating of the emitter

III.3.1.3 Experimental protocol

An example of several signals acquired during a 120 s session is represented in Figure III.14. The first panel shows the voltage applied to the z-piezoelectric positioner, from 0 to 100 V, and the corresponding displacement from 0 to 5 µm. During the approach phase, the voltage increases and the piezo expands so the emitter gets closer to the sample surface. The unbalance voltage V_{AB} of the bridge and V_{heat} are measured, allowing to calculate the electrical resistance of the emitter with the following equation:

$$R_{emitter} = \frac{R_V}{\left(\frac{R_1}{R_1 + R_2} - \frac{V_{AB}}{gV_{heat}}\right)^{-1} - 1} \qquad (III.3)$$

In the equation, R_V is the resistance of the programmable resistance, R_1 and R_2 are the electrical resistances of the manually adjustable resistances in the Wheatstone bridge and g is the gain provided by the voltage amplifier. At some point during the approach, the emitter goes into contact with the sample. It can be seen on the resistance signal in Figure III.14 where the value suddenly changes. After the contact point, the z-piezoelectric positioner keeps moving until it reaches a 5 µm displacement. Then the voltage decreases rapidly to 0 so the emitter is withdrawn from the surface and is no longer in contact.

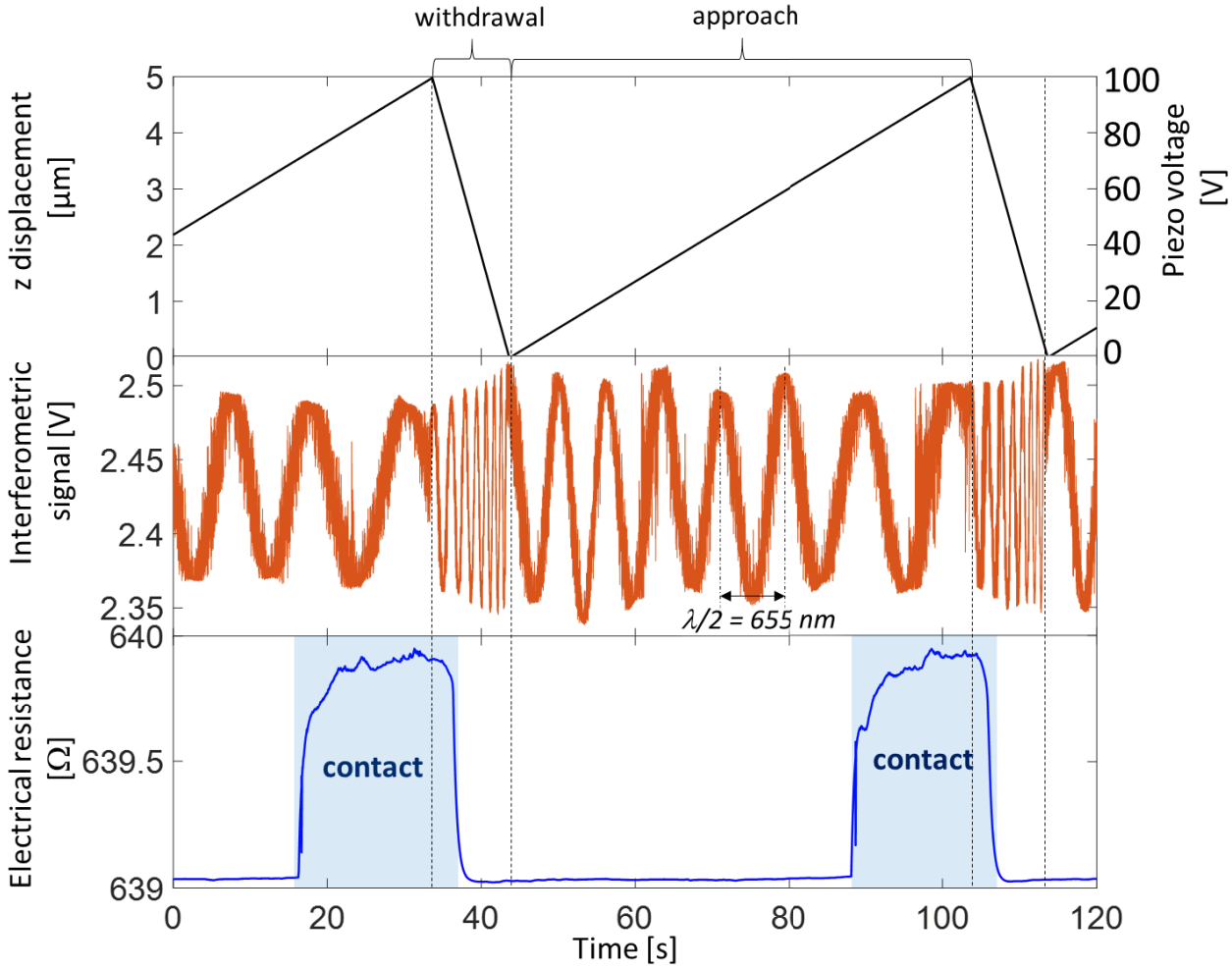

Figure III.14: Example of simultaneously acquired signals

The duration of an approach was set to 60 s, corresponding to a speed of approximately 80 nm.s^{-1}. The withdrawal duration is 10 s because the resistance signal during this phase is not of interest for the experiments. However, the withdrawal speed must not be too fast because it would induce strong hysteresis in the displacement. Along with the displacement and resistance signals, the interferometric signal provides information about the displacement and vibrations of the system. When the optical fiber moves along a distance λ corresponding to the wavelength of the laser, the optical path is modified by 2λ. So one period of the interferometric signal corresponds to a $\lambda/2$ displacement of the fiber, equal to 655 nm. It is clearly seen on the interferometric signal in Figure III.14 that during an approach, the time between the maxima is larger than that during a withdrawal because of the speed difference. A more detailed analysis of the interferometric signal will be given in section III.4.2.3. Near-field radiative heat transfer measurements consist in measuring the small change in electrical resistance according to the displacement of the emitter, which is correlated to a temperature drop due to the increase in the radiative thermal conductance between the emitter and the sample.

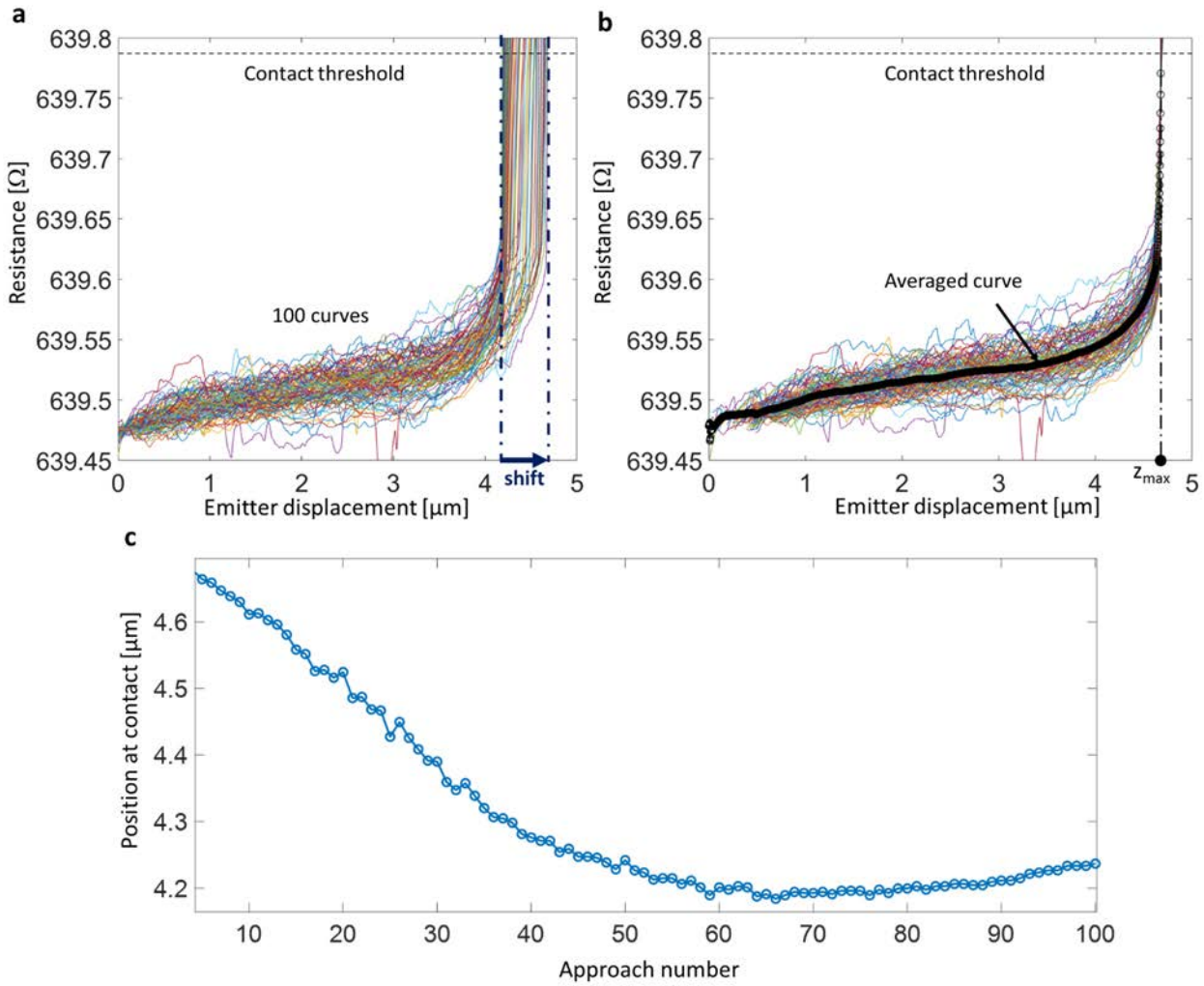

Figure III.15: Series of 100 resistance-displacement approach curves.
(a) Raw resistance curves. (b) Curves shifted in distance. (c) Displacement value at the contact point

The signal variations are very weak so series of 100 approaches are usually made and averaged to obtain a smooth signal (Figure III.15a,b). The consecutive approaches are extracted from the electrical resistance signal using the z displacement signal as reference with $z = 0$ and $z = 5$ µm as starting and ending points. There is a small drift in the position of the contact point between consecutive approaches (Figure III.15c). A threshold value of the electrical signal is used to determine the contact points of each approaches. Then, the curves are shifted to set their contact points at the same displacement value z_{max} to correct the mechanical drift.
An average electrical resistance curve can be calculated to obtain a clean approach curve. In the end, only the values before contact are used in this study. Concerning the thermal drift of the emitter temperature, it is very weak (Figure III.13) and does not need to be corrected if the approaches are made at a relatively fast speed. Finally, a sliding average is made on the previously averaged curve to get rid of the electrical 50 Hz noise. Considering a 2 kHz acquisition rate, this results in a sliding average over 40 points. Considering a 5 µm displacement performed with a duration of 60 s, a 2 kHz acquisition rate followed by a sliding average over 40 points result in one point every ~1.7 nm displacement.

III.3.1.4 Temperature and conductance calculations

Once a clean resistance approach curve is obtained, the *R(T)* calibration curve is used to determine the temperature (Figure III.16a,b). Either the increasing ($T < T_{Rmax}$) or the decreasing ($T > T_{Rmax}$) part of the curve is used to calculate the temperature, depending on the initial temperature of the emitter. Then the variations of thermal conductance during the approach, corresponding to the near-field contribution, are calculated using:

$$G_{tot} = \frac{P}{\theta}, \tag{III.4}$$

$$\frac{\Delta G}{G_{tot}} = \frac{\Delta P}{P} - \frac{\Delta \theta}{\theta}. \tag{III.5}$$

Here, G_{tot} is the total thermal conductance of the emitter and is calculated by dividing the supplied electrical power P by the temperature elevation $\theta = T\text{-}T_{amb}$ at the largest distance. Then the variation of conductance $\Delta G(d)$ can be calculated with the variations of electrical power ΔP and the difference in temperature elevation $\Delta\theta = T\text{-}T_{ref,}$ with T_{ref} the temperature at the largest distance. The electrical power and its variations can be expressed as a function of the emitter electrical resistance R and current I, along with their variations ΔR and $\Delta I = I - I_{ref}$ where I_{ref} is the current at the largest distance:

$$P = RI^2 \tag{III.6}$$

$$\frac{\Delta P}{P} = \frac{\Delta R}{R} + 2\frac{\Delta I}{I} \tag{III.7}$$

Combining Eq. (III.5) and (III.7) gives the conductance variations according to the electrical resistance, the current and the temperature variations:

$$\frac{\Delta G}{G_{tot}} = \frac{\Delta R}{R} + 2\frac{\Delta I}{I} - \frac{\Delta \theta}{\theta} \tag{III.8}$$

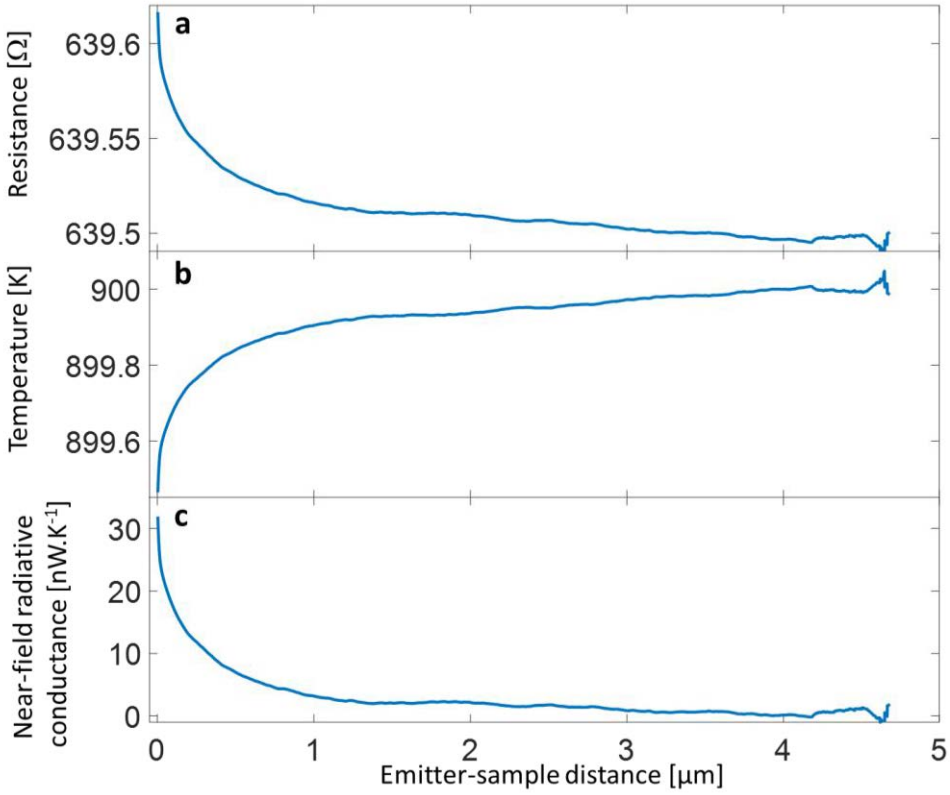

Figure III.16: Resistance (a), temperature (b) and near-field radiative conductance (c) according to emitter-sample distance

By expressing the resistance variations as a function of the temperature coefficient α, the final equation (III.10) giving the near-field radiative conductance $G_{NF}(d)$ can be written as:

$$\Delta\theta = \frac{1}{\alpha}\frac{\Delta R}{R} \tag{III.9}$$

$$\Delta G = G_{NF} = G_{tot}\left[\Delta\theta\left(\alpha - \frac{1}{\theta}\right) + 2\frac{\Delta I}{I}\right] \tag{III.10}$$

Let us note that in the experimental setup, the total current provided by the current source is constant but the fraction that is going to the probe varies because of the Wheatstone bridge. At the largest distance when the bridge is balanced, half of the current goes into the emitter side while the other half goes into the variable resistance side. As the emitter-sample distance decreases, the emitter resistance changes so the bridge becomes no longer balanced and the fraction of the total current going to the emitter changes too. The resulting G_{NF} curve (Figure III.16c) is plotted as a function of emitter-sample distance, which is obtained with the emitter displacement z considering the point z_{max} as the minimum distance before contact so $d = |z - z_{max}|$. At the largest distance, G_{NF} is set equal to 0 because it is defined as a variation of conductance calculated from the total thermal conductance at the largest distance. In practice, the near-field contribution at distances $d > 5$ µm is almost 0 because $d > \lambda_{Wien}$ (3.2 µm at 900 K). For comparison with theory, the simulated values will be shifted in conductance to be set to 0 close the largest experimentally measured distance where the signal-to-noise is not too low.

III.3.2 Cooling system

The radiative measurements with bulk samples do not require specific cooling. However, the InSb TPV cells need to be cooled to cryogenic temperatures to work properly (see Sec. VI.2.3.1).

III.3.2.1 Design

In addition to the experimental setup design shown in Figure III.10, a liquid helium cryostat can be inserted into the vacuum chamber and cool the sample when needed (Figure III.17 and Figure III.18b,c). The cryostat is fixed to the vacuum chamber by the vacuum flange, and to the base of the setup by one extremity. Liquid helium (LHe) is transferred from the dewar to the cryostat with a transfer tube. At the end of the tube, the cold finger is cooled by the flowing liquid helium, which then evaporates into gaseous helium He and is removed.
In some cases, a cooled radiative shield can me mounted on top of the cold finger in order to protect the sample from thermal radiation coming from the environment. It is particularly needed to reach temperatures below 15 K or to measure dark current-voltage (I-V) characteristics of the TPV cells. The cryostat has also 8 BNC electrical connections to the inside of the vacuum chamber that are used to connect and perform measurements with the TPV cells. The helium circuit is in the inner part of the cryostat so there is no gas flowing in the interior of the vacuum chamber. The sample is glued on the cold finger with silver paste that plays the role of adhesive and good thermal conductor to extract efficiently the heat from the sample. The temperature of the cold finger is measured by a temperature sensor, located close to the base of the cold finger, and regulated by a heater at the same place. To monitor the temperature, a set point is given to the cryostat controller that adjusts the heater power (given in percentage) to balance the cooling effect of the LHe and reach the target temperature. The helium flow is driven by the pressure inside the dewar. It is measured by the flow meter and regulated by a manual valve to be as low as possible. The objective is to set a flow high enough to cool the sample at the desired temperature but not too high so the heater is not too much required, thus limiting the helium losses.

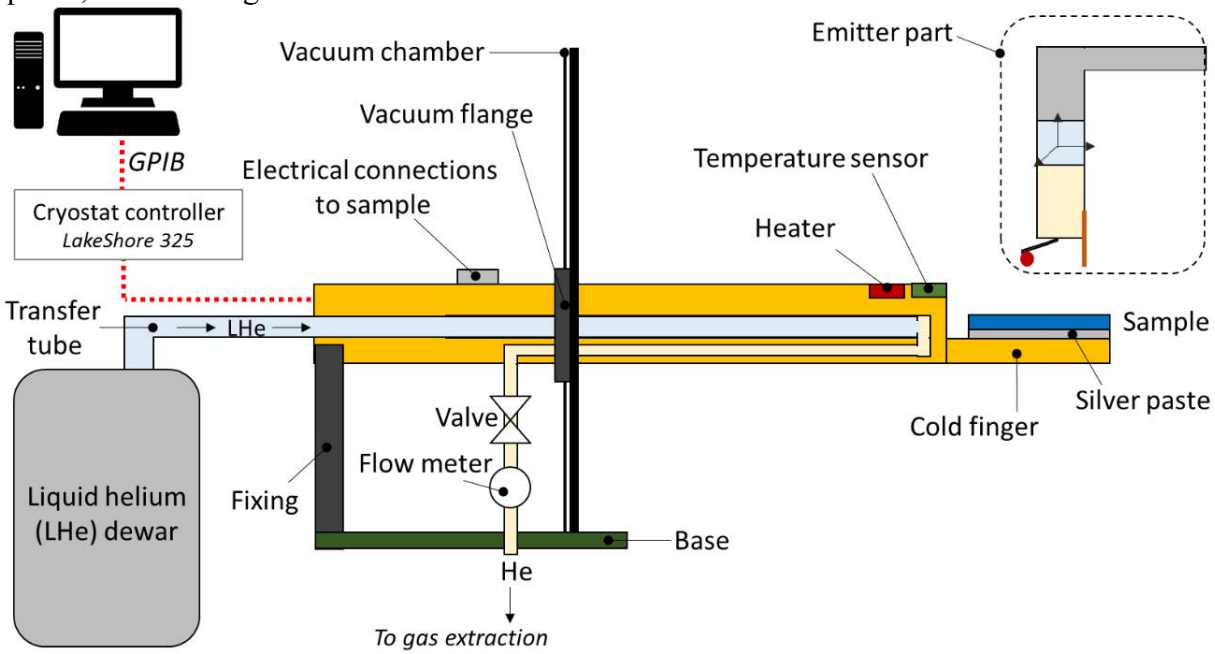

Figure III.17: Schematic of the cryogenic cooling system

III.3.2.2 Mechanical drift due to cooling

During the cooling process, thermal contraction causes a strong motion in cryostat.
Its extremity is shifted by ~ 750 µm, during approximately an hour after starting the cooling (Figure III.18a). The cold finger is made of copper so an estimation of the expected contraction can be made. The thermal expansion coefficient of copper is 17 µm.K.m^{-1} and the temperature difference corresponding to a cooling from room temperature down to 77 K is 220 K. The calculation gives a contraction ranging from 560 to 1125 µm, considering either the part inside the vacuum chamber (15 cm) or the full length (30 cm), in good agreement with the observed value. After an hour, small displacements of the cold finger are still observed in x/y and z directions and are correlated to the slight variations of the helium flow. For the near-field thermophotovoltaic experiments, the position of the emitter has to be regularly controlled in the 3 directions of space due to this phenomenon. Another effect of the cooling is the lowering of pressure. The cold finger acts as a cryo-trapper by condensing residual gases on its surface. Usually, at a working temperature of 77 K, the pressure drops from 10^{-6} down to 10^{-7} mbar, which has no incidence on the experiment.

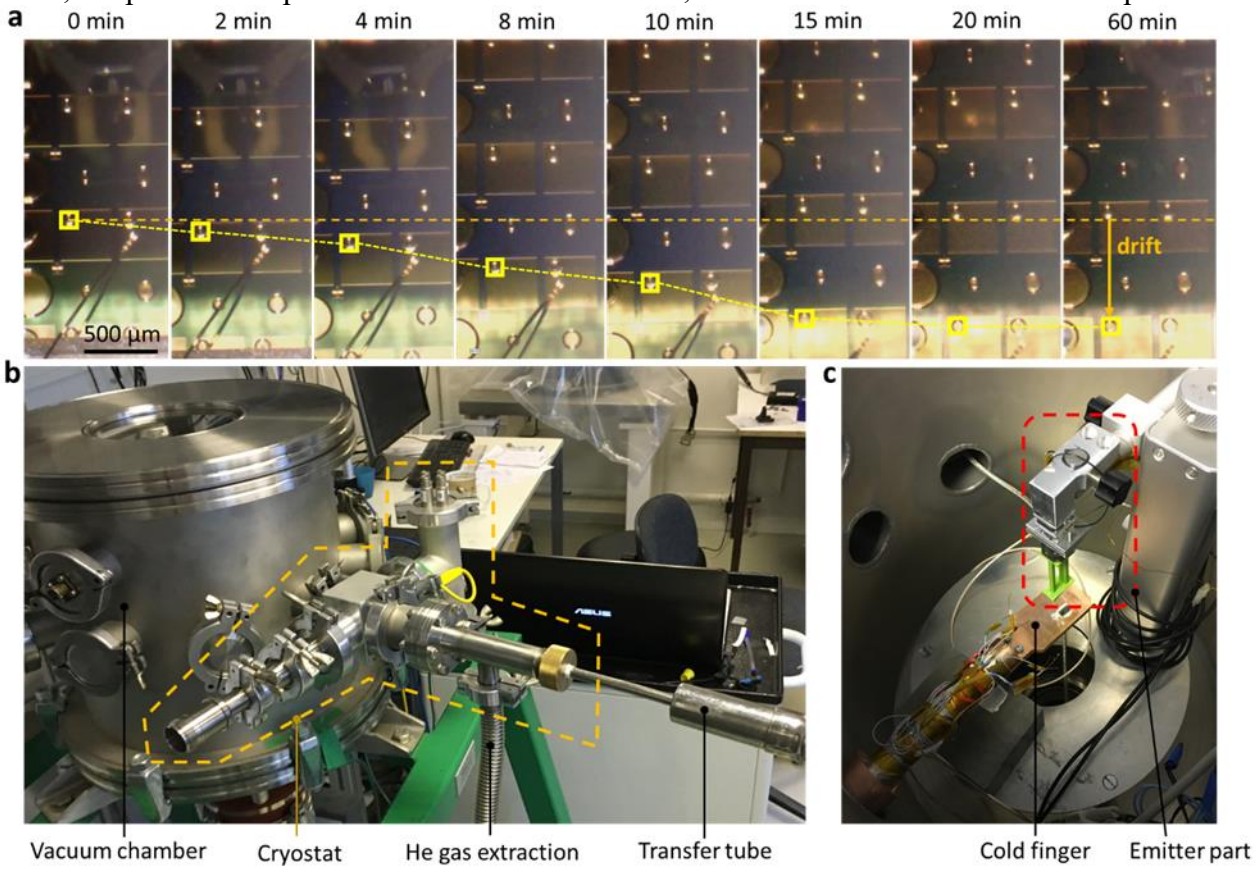

Figure III.18: Images of the cooling setup.
(a) Drift over time due to cooling, seen on TPV cell sample. (b) Image of the cryostat part outside the vacuum chamber. (c) Inside view of the vacuum chamber showing the cold finger and the emitter part

III.3.2.3 Effect of the cooling on the emitter part

To quantify the potential cooling effect of the cold finger on the emitter part during the experiments, two thermocouples were fixed close to the emitter and close to the z-piezoelectric positioner (*TC2*

and *TC1* on Figure III.19a). *TC2* measures the temperature of the emitter holder while *TC1* is used to determine the temperature of the z-piezoelectric positioner, which has an influence on the displacement/voltage ratio. For instance, the supplier gives a 5 µm/100 V at room temperature and 0.8 µm/150 V at 4 K. The temperatures at this two points along with the one of the emitter at low current (100 µA) placed at $d < 100$ µm above the sample were measured while the cold finger was cooled from room temperature down to 77 K in less than 20 min. Figure III.19b shows the decrease of the three temperatures. As expected, the effect of the cold finger is more important for the points closest to it. The emitter temperature *T* drops from room temperature (26.6 °C) to a stable value of 11.6°C after 20 min, *i.e* a temperature difference of 15 K is observed. At *TC2* the temperature difference is around 2.6 K after 100 min compared to only 1.6 K for *TC1*. It can also be noted that the stabilization time for the three temperatures varies from 20 min for the *TC* closest to the cold finger, to more than 100 min for the farthest. The drop in the emitter temperature is compensated during the experiments by providing more current to the emitter to reach the desired temperature. Along with the drift induced by the thermal expansion coefficient, all the experiments with the cooling system are started after a waiting time of 2 hours to make sure that the system is stable both mechanically and thermally.

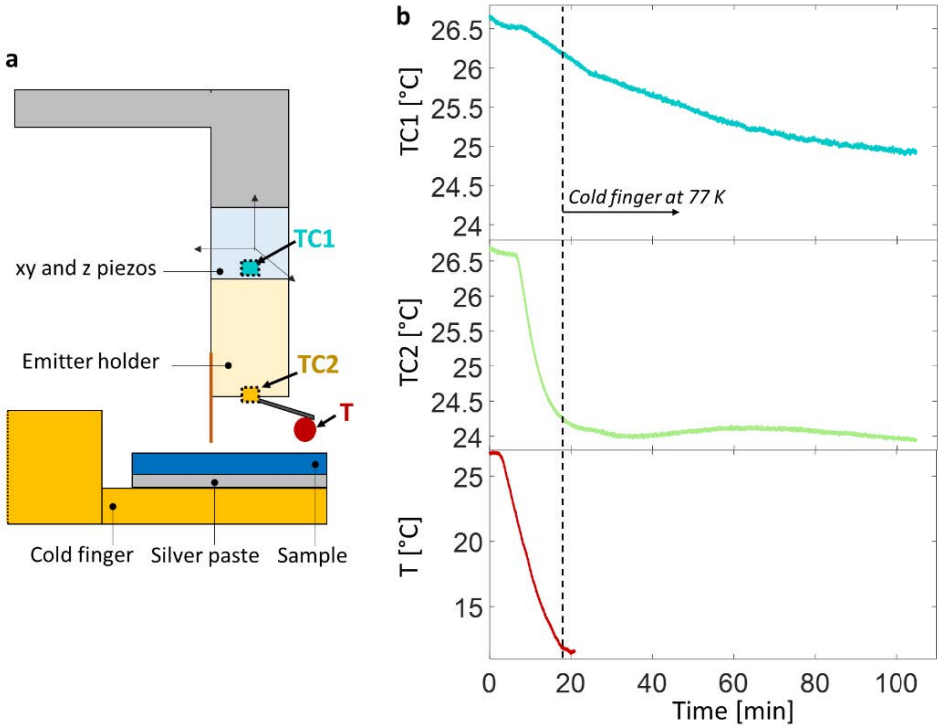

Figure III.19: Impact of the cooling system on emitter temperature.
(a) Schematic of the emitter and its holder, located above the cold finger. (b)Temperatures of the emitter and holder as a function of time when the cold finger is cooled from room temperature to 77 K

III.4 Setup characterization

In order to characterize the experimental setup, optical properties of the silica emitters and substrates were measured and compared to literature values that were used for theoretical calculations. In addition, the uncertainty of the near-field radiative conductance measurement was investigated and compared to the accuracy of similar experimental setups

III.4.1 Infrared reflectivity measurements

Optical properties of some of the materials made of SiO_2 used during the experiments were investigated by measuring the reflectivity in the infrared spectrum. The spectrometer used is a Bruker 66V FTIR (Fourier Transform Infrared Spectrometer), combining an infrared source and an integrating sphere. The integrating sphere, with a gold surface (Figure III.20a), was used to measure the reflected power signal on the sample $P_R^{sample}(\lambda)$ and that reflected on a reference sample $P_R^{ref}(\lambda)$. The reference sample is a diffuse reflection gold surface with a reflectivity equal to 1 in the spectral range of the FTIR. The incident power $P_0(\lambda)$ is emitted from a source covering a part of the infrared spectrum. The reflectivity is calculated as the power reflected on the sample divided by that reflected on the reference sample $P_R^{sample}(\lambda)/P_R^{ref}(\lambda)$. The spectral range available with this spectrometer goes from 2 µm to 14 µm approximately so only one of the two reflectivity peaks of SiO_2 (the one near λ = 9 µm, see Sec. II.2.2.1) could be investigated.

III.4.1.1 Flat SiO_2 substrate

The measured data are compared to others from literature[72] that were used for theoretical calculations due to their wide wavelength range from λ = 1 µm to λ = 10 mm, and due to their determination as a function of the temperature. For comparison, the bulk flat SiO_2 sample is at room temperature in both cases. The reflectivity measurement made in this work is in a very good agreement with the ones from literature (Figure III.20b). The reflectivity peak emerges at 8.92 µm compared to 8.93 µm for the measurements found in the literature[72]. Below 4 µm wavelength, a small deviation appears between the two measurements. This could be explained by large variations of the data from this work, highlighted by the large standard deviation that can be seen at λ = 2-4 µm.

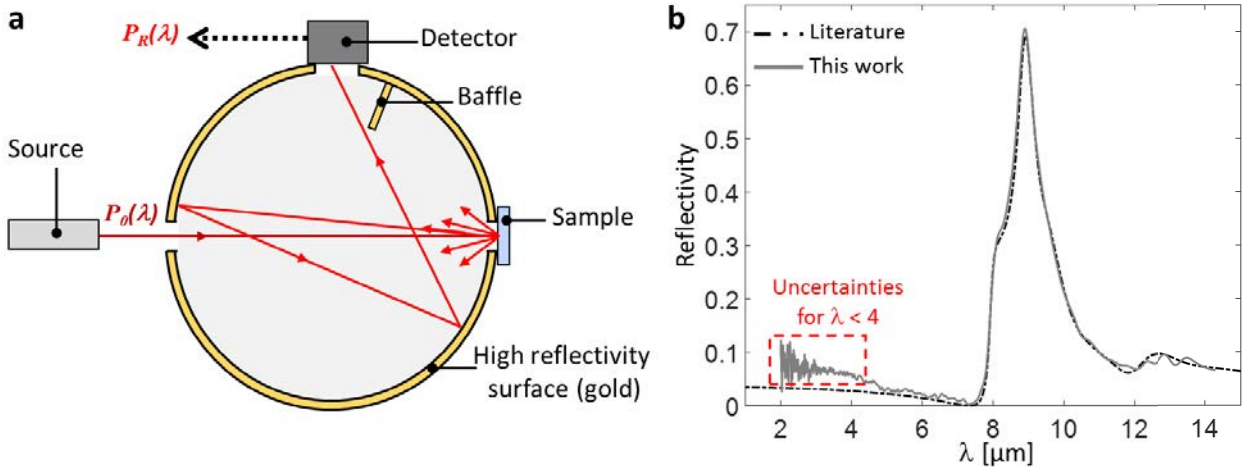

Figure III.20: Infrared reflectivity measurements on SiO_2 flat sample.
(a) Schematic of the reflectivity measurements with an integrating sphere. (b) Comparison of reflectivity measurements of a bulk flat SiO_2 substrate as a function of wavelength

III.4.1.2 SiO_2 spheres

The reflectivity of a sample made of SiO_2 spheres was measured and compared to that of the bulk flat SiO_2 substrate. The objective of this measurement is to know if the spheres, that were purchased

with very little information, are made of amorphous silica, of a crystalline form (α,β-quartz for examples), or contains impurities. Crystallography can affect the optical properties of the materials and by extension the results of radiative heat transfer calculations. A certain amount of spheres was deposited on the surface of a polymer substrate in order to create a sphere layer of thickness of ~2 mm (Figure III.21a, inset). In Figure III.21a the reflectivity of the spheres is compared to that of the flat bulk SiO_2 substrate. The two reflectivities exhibit very significant differences. The spheres reflectivity is much larger at $\lambda < 8$ µm compared to that of the flat substrate. The reflectivity peak is seen only on the flat substrate signal. These differences may be explained by the fact that the measured reflectivity comes from almost purely specular reflection for the flat substrate, and from diffuse reflection for the spheres. Similar measurements were performed by Eickhoff *et al.*[91] with 4-40 µm in diameter amorphous SiO_2 spheres deposited on a substrate with a sphere layer thickness of 2 mm. They performed diffuse reflectance infrared Fourier transform spectroscopy (DRIFT) measurements and extracted spectra that were then normalized. Their data are presented in Figure III.21b as a function of wavenumber (in cm^{-1}) and compared to the measurements performed during this work and which were normalized. The behavior is very similar to that from the literature with a reflectivity drop under 2000 cm^{-1} and no peak visible near 1050 cm^{-1} (λ = 9 µm). The wavelength where the reflectivity decreases close to 0 is called the Chistiansen wavelength[92] (λ_{Chr}).

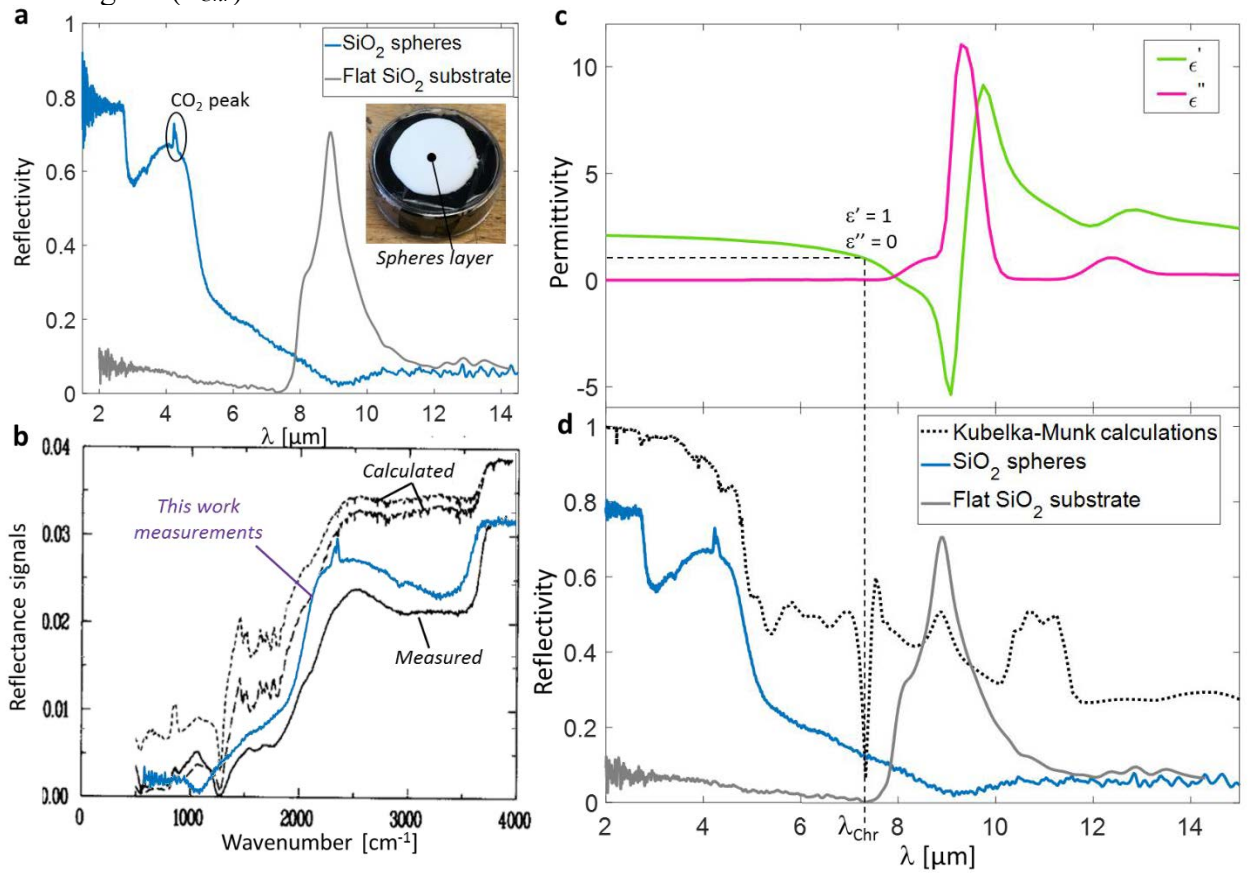

Figure III.21: Reflectivity measurements on the SiO_2 spheres compared to the flat substrates. (a) Reflectivity of SiO_2 spheres and flat substrate as a function of wavelength. (b) Comparison between this work, and measurements and calculations found in the literature. (c) Real and imaginary parts of the dielectric function of SiO_2 as a function of wavelength. (d) Kubelka-Munk calculations compared to reflectivity measurements for the SiO_2 spheres and flat substrate

The Chistiansen effect occurs when the refractive index of a material is the same as that of its environment (air in our case). Scattering nearly vanishes and almost all the light is transmitted if the material is not absorbing at λ_{Chr}. A shift of λ_{Chr} is observed between our measurements and those of Eickhoff *et al*., meaning that dielectric functions are different. The observed diffuse reflectivity of a media containing microparticles having diameters $d > \lambda$ can be estimated with the Kubelka-Munk[93] theory assuming multiple scattering from one particle to another. Diffuse reflectivity calculations for spheres having a diameter of 40 µm were made using bulk SiO_2 dielectric function measurements from literature[72] (Figure III.21c) and compared to the bulk flat substrate and sphere reflectivity measurements (Figure III.21d). The reflectivity R_∞ of an opaque sphere layer is calculated using the equation:

$$\frac{K}{S_c} = \frac{(1-R_\infty)^2}{2R_\infty}, \qquad (III.11)$$

where K and S_c are the absorption and scattering coefficients estimated with Mie scattering theory calculations[94,95]. The Chistiansen reflectivity is observed at the wavelength where $\varepsilon' = 1$ and $\varepsilon'' = 0$, both on the calculations and the bulk flat substrate measurements. However, λ_{Chr} is shifted by 2 µm for the spheres layer. This comparison allows to conclude that the dielectric function of the SiO_2 spheres is different from that of the flat substrate.

III.4.2 Distance determination close to contact

The determination of the smallest distance before contact is a very important step in order to determine the limits of the experimental setup. Three different effects were studied. The first one is related to the roughness of the spherical emitters and the samples, measured by atomic force microscopy (AFM). The second one is the bending of the SThM probe cantilever, induced by a temperature gradient or caused by snap-in of the emitter due to the attraction forces at low distances that suddenly brings the emitter into contact with the sample. The last effect is related to mechanical vibrations between the emitter and the sample measured by interferometry. All these effects are combined in order to provide an estimation of the minimum emitter-substrate distance reachable by the experimental setup.

III.4.2.1 Roughness

At low distances, the effect of surface roughness can become important when studying the near-field regime. Roughness measurements on both spherical emitters and samples were made using AFM to acquire topographic images (Figure III.22a). The principle of this technique is to focus a laser on the tip of a probe that is reflected on a quadrant photodiode. The sample is scanned in xy directions with the tip in contact and the change in altitude δz, corresponding to the topography of the sample, is deduced by measuring the laser reflection displacement δx on the photodiode. The root-mean-square roughness R_{RMS}, and more importantly, the maximum and minimum altitudes with respect to the mean level were determined from these measurements. In the case of a measurement on a sphere, an additional data processing was necessary since the surface is not flat. A spherical shape with the corresponding radius of curvature was subtracted from the measured data to obtain a flat topographic image (Figure III.22b) using the software Gwyddion. The measurement (Figure III.22c) shows that the cells and the InSb bulk samples are almost perfectly flat with R_{RMS} = 0.1-0.4 nm. Concerning the spheres, graphite ones appear to have the highest

roughness R_{RMS} = 5.2 nm with +29.9 nm and -28.7 nm as maximum and minimum altitudes respectively, which is almost twice the values measured for the SiO_2 spheres. When the sphere is considered to be in contact with the cell at d = 0, the effective distance is therefore probably $d \approx 30$ nm in the case of the graphite sphere, with respect to the mean spherical shape. This study indicates that the near-field experiments with this setup are restricted to distances larger than 20-30 nm depending on the emitter-sample configuration, if one wants to compare to simulations neglecting roughness.

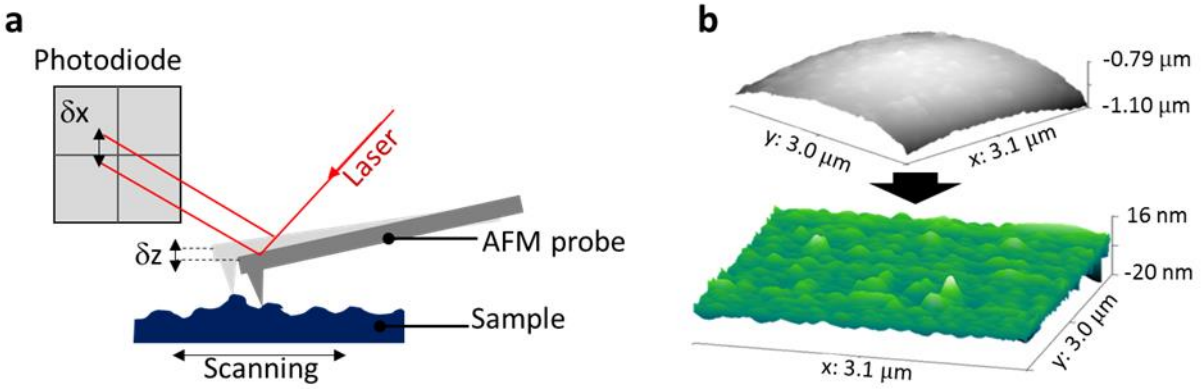

c

Sample	R_{RMS} (nm)		Minimum (nm)	Maximum (nm)	Mean spacing of irregularities (µm)
SiO_2 bulk	1.1	1.3	-4.1	5.0	2.57
InSb bulk	0.1	0.2	-0.7	0.8	4.91
InSb cell	0.3	0.4	-1.3	1.0	4.72
SiO_2 sphere	2.6	3.4	-19.9	15.8 (a few peaks > 100 nm)	0.05
Graphite sphere	5.2	6	-28.7	29.9	0.03

Figure III.22: Roughness measurements using AFM

III.4.2.2 Cantilever vertical deflection

When the emitter is few nanometers close to contact, accuracy of the knowledge of the distance between the sphere and the sample can depend on the cantilever vertical deflection. The bending of the cantilever can be induced by attraction forces between the sphere and the substrate, causing a snap-in effect close to contact. The temperature profile in the heated cantilever can also cause a deflection. These two effects are investigated in the following sections, based on an AFM measurement setup.

III.4.2.2.1 Attraction forces

These forces are expected to bend the SThM probe cantilever and thus bring the sphere into contact. In order to quantify the distance where the snap-in occurs, cantilever deflection measurements were performed as a function of distance at room temperature for different emitter temperatures (Figure III.23). The deflection was measured with a photodiode system in an NTMDT AFM equipped with

a moderate-vacuum chamber (10^{-1} mbar). In this experiment, a laser was focused on the edge of a SThM probe with a sphere glued on the tip, and the deflection was observed as a function of distance. In far-from-contact position, the deflection of the probe is constant because there is no interaction between the probe and the sample. In the approach curve close to contact, the cantilever bends slightly due to the attraction forces. The snap-in is estimated to be around 2-3 nm and is not affected by the emitter temperature (Figure III.23, inset).It can also been noticed that the adhesion forces, taking place when the probe is withdrawn, lead to a much larger deflection, greater than 30 nm. These adhesion forces could be an explanation for the hysteresis between the approach and withdrawal curves, and also for the drift in the contact point during the NFRHT experiments (Figure III.15c).

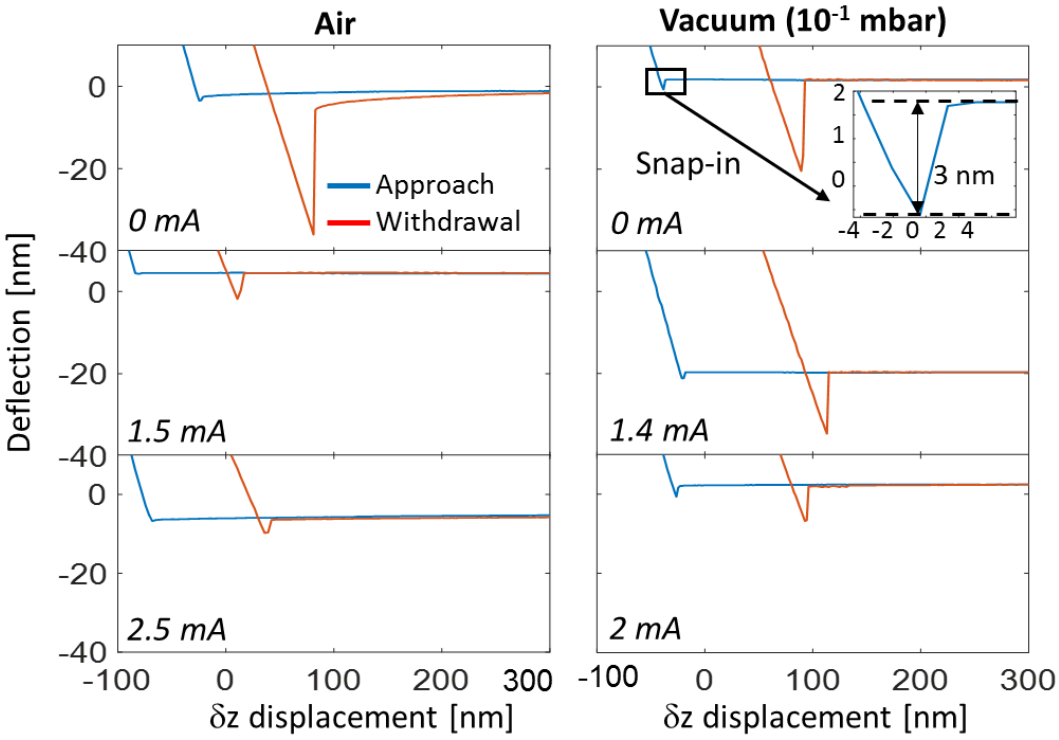

Figure III.23: Deflection of the cantilever according to the displacement for different joule heating current, in air or under low vacuum conditions

III.4.2.2.2 Temperature gradient effect

A bending of the probe cantilever can also be induced by a temperature gradient. The deflection was measured according to the electrical current supplied to the emitter in far-from-contact position (Figure III.24a). The study of 3 different emitters led to observe different behaviors. For some emitters the deflection is always increasing, meaning that the cantilever bends in the upward direction when the current-induced temperature increases. In some cases, the cantilever starts to bend down, then bends up at 1.8-2 mA which corresponds approximately to the current a T_{Rmax} in Figure III.8. The case of emitter 3 under vacuum condition is highlighted in Figure III.24b where the bending is plotted against the tip temperature of the emitter. The figure shows that the quick change in the cantilever deflection corresponds to the zone where the temperature increases rapidly. For all the emitters, deflection levels off at high currents. The shift between the curves measured in air or vacuum is explained because under vacuum, there is no air to extract heat from the probe

by conduction and convection (Figure III.24c). So in that case the temperature of the emitter is higher for the same current compared to the curves made in air. Close to contact, the temperature drop due to near field radiative heat transfer is expected to be very weak (0.1 – 1 K) so the distance uncertainty due to the thermally induced deflection is negligible.

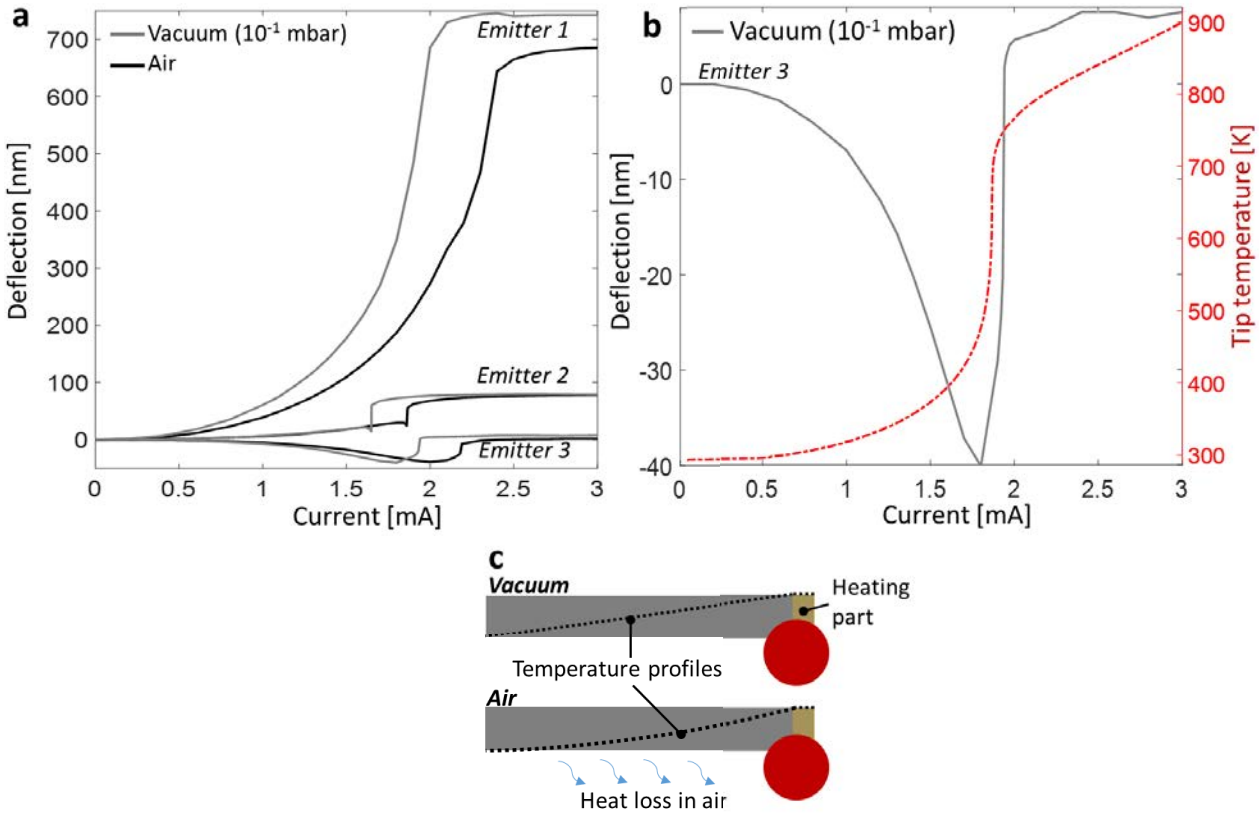

Figure III.24: Study of the probe deflection induced by temperature.
(a) Deflection according to current for three emitters in air and under vacuum. (b) Deflection and tip temperature of emitter 3 according to current under vacuum. (c) Schematic of the temperature profiles in the cantilever

III.4.2.3 Vibrations

The last cause affecting the distance uncertainty is the vibration of the setup in the two different configurations, corresponding to with and without the cooling system. The cold finger is 15 cm long inside the vacuum chamber so the continuous flow of LHe in the finger induces mechanical oscillations. The interferometer of the emitter part of the setup presented in Figure III.10 was used in order to measure the amplitude of the cold finger vibrations. The fiber was roughly placed close to the surface of the cold finger at a few tens of micrometers. Then it was moved at a constant speed over a 5 µm range by doing a series of approach/withdrawal motions with the z-piezoelectric positioner while the periodic interferometric signal was acquired (middle panel in Figure III.14). The signal can be deduced for half a period corresponding to a $\lambda/4 = 327.5$ nm displacement and a local linear fit for the data can be found (Figure III.25a). Knowing the displacement and the motion speed of the fiber, a relation is easily established between the intensity of the signal and the displacement. Then the vibration amplitudes are calculated around the average position given by

the linear fit. The histogram of the positions of the cold finger (Figure III.25b, right) shows strong oscillations around the mean position of ± 83 nm. As a comparison, the same measurements were made for the configuration without the cold finger. It is clearly seen on the two normalized interferometric signals put together (Figure III.25b) for a $\lambda/4$ displacement that the configuration without the cold finger is much more stable because the amplitude is only ± 7 nm around the mean position. In any case, the observed vibrations can come from the sample and/or from the part holding the emitter. To sum up, the distance uncertainty for the NFRHT experiment, when the cold finger is not needed, is ~30 to 40 nm considering the vibrations, the roughness and the snap-in. For the NF-TPV experiments, the cold finger induces large vibrations that extends the uncertainty to approximately 100 nm.

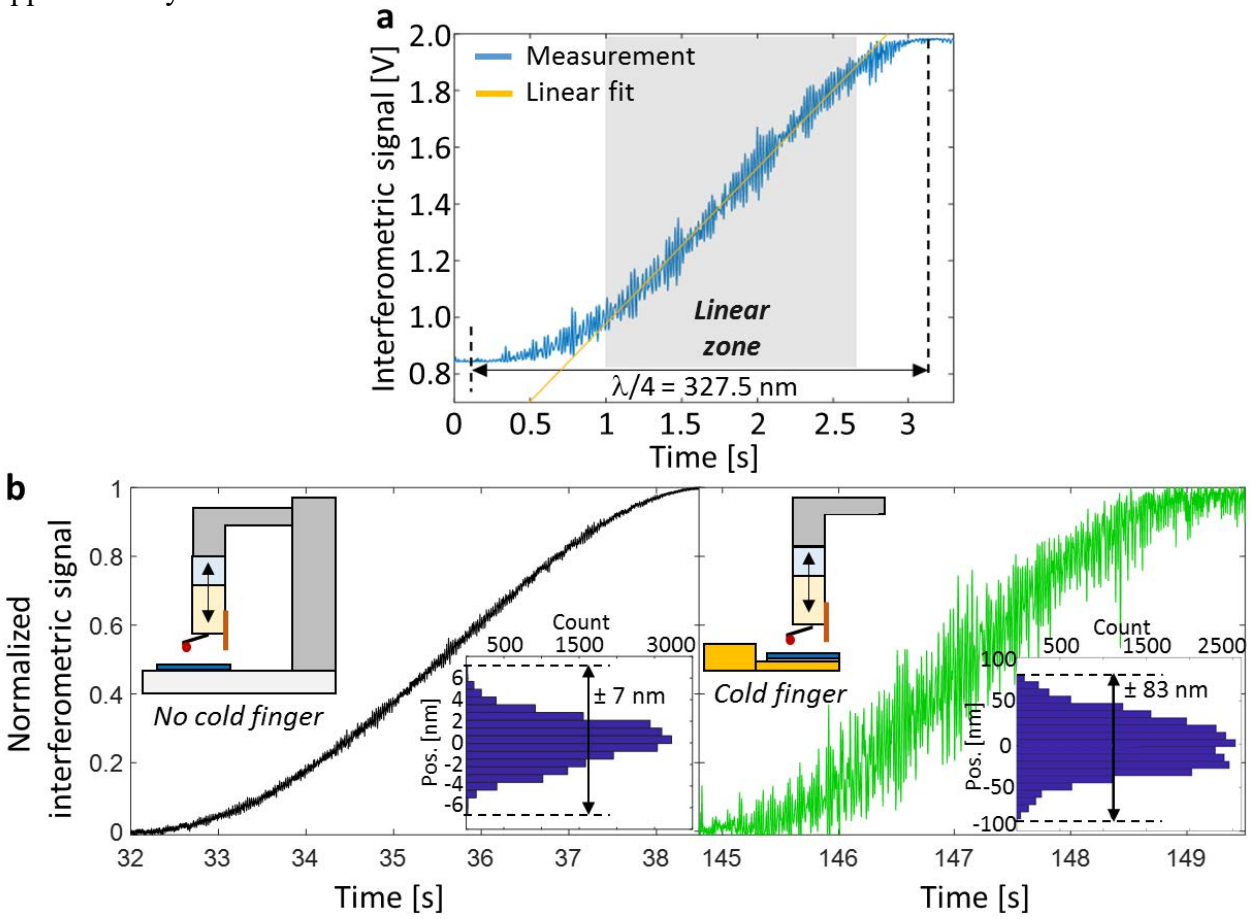

Figure III.25: Vibration amplitude determination from interferometric signal.
(a) Linear fit of the interferometric signal. (b) Normalized interferometric signals for the configuration without left) and with (right) the cold finger

III.4.3 Statistical error and conductance uncertainties

In order to determine the resolution for the temperature and conductance measurements, it is very important to quantify the accuracy of the experimental setup. The main parameters influencing the uncertainty of the final results are the *R(T)* calibration curve and the electrical noise of the measurement devices.

III.4.3.1 Statistical error from the random electrical noise

The electrical resistance is measured using a Wheatstone bridge differential circuit with a 100x voltage amplification. The uncertainty on this measurement depends on the random, also called Gaussian, electrical noise, and can have a non-negligible impact on measurements of small electrical resistance variations. To study this parameter, the standard deviation of the resistance measurements and inferred temperatures are represented in Figure III.26a,b as a function of the number of curves accounted for averaging. The standard deviation is calculated over 1200 points of the approach curve in the regime where the signal is constant. The calculated standard deviation is compared with a $\frac{1}{\sqrt{N}}$ evolution corresponding to a Gaussian noise[96]. It can be seen that averaging a number N of curves indeed leads to a $1/\sqrt{N}$ evolution of the standard deviation. After averaging 100 curves, the remaining random noise δR on the electrical resistance signal is 0.7 mΩ, which translates into 0.6 mK for the δT temperature noise. The calculation of the standard deviation of the averaged signal is performed for each experiment to determine the δT and δR in the studied experimental conditions.

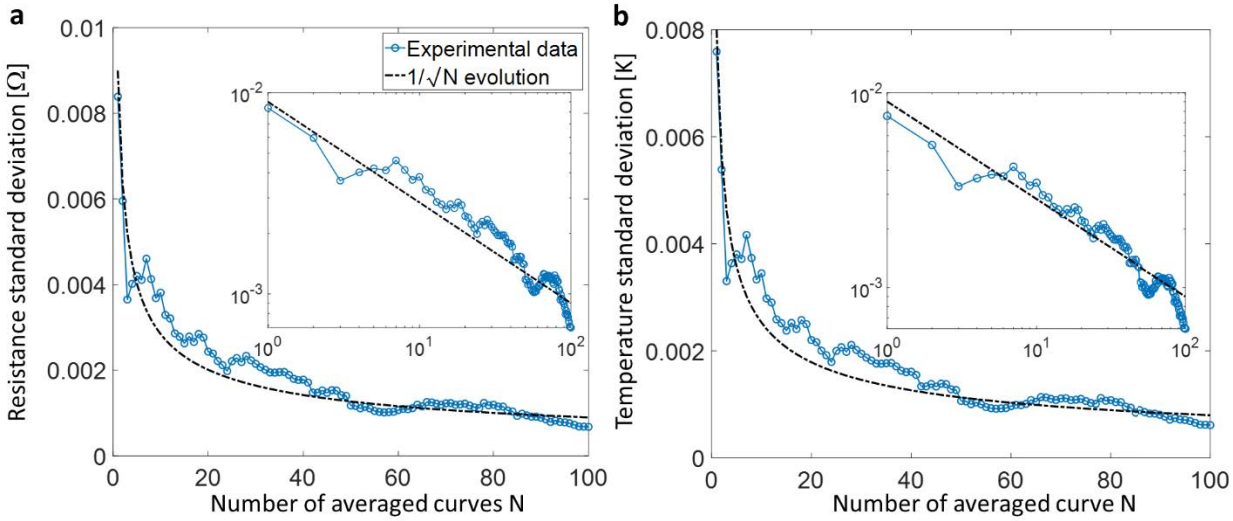

Figure III.26: Evolution of the resistance and temperature standard deviations as a function of the number of averaged curves

III.4.3.2 Uncertainties of the near-field radiative conductance measurements

From all the parameters, it is possible to calculate the uncertainties of the measurements in terms of conductance. Here the uncertainty will be expressed by considering that all phenomena are correlated and that all uncertainties add. Using Eq. (III.10), the relative uncertainty of the near-field conductance measurements can be expressed as the following:

$$\frac{\delta G_{NF}}{G_{NF}} = \frac{\delta G_{tot}}{G_{tot}} + \frac{\delta\left[\Delta\theta\left(\alpha - \frac{1}{\theta}\right) + 2\frac{\Delta I}{I}\right]}{\Delta\theta\left(\alpha - \frac{1}{\theta}\right) + 2\frac{\Delta I}{I}}. \qquad (III.12)$$

Here the symbol δ is used to represent an uncertainty. To express δG_{NF} as a function of known parameters, each terms of the equation has to be developed. The first term can be expressed according to the electrical power P and the temperature elevation θ:

$$\frac{\delta G_{tot}}{G_{tot}} = \frac{\delta P}{P} + \frac{\delta \theta}{\theta}, \tag{III.13}$$

$$\frac{\delta P}{P} = \frac{\delta R}{R} + 2\frac{\delta I}{I}. \tag{III.14}$$

In Eq. (III.14), the uncertainty of the emitter current δI is calculated as a function of the total current I_{heat} and the electrical resistances of the circuit R_1, R_2, R_V and R the resistance of the emitter (see appendix 2):

$$I = I_{heat}\left[1 - \left(1 + \frac{R_1 + R_V}{R_2 + R}\right)^{-1}\right], \tag{III.15}$$

$$\frac{\delta I}{I} = \frac{\delta I_{heat}}{I_{heat}} + \frac{\frac{R_1 + R_V}{R_2 + R}\left[\frac{\delta R_1 + \delta R_V}{R_1 + R_V} + \frac{\delta R_2 + \delta R}{R_2 + R}\right]}{\left[1 - \left(1 + \frac{R_1 + R_V}{R_2 + R}\right)^{-1}\right]\left[1 + \frac{R_1 + R_V}{R_2 + R}\right]^2}. \tag{III.16}$$

The current going into the emitter is calculated using Eq. (III.15) and its relative uncertainty is given by Eq. (1). The uncertainty of the total current δI_{heat} is given by the specifications of the current source and is equal to $5.10^{-4} I_{heat}$ + 10 µA. Resistances uncertainties are given by the suppliers to be $\delta R_V = 3.10^{-5} R_V$, $\delta R_1 = \delta R_2 = 10^{-3} R_{1\text{-}2}$.

The other parameter to be determined in Eq. (III.13) is the temperature elevation uncertainty $\delta\theta$. Because $\theta = T - T_{amb}$, the following relation can be written as a function of the temperature uncertainty due to the systematic calibration error err_T= 0.20 and the random electrical noise δT:

$$\delta\theta = err_T\theta + \delta T. \tag{III.17}$$

Finally, the relative uncertainty of G_{tot} can be developed as:

$$\frac{\delta G_{tot}}{G_{tot}} = \frac{\delta R}{R} + 2\left[\frac{\delta I_{heat}}{I_{heat}} + \frac{\frac{R_2 + R}{R_1 + R_V}\left[\frac{\delta R_2 + \delta R}{R_2 + R} + \frac{\delta R_1 + \delta R_V}{R_1 + R_V}\right]}{1 - \left(1 + \frac{R_1 + R_V}{R_2 + R}\right)^{-1}\left[1 + \frac{R_1 + R_V}{R_2 + R}\right]^2}\right] + \frac{err_T\theta + \delta T}{\theta}. \tag{III.18}$$

The second term in equation (III.12) also has to be developed to be able to calculate δG_{NF} (see details in appendix 2):

$$\begin{aligned}\delta\left[\Delta\theta\left(\alpha - \frac{1}{\theta}\right) + 2\frac{\Delta I}{I}\right] &= \alpha\Delta\theta\left[\frac{2\delta R}{\Delta R} + \frac{\delta R}{R} + \frac{err_T\Delta T + 2\delta T}{\Delta T} + \frac{err_T\Delta\theta + 2\delta T}{\Delta\theta}\right] \\ &+ \frac{\Delta\theta}{\theta}\left[\frac{err_T\Delta\theta + 2\delta T}{\Delta\theta} + \frac{err_T\theta + \delta T}{\theta}\right] + 2\frac{\delta I}{I}\left[2 + \frac{\Delta I}{I}\right].\end{aligned} \tag{III.19}$$

Finally, the expression of the relative uncertainty of the near-field conductance can be expressed as the following equation, knowing the current uncertainty δI calculated using equation (III.16):

$$\begin{aligned}\frac{\delta G_{NF}}{G_{NF}} &= \frac{\delta R}{R} + 2\frac{\delta I}{I} + \frac{err_T\theta + \delta T}{\theta} \\ &+ \frac{\alpha\Delta\theta\left[\frac{2\delta R}{\Delta R} + \frac{\delta R}{R} + \frac{err_T\Delta T + 2\delta T}{\Delta T} + \frac{err_T\Delta\theta + 2\delta T}{\Delta\theta}\right] + \frac{\Delta\theta}{\theta}\left[\frac{err_T\Delta\theta + 2\delta T}{\Delta\theta} + \frac{err_T\theta + \delta T}{\theta}\right] + 2\frac{\delta I}{I}\left[2 + \frac{\Delta I}{I}\right]}{\Delta\theta\left(\alpha - \frac{1}{\theta}\right) + 2\frac{\Delta I}{I}}\end{aligned} \tag{III.20}$$

As an example, Figure III.27 shows the near-field radiative conductance G_{NF} and its uncertainty δG_{NF} as a function of emitter-sample distance for the case of a graphite emitter at 900 K and a graphite bulk substrate at room temperature. It can be seen that δG_{NF} is smaller for the largest distances then increases when the distance decreases. For large distances, the uncertainty reaches a value of around 30 pW.K^{-1} (18 nW or 0.4 nW/$\sqrt{Hz}$ considering the 2 kHz acquisition rate) which is essentially due to the Gaussian electrical noise affecting the electrical resistance and temperature measurement. The values of δT and δR do not depend on distance so the fact that δG_{NF} increases at low distance is due to the increasing temperature difference which is determined considering the systematic error err_T coming from the *R(T)* calibration curve. At low distances the calibration error becomes the main uncertainty phenomenon because in the case of an emitter at 900 K, the uncertainty of the measured $\Delta\theta$ = 0.6 K at the lowest distance (Figure III.16b) is $err_T \Delta\theta$ = 120 mK from the systematic calibration error and $2\delta T$ = 1.2 mK from the random noise (Eq. (8) in appendix 2). The maximum conductance uncertainty reaches 3.16 nW.K^{-1} at the lowest distance. This is two orders of magnitude higher compared to the 30 pW.K^{-1} random noise induced uncertainty at large distances. At the largest distances, ΔT and $\Delta\theta$ are close to 0 but $\theta = T - T_{amb} > 0 >> \delta T$ so Eq. (III.20) can be written as:

$$\frac{\delta G_{NF}}{G_{NF}} = \frac{err_T\theta + \delta T}{\theta} + f(R,T,\delta R,\delta T) \approx err_T + f(R,T,\delta R,\delta T) \qquad (III.21)$$

The previous equation tells that at the largest distances, for d > 3 µm where the temperature has not started to drop, the relative uncertainty of G_{NF} is equal to the sum of err_T and another term $f(R,T,\delta R,\delta T)$ that is a function of the random electrical noise. It can be seen on Figure III.27 (right) that this second term is clearly more important than err_T in this distance range. However, the relative uncertainty of G_{NF} decreases from around 30-40 % to approximately err_T (20 %) when the distance decreases due to the rise of the signal-to-noise ratio.
A way for reducing the conductance uncertainty would be to acquire more than 100 curves but, due to the $\frac{1}{\sqrt{N}}$ evolution of the electrical noise, the experimental time needed to significantly lower the noise can become important.

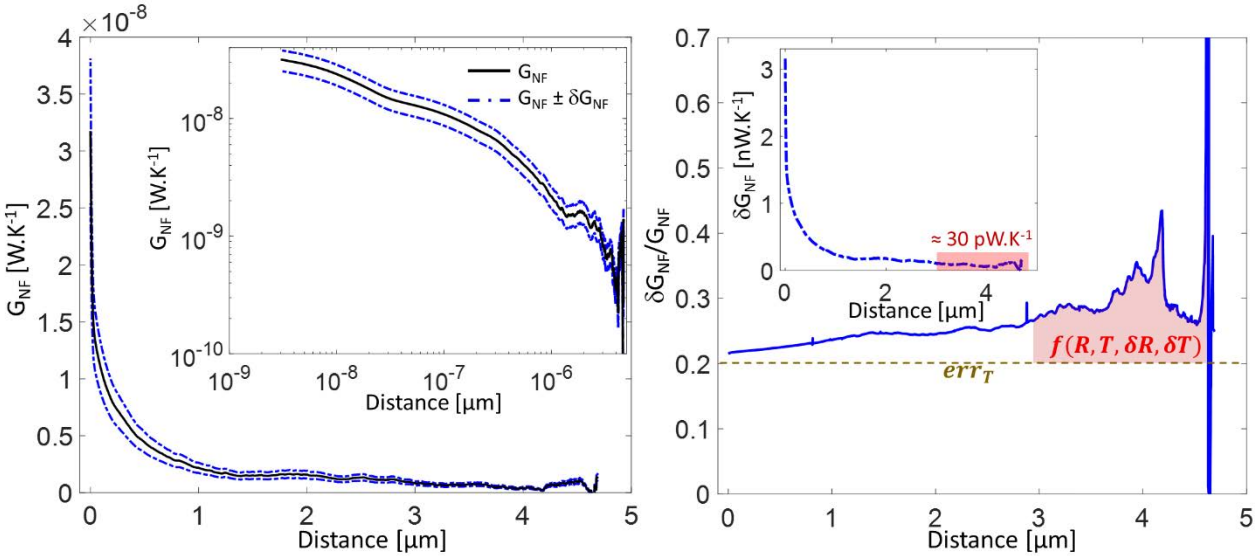

Figure III.27: Near-field radiative conductance and its uncertainty as a function of distance

For instance, it takes approximately 3 hours to get 100 curves for a single temperature/material configuration. In addition, the experimental time parameter is very important when the cooling system is used because it consumes liquid helium continuously, which is an expensive and limited resource. Another solution for lowering the uncertainty of the conductance would be to determine more accurately the *R(T)* calibration curve to limit the uncertainties at low distances.

III.4.3.3 Comparison with other experimental works

This work can be compared to other sphere-plane near-field radiative heat transfer measurements found in the literature (see Table III.1). The most similar work is that from Menges *et al*.[24] where a doped-Si thermoresistive scanning probe was used to heat and measure the temperature of a silica sphere. They also acquired 100 curves and made an average to improve the heat flux measurement resolution. With their method, they found a 10 nW sensitivity with an accuracy of 20 % for a maximum of 159 K temperature difference between the emitter and the substrate. This is comparable to the performances of our setup with a 18 nW resolution and a 20 % relative uncertainty. Another experiment from Shen et al.[44] used the temperature-induced deflection of a bi-material (SiN_x/Au) AFM cantilever, with a gold-coated SiO_2 sphere attached, to measure the conductance increase in the near field. With a planar gold-coated SiO_2 sample, they reported a resolution of 13 nW for a 33.5 K temperature difference which is in the same order of magnitude as this work and that of Menges. These values can also be compared with the work of Song *et al*.[47] where a SiO_2 sphere is glued next to a platinum resistor heated by Joule effect with an AC modulated current. The temperature rise of the planar SiO_2 receiver is also measured by a platinum sensor with a 100 pW resolution. In the end, a standard deviation of around 5 nW is reached on the near-field radiative heat flux with a 10 K temperature difference. In terms of resolution, one of the best performances was obtained in the works of Mosso *et al*.[97] and Cui *et al.*[98] for the measurements of the thermal conductance by conduction of single-molecule junctions. They reached sensitivities of the order of a few picowatts per kelvin for a temperature difference of around 50 K using respectively custom-built scanning tunneling microscope (STM) and SThM probes. This gives a sensitivity, in terms of power, lesser than 0.1 nW which is two orders of magnitude lower than the sensitivity levels reached for the sphere-plane near-field radiative power measurements.
The comparison with other similar works indicates that the experimental setup that was developed here shows comparable performances in terms of heat flux and radiative conductance resolution while allowing measurements with much higher temperature differences. The large temperature difference is a reason of the better conductance sensitivity compared to other similar works.

Table III.1: Measurements sensitivity for different experimental setups

Source	Experiment type	ΔT [K]	Power sensitivity [nW]	Conductance sensitivity [pW.K^{-1}]
Menges *et al.*[24]	Sphere-plane NFRHT	159	10	60
Shen *et al.*[44]		33.5	13	390
Song *et al.*[47]		10	5	500
Mosso *et al.*[97]	Conduction through single-molecule junction	50	0.2	5
Cui *et al.*[98]		45	0.1	2
This work	Sphere-plane NFRHT	600	18	30

III.5 Conclusions

In this part, the fabrication process and characterization of the emitter has first been described. The emitters are made of a SiO_2 or graphite sphere attached to a SThM probe that can be heated by Joule effect up to 1600 K. After the *R(T)* calibration, the temperature variation sensitivity of the emitter is determined by the calculation of the temperature coefficient α. The temperature where the sensitivity is maximum is around 732 K. Above this temperature, measurements can still be performed but the temperature variation sensitivity drops to a value close to 0 near 1400 K. Then the emitter is integrated into a 3-axis piezoelectric positioning system placed in a high vacuum environment allowing to monitor its lateral displacement and its distance relative to the sample located below the emitter while recording its electrical resistance. A liquid helium cryogenic system can be integrated in the vacuum chamber to cool down the sample to 10 K when required. This feature will be used mainly during the near-field thermophotovoltaic experiments. The temperature and thermal conductance are deduced from the resistance measurements using the *R(T)* calibration curve of the emitter. The minimum achievable emitter-sample distance with respect to a mean surface is around 30-40 nm without the cooling system and 100 nm with it, considering the roughness, the attraction forces, the deflection due thermal bending of the cantilever, and the vibrations. The optical parameters of the silica spheres and sample have been verified by measuring their reflectivity in the infrared and match the results from the literature. Finally, the study of the uncertainty of the near-field radiative conductance measurement has revealed that it depends strongly on the Gaussian electrical noise at large distances and more on accuracy of the emitter calibration at low distances, where the emitter temperature varies the most. In the end, the relative uncertainty is approximately 20 % with a 30 $pW.K^{-1}$ (0.67 $pW.K^{-1}/\sqrt{Hz}$) sensitivity which is comparable to other experimental setups[24,44,47] studying near-field radiative heat transfer between a sphere and a planar surface.

Chapter IV

Near-field radiative heat transfer experiments

IV.1 Introduction

In this chapter, measurements of near-field radiative conductance between a thermal emitter and a planar substrate are reported. The present experimental study aims in particular to investigate radiative heat transfer in the near field for large temperature differences above 500 K, which are not reported in the literature. High temperature differences are useful for enhancing the conversion efficiency and the generated power of energy harvesting devices. Applications of near-field radiative heat transfer enhancement coupled to a thermophotovoltaic conversion device will be provided in chapter VI. Another goal is to determine the dependence on temperature of near-field thermal radiation, which strongly differs from the far field one (see Sec. II.4.2), and could not be easily studied in previous experiments due to limited temperature differences (see Sec. I.4)
Materials selected for sphere-plane experiments are SiO_2, graphite and InSb. SiO_2 was chosen because it is widely studied in the literature, especially for the sphere-plane configuration. Graphite and InSb are the emitter/substrate pair that was estimated to be the most efficient for the near-field enhancement of photocurrent generation by an InSb TPV cell at short distances. Different emitter/substrate combinations of the selected materials are investigated and the results are compared with theoretical calculations detailed in chapter II. Some experiments are performed with the substrate cooled at 77 K.
A few experiments are also performed for studying the tip-plane geometry. In this case, a doped-Si SThM probe is used without any modification. The tip of the probe has a radius of curvature of ~20 nm, therefore near-field radiative conductance is expected to be much smaller in the case of spherical emitters.

IV.2 Tip-plane geometry

In this section, tip-plane geometry experiments are presented, with the aim of observing the influence of the SThM probe, without any sphere, on near-field radiative heat transfer. Tip-plane geometry measurements of near-field radiative heat transfer were studied in the literature for temperature differences up to 200 K[17,37] (see Sec. I.4). This configuration allows to investigate gap distances of the order of the nanometer. Because of the small radius of curvature, there is no roughness parameter issue, for the emitter, which limits the minimum reachable distance. Vibrations and attraction forces are the only phenomena influencing the distance determination close to contact. In this work, the same kind of doped-Si SThM probe, on which spheres are usually glued, are used to measure near-field radiative conductance between the tip apex and a flat bulk substrate.

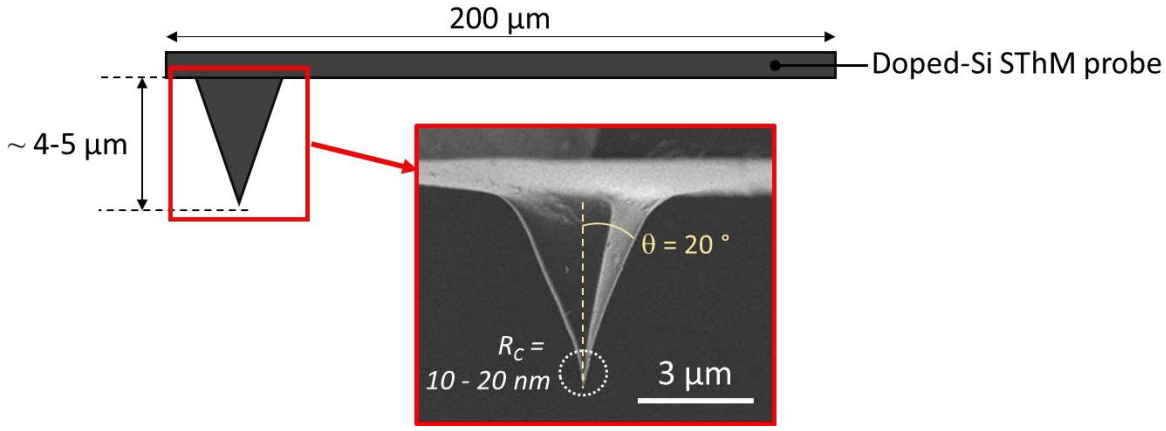

Figure IV.1: Details on dimensions of the doped-Si SThM probe

A schematic view of the probe is presented in Figure IV.1. The tip is very small compared to the rest of the probe so the schematic view is not to scale. The tip has a height of ~4 – 5 µm with a radius of curvature R_C = 10 – 20 nm. The radius of curvature is three orders of magnitude smaller than the radius of the spheres used for measuring near-field radiative heat transfer. The expected conductance is therefore much lower than that with spherical emitters.
In order to improve the signal-to-noise ratio, the probe temperature was set to 732 K, corresponding to the temperature of maximum sensitivity, where the temperature coefficient α is maximum. Such temperature gives a large temperature difference of 436 K that also contributes to enhancing the signal-to-noise ratio. Figure IV.2 shows the near-field radiative conductance as a function of distance between the heated tip at 732 K and a bulk flat substrate, made either of silicon or SiO_2 at room temperature. The grey shaded area represents the range where there is an uncertainty on distance determination. Therefore, curves are plotted as a function of z-piezo positions relative to the contact, with each point located 1.7 nm away from the neighboring ones. Close to contact, the measured conductance reached a maximum value of 0.20 $nW.K^{-1}$ for the configuration with a Si substrate and 0.11 $nW.K^{-1}$ with SiO_2. These values are one to two orders of magnitude lower than that measured with spherical emitters for similar temperature differences (*Table IV.1*). Therefore, the SThM probe is expected to have a very small influence on near-field radiative conductance measurements during experiments with a sphere attached on the tip. It has to be noticed that the random electrical noise is low, with 15 and 20 $pW.K^{-1}$ for the configurations with a Si and SiO_2 substrate respectively. These low values may be explained by the absence of sphere and adhesive on the tip of the probe.

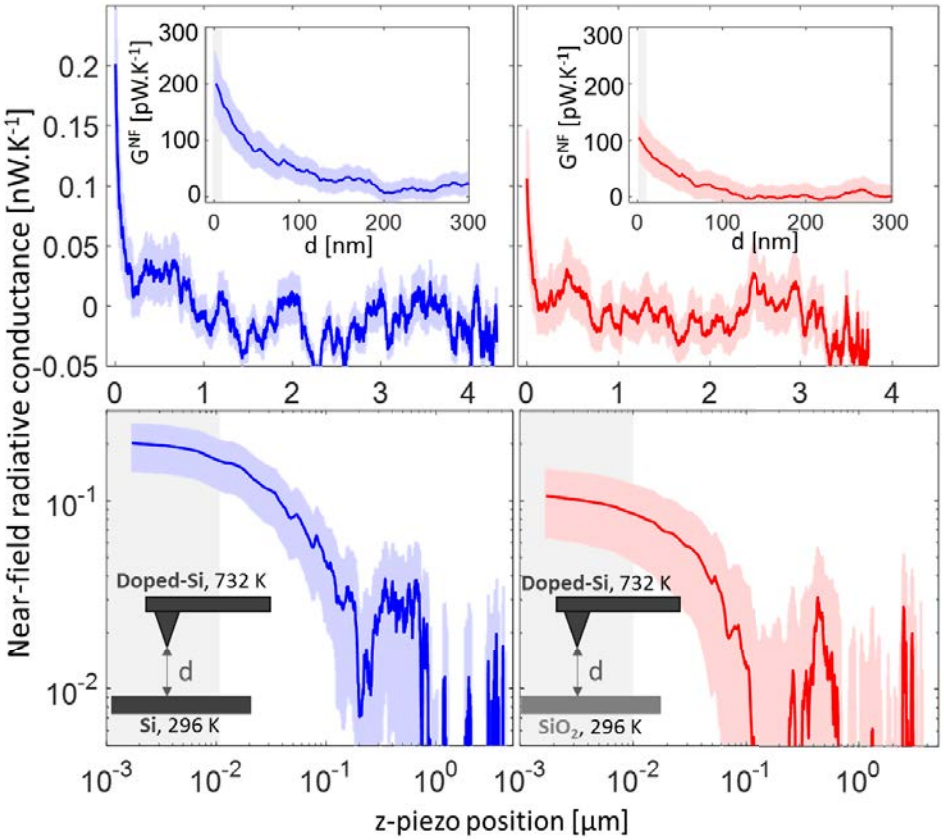

Figure IV.2: Near-field radiative conductance as a function of distance between a 732 K tip of a doped-Si SThM probe and a Si or SiO_2 bulk flat substrate at room temperature. Grey shaded areas represent the range where there is uncertainty on distance determination

Unlike with spherical emitters where near-field radiative conductance increases below ~ 3 µm, with the tip the increase starts to be detected at lower distances, of the order of 100 to 200 nm. This increase is clearly seen in insets of linear plots of Figure IV.2, where the distance is shown in nm and the conductance is in $pW.K^{-1}$. In the logarithmic scale plots, conductance has the same behavior for Si and SiO_2 substrates, with a levelling off at low distances. In order to discriminate if the cause of the levelling off is due to the distance uncertainty or due to the emitter-substrate material combinations, PFA calculations are performed.

In Figure IV.3a, a schematic of the three different emitter geometries, considered in PFA calculations, are presented:

- *Case 1* is for a spherical emitter with a radius of 20 nm, corresponding to an estimation of the radius of curvature of the tip apex. In this case, only near-field radiative heat transfer at the apex of the tip is considered.
- *Case 2* represents the real geometry of the tip. It takes into account an apex with a radius of curvature of 20 nm and tip with a height of 5 microns, with a 20° opening angle.
- *Case 3* is similar to case 2 but the radius of curvature at the apex is 10 times larger, with R_C = 200 nm. This case gives best matching calculations compared to experimental measurements.

In Figure IV.3b, experimental measurements and their uncertainties are compared to PFA calculations for the three cases described. Blue curves are for the Si substrate, while red curves are for the SiO_2 substrate. Comparison with *case 1* shows that calculations are several orders of magnitude below experimental measurements. It is expected because of the tip opening angle of 20° provides more exchange area for radiative heat transfer. Calculations from *case 2*, considering the real dimensions of the tip, show a better agreement with measurements. Calculated conductances are of the same orders of magnitude as measured conductances. However, deviations appear at low distances, with calculated values lower than measurements for both substrate materials. On the plots in inset of the figure, the conductance enhancement near 100-200 nm is seen only for experimental measurements. Best matching calculations from *case 3* show a conductance enhancement but for lower distances, of the order of 10 nm.
Comparisons with PFA calculations for the tip-plane geometry appear very challenging. At low distances, below 100-200 nm, experimentally measured conductances are up to a factor 3 higher than that calculated considering the real emitter dimensions. Instead of the real R_C = 20 nm, a radius of curvature R_C = 200 nm has to be considered in order to find the best match between calculations and experiments. The disagreement with calculations tells that PFA is not reliable for simulating near-field radiative heat transfer between a tip and a plane[82]. Also, experimental uncertainties such as tip inclination may change the real geometry of the exchange area for near-field radiative heat transfer. In the literature, Kloppstech *et al*.[25] studied near-field radiative heat transfer between a gold tip with R_C = 30 nm and a gold flat substrate. Similarly, they measured an exchanged heat flux four orders of magnitude higher than calculations, despite performing numerical calculations with the boundary-element method instead of PFA. Cui *et al.*[53] performed similar experiments and suggested that cleaning and contamination of the tip may strongly impact the measured near-field radiative conductance. Other reasons might also explain this difference and are currently subject of investigations. Averaging the experimental data could be done considering the amplitude of the vibration of the system and may lead to a better agreement with calculations. Understanding near-field radiative heat transfer between a tip and a plane is an interesting field of study. It may be

worth performing experimental measurements with various materials and studying the influence of temperature differences, as it was done for sphere-plane configurations.

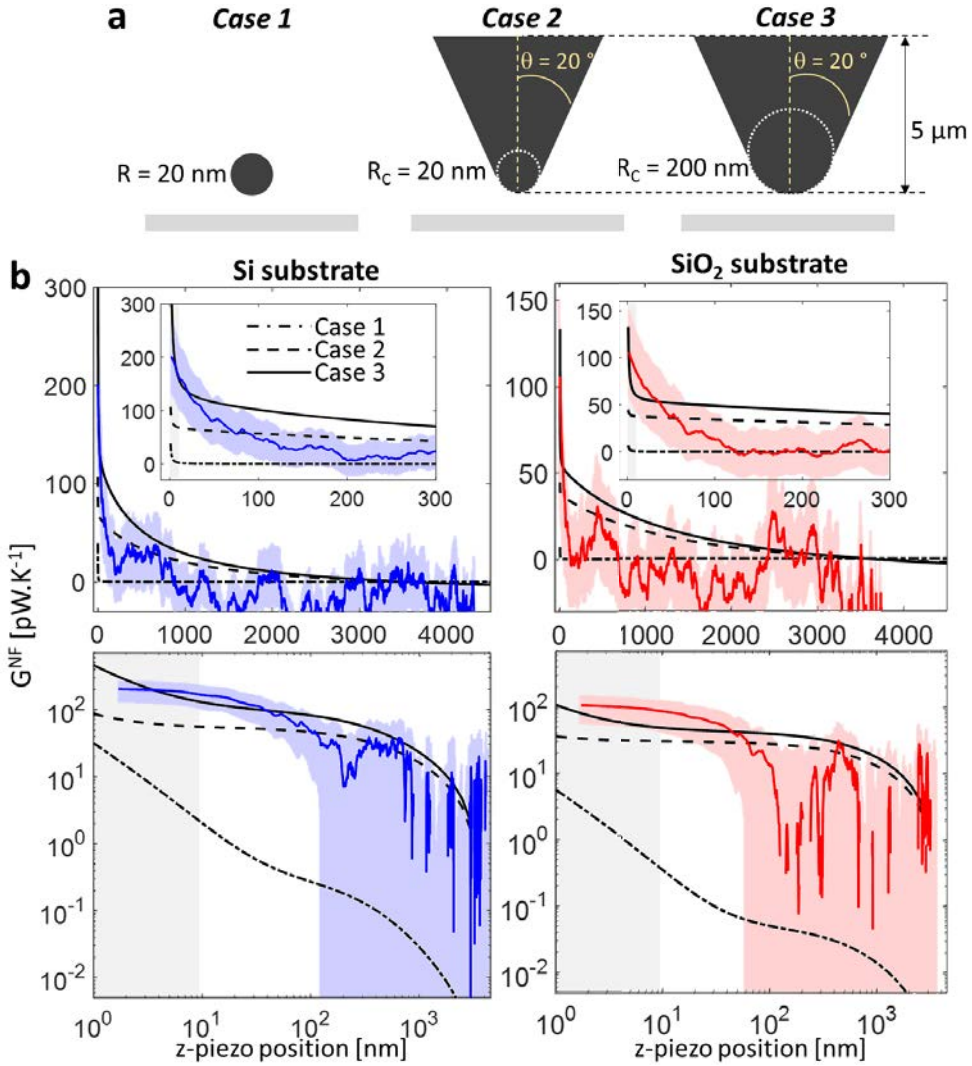

Figure IV.3: Measurements and PFA calculations comparison of near-field radiative conductance between a 732 K doped-Si tip and a room temperature bulk flat substrate made of Si (blue) or SiO_2 (red).
(a) Geometries of emitters considered in PFA calculations. (b) Comparison between measurements and calculations.

IV.3 Study of temperature and material dependence for the sphere-plane geometry

In order to study the influence of temperature and materials on near-field radiative heat transfer, several experiments were performed with a room temperature or cooled-down substrate and a heated emitter. Near-field radiative conductance curves as a function of distance and emitter temperature are presented and compared to PFA calculations (see Sec. II.3.2). For comparison, all experimental and calculated curves are set to a conductance equal to 0 at large distances (d ~ 3-4 µm), where the evanescent wave contribution to radiative heat transfer is negligible. Measurements represent variations of radiative conductance from a reference in the far field, which

cannot be measured with the experimental setup. Therefore, we chose this reference to be 0 and to plot only the near-field contribution of the radiative conductance. For distances comprised between 3 and 5 μm, averaging of experimental curves do not consider always 100 curves depending on distance. In fact, the distance range covered by one individual curve (before averaging) varies as a function of time due to the distance drift of the contact point, as shown in Figure III.15c. As a consequence, a majority of curves cover distances from 0 to ~ 3 μm only, while a few curves cover larger distances. Therefore, the averaging considers 100 curves for distances smaller than 3 μm but considerer fewer curves above this distance, tending to one curve at the largest distance.

IV.3.1 Estimation of the minimum emitter-substrate distance

When the emitter is close to contact with the substrate, it was demonstrated in the previous chapter that the distance determination depends on attraction forces, temperature-induced bending of the cantilever, roughness and vibrations. All these effects combined were estimated to limit the minimum achievable effective distance d_{min} up to several tens of nanometers. In the literature, the minimum distance was also often estimated with accounting for these effects[40,41,47]. For instance, Rousseau et al.[40] measured a ~ 40 nm characteristic roughness for a SiO_2 sphere used as the emitter and having a diameter of 40 μm. They found a 31.8 nm shift in distance in order to best match their experimental data to theoretical calculations from PFA. Using a similar method, the estimation of $d_{min,}$ for measurements performed during this work is made in order to best fit experimental data with PFA calculations. This method is applied for distances below 300 nm where PFA calculations are expected to be more accurate (see Sec. II.3.2). This is achieved by applying a distance shift to the experimental conductance values, with the aim of minimizing the root-mean-square level of the difference with calculations in the sub-300 nm distance range. Figure IV.4a shows the near-field radiative conductance calculated with PFA as a function of distance, for SiO_2-SiO_2 and graphite-InSb sphere-plane configurations. These configurations are selected because their conductances exhibit either a sharp or a smooth enhancement as distance decreases. Red curves are ideal sphere-plane near-field radiative conductances G_{sp}^{ideal} where there is no distance shift close to contact (d_{min} = 0), while blue curves (100 for each configuration) are calculated with $d_{min} > 0$, ranging from 10 up to 70 nm. The distance distribution used for calculations, shown in Figure IV.4b, corresponds to a pseudo-random distribution with a Gaussian behavior similar to that observed experimentally (see Figure III.25). The distribution is centered on 40 nm, corresponding to the expected minimum distance determined in Sec. III.4.2. The minimum distance distribution is wide because it should describe what happens experimentally for individual approaches, with potentially large differences from one approach to another. The black-dashed curve is the mean sphere-plane near-field radiative conductance G_{sp}^{mean} representing the average of the 100 individual curves. The mean curve is then shifted in distance by increasing its minimum distance from 1 up to 200 nm with 1 nm steps (Figure IV.4c). At each step, the root-mean-square level *rms* of the difference between the mean the ideal curve is calculated, considering only distances below 300 nm. The point where the root-mean-square level is the minimum corresponds to the d_{min} where the mean curve best matches the ideal curve. The value of d_{min} of the mean curve corresponds to the mean value of d_{min} used for calculating individual curves. In Figure IV.4a, the back-dash-dotted curve is the mean curve where a d_{min} of 40 nm is consider, and is superimposed with the ideal curve. This method will be applied in order to find the minimum distances reached during sphere-plane near-field radiative heat transfer experiments. It has to be mentioned that this method does not aim to provide a quantitative value of d_{min}, due to the probable inaccuracy of PFA calculations, but an estimation of the order of magnitude.

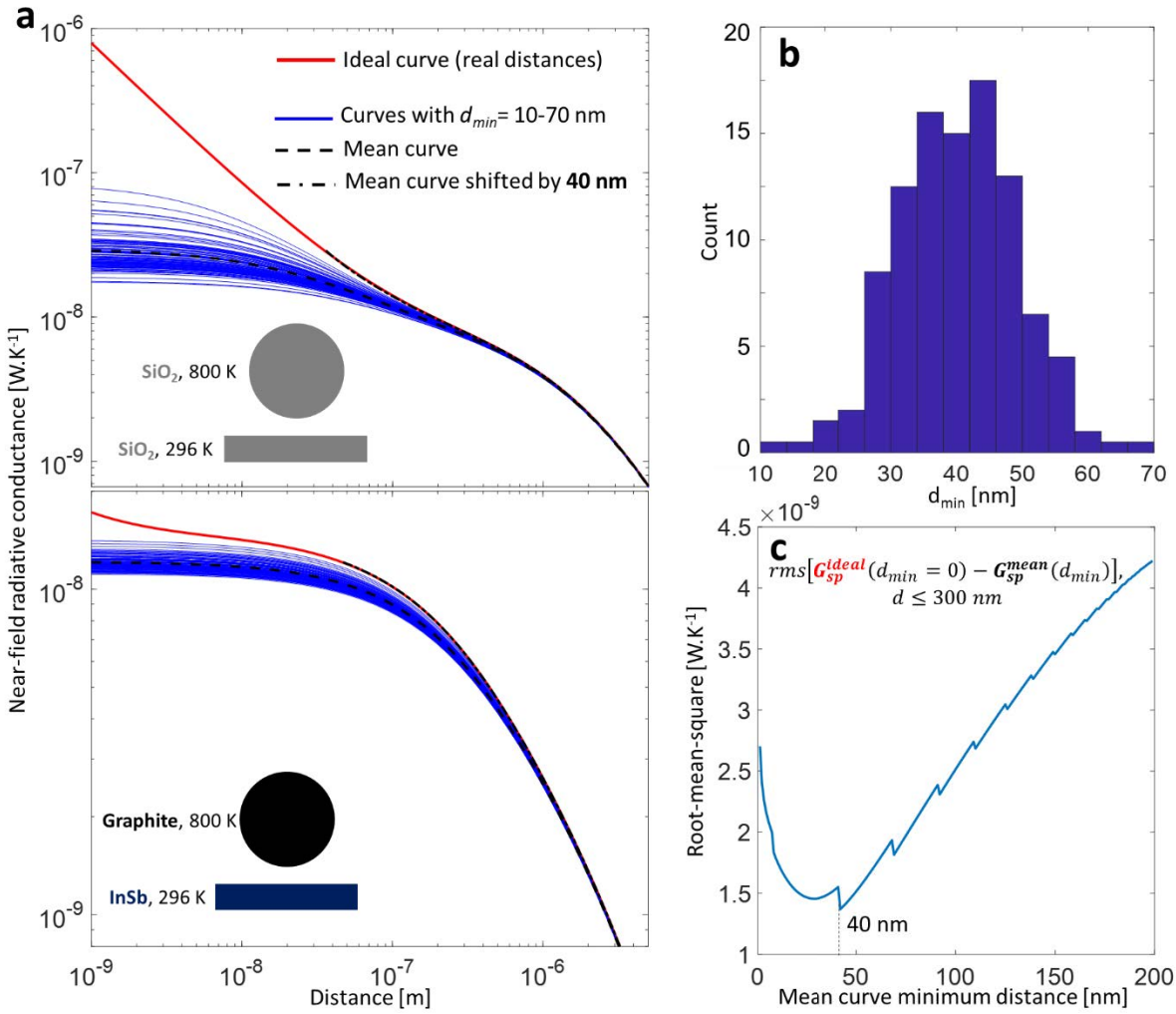

Figure IV.4: Method for estimating the minimum emitter-substrate distance.
(a) Near-field radiative conductance calculated with PFA as a function of distance, for SiO_2-SiO_2 and graphite-InSb sphere-plane configurations. The red curve considers real distances, blue curves consider shifted distances, black-dashed curve is the mean curve considering curves with shifted distances, and the black-dash-dotted curve is the shifted mean curve. (b) Minimum distance distribution used during PFA calculations. (c) Root-mean-square level of the difference between the ideal and shifted mean curve, for distances below 300 nm

IV.3.2 Emitter-substrate material configurations studied experimentally

For this study, different pairs of materials were selected based on different motivations summarized as follows:

- SiO_2-SiO_2: The symmetrical configuration with SiO_2, both used as emitter and substrate, is the classically studied case for near-field radiative heat transfer measurements. Surface phonon polaritons are expected to enhance by one to two orders of magnitude radiative heat transfer at low distances close to contact, because of the same optical properties of the emitter and the substrate.
- SiO_2-InSb: Combination of a SiO_2 emitter with an InSb substrate is an interesting configuration to compare experimentally with the configuration using a graphite emitter. For near-field

thermophotovoltaic applications, graphite is theoretically expected to provide a better enhancement of the radiative heat flux in the near field compared to a SiO_2 emitter.

- Graphite-SiO_2 and SiO_2-graphite: The experimental setup also allows to study these two configurations, where the emitter and the substrate are exchanged. Thermal rectification may be observed when comparing results from the two configurations.
- Graphite-Graphite: This configuration is also symmetrical, and therefore is expected to provide a large enhancement of radiative heat transfer in the near field.
- Graphite-InSb: For a TPV cell made of InSb, calculations performed in Sec. II.4.1 demonstrated that graphite was the most promising material, among those selected, to be used as emitter for enhancing radiative heat transfer in the near field.

IV.3.3 SiO_2-SiO_2

Measurements are performed between a sphere having a diameter of 44 µm, and a substrate at room temperature or cooled down to 77 K.

IV.3.3.1 Room temperature substrate

Results presented in Figure IV.5 are measurements of near-field radiative conductance between a hot SiO_2 sphere and a room temperature SiO_2 bulk flat substrate, as a function of z-piezo position and for five different emitter temperatures, from 417 to 789 K. Black dashed-dotted lines are calculations from the proximity approximation (PFA) at the experimentally measured temperatures, and colored lines are measurements. Measurements were performed from a few nanometers close to contact, and up to 5 µm distance. For each temperature, the conductance value is around 0 at distances above ~ 3 µm. In this distance range close to the wavelength of maximum thermal radiation λ_{Wien}, contribution of evanescent waves to radiative heat transfer is expected to be small. It appears clearly in Figure IV.5a that experimental measurements are smaller than PFA predictions. Differences cannot be attributed to measurement uncertainties, as seen in Figure IV.5b. It is reminded that PFA calculations have been demonstrated not to be perfectly accurate, and may provide results relatively different than exact sphere-plane calculations[83] (see Sec. II.3.2). Moreover, measured conductances are largely below that calculated in the far field, because of the spherical shape of the emitter limiting enhancement of radiative conductance in the near field (Sec. II.3). In Figure IV.5c,d, experimental values level off at small distances. Close to contact, differences between experimental measurements and PFA calculations are larger than one order of magnitude. However, deviations from calculations appear to decrease when the temperature is high. For the curve at 789 K, calculated values are almost included in the measurement uncertainties of experimental measurements. Similarly to tip-plane experiments, grey shaded areas are highlighting the distance range where there is uncertainty on distance determination, as described in Sec. III.4.2. For a room temperature substrate, the limit is ~ 30-40 nm. In order to correct the levelling off of the experimental data, adjustment of the minimum distance of measurements is performed. Due to large differences with PFA calculations at all distances, method described in Sec. IV.3.1 for estimating d_{min} cannot be used. Instead, d_{min} is estimated using a trial and error approach by shifting in distance the experimental values, in order to retrieve the same evolution as that of the calculated curve. As a consequence, values of d_{min} estimated for this case should be considered only as informational.

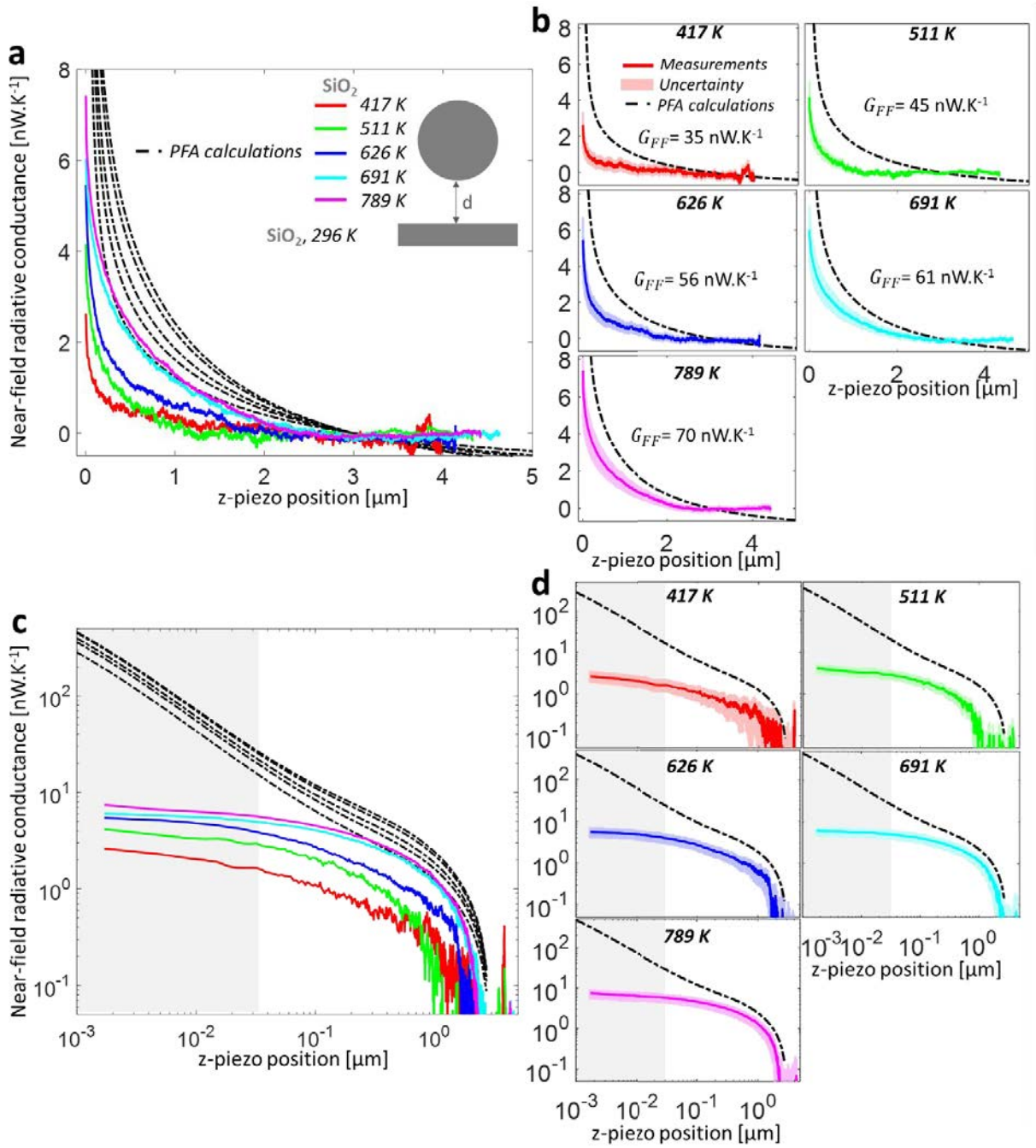

Figure IV.5: Near-field radiative conductance between a hot SiO_2 sphere and a room temperature SiO_2 bulk flat substrate, as a function of z-piezo position and emitter temperature.
(a) Linear scale. (b) Individual curves and their uncertainty with a linear scale. (c) Logarithmic scale. (d) Individual curves and their uncertainty with a logarithmic scale

Figure IV.6a shows a logarithmic scale plot of near-field radiative conductance as a function of distance and emitter temperature, with adjusted d_{min}. Unlike other material configurations, an agreement could not be found between experiments and calculations. Estimated values of d_{min} are ranging from 53 to 118 nm, which is higher than expected but in agreement with values found for the SiO_2-InSb configuration (Figure IV.14).

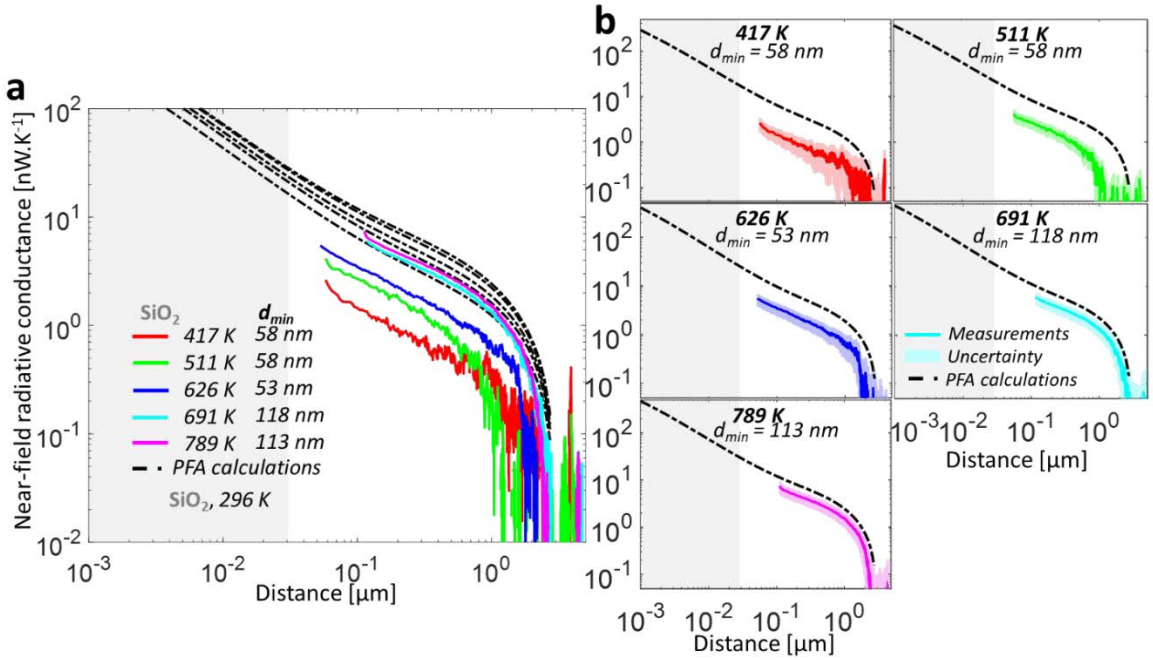

Figure IV.6: Near-field radiative conductance between a hot SiO_2 sphere and a room temperature SiO_2 bulk flat substrate, as a function of distance and emitter temperature with adjusted minimum distances. (a) Logarithmic scale. (b) Individual curves and their uncertainty with a logarithmic scale

In Figure IV.6b, it appears that for each temperature, measured near-field conductances can have the same evolution as a function of distance as calculations from PFA. As temperature increases, deviations between experiments and calculations decrease clearly. Characterization of SiO_2 spheres, detailed in Sec. III.4.1.2, concluded that optical properties of spheres were probably very different from that of bulk SiO_2. It is reminded that the sphere and the substrate were not provided by the same supplier. Therefore, high uncertainties have to be considered on PFA calculations since they are based on optical properties measured on bulk SiO_2 substrates. An experimental work from literature, studying a SiO_2-SiO_2 configuration, also showed a qualitative-only agreement comparing experimental measurements with PFA[47]. In order to quantify deviations from calculations, experimental data are fitted with a conductance multiplicative factor, corresponding to their relative differences with calculations. Figure IV.7a shows experimentally measured near-field radiative conductance with adjusted d_{min} and fitted conductance. Fitted experimental data are compared with PFA calculations. Conductance differences are ranging from a factor 4 to 1.65 when the emitter temperature goes from 417 up to 789 K. The multiplicative factor is plotted as a function of emitter temperature on Figure IV.7b. Evolution of the multiplicative factor as a function of emitter temperature is not simple and can be fitted with a linear law providing only a suggestion of the general evolution. Temperature dependence of the multiplicative factor may indicate that optical properties of SiO_2 spheres undergo strong variations as a function of temperature. These variations may be higher than those observed on the measured data for a bulk substrate[72] (see Figure II.2), which were already considered in PFA calculations. Infrared reflectivity measurements of SiO_2 spheres did not allow direct measurements of optical properties. Study of the Christiansen wavelength indicated that the dielectric function of spheres may be shifted by 2 µm in wavelength. Although such a large shift seems very unlikely, PFA calculations can be made considering a shifted dielectric function for SiO_2 spheres.

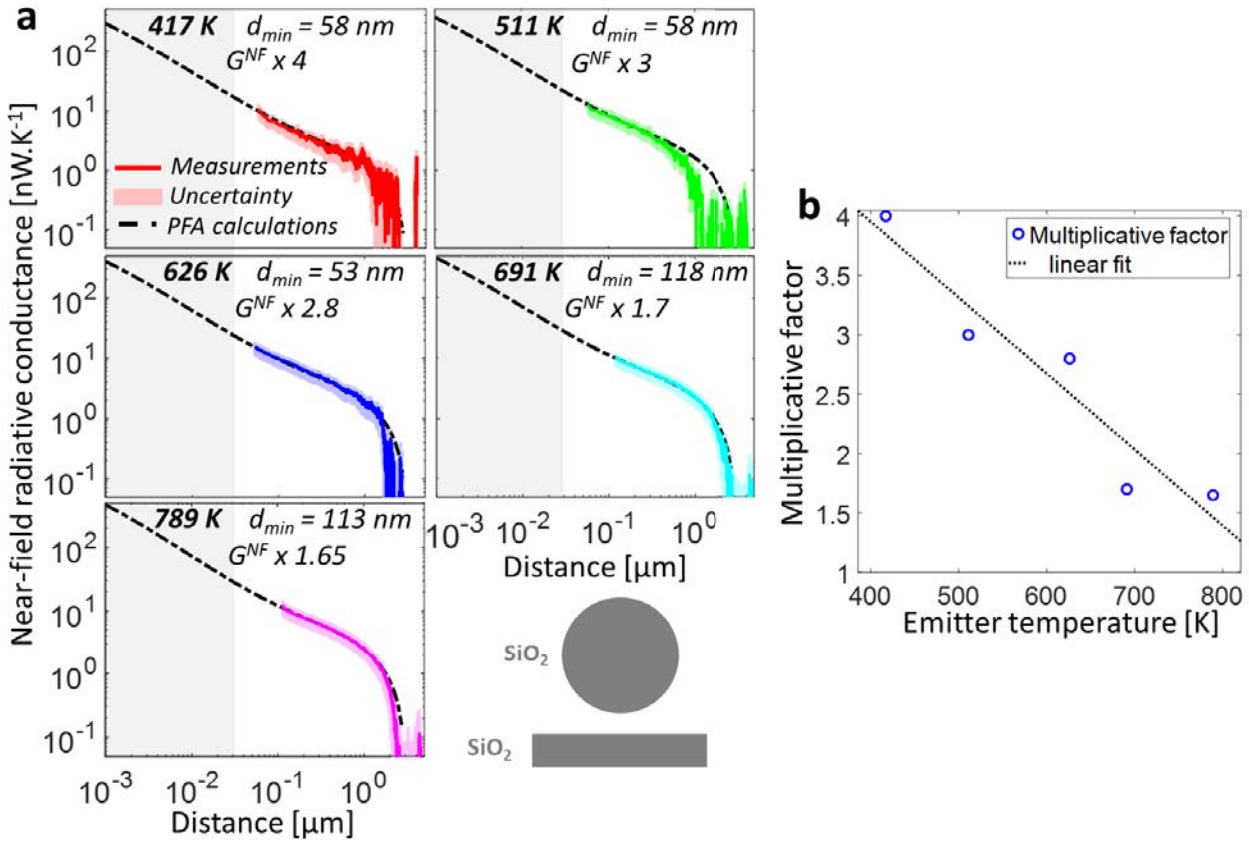

Figure IV.7: Experimental measurements for the SiO_2-SiO_2 configuration fitted to PFA calculations.
(a) Near-field radiative conductance between a hot SiO_2 sphere and a room temperature bulk flat SiO_2 substrate as a function of distance for different temperature, with adjusted minimum distances and fitted conductance. (b) Multiplicative factor as a function of emitter temperature

Figure IV.8b shows the near-field radiative conductance as a function of distance between a 417 K SiO_2 sphere and a flat bulk SiO_2 substrate at room temperature. Experimental values are compared with PFA calculations based on unshifted optical properties and shifted in wavelength by 2 µm for the substrate only (Figure IV.8a). Calculations with the shifted dielectric function deviate from calculations with unshifted data. Relative difference between unshifted and shifted-based PFA calculations goes from a factor ~1 at the largest distance to a factor 4 at d = 1 nm. However, even calculations with a large wavelength shift of 2 µm fail to agree with experimental measurements. Uncertainty on the composition of SiO_2 spheres may be a cause of the disagreement. Some residual compounds from the fabrication process, or pollution of the spheres may be present, thus largely modifying the dielectric function. The structure of SiO_2 may also present crystalline parts, affecting the dielectric function. More advanced analyses of the composition of the spheres should be performed in order to clarify this uncertainty.
Temperature dependence of near-field radiative heat flux Q^{NF} is investigated in Figure IV.9. Distances were chosen following a logarithmic step, from 10 nm to 1 µm. Larger distances were not studied because of the low signal-to-noise ratio. Experimental data are represented by squares with error bars corresponding to uncertainties, while dotted lines represent PFA calculations.

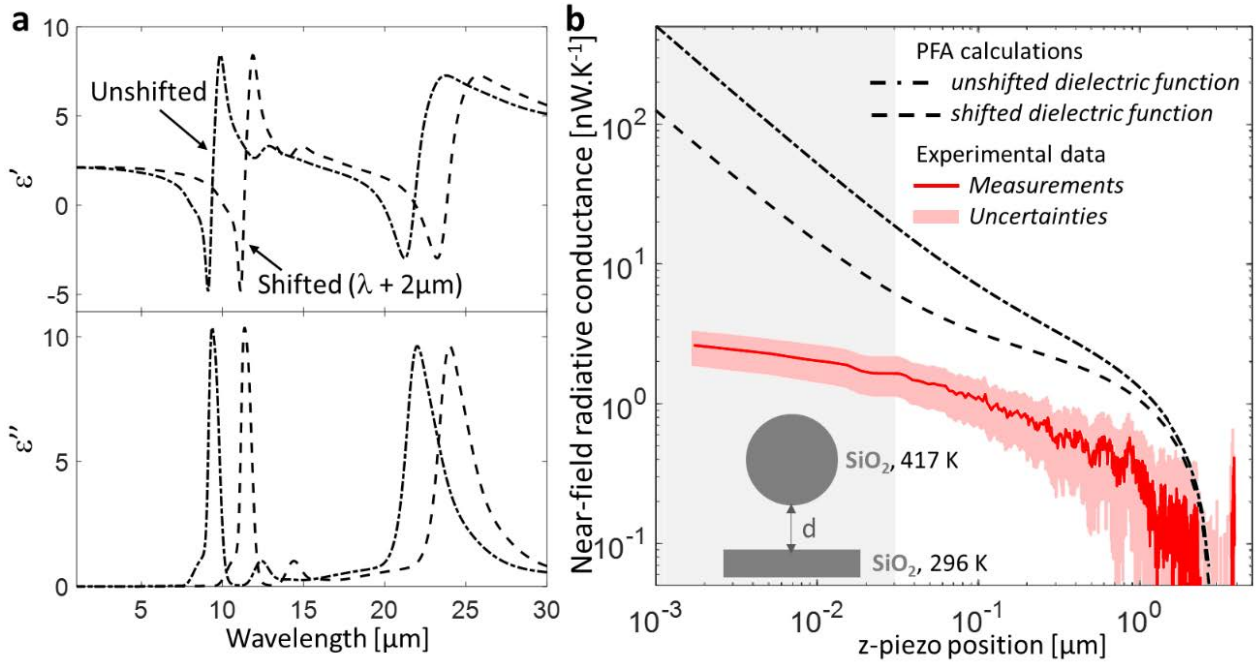

Figure IV.8: Experimental data compared to PFA calculations based on shifted and unshifted dielectric functions.
(a) Real (top) and imaginary part (bottom) of the dielectric function of bulk SiO_2 at 417 K, considering no wavelength shift (dash-dot curve) or a 2 μm shift (dash curve). (b) Experimental and calculated near-field radiative conductance between a 417 K SiO_2 sphere and a room temperature bulk SiO_2 substrate

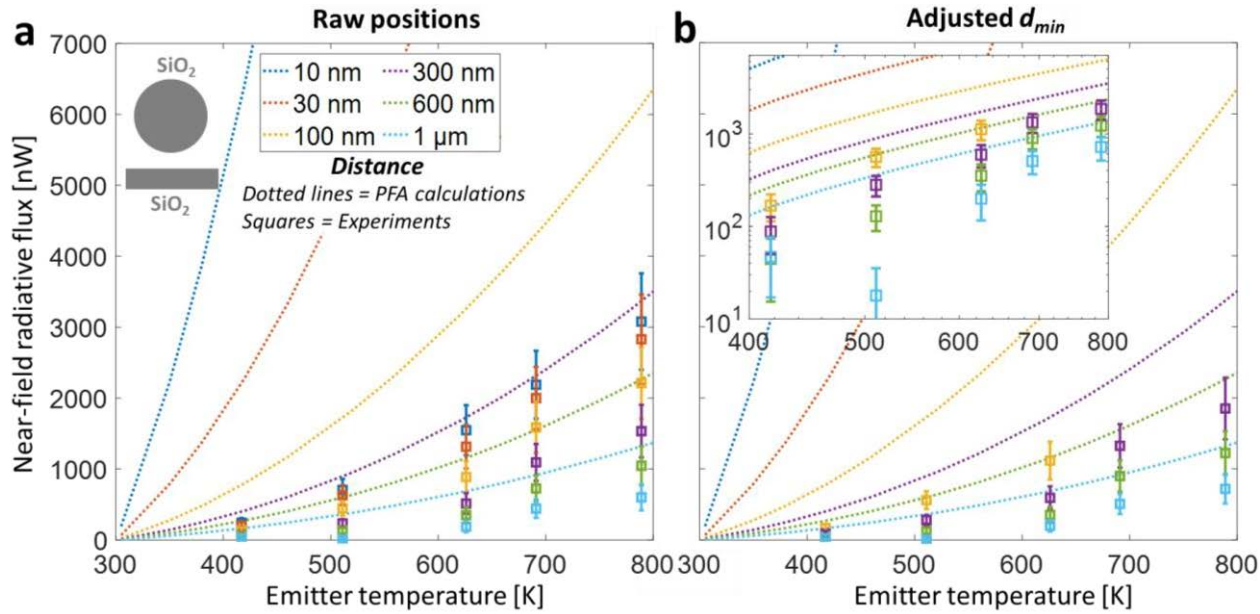

Figure IV.9: Near-field radiative heat flux between a hot SiO_2 sphere and a room temperature SiO_2 bulk flat substrate, as a function of temperature for several distances.
(a) Experimental data with raw positions inferred from z-piezo position. (b) Experimental data with adjusted minimum distances.

In Figure IV.9a, experimental data are considered using raw positions inferred from the z-piezo displacement. It appears clearly in Figure IV.9a and Figure IV.9b that experimental results strongly disagree with calculations. These differences are well observed on the logarithmic plot in inset of Figure IV.9b. In addition, the slopes seem to be different between measurements and calculations indicating different temperature power law exponents. Since temperature power law exponents depend on materials, different experimentally measured exponents compared to calculations may confirm the hypothesis of the uncertainty of the material composition of the spheres.
Evolution of the temperature power law exponents as a function of distance is shown in Figure IV.10, considering raw positions and adjusted d_{min}. The exponent of the temperature power law is calculated with the same method as that used for theoretical calculation described in chapter II (see Sec. II.4.2.1). This method consists in fitting the measured radiative conductance as a function of the emitter temperature by the theoretical expression derived from the Stefan-Boltzmann law (Eq. (II.15)). The behavior of experimentally measured exponents is similar to that predicted by PFA calculations but shifted to higher values reaching that calculated in the far field (n_{FF} = 4.15) near 100 nm. It has to be noted that adjusted minimum distances should be considered as qualitative only since there are uncertainties on the sphere dielectric function, and on PFA calculations as a consequence. Therefore, it cannot be certified that the analysis of the temperature power law exponent is more reliable taking into account adjusted minimum distances.
The SiO_2-SiO_2 configuration provided unexpected results with a lower conductance by a factor up to 4, depending on emitter temperature. Analysis of infrared reflectivity (see Sec. III.4.1) and temperature dependence of near-field radiative heat flux could indicate that uncertainties on material composition of SiO_2 spheres. However, experimental measurements from other configurations using SiO_2 spheres led to good agreement with calculations (Sec. IV.3.4 and IV.3.5). This could be explained by the difference of wavelengths of the surface phonon polaritons (SPhPs) between SiO_2 and the other material (see Sec. II.2.2). For the symmetrical SiO_2-SiO_2 configuration, SPhPs are expected to be approximatively at the same wavelength, thus enhancing drastically radiative heat transfer in the near field (see Figure II.20).

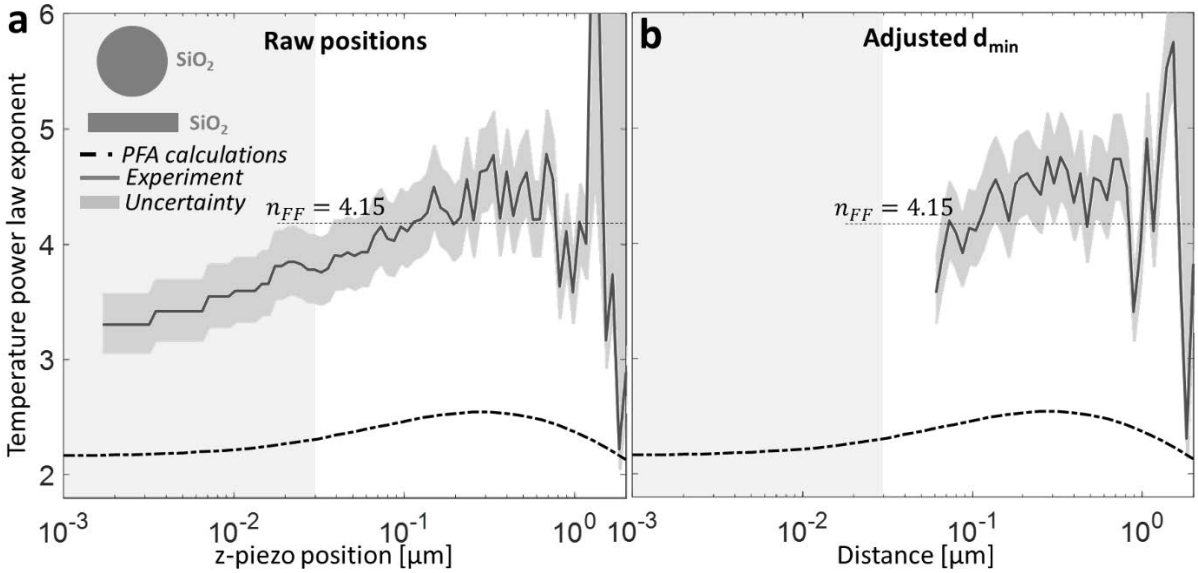

Figure IV.10: Temperature power law exponent as a function of distance between a SiO_2 sphere, from 417 to 789 K, and a room temperature SiO_2 bulk flat sample.
(a) Experimental data with raw positions inferred from z-piezo position. (b) Experimental data with adjusted minimum distances.

A small wavelength shift of the dielectric function leads to a non-matching of the SPhPs wavelengths between the emitter and the substrate. For configurations with a substrate made of another material than SiO_2, there is no expected matching of SPhPs wavelengths. Therefore, a shifted or slightly different dielectric function of the SiO_2 spherical emitter is not expected to have a significant impact on near-field radiative heat transfer.

IV.3.3.2 Cooled substrate

The experimental setup allows to cool the substrate down to cryogenic temperatures (see details in Sec. III.3.2). In order to check the feasibility of near-field radiative conductance measurements with the working cooling system, the SiO_2 substrate was cooled down to 77 K while the SiO_2 sphere was heated to 647 K. This configuration exhibits a large temperature difference of 570 K. In Figure IV.11, near-field radiative conductance measurements are shown as a function of distance and compared with PFA calculations. One issue is the very large random electrical noise affecting experimental measurements, despite a large number of curves considered for averaging. In conductance, this measured noise is ~ 1.8 $nW.K^{-1}$, which is almost two orders of magnitude higher than that measured with a room temperature substrate. The noise is also noticeably larger than that measured with cooled substrates studied for the previous material configurations. The presence of the cooling system clearly affects near-field radiative heat transfer measurements accuracy. This experiment was the first to be performed with a cooled substrate. At that time, issues such as thermal drift (Figure III.18a) and vibration (Figure III.25) were not known. For instance, the cryostat was fixed to the vacuum chamber by one point only, instead of three later on. Improvements were made afterwards before performing near-field thermophotovoltaic measurements. The behavior of conductance as a function of distance is similar to that of the room temperature substrate with a levelling off at low distances. Because of the large random noise, experimental measurements may agree with PFA calculations for distances above 100 nm, which was not the case with a room temperature substrate for the SiO_2-SiO_2 configuration. Below 100 nm, the levelling off can be corrected by adjusting the minimum distance.
Figure IV.12a shows near-field radiative conductance as a function of distance with an adjusted minimum distance.

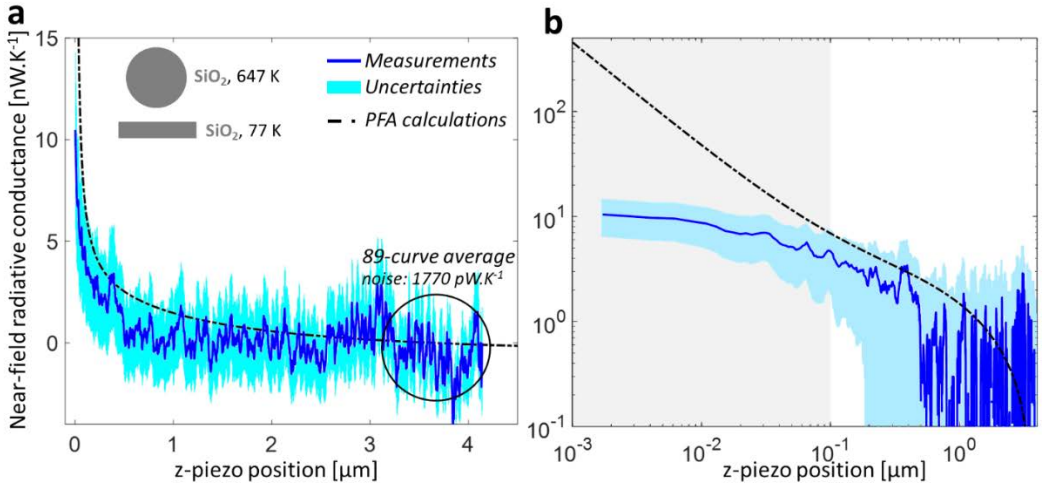

Figure IV.11: Near-field radiative conductance as a function of distance between a 647 K SiO_2 sphere and a 77 K flat bulk SiO_2 substrate.
(a) Linear scale. (b) Logarithmic scale

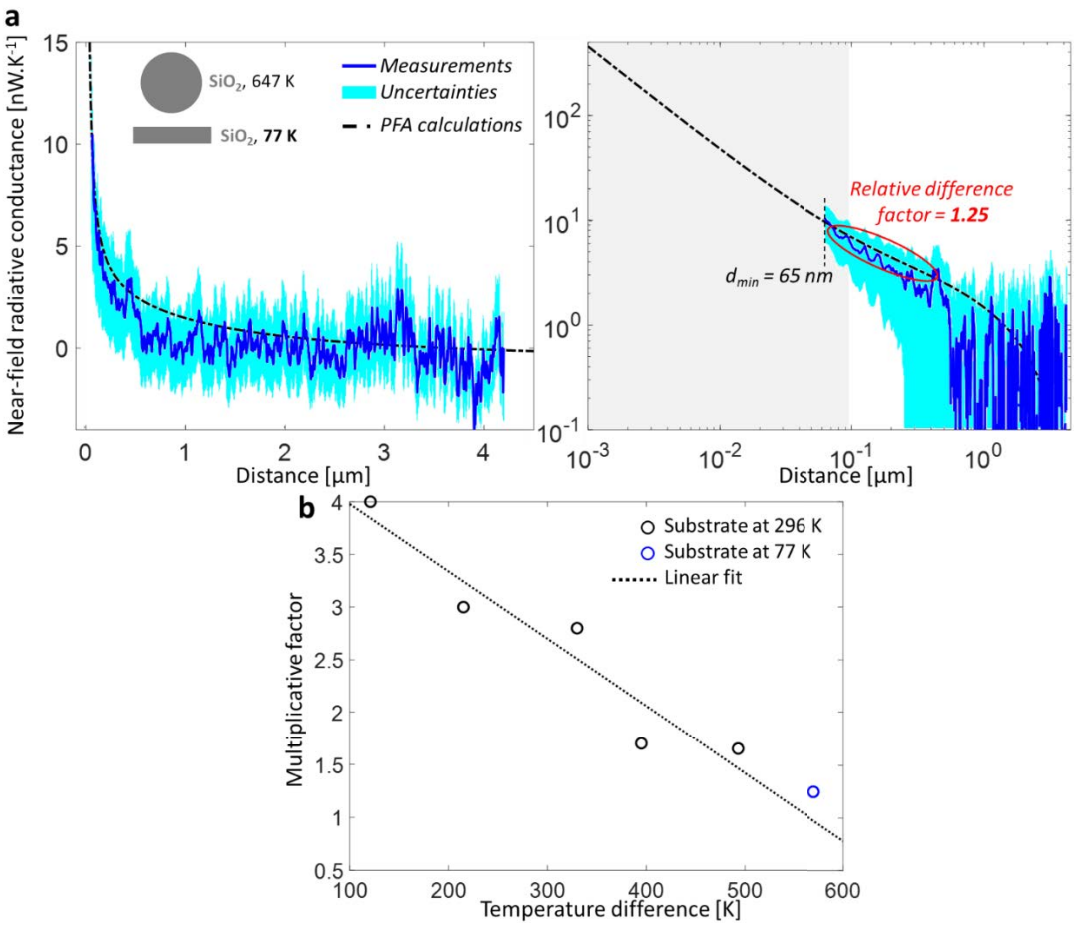

Figure IV.12: Effect of adjusted d_{min} on conductance measurements with a cooled substrate. (a) Near-field radiative conductance as a function of distance between a 647 K SiO_2 sphere and a 77 K flat bulk SiO_2 substrate with adjusted minimum distance. (b) Multiplicative factor as a function of emitter-substrate temperature difference

The best match with PFA calculations was found with d_{min} = 65 nm. This value of d_{min} is in the expected distance range of ~ 100 nm, caused by higher amplitude of vibrations when the cooling system is used. The configuration with a 77 K substrate is the only case where there could be an agreement between experiments and theory for the SiO_2-SiO_2 configuration considering uncertainties. The relative difference factor between PFA calculations and measurements is plotted on Figure IV.12b. Black circles are from previous measurements with a room temperature substrate, while the blue circle represents the relative difference measured with the cooled substrate, which is 1.25. It appears that the relative difference for the cooled substrate matches very well with the behavior previously found with the substrate at room temperature. Therefore, it seems that as the temperature difference gets larger, the difference between measurements and PFA calculations decreases. This observation is in agreement with the hypothesis of a difference of dielectric functions between the spheres and the substrate. Since the dielectric function of SiO_2 depends on temperature, then a suitable temperature difference may provide a matching of SPhPs wavelengths between the sphere and the substrate. Some experiments might be performed with a sphere at room temperature and a heated substrate, in order to measure if differences between experiments and calculations evolve with a behavior similar to or different from that measured during this work.

IV.3.4 SiO_2-InSb

Experiments were performed between a 44 µm diameter SiO_2 sphere and a bulk non-intentionally n-doped InSb substrate at room temperature. Measurements were also performed with an InSb TPV cell cooled down to 77 K (see chapter VI).

IV.3.4.1 Room temperature substrate

It was chosen to study emitter temperatures higher than the melting point of InSb. SiO_2 has a thermal conductivity of 1.4 $W.m^{-1}.K^{-1}$, which is one to two orders of magnitude lower than that of graphite (25-470 $W.m^{-1}.K^{-1}$)[99,100]. The contact resistance between the sphere and the substrate, coupled with the low thermal conductivity of SiO_2 are expected to prevent excessive local heating or melting of InSb, in contact with a hot emitter.

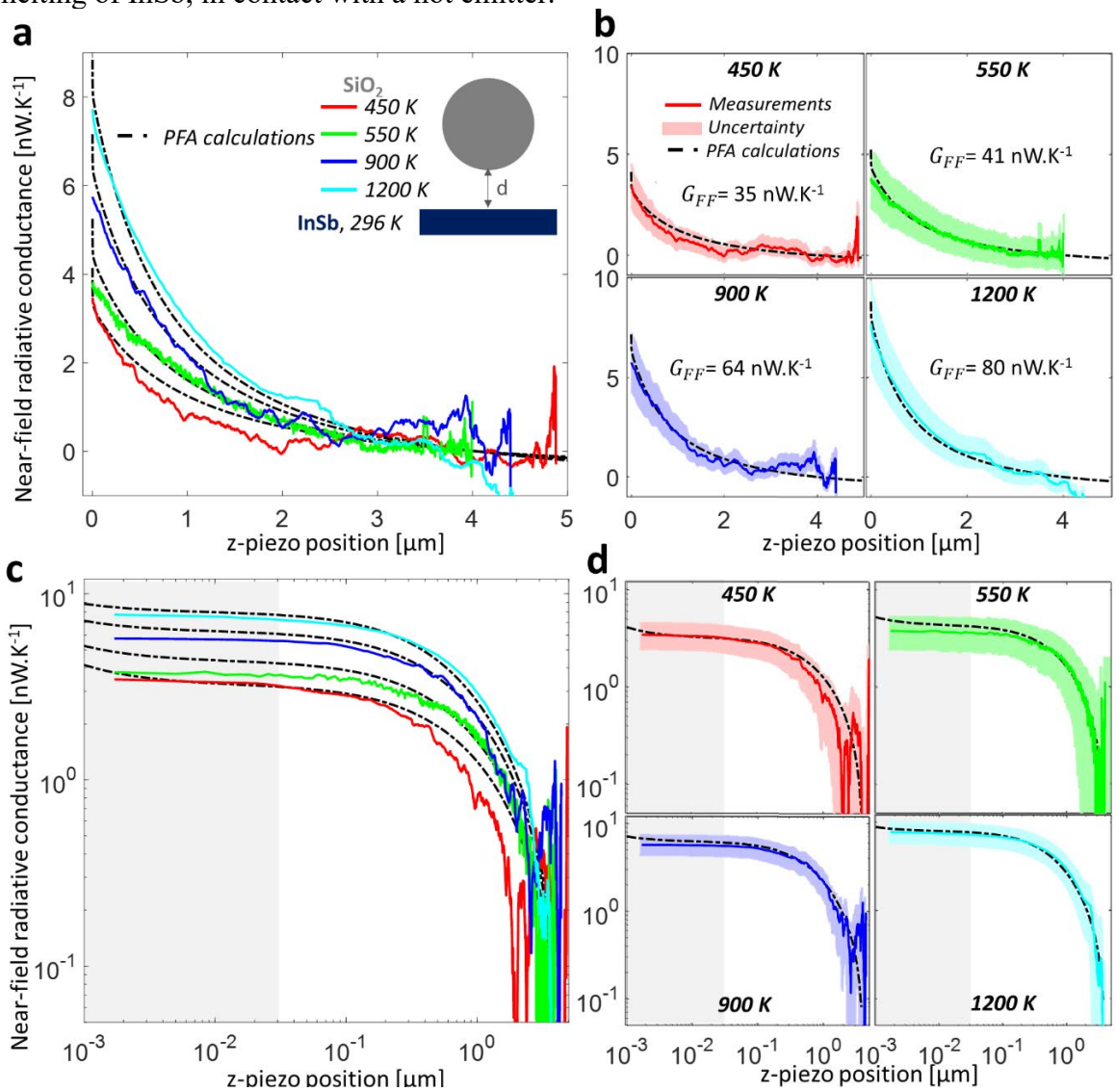

Figure IV.13: Near-field radiative conductance between a hot SiO_2 sphere and a room temperature InSb bulk flat substrate, as a function of z-piezo position and emitter temperature.
(a) Linear scale. (b) Individual curves and their uncertainty with a linear scale. (c) Logarithmic scale. (d) Individual curves and their uncertainty with a logarithmic scale

Figure IV.13 shows the near-field radiative conductance as a function of z-piezo position for four emitter temperatures. In Figure IV.13b, it can be seen that uncertainties from the random electrical noise are higher than usual. The effect is the most important on the curve at an emitter temperature of 550 K. Still, a good agreement is found with calculations. At low distances, experimental values level off as visible in Figure IV.13c,d. Therefore, adjusted minimum distances have to be considered to correctly compare experimental data. With this material configuration, and others later on, minimum distances are estimated following the method described in Sec. IV.3.1.

Near-field radiative conductance as a function of distance with adjusted d_{min} is presented in Figure IV.14. Values of d_{min} are estimated to be ranging from 4 to 103 nm. These distances are higher than expected for the SiO_2-InSb configuration (grey shaded area). The curves at 450 and 550 K have respectively the lowest and highest random electrical noise, and the lowest and highest estimated minimum distance. Therefore, a correlation between random electrical noise and minimum distance seems reasonable. Again, causes of noise and large d_{min} may be pollution of the emitter or the substrate, along with mechanical vibrations higher than expected. The curves levelling off at small distances may induce uncertainties on the estimation of d_{min}, compared to a curve with a sharp conductance enhancement. Measurements at 900 and 1200 K do not exhibit any unexpected behavior, despite being performed at emitter temperatures higher than the melting point of InSb. This may support the fact that the InSb substrate is not excessively heated at contact with a hot SiO_2 sphere.

Near-field radiative heat flux as a function of temperature for five different distances is presented in Figure IV.15. Considering raw positions in Figure IV.15a, the agreement with PFA calculations is found only from 100 nm to 1 µm. With adjusted d_{min} (Figure IV.15b), comparison with calculations for d = 10 and 30 nm cannot be made. In fact, only the experimental curve at 450 K has a d_{min} small enough and at least two points are required to fit the data in order to estimate the exponent of the temperature power law. Therefore, temperature dependence can be studied only for distances above 52 nm, corresponding to the second smallest d_{min}. The logarithmic scale plot in inset of Figure IV.15b shows a good agreement between measurements and calculations.

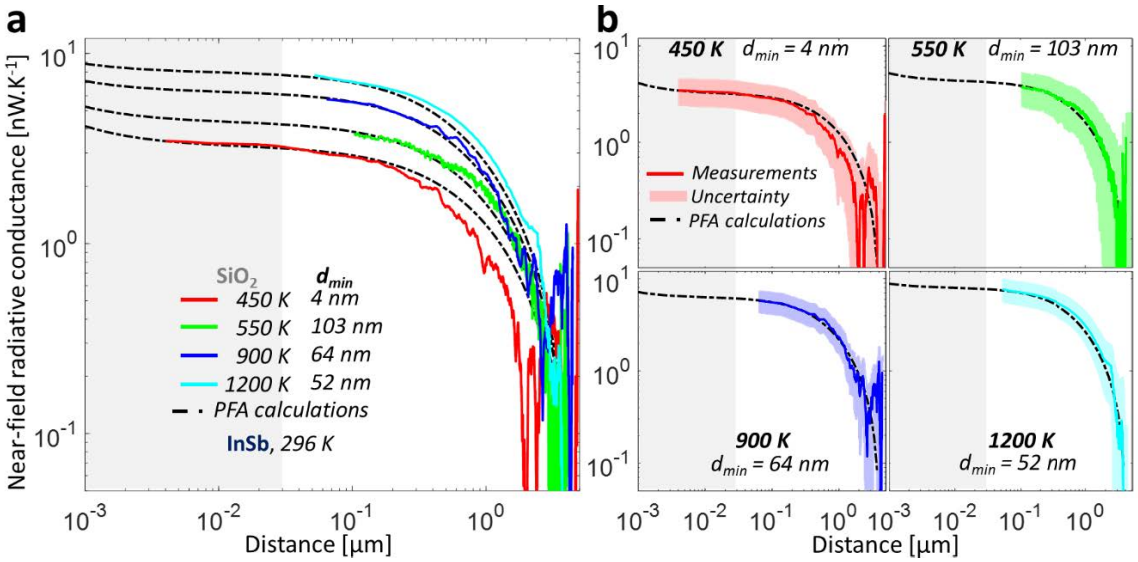

Figure IV.14: Near-field radiative conductance between a hot SiO_2 sphere and a room temperature InSb bulk flat substrate, as a function of distance and emitter temperature with adjusted minimum distances.
(a) Logarithmic scale. (b) Individual curves and their uncertainty with a logarithmic scale

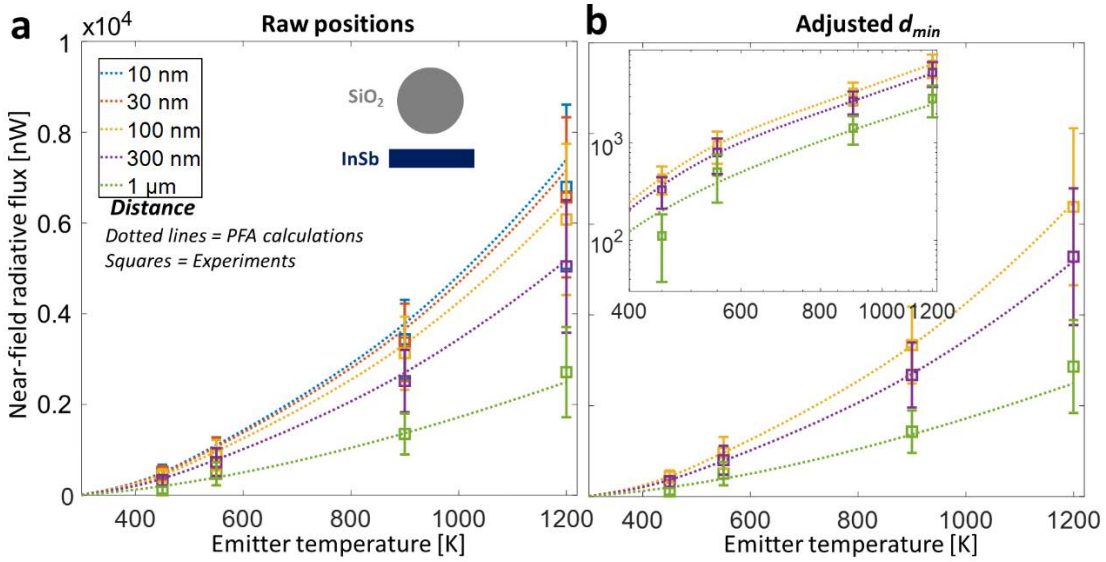

Figure IV.15: Near-field radiative heat flux between a hot SiO_2 sphere and a room temperature InSb bulk flat substrate, as a function of temperature for several distances.
(a) Experimental data with raw positions inferred from z-piezo position. (b) Experimental data with adjusted minimum distances.

Exponent of the temperature power law of the near-field radiative conductance is shown in Figure IV.16 as a function of distance, for raw positions (Figure IV.16a) and for adjusted d_{min} (Figure IV.16b). The behavior of experimentally estimated exponents is similar to theoretical predictions below 500 nm for both raw positions and adjusted d_{min}. Strong deviations from calculations are observed for distances of the order of 1 µm. This is due to the larger measurement uncertainty from the random electrical noise, as previously explained. Contrary to the previous SiO_2-SiO_2 configuration, the measured exponents are, as expected, always smaller than that calculated in the far field corresponding to $n_{FF} = 4.07$.

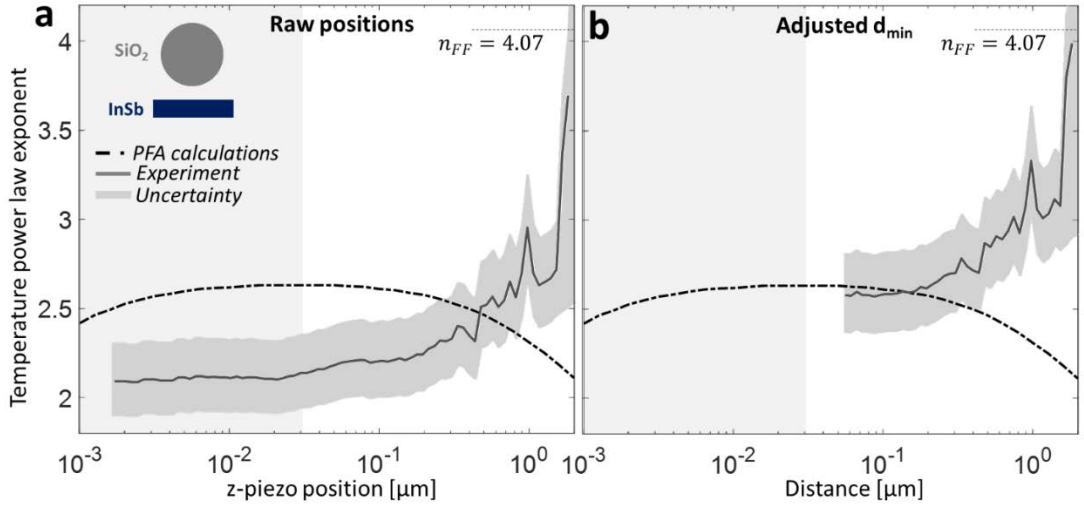

Figure IV.16: Temperature power law exponent as a function of distance between a SiO_2 sphere, from 450 to 1200 K, and a room temperature InSb bulk flat sample.
(a) Experimental data with raw positions inferred from z-piezo position. (b) Experimental data with adjusted minimum distances.

IV.3.4.2 Cooled InSb TPV cell substrate

Figure IV.17 shows near-field radiative conductance measurements as a function of distance, between a 732 K SiO_2 sphere and an InSb TPV cell at 77 K. The high random electrical noise (1230 $pW.K^{-1}$) is due to the averaging, taking only 6 curves into consideration. The noise level is similar to that found for the graphite-InSb cell configuration, where a 7-curve average resulted in a 1100 $pW.K^{-1}$ random noise (Figure IV.37b). Because the conductance between a SiO_2 sphere and an InSb substrate is expected to be of the order of a few $nW.K^{-1}$, a large random noise leads therefore to a low signal-to-noise ratio. The maximum measured conductance is then 5.9 ± 2.4 $nW.K^{-1}$. In Figure IV.17, experimental measurements seem to agree with calculations. However, this agreement is only qualitative due to high uncertainties. Therefore, trying to estimate the minimum distance of experimental data is irrelevant.
The study of the SiO_2-InSb configuration has demonstrated that it was possible to perform experiments with emitter temperatures much higher than the melting temperature of InSb. Also, minimum reached distances have been determined, from conductance measurements, to be higher than expected when an abnormally high random electrical noise was measured. Experiments with a cooled substrate have only shown a qualitative agreement with PFA calculations, due to the large noise affecting measurements and limited averaging.

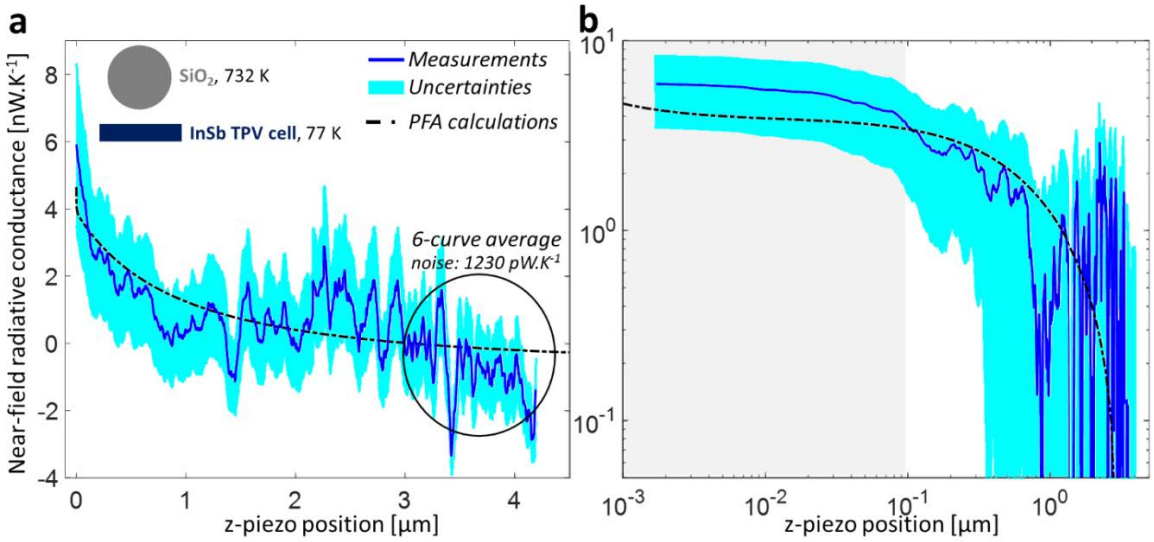

Figure IV.17: Near-field radiative conductance as a function of distance between a 732 K SiO_2 sphere and an InSb TPV cell at 77 K. (a) Linear scale. (b) Logarithmic scale

IV.3.5 SiO_2-Graphite

Near-field radiative conductance between a hot SiO_2 sphere and a room temperature graphite bulk flat substrate is shown as a function of z-piezo position and emitter temperature in Figure IV.18. Measurements were performed at four different emitter temperatures, ranging from 450 to 1200 K. For positions ranging between 3 and 5 µm, experimental curves have large fluctuations around 0 due to the averaging of experimental curves that do not consider always 100 curves depending on distance. Figure IV.18b shows a good agreement between experimental data and PFA calculations, considering uncertainties.

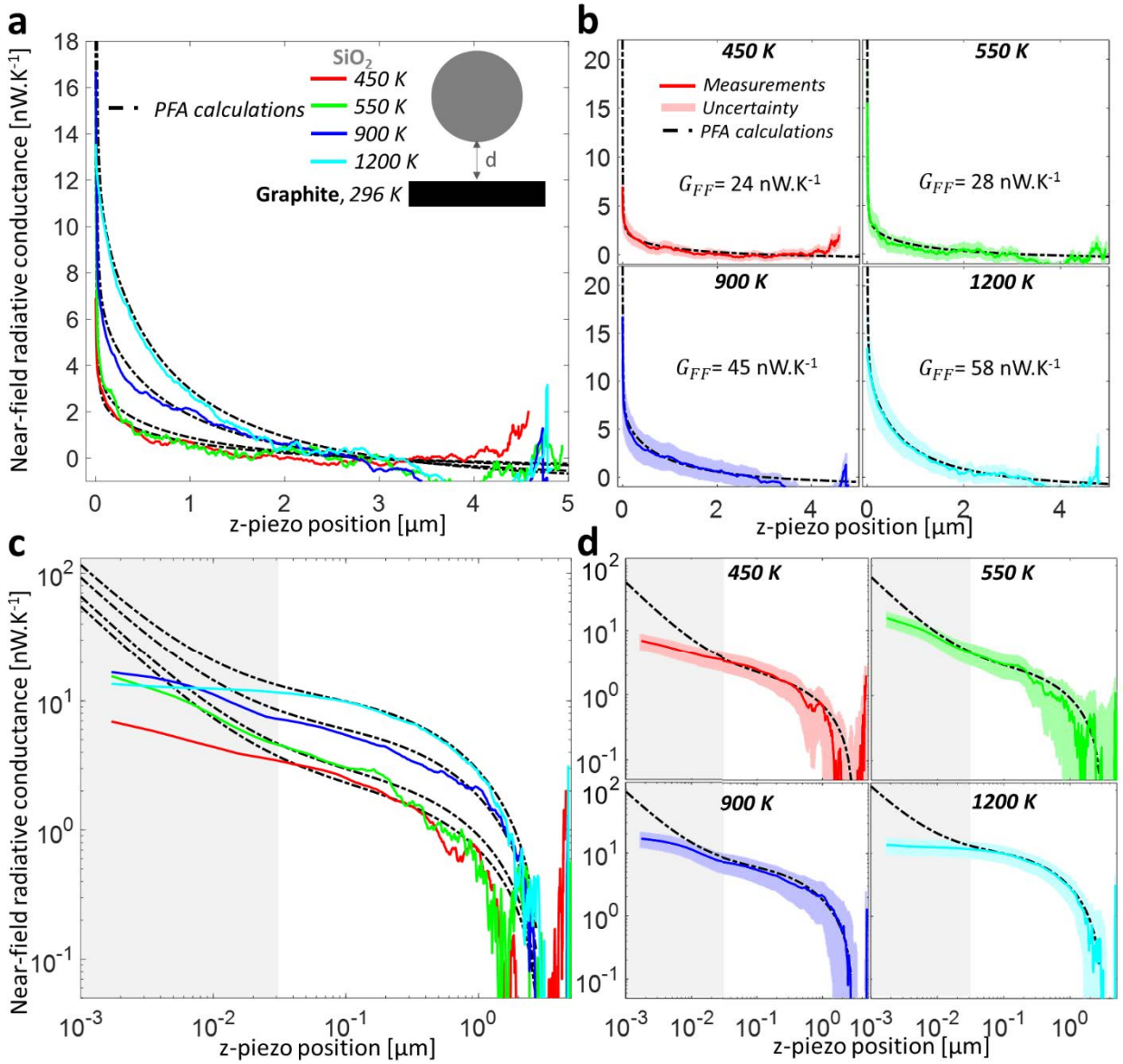

Figure IV.18: Near-field radiative conductance between a hot SiO_2 sphere and a room temperature graphite bulk flat substrate, as a function of z-piezo position and emitter temperature.
(a) Linear scale. (b) Individual curves and their uncertainty with a linear scale. (c) Logarithmic scale. (d) Individual curves and their uncertainty with a logarithmic scale

Figure IV.18c,d highlight a leveling off of experimental measurements at low distances, which seems to be corrected by adjusting d_{min}. Values of d_{min} have a large influence because close to contact because the curve at the emitter temperature of 1200 K is below the ones at 900 and 550 K. This may indicate strong differences of d_{min} for each curve.
Figure IV.19 shows experimental measurements with adjusted d_{min}. As expected, large differences are observed from one curve to another. The curve at 1200 K has an estimated d_{min} of 25 nm, while the other curves have d_{min} estimated to be ranging from 5 to 12 nm. Adjusted curves agree well with PFA calculations for all distances and temperatures, and the curve at 1200 K does not cross the ones at 900 and 550 K anymore. These estimated values of d_{min} are of the same order of magnitude as the roughness of SiO_2 spheres.

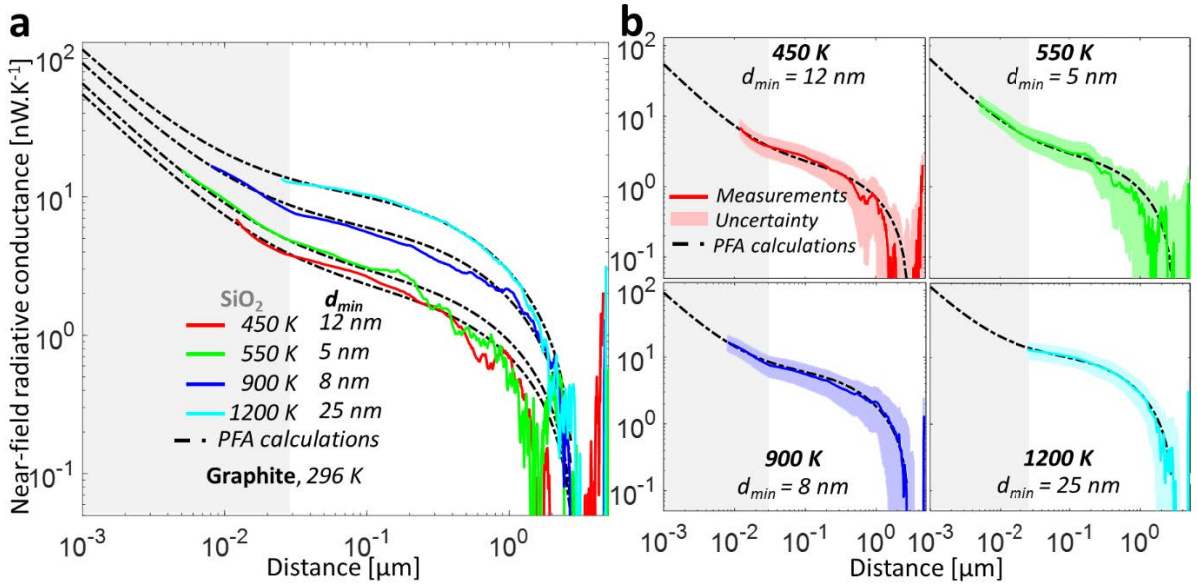

Figure IV.19: Near-field radiative conductance between a hot SiO_2 sphere and a room temperature graphite bulk flat substrate, as a function of distance and emitter temperature with adjusted minimum distances.
(a) Logarithmic scale. (b) Individual curves and their uncertainty with a logarithmic scale

An analysis of the temperature dependence of near-field radiative heat flux is given in Figure IV.20. In Figure IV.20a, the raw positions are considered for experimental data, while Figure IV.20b shows experimental data with adjusted d_{min}.

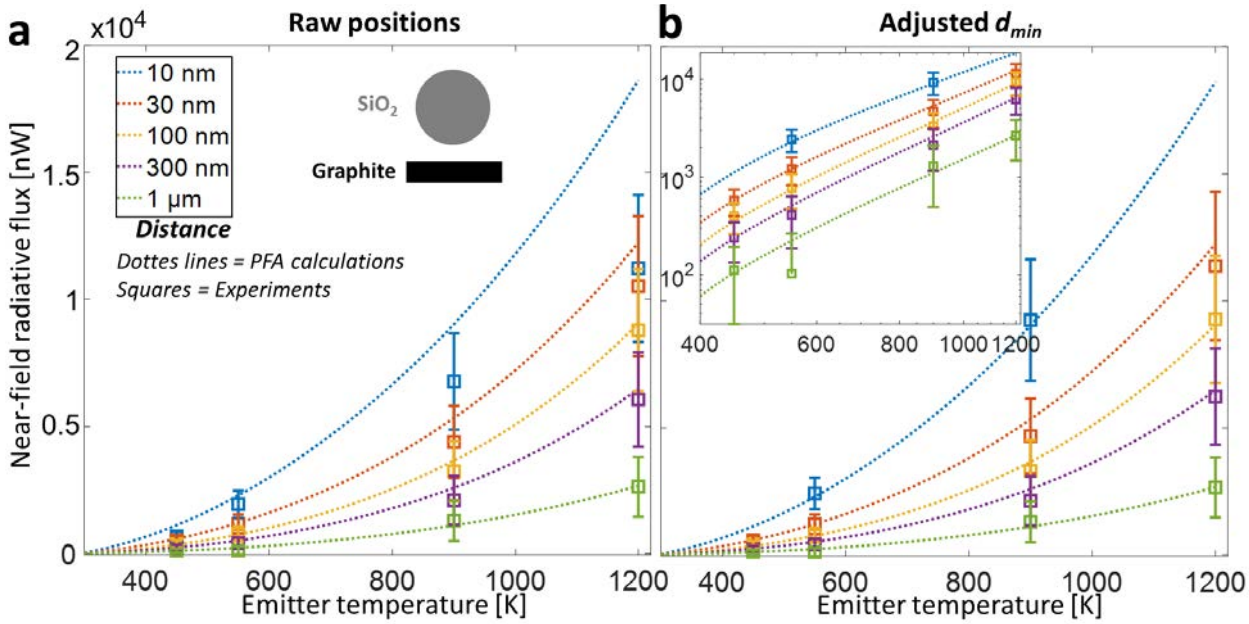

Figure IV.20: Near-field radiative heat flux between a hot SiO_2 sphere and a room temperature graphite bulk flat substrate, as a function of temperature for several distances.
(a) Experimental data with raw positions inferred from z-piezo position. (b) Experimental data with adjusted minimum distances.

The curves at d = 10 nm only have two experimental points from the experiments at 550 and 900 K. It is explained because minimum distances of the two other curves are larger than 10 nm. The logarithmic scale plot, in inset of the figure, also shows a good agreement between experimental data and PFA calculations.
Considering measurement uncertainties, the experimentally deduced exponent considering raw positions (Figure IV.21a) and adjusted d_{min} follows the same evolution as that of the calculated exponent. As both cases lead to a relatively good agreement with calculations, the necessity to consider adjusted minimum distances can be discussed. It was shown previously in Figure IV.18 that at very low distances, the experimental curve at 1200 K crosses the curves at 550 and 900 K. This phenomenon is theoretically unexpected because near-field radiative conductance increases with temperature and smaller distances. Therefore, experimental results imply that minimum reached distances were probably different depending on the studied emitter temperature. As a result, it seems that a better analysis may be provided by estimating d_{min} for each curve, which are of the order of the roughness parameters of the SiO_2 sphere. In the next section, a study of the inverse graphite-SiO_2 configuration is presented and comparisons are made with results obtained with the SiO_2-graphite configuration. As shown in Figure II.28, near-field radiative conductance is expected to be very similar when comparing these two configurations, with a few percent differences only.

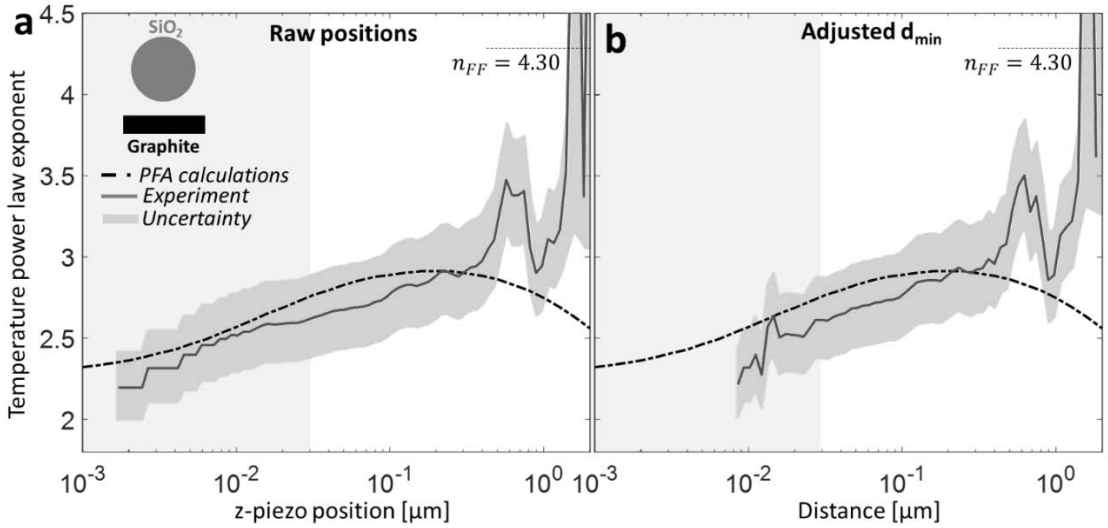

Figure IV.21: Temperature power law exponent as a function of distance between a SiO_2 sphere, from 450 to 1200 K, and a room temperature graphite bulk flat sample.
(a) Experimental data with raw positions inferred from z-piezo position. (b) Experimental data with adjusted minimum distances

IV.3.6 Graphite-SiO_2

In order to compare with the inverse SiO_2-graphite configuration, PFA calculations were performed as a function of distance for three emitter temperatures. The calculated relative difference of near-field radiative conductance between the two configurations is plotted in Figure IV.22, for emitter temperatures of 450, 550 and 900 K. The spheres have slightly different diameters influencing radiative heat transfer. Also, the dielectric function of SiO_2 depends on temperature, while that of graphite was considered the same at all temperatures, potentially leading to thermal rectification (see Figure II.28).

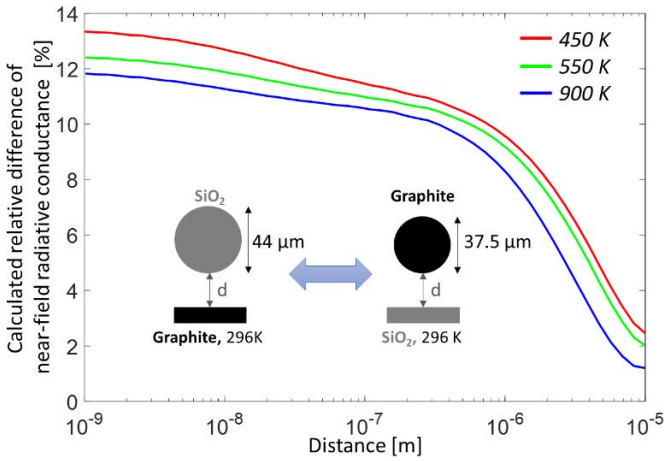

Figure IV.22: Calculated relative difference of near-field radiative conductance as a function of distance for three emitter temperatures, between SiO_2-graphite and graphite-SiO_2 configurations

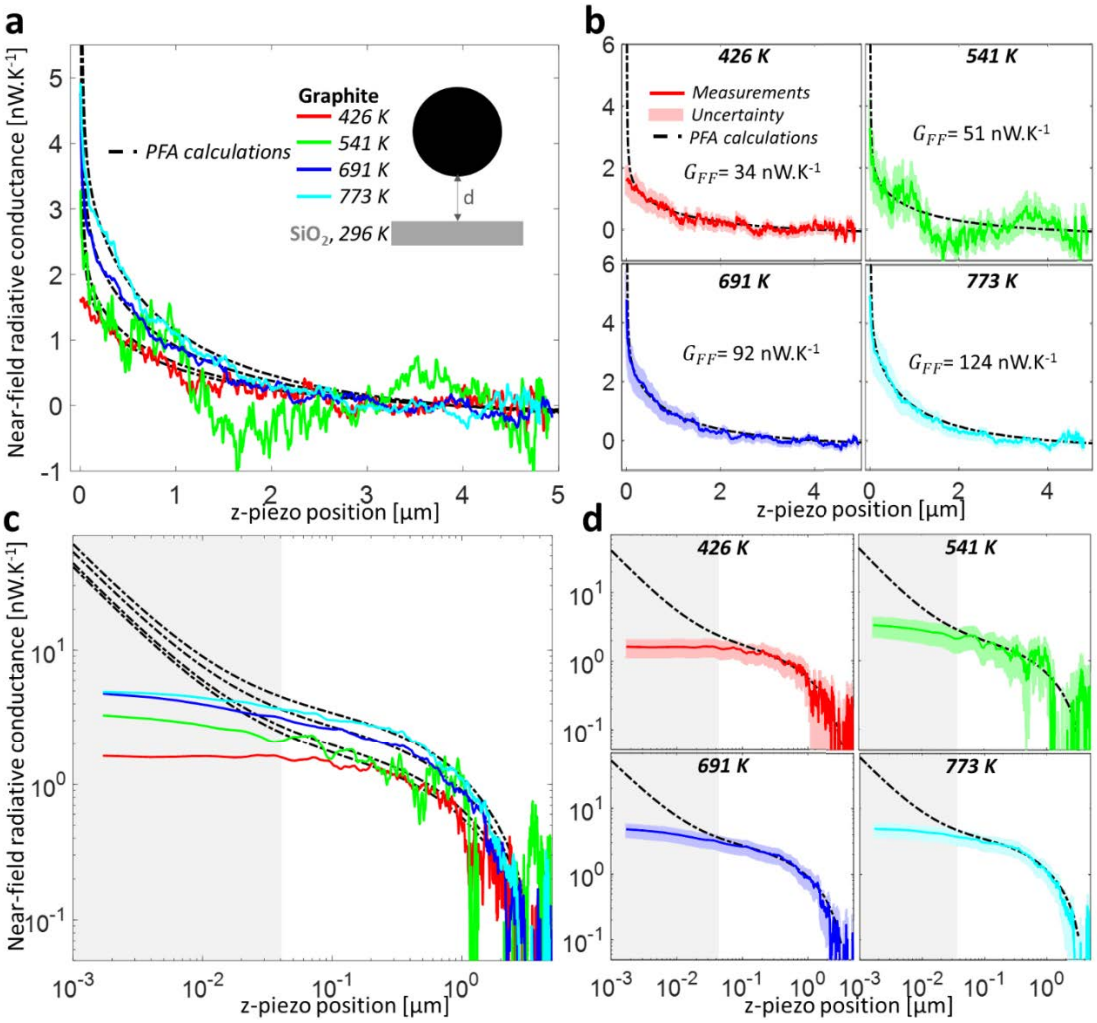

Figure IV.23: Near-field radiative conductance between a hot graphite sphere and a room temperature SiO_2 bulk flat substrate, as a function of z-piezo position and emitter temperature. (a) Linear scale. (b) Individual curves and their uncertainty with a linear scale. (c) Logarithmic scale. (d) Individual curves and their uncertainty with a logarithmic scale

The largest relative differences are found for distances below 1 µm and are of the order of 11 to 14 %, depending on emitter temperature. Larger emitter temperatures lead to smaller differences. A quantitative comparison of experimental data measured for the two configurations is therefore not possible. For this configuration and others involving a graphite emitter, the graphite sphere has a diameter of 37.5 µm.

Figure IV.23 shows near-field radiative conductance between a hot graphite sphere and a room temperature SiO_2 bulk flat substrate, as a function of z-piezo position for four different emitter temperatures. It is clearly seen that measurements performed at an emitter temperature of 541 K have a much higher random noise than measurements at other temperatures. Analysis of the 100 curves considered for averaging shows that the random noise is large for all curves. This may be explained by an isolated case of contamination of the emitter or the sample, since it is not seen for other temperatures. At low distances, the signal-to-noise ratio for the experiment at 541 K is still high enough to observe a clear evolution of near-field radiative conductance as a function of distance. From 426 to 773 K, the maximum conductance increases from ~ 2 to 5 $nW.K^{-1}$. However, the logarithmic scale plot (Figure IV.23c) shows that experimental data are levelling off at low distances, in the distance uncertainty area, while PFA calculations keep increasing. Even when conductance uncertainties are considered (Figure IV.23d), experimental measurements deviate from calculations for distances below 100 nm, due to the minimum distances.

Near-field radiative conductance experiments with adjusted d_{min} are presented in Figure IV.24. Values of d_{min} for experiments performed at an emitter temperature from 541 to 773 K are estimated between 23 and 33 nm. This distance range corresponds to the maximum height of irregularities of graphite spheres shown in Figure III.22. The curve at 426 K is best fitted to calculations with d_{min} = 103 nm. This value is twice the expected value considering all distance uncertainty effects for this configuration. Reasons of this large d_{min} may be the sphere or the sample polluted by a small particle, thus bringing the sphere into mechanical contact with the sample at distances larger than expected. This hypothesis may agree with the large random noise found on measurements performed at 541 K. Similarly to the SiO_2-InSb configuration, a high d_{min} is estimated in parallel with a high random electrical noise.

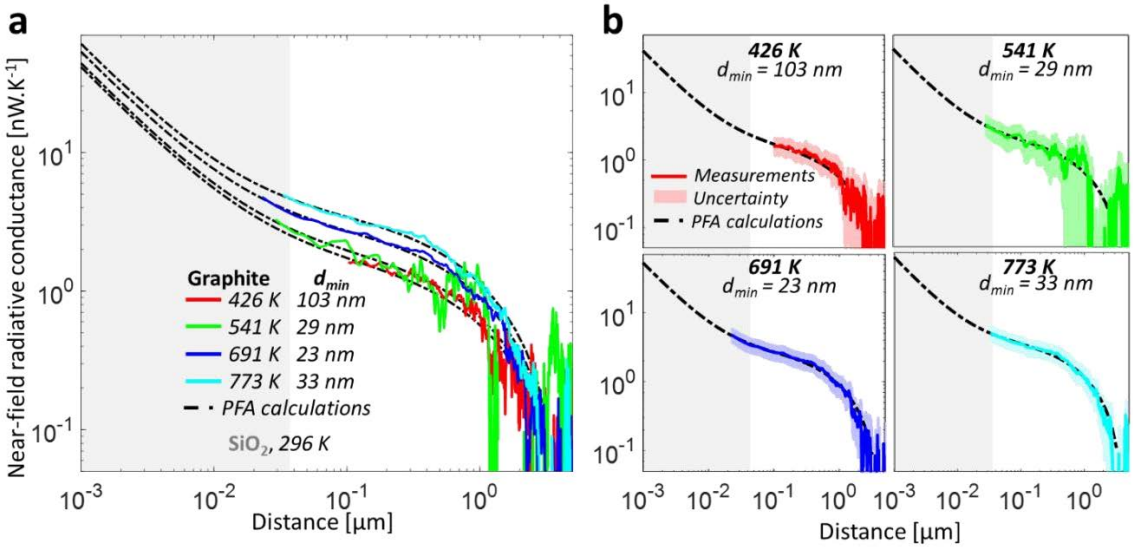

Figure IV.24: Near-field radiative conductance between a hot graphite sphere and a room temperature SiO_2 bulk flat substrate, as a function of distance and emitter temperature with adjusted minimum distances.
(a) Logarithmic scale. (b) Individual curves and their uncertainty with a logarithmic scale

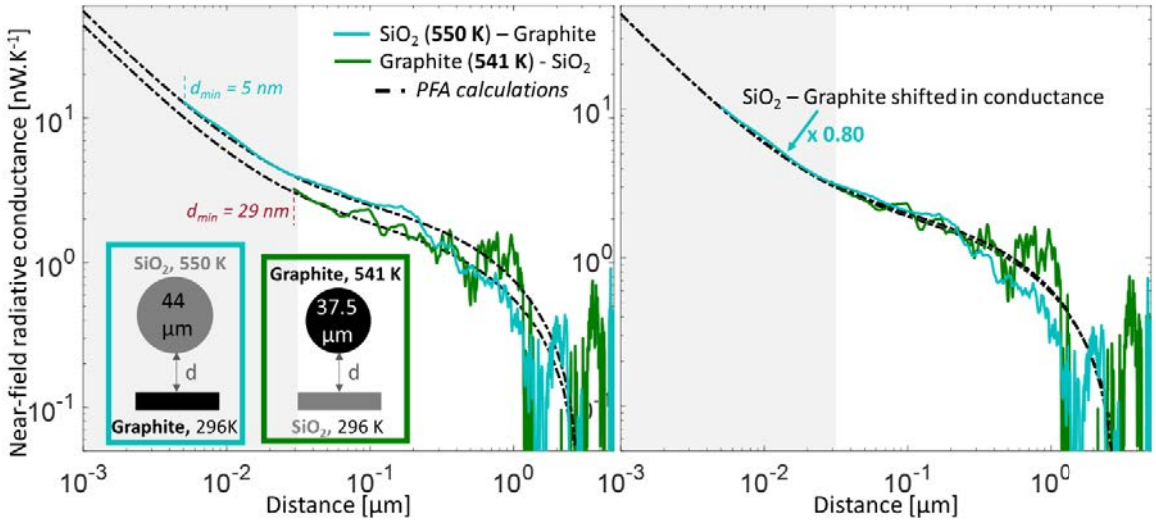

Figure IV.25: Comparison of near-field radiative conductance as a function of distance between SiO_2-graphite and graphite-SiO_2 configurations for similar temperatures

Pollution of the sphere may add heat transfer mechanisms between the sphere and the pollutant, leading to a fluctuating thermal signal. Another explanation may be higher vibrations than usual at the time when experiments were performed. Unfortunately, this second hypothesis cannot be verified because the vibrations measurements setup (optical fiber) was not included in the experimental setup when these graphite-SiO_2 measurements were performed.

Figure IV.25 compares SiO_2-graphite and graphite-SiO_2 configurations for experiments made at 550 and 541 K. These temperatures are chosen because they are the most similar available between the two configurations. As expected, differences appear between the two configurations. These differences are partly due to the difference of sphere diameters, and difference of emitter temperature between SiO_2-graphite and graphite-SiO_2 configurations. For instance, calculations presented in Figure IV.22 showed a relative difference of ~12 % when both emitters have a temperature of 550 K.

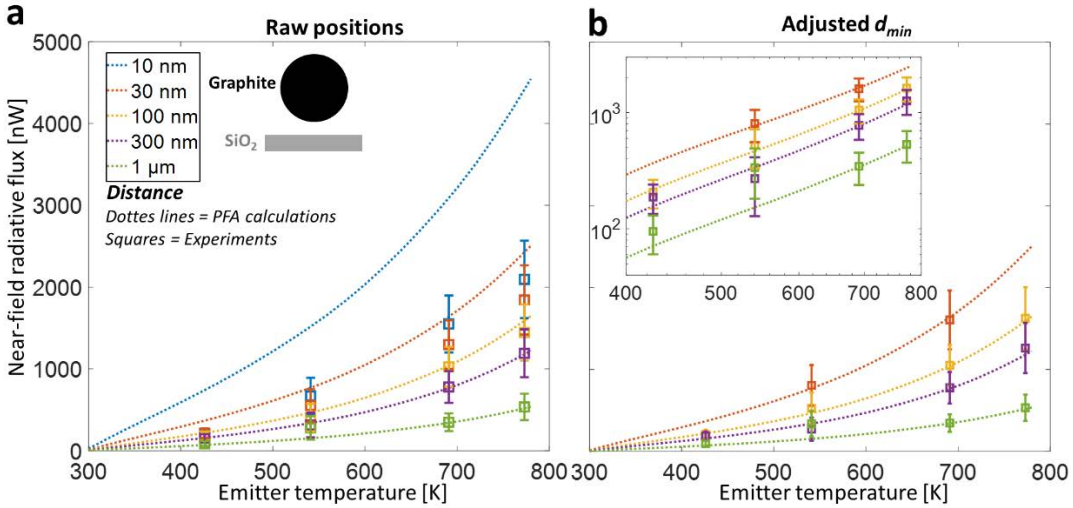

Figure IV.26: Near-field radiative heat flux between a hot graphite sphere and a room temperature SiO_2 bulk flat substrate, as a function of temperature for several distances.
(a) Experimental data with raw positions inferred from z-piezo position. (b) Experimental data with adjusted minimum distances.

Shifting one curve in conductance by 20% (Figure IV.25, right), corresponding to the relative difference of conductance calculated with PFA between the two configurations, leads to a good agreement over two orders of magnitude between measurements and calculations for the two configurations. This comparison proves that these two configurations provide very similar results as expected theoretically (see Sec. II.4.2.2).

Study of near-field radiative heat flux as a function of emitter temperature for different distances is provided in Figure IV.26. The effect of estimated large minimum distances is clearly observed comparing cases considering raw positions and adjusted d_{min}. In Figure IV.26a, there is a good agreement between experiments and calculations for distances above 100 nm, but large deviations for smaller distances. In Figure IV.26b, where adjusted d_{min} are taken into account, the curve at d = 10 nm is not represented because there is no experimental data available. The curve at d = 30 nm in made with only two experimental points, corresponding to experiments performed at 541 K (d_{min} = 29 nm) and 691 K (d_{min} = 23 nm).

Exponents of the temperature power law of near-field radiative exchanged heat flux are calculated as a function of distance considering raw positions and adjusted d_{min} (Figure IV.27a,b). Strong deviations between experimentally determined power law exponents and those calculated with PFA appear at distances below 40 nm. At this distance range, calculated exponents decrease from 2.78 to 2.29 while measured exponents increase from 2.9 to 3.7. These deviations completely disappear with adjusted d_{min}. In this case (Figure IV.27b), experimental values follow the same evolution as that predicted by PFA calculations, with an agreement from 29 nm to 600 nm considering uncertainties. We observe that when accounting for adjusted d_{min} the comparison between the measured temperature dependence of near-field radiative heat transfer and calculations appears favorable. As expected, the comparison with the inverse configuration (SiO_2-graphite) has demonstrated similar near-field radiative conductances. A comparison has been made considering the slight differences in sphere diameters and emitter temperatures between the two configurations. In addition, it has to be highlighted that doped-Si SThM cantilevers used as heater/thermometer were different for the two configurations and were both calibrated independently. The fact that experimental results are comparable between the two different configurations is therefore a proof of the reliability of the calibration and measurement process.

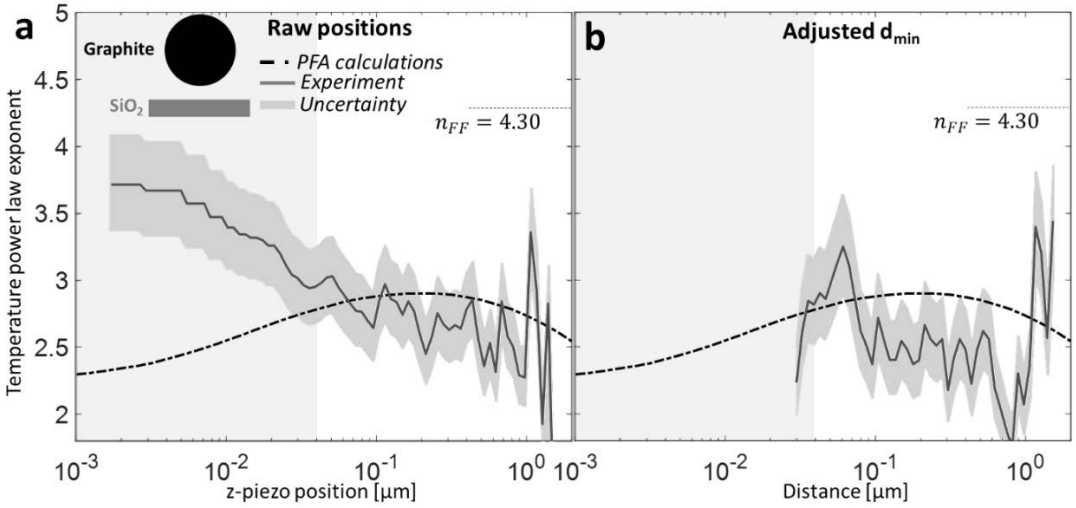

Figure IV.27: Temperature power law exponent as a function of distance between a graphite sphere, from 426 to 773 K, and a room temperature SiO_2 bulk flat sample.
(a) Experimental data with raw positions inferred from z-piezo position. (b) Experimental data with adjusted minimum distances.

IV.3.7 Graphite-Graphite

The symmetrical graphite-graphite configuration was studied with high emitter temperatures up to 1200 K. The limit temperature corresponds to the sensitivity limit of the emitter. As explained in Sec. III.2.3, the temperature coefficient α (in absolute values) of the emitter decreases above the temperature of maximum electrical resistance T_{Rmax} (~732 K). Above 1400 K, α tends to 0 implying that measurements of temperature variations become very challenging.

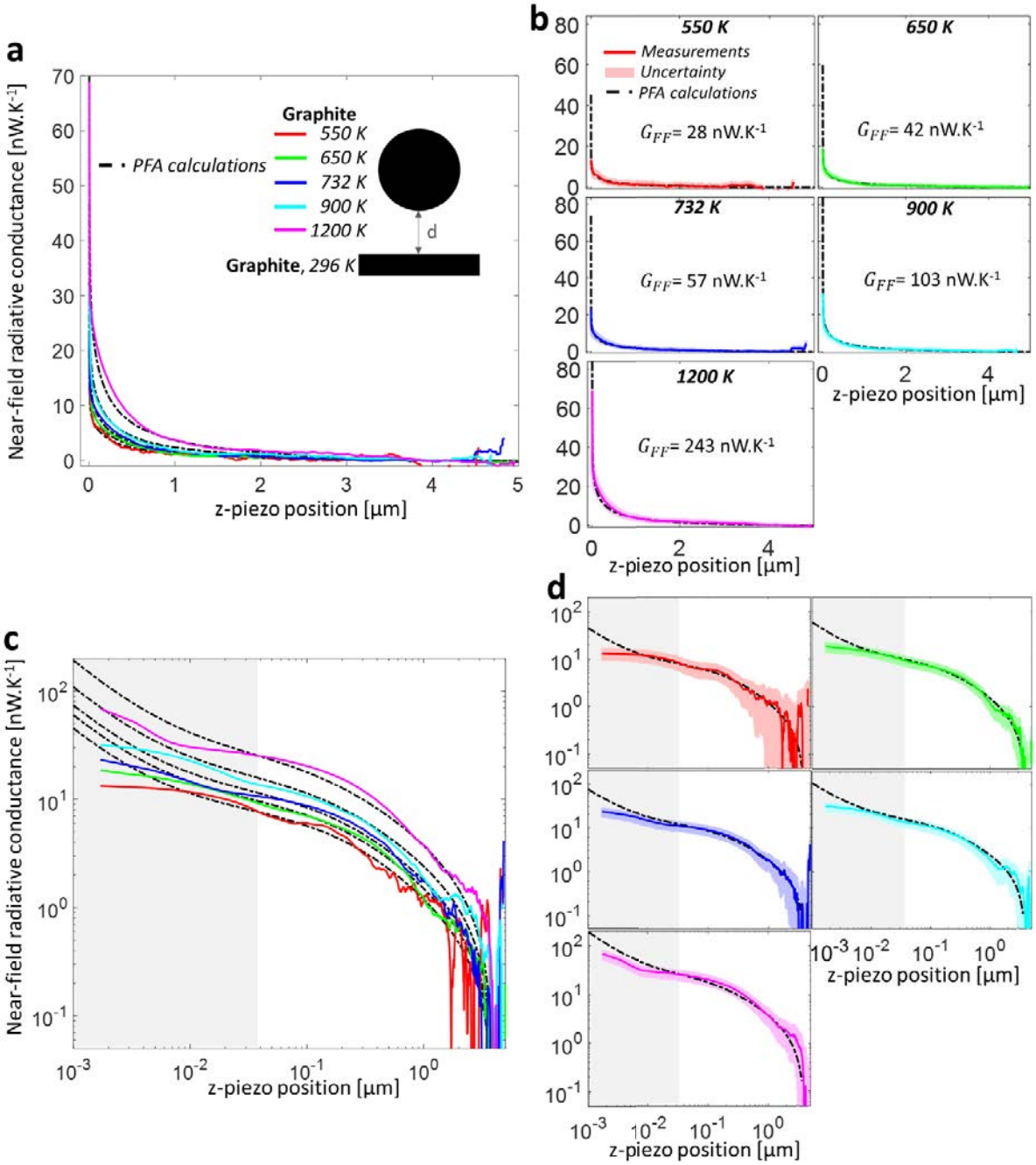

Figure IV.28: Near-field radiative conductance between a hot graphite sphere and a room temperature graphite bulk flat substrate, as a function of z-piezo position and emitter temperature. (a) Linear scale. (b) Individual curves and their uncertainty with a linear scale. (c) Logarithmic scale. (d) Individual curves and their uncertainty with a logarithmic scale

Figure IV.28 shows near-field radiative conductance between a hot graphite sphere and a room temperature graphite bulk flat substrate, as a function of z-piezo position for five different emitter temperatures from 550 to 1200 K. High temperature differences, over 900 K, are achieved during these experiments. Such large temperature differences are expected to result in large radiative heat transfer with great signal-to-noise ratio. In Figure IV.28a,b, the increase of near-field radiative conductance is clearly observed close to contact, from 550 to 1200 K, rising from ~ 15 to 70 nW.K^{-1}. These values are still lower than those calculated in the far field. There is also a good agreement between experimental measurements and PFA calculations. In Figure IV.28c, experimental values tend to level off in the last nanometers when raw positions are considered, except at 1200 K. For all temperatures, experimental data agree with theory considering measurement uncertainties. The curve at 550 K (Figure IV.28d) has a larger random noise compared to measurements at the other temperatures, inducing large uncertainties for distances above 1 µm. Levelling off of experimental data in the last nanometers can be corrected by adjusting the minimum distance.

In Figure IV.29, d_{min} is adjusted for each curve. The adjustment gives values estimated to be ranging from 5 to 8 nm, similar to those from the graphite-InSb case (Figure IV.33). With adjusted d_{min}, it is seen on the logarithmic scale plot that experimental values do not level off at low distances and follow better theoretical calculations from PFA.

Near-field radiative heat flux is shown in Figure IV.30 as a function of emitter temperature for six distances ranging from 10 nm to 1 µm, considering either raw positions (Figure IV.30a) or adjusted d_{min} (Figure IV.30b). Considering raw positions, experimental data agree well with calculations, except for d = 10 nm at 1200 K.

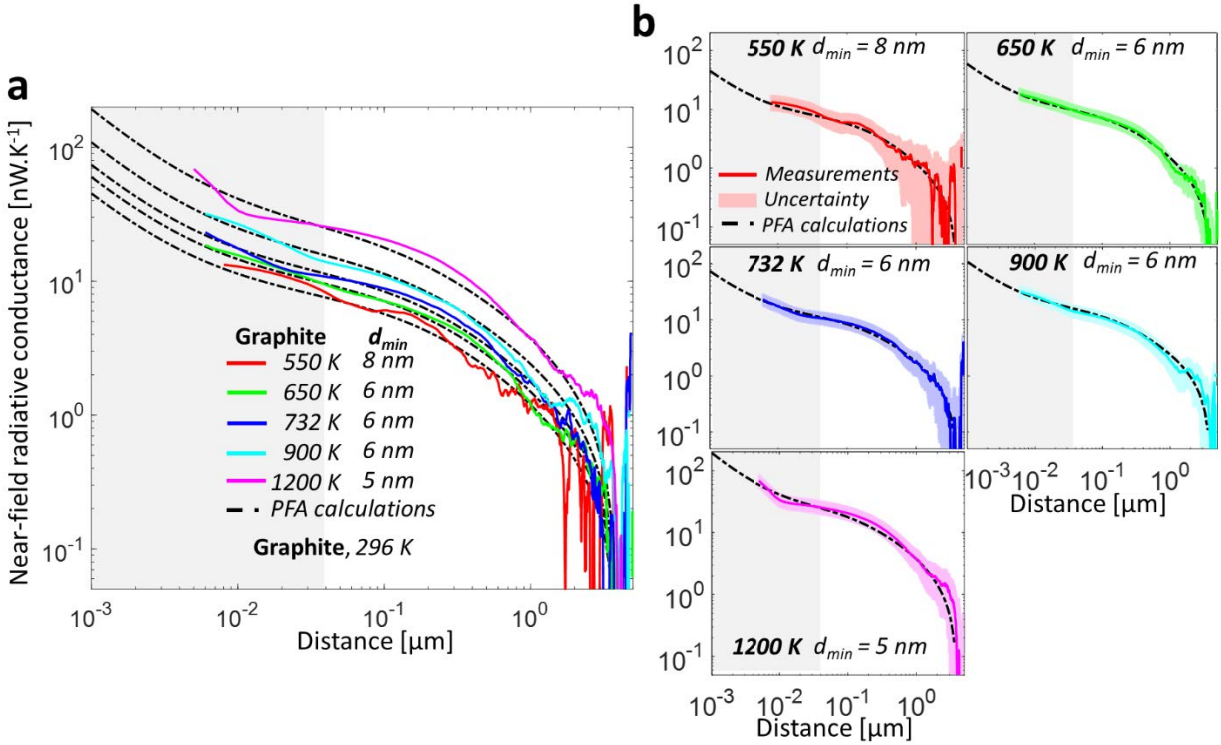

Figure IV.29: Near-field radiative conductance between a hot graphite sphere and a room temperature graphite bulk flat substrate, as a function of distance and emitter temperature with adjusted minimum distances.
(a) Logarithmic scale. (b) Individual curves and their uncertainty with a logarithmic scale

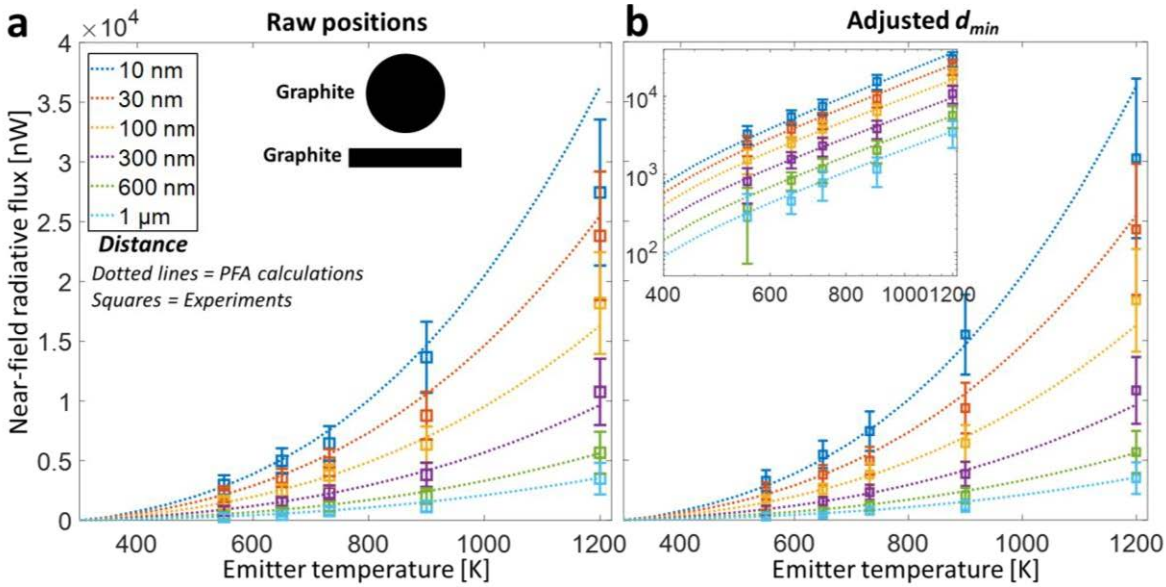

Figure IV.30: Near-field radiative heat flux between a hot graphite sphere and a room temperature graphite bulk flat substrate, as a function of temperature for several distances.
(a) Experimental data with raw positions inferred from z-piezo position. (b) Experimental data with adjusted minimum distances.

The inset in Figure IV.30b is a logarithmic scale plot of the data showing similarities in the temperature dependence of radiative heat transfer between experiments and calculations.
The exponent of the temperature power law is represented in Figure IV.31 as a function of distance for raw positions (Figure IV.31a) and for adjusted d_{min} (Figure IV.31b). Despite large variations in the experimentally determined exponents, the evolution as a function of distance follows the same trend as that predicted by calculations.

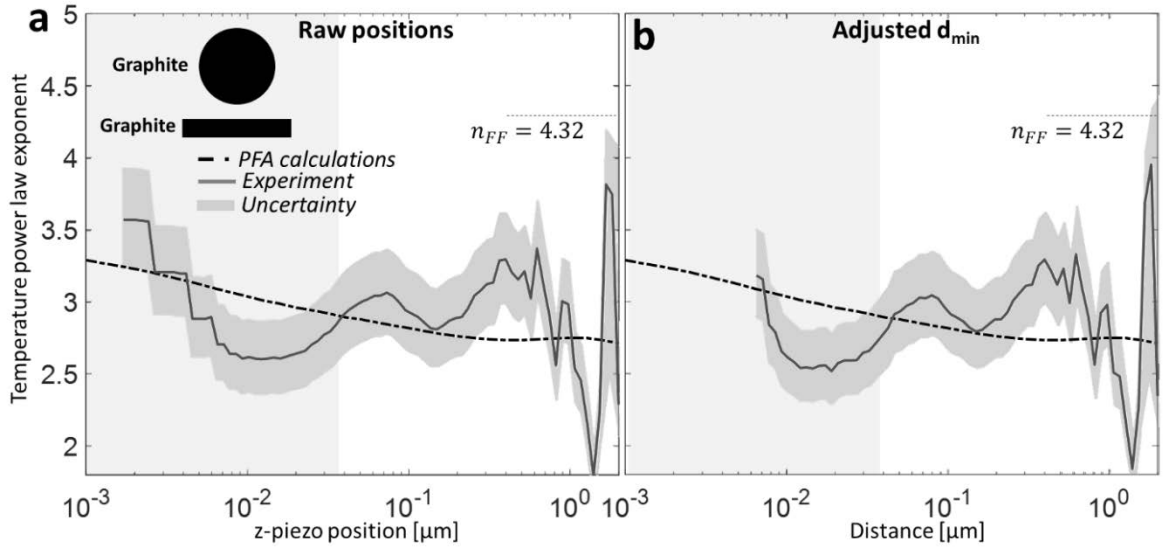

Figure IV.31: Temperature power law exponent as a function of distance between a graphite sphere, from 550 to 1200 K, and a room temperature graphite bulk flat sample.
(a) Experimental data with raw positions inferred from z-piezo position. (b) Experimental data with adjusted minimum distances.

Lower deviations from PFA calculations at small distances are found with adjusted d_{min}. The agreement with calculations is found up to a relatively large distance $d \sim 1.3$ µm. This may be due to the large temperature difference providing a high signal-to-noise ratio.
The original study of the symmetrical graphite-graphite configuration shows a good agreement with calculations. Large temperature differences up to 900 K lead to near-field radiative heat fluxes up to 30 µW.

IV.3.8 Graphite-InSb

Measurements presented in this section include experiments performed with a room temperature InSb substrate, in addition to experiments with a cooled InSb TPV cell.

IV.3.8.1 Room-temperature substrate

Experiments were performed with an emitter temperature from 456 K to 744 K.

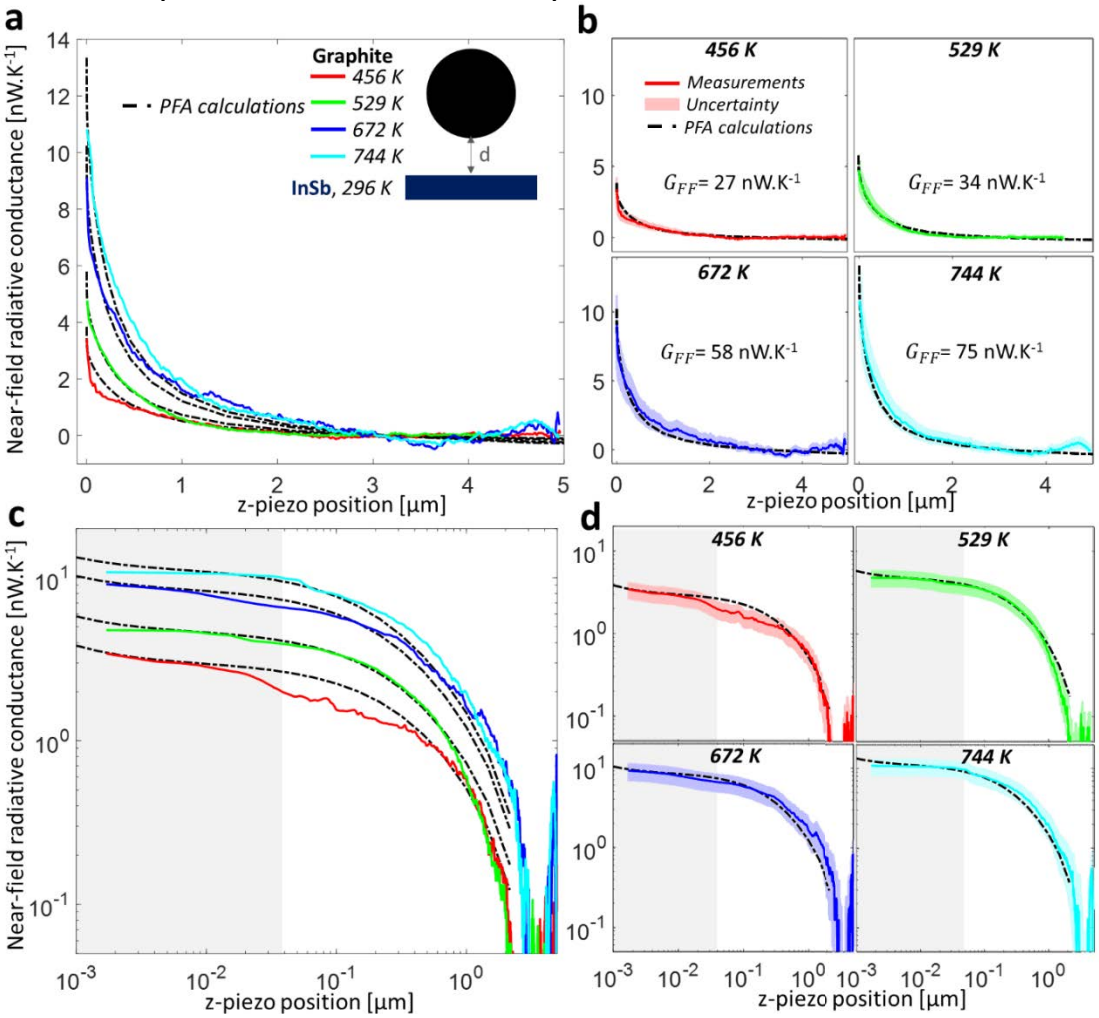

Figure IV.32: Measured and calculated near-field radiative conductance between a hot 37.5 µm diameter graphite sphere and a room temperature InSb bulk flat substrate, as a function of z-piezo position and emitter temperature.
(a) Linear scale. (b) Individual curves and their uncertainty with a linear scale. (c) Logarithmic scale. (d) Individual curves and their uncertainty with a logarithmic scale

The emitter temperature is limited by the melting temperature of InSb, which is 800 K. To avoid damaging the emitter at the contact with the substrate, or evaporating InSb into the vacuum chamber, the emitter temperature was therefore kept under 750 K. The InSb sample is a non-intentionally n-doped ($N_D \sim 10^{15}$ cm^{-3}) flat bulk substrate.

Figure IV.32 shows the measured and calculated near-field radiative conductances between a 37.5 µm diameter graphite sphere and a room temperature InSb bulk flat substrate, as a function of z-piezo position and emitter temperature. Linear plot of near-field radiative conductance is shown in Figure IV.32a,b. Considering uncertainties, experimental curves agree well with PFA calculations for all temperatures. The effect of temperature when the emitter varies from 456 to 744 K is clearly observed, as the conductance close to contact increases from 3 to 11 nW.K^{-1}. It is interesting to focus on small distances where PFA is more accurate than at micrometer-scale[83], as shown in Sec. II.3.2. In Figure IV.32c, near-field radiative conductance tends to level off at low distances as calculated. It is reminded that conductance levels off due to the very small contribution of surface modes on radiative heat transfer between graphite and InSb. At distances above 2 µm, experimental data appear very fluctuating because of the random electrical noise. The smaller the distance, the higher the signal-to-noise ratio. In general, experimental curves have the same evolution as that predicted by PFA, and quantitatively agree considering uncertainties (Figure IV.32d).

Figure IV.33 shows measurements performed during this work with adjusted minimum distances, independently for each temperature. Resulting d_{min} are estimated to be ranging from 2 to 8 nm depending on emitter temperature, but without apparent correlation to temperature. Regarding both graphite-InSb and graphite-graphite configurations, temperature does not seem to have an influence on the estimation of d_{min}. These values correspond to the vibrations and measured R_{RMS} roughness of the graphite spheres but are one order of magnitude lower than the maximum height of irregularities of spheres (~30 nm, see Sec. III.4.2.1). Low estimated d_{min} may be explained by a contact area flatter than expected between the graphite sphere and the substrate.

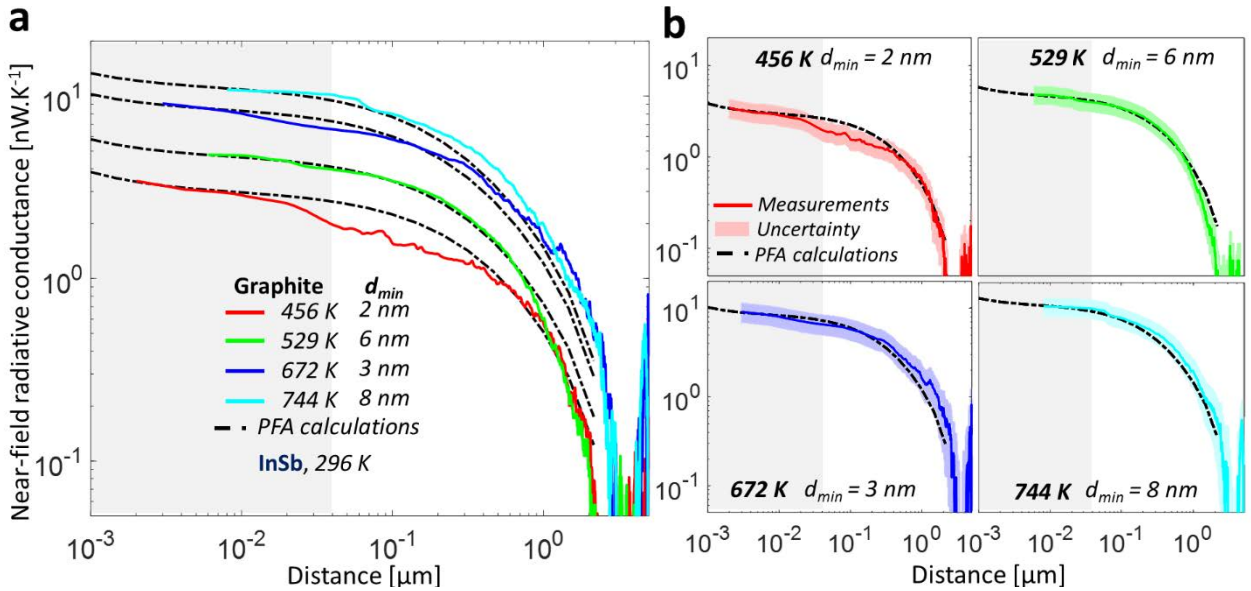

Figure IV.33: Near-field radiative conductance between a hot graphite sphere and a room temperature InSb bulk flat substrate, as a function of distance and emitter temperature with adjusted minimum distances.
(a) Logarithmic scale. (b) Individual curves and their uncertainty with a logarithmic scale

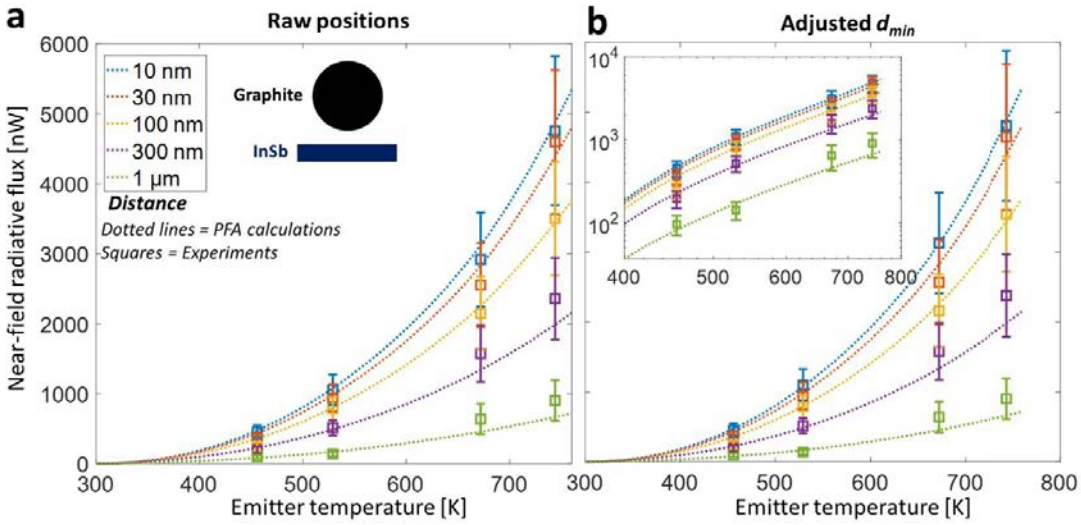

Figure IV.34: Near-field radiative heat flux between a hot graphite sphere and a room temperature InSb bulk flat substrate, as a function of temperature for several distances. (a) Experimental data with raw positions inferred from z-piezo position. (b) Experimental data with adjusted minimum distances.

Some irregularities of the graphite sphere may have been reduced during the contact due to the force applied on the sphere. In order to be confirmed, such hypothesis would require additional post-experiment characterizations of the sphere, with SEM images or AFM topography images.
Temperature dependence of near-field radiative heat transfer is studied by plotting the exchanged radiative heat flux as a function of emitter temperature for several emitter-sample distances (Figure IV.34). Considering measurement uncertainties, evolution of near-field radiative heat flux as a function of temperature agrees well with that predicted by theoretical calculations. The inset shows data plotted in logarithmic scale. For the selected distances, experimental data are in good agreement with calculations.

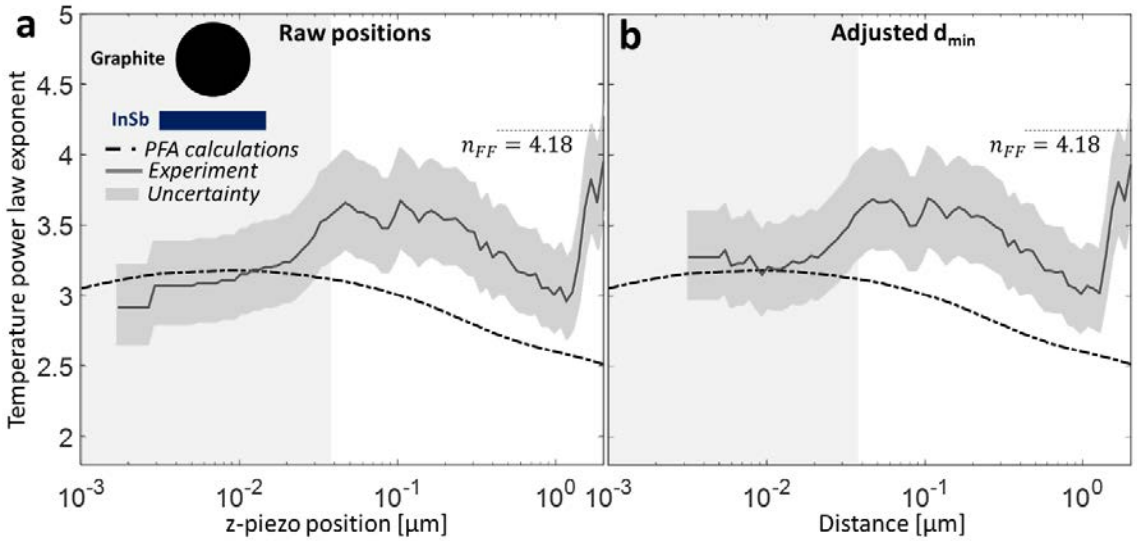

Figure IV.35: Temperature power law exponent as a function of distance between a graphite sphere, from 456 to 744 K, and a room temperature InSb bulk flat sample.
(a) Experimental data with raw positions inferred from z-piezo position. (b) Experimental data with adjusted minimum distances.

Figure IV.35 shows the exponent of the temperature power law of the radiative conductance as a function of distance, considering raw distances (Figure IV.35a), and adjusted d_{min} (Figure IV.35b). Considering uncertainties, adjusting the minimum distances does not provide a better agreement of the measurements with the calculations. The experimentally measured exponents seem to be larger than those predicted for distances above 40 nm but follow a similar evolution as a function of distance. In Figure IV.35a, the experimental exponent has a decreasing behavior between 300 and 3 nm, which is different from that of the calculations where the exponent is almost stable. Taking adjusted d_{min} into account gives a slightly more stable evolution of the experimentally determined exponent. Above 1 µm, large deviations appear between experiments and calculations. These deviations are due to low signal-to-noise ratio. Qualitative comparisons can be made between SiO_2 and graphite emitters paired with an InSb substrate.
In Figure IV.36, near-field radiative conductance as a function of distance is compared between the two different emitter materials, for similar temperatures of 450 and 456 K. Evolution as distance decreases is different, with a faster increase for the graphite emitter.

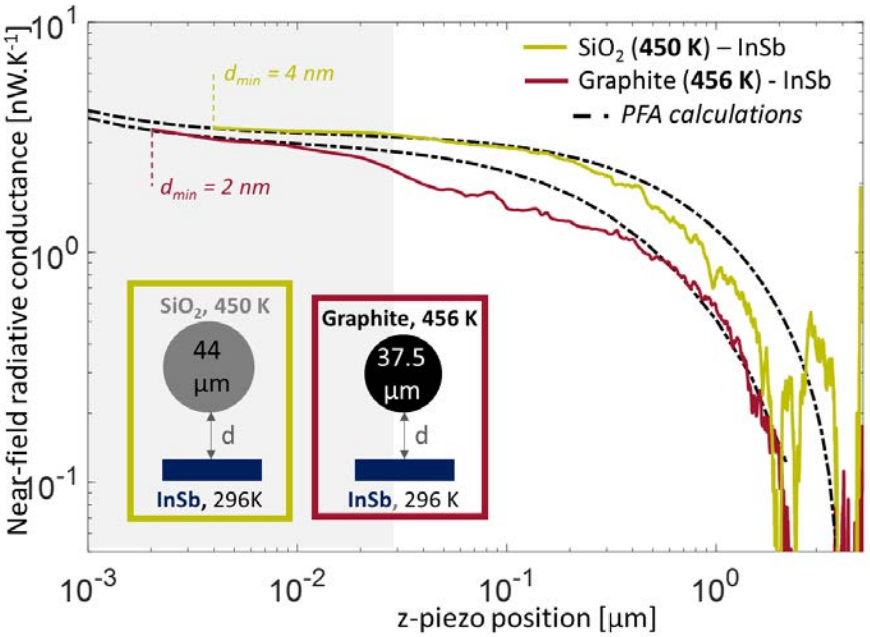

Figure IV.36: Comparison of near-field radiative conductance as a function of z-piezo position between SiO_2-InSb and graphite-InSb configurations for similar temperatures

IV.3.8.2 Cooled InSb TPV cell substrate

Here, InSb cells are cooled down to 77 K while a graphite spherical emitter is heated up to 900 K. Figure IV.37 shows measurements of near-field radiative conductance between a heated graphite sphere and a 77 K InSb TPV cell. For these experiments, emitter temperatures are ranging from 732 to 900 K. Experiments performed with an emitter temperature of 900 K did not damage the cell. This may be explained by the contact resistance between the sphere and the cell, limiting heat transfer via conduction, thus preventing overheating of the cell. Measurements with an emitter temperature of 1200 K were attempted but the cell was damaged.

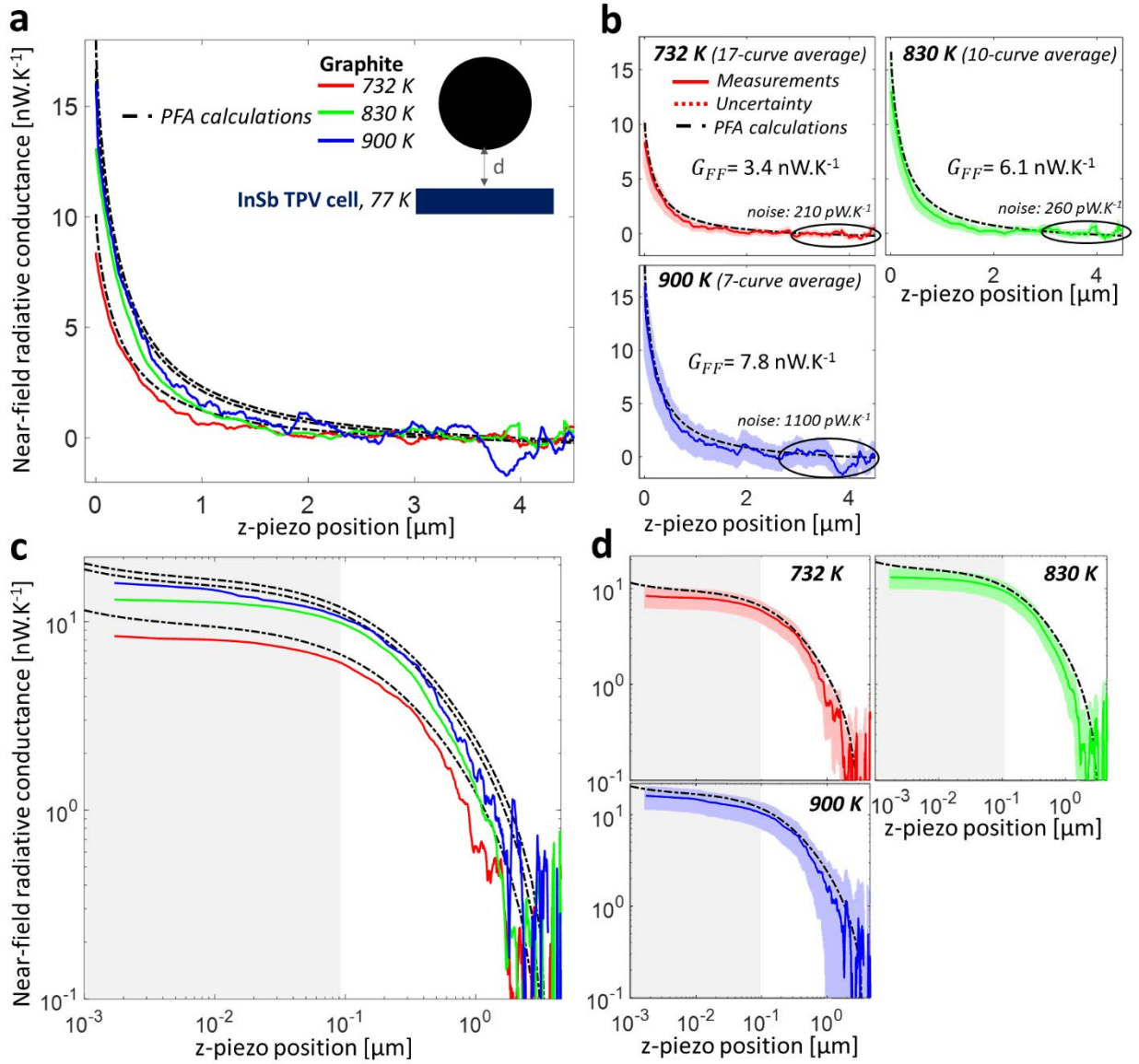

Figure IV.37: Measured and calculated near-field radiative conductance between a hot 37.5 µm diameter graphite sphere and a 20 µm in diameter InSb TPV cell cooled down to 77 K, as a function of z-piezo position for three emitter temperatures.
(a) Linear scale. (b) Individual curves and their uncertainty with a linear scale. (c) Logarithmic scale. (d) Individual curves and their uncertainty with a logarithmic scale

Because of technical issues caused by the cooling system (see Sec. III.3.2.2), less than the usual 100 curves were measured before averaging. For instance, averaged curves shown in the figure are considering 17, 10 and 7 curves for the experiments at 732, 830 and 900 K respectively. The effect is seen as a large random noise on near-field conductance measurements. In the logarithmic scale plot, experimental values level off at low distances. Compared to the InSb substrate at room temperature (Figure IV.32), deviations from calculations due to the levelling off are more important. These deviations are expected because of large mechanical vibrations induced by the cooling system. Maximum amplitude of the vibrations were measured at ± 83 nm around the mean position. As a result, minimum reached distances are expected to be larger with a cooled substrate

than with a room temperature one. For calculations, the dielectric function of the InSb TPV cell was calculated at 77 K considering a p-doping level of 10^{18} cm^{-3}, and an n-doping level of 10^{15} cm^{-3}. Since the diameter of the sphere (37.5 µm) is larger than that of the cell (20 µm), PFA calculations are performed considering a maximum radius $r = R_{cell}$ (see chapter II, Figure II.12a). Also, the small size of the cell lowers the far-field radiative conductance, as expected theoretically (Figure II.29). These experiments are the only ones exhibiting near-field conductances larger than those calculated in the far field.

Figure IV.38 shows experimental measurements for a cooled InSb TPV cell substrate with adjusted minimum distances. As expected, d_{min} is estimated between 35 and 53 nm, which is one order of magnitude larger than the case with a room temperature InSb substrate.

In general, the experimental study of the configuration of a graphite emitter paired with an InSb substrate resulted in a good agreement with theoretical predictions. Radiative heat fluxes were measured for different emitter and substrate temperatures and reached values larger than ten microwatts. For the low substrate temperature case, the minimum reached distance is estimated to be much larger than that with a bulk substrate, due to vibrations from the cooling system. However, emitter temperatures higher than the melting temperature of InSb were reached

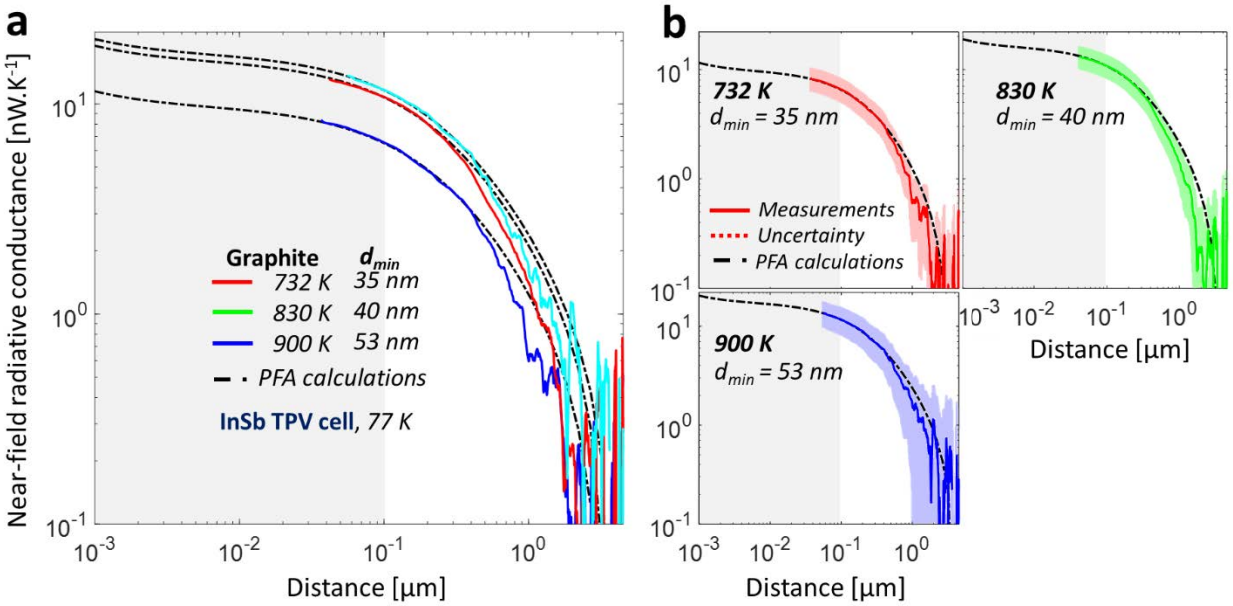

Figure IV.38: Near-field radiative conductance between a hot graphite sphere and a cooled InSb TPV cell, as a function of distance and emitter temperature with adjusted minimum distances. (a) Logarithmic scale. (b) Individual curves and their uncertainty with a logarithmic scale

IV.3.9 Summary of main results

Investigation of near-field radiative heat transfer has been made for six different emitter-substrate pairs of materials. For each configuration, a summary of maximum emitter-substrate temperature difference, mean estimated minimum distance and maximum measured near-field radiative conductance is presented in *Table IV.1*. In general, smaller distances are reached with the graphite sphere than with the SiO_2 one. In addition, a large d_{min} induces a smaller measured maximum conductance. At contact, a force is applied on the sphere, which may induce friction and crushing of irregularities on the surface of the sphere, resulting in a flattened area.

Table IV.1: Main results from the different material configurations

Configuration	ΔT_{max} [K]	Mean estimated d_{min} [nm]	Maximum G_{NF} [nW.K-1]	Temperature power law exponent of the near-field radiative conductance: Measured d = 100 nm	PFA d = 100 nm	Far-field
Graphite-InSb (296 K)	448	5	10.8 ± 2.1	3.58 ± 0.34	3.01	4.18
Graphite-InSb cell (77 K)	823	43	17.1 ± 3.8		-	
Graphite-Graphite	904	6	68.9 ± 13.7	2.91 ± 0.29	2.82	4.32
Graphite-SiO_2	477	47	4.9 ± 1.0	2.71 ± 0.31	2.88	4.30
SiO_2-Graphite	904	13	16.7 ± 3.3	2.78 ± 0.27	2.89	4.30
SiO_2-InSb (296 K)	904	56	7.6 ± 2.1	2.58 ± 0.22	2.61	4.07
SiO_2-InSb (77 K)	655	-	5.9 ± 2.4		-	
SiO_2-SiO_2 (296 K)	493	*80**	7.4 ± 1.5	4.11 ± 0.33	2.46	4.15
SiO_2-SiO_2 (77 K)	570	*65**	10.5 ± 3.8		-	

Graphite is less resistant to compression than SiO_2 with respective bulk moduli of 2.3-15 and 33.5-36.8 GPa. Therefore, the surface of the graphite sphere was probably more flattened than the surface of the SiO_2 sphere after multiple contacts with a substrate. It is reminded that the values of d_{min} should not be considered quantitatively and may be strongly impacted by the probable inaccuracy of PFA calculations. In addition, theoretical calculations may be affected by the temperature dependence of the optical properties of the materials that were considered only for SiO_2 for which the data were available, and were considered at 300 K for the other materials.

The highest measured near-field radiative conductance is found for the symmetrical graphite-graphite configuration. In this case, both large temperature differences and small distances lead to high near-field radiative conductances. The experiments for the symmetrical configuration with SiO_2 as emitter and substrate do not quantitatively agree with calculations when the substrate is at room temperature. This disagreement is probably due to differences in dielectric functions between SiO_2 spheres and the substrate. This implies that PFA calculations and estimations of the minimum distance are impacted (represented by an asterisk symbol in the table). The cryogenic cooling system allows to investigate high temperature differences by lowering the temperature of the substrate. However, large mechanical vibrations are limiting the minimum achievable emitter-substrate distance. A larger random electrical noise was also observed during the experiments with a cooled substrate. Globally, this study has demonstrated a good agreement between experimental measurements and calculations of near-field radiative conductance, both as a function of distance and temperature.

Temperature dependence was investigated for each pair of materials. Exponents of the temperature power law of the near-field radiative conductance were deduced from measurements and were quantitatively compared to those from PFA calculations. It is interesting to remark that for the inverse graphite-SiO_2 and SiO_2-configurarions, the maximum measured conductances are very

different because these values may be affected by the differences of minimum distances reached for these two configurations.

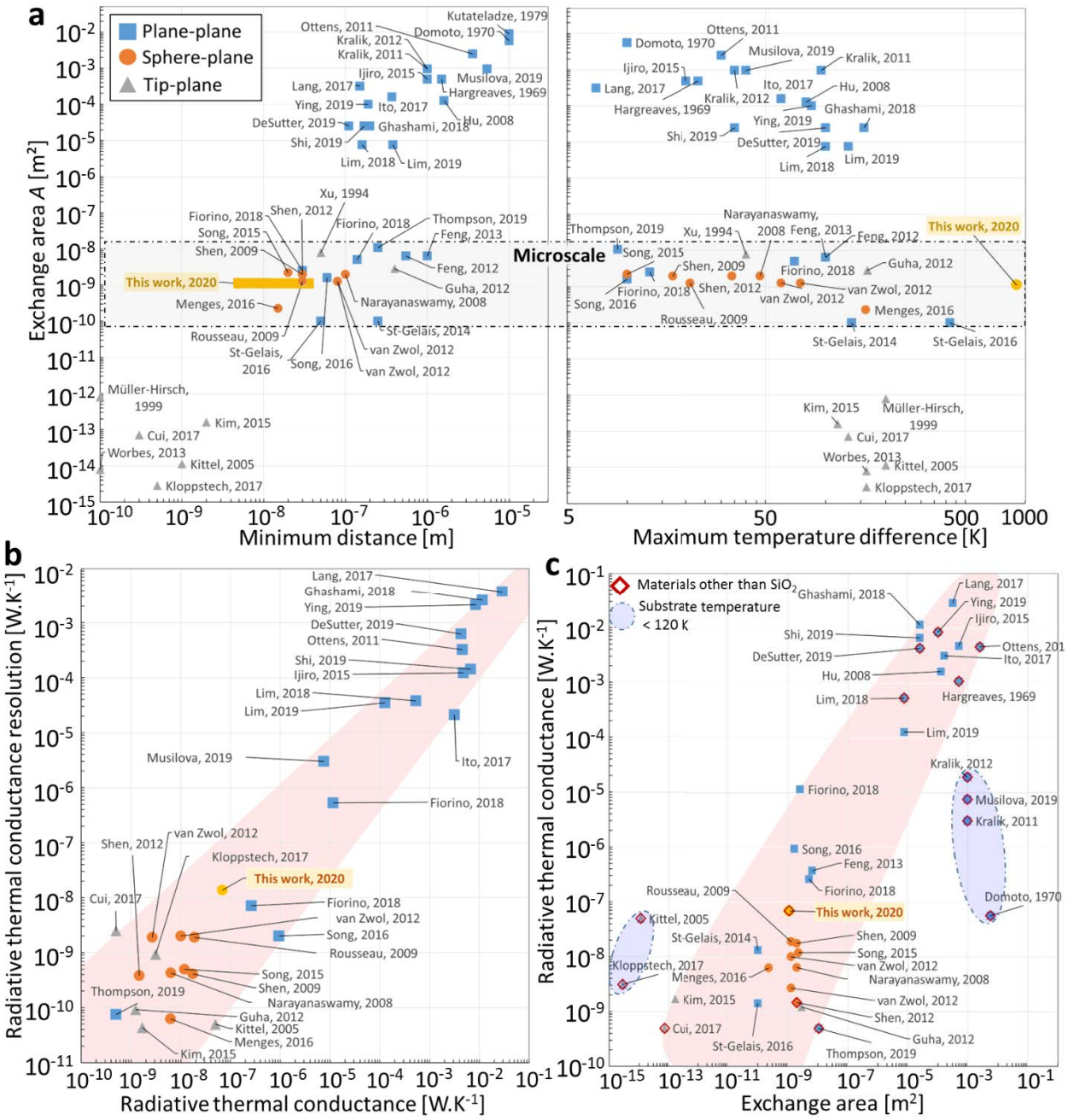

Figure IV.39: Comparison of the performances measured during this work compared to those reported in published experimental works.
(a) Exchange area as a function of minimum distance and maximum temperature difference. (b) Radiative thermal conductance resolution as a function of measured radiative thermal conductance. (c) Measured radiative thermal conductance as a function of exchange area. Experimental works studying materials other than SiO_2 are highlighted with diamond-shaped markers, while substrate temperature below 120 K are underlined with blue areas.

However, studying the temperature dependence with adjusted d_{min} leads as expected to comparable exponents of the near-field conductance temperature power law of 2.71 ± 0.31 and 2.78 ± 0.27 respectively. Unfortunately the uncertainty on these measurement is too large for concluding on an observation or not of any thermal rectification effects.
In Figure IV.39, the performances are compared to those from published experimental works. This work proves that using a SThM probes as the heater and temperature sensor allows studying large temperature differences up to 900 K. Considering the minimum distances, they were estimated in this work by comparing the measurements with PFA calculations but not directly measured. Therefore, the minimum distances are shown ranging from a few nanometers up to 40 nm corresponding to the result of the analysis reported in Sec. III.4.2. The highest temperature difference is reached considering all published experimental works. In terms of radiative thermal conduction resolution, it is seen in Figure IV.39b that the performances reached during this work follow the general trend considering the radiative conductance levels that were measured. In Figure IV.39c the maximum near-field radiative conductance measured during this work appears to be the highest among all experiments based on the sphere-plane configuration for similar exchange areas. In addition, this work differs from other works studying the sphere-plane configuration because the best results were obtained while investigating materials other than SiO_2.

IV.4 Conclusion

Near-field radiative heat transfer measurements for various material configurations have been presented. Spheres made of SiO_2 and graphite, as well as doped-Si SThM tips have been used as thermal infrared emitters. In terms of near-field radiative conductance, the highest value of 68.9 $nW.K^{-1}$ is measured for the graphite-graphite configuration, where high temperature differences over 900 K and low distances down to a few nanometers have been reached. In general, good agreements have been found between experimental measurements and PFA calculations for the sphere-plane geometry. Strongest deviations from theory have been observed with SiO_2-SiO_2 configurations and may be explained by uncertainties on the composition of SiO_2 spheres. However, large temperature differences between the emitter and the substrate tend to lower deviations between measurements and calculations. For instance, calculations agree with experimental measurements, considering uncertainties, with the SiO_2 substrate cooled at 77 K. Experiments with cooled substrates have shown that the cooling system has an impact on the accuracy of conductance measurements. Using the cooling system increases significantly the random electrical noise, due to high vibrations. It also makes near-field radiative measurements more challenging, thus limiting the number of measurements.
PFA calculations failed to match with measurements performed for the tip-plane geometry. In this configuration, low near-field radiative conductance of ~200 $pW.K^{-1}$ has been observed, being one to two orders of magnitude lower than measurements with a spherical emitter. The enhancement of conductance also occurs at a smaller distance range compared to the sphere-plane geometry, in the lasts 100-200 nm before contact. For a better comparison with theoretical calculations, material and temperature dependence of near-field radiative heat transfer for the tip-plane geometry should be investigated.
Measurements for the sphere-plane configuration at different emitter temperatures have indicated that the temperature dependence of near-field radiative heat transfer is different from one material configuration to another considering only the contribution of evanescent waves. In the far field, radiative heat transfer occurs with the contribution of propagative waves and follow a temperature power law with an exponent of 4 in the case of a blackbody, and an apparent exponent above 4 for

the studied material configurations (see Sec. II.4.2.1). The exponents measured during this work are significantly below those expected in the far field and account for the contribution of evanescent waves. As distance between the emitter and the substrate decreases, the exponent of the temperature power law of the near-field radiative heat flux varies. A decreasing behavior of the exponent is observed experimentally for distances below ~1 µm for all material configurations except for the graphite-graphite and graphite-InSb ones where the measurements have shown as expected a slightly increasing and almost stable exponent respectively.

In this chapter, we have demonstrated the ability of the experimental setup to perform measurements with hot spherical emitters up to 1200 K. Such a high temperature is well suited for thermophotovoltaic applications. The next experimental step, detailed in chapter VI, consists in using a cooled TPV cell as the substrate in order to simultaneously measure near-field radiative heat transfer and generated electrical power as a function of emitter-cell distance.

PART II – NEAR-FIELD THERMOPHOTOVOLTAICS

Chapter V

V Fundamentals of photovoltaics and thermophotovoltaic experimental works

V.1 Introduction

Photovoltaics (PV) is the conversion of electromagnetic radiation power into electrical power. If the converted radiation is thermal radiation of bodies on Earth then it is referred to as thermophotovoltaics (TPV). Devices converting thermal photons into electricity are TPV cells, and differ from conventional solar PV cells in terms of materials. Photons converted by TPV cells are in the infrared wavelength range and have a lower energy compared to photons in the visible range harvested in solar PV. Therefore, low-energy bandgap semiconductors are required for TPV cells in order to convert infrared radiation into electrical power.
In this chapter, some energy harvesting techniques are presented and compared, then basics of the photovoltaic effect are reminded highlighting the photon conversion mechanisms. A focus is done on low-energy bandgap semiconductors suitable for TPV applications. A state of the art of experimental TPV conversion devices is established, considering classical far-field illumination and recently investigated near-field illumination. The objective is to find parameters to optimize in order to design a near-field TPV device with improved performances.

V.2 Energy harvesting

Energy harvesting refers to the conversion of ambient energy from the environment into electrical energy[101]. The main energy sources are kinetic, thermal and solar energy. For instance, kinetic energy such as vibration, pressure and stress-strain can be converted using piezoelectric devices[102]. Solar energy is abundant and provided by the sun with an average irradiation level[103] of ~1 $kW.m^{-2}$. It can be converted into thermal energy by using solar thermal devices absorbing solar radiation and converting it into heat[104]. Sunlight energy can also be converted into electrical energy via the photovoltaic effect where efficiencies up to 25 % are usually achieved using poly-crystalline silicon PV cells[102].
Finally, thermal energy can be found in the environment or from wasted heated during technological or industrial processes[105]. Usually, thermoelectric (TE) devices are used in order to convert a temperature difference into electrical energy via the Seebeck effect with typical efficiencies of the order of 5-10 % limiting their large scale practical use[106,107]. The electrical power density supplied by such devices was shown to be evolving following the square of the temperature difference[108], making them more suitable for recovering energy from high temperature sources. Another way of harnessing thermal energy consists in using thermophotovoltaic devices converting thermal radiation power into electrical power. TPV devices can be used in a wide range of applications where high temperatures (> 1000 °C) sources are found such as concentrated solar radiation, nuclear fuels and waste heat[10]. Thermophotovoltaic converters are very promising for recovering thermal energy, due to their high theoretical efficiency up to 85.4 % in the case of a concentrated solar TPV device[109]. Both thermoelectric and thermophotovoltaic devices are used in order to convert thermal power into electrical power. A study presented in the work of Tedah *et al.*[8] compares these two techniques in terms of efficiency and electrical power density as a function of temperature of the thermal source. Around 1300 K, the best reported TPV cells have about twice higher efficiencies than the best reported TEG near 1000 K. For energy harvesting, the output energy density is usually more important than the efficiency. In Figure V.1, Tedah *et al.* reported simulated and experimental electrical power densities as a function of temperature of the thermal source (hot-side temperature), comparing thermoelectric[110–113], thermophotovoltaic[114–116] and near-field thermophotovoltaic[20–22] devices. From room temperature up to 600 K, TE devices are superior to TPV or NF-TPV ones because at such temperatures the thermal radiation spectrum is restrained

to low frequencies (see Sec. I.2.2). At such temperatures, thermal energy carried by photons is not efficiently converted because of the limited range of energy bandgap of TPV cell materials (see Figure V.6).Above 1000 K, TPV is preferred over TE because it is challenging to fabricate stable TE devices at such temperature. Above 2000 K, TE and TPV devices are comparable and reach their limits with stability issues for TE materials and over-heating of TPV cells. Up to now, thermal energy from sources having medium temperatures ranging from 600 to 1000 K is best harvested by high-temperature thermoelectrics, but may be exploited also by near-field thermophotovoltaic devices (see VI.4) reaching output electrical power density of almost 1 W.cm^{-2}.

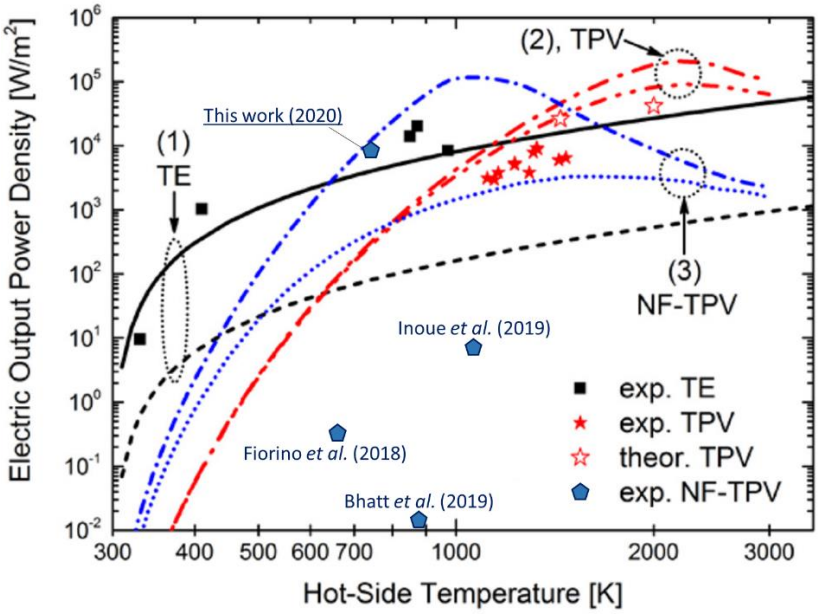

Figure V.1: Electrical output power density as a function of hot-side temperature, comparing thermoelectric (TE) in black, thermophotovoltaic (TPV) in red and near-field thermophotovoltaic (NF-TPV) devices in blue. Reported from the work of Tedah et al[8] and completed with NF-TPV experiments published in the literature. For TE, the solid and dashed lines represent respectively a strong and weak thermal coupling scenario. For TPV, the dash-dot and dash-dot-dot lines are for calculations without and with sub-bandgap radiation. For NF-TPV, the dash-dot and dotted lines are for calculations without and with sub-bandgap radiation.

V.3 Basics of the photovoltaic effect

In this section, basic principles of photovoltaic conversion are described[71,117] from electrical charge generation to their extraction by means of a p-n junction. Different doping types are reviewed and influence of temperature on semiconductors is explained.

V.3.1 Generation of free electrical charge carriers

PV cells are made of semiconductor materials absorbing photons, and generating free electrical charges via the photoelectric effect. Charge generation occurs if the energy of an absorbed photon is higher than the threshold energy required to shift an electron from the valence band to the conduction band. This threshold energy is called bandgap energy, referred to as E_g, with its corresponding bandgap wavelength λ_g. Therefore, the energy bandgap is the difference between

the maximum energy of the valence band and the minimum energy of the conduction band: $E_g = E_C - E_V$. The vacancy of electron (e) created in the valence band corresponds to a positive charge called hole (h). The system composed by the negatively (electron) and the positively (hole) charges generated by the absorption of a photon is called electron-hole pair (Figure V.2). If the energy of a photon is smaller than the energy bandgap then a photon absorbed in the material is expected to interact with heat carriers of the PV cell material generating only heat. For semiconductors, heat carriers are waves of the crystalline lattice of atoms, known as phonons, or the free electrical charges. For photons with energy E higher than the bandgap, the excess of energy $E - E_g$ is quasi-instantaneously transferred to heat carriers and also generates heat inside the material. Photogenerated electron-hole pairs can be collected in order to produce electrical power. To do so, a p-n junction made of semiconductors with different doping types is the typical approach to use, even though it has been demonstrated not to be necessary[118].

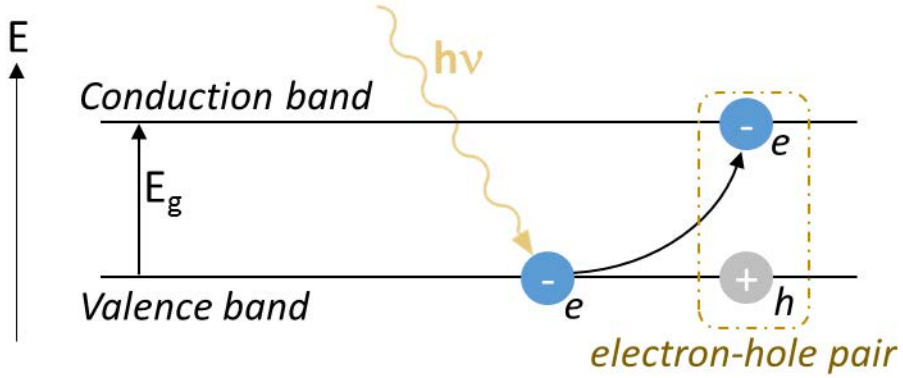

Figure V.2: Schematic of an electron-hole pair generation via absorption of a photon

V.3.2 Doping

For semiconductors, doping consists in adding atoms of other elements than those constituting the structure of the semiconductor material. The purpose of doping is to modify electrical properties of a semiconductor. Two doping types exist according to the doping material properties:

- n-type: n-doping is when the doping material provides additional free negative charges. Such materials are referred to as donors.
- p-type: p-doping is the opposite of n-doping when the doping element lowers the number of free negative charges. Likewise, such materials are referred to as acceptors.

Semiconductors made of group IV (*e.g.* silicon) and groups III-V (*e.g.* InSb) materials have four valence electrons per atom. Therefore, n-type doping is achieved by adding pentavalent atoms (5 valence electrons) while p-type requires trivalent (3 valence electrons) atoms. A schematic of the two different doping types is provided in Figure V.3. In the figure, semiconductor atoms are tetravalent (group IV). A valence bond between two atoms involves one valence electron from both atoms. For the n-type doping, the pentavalent atom has 5 electrons for 4 valence bonds resulting in one extra electron. For p-type, the trivalent atom only has 3 electrons for 4 valence bonds resulting in one lack of electron (hole). As an example, donor pentavalent atoms are from group V (*e.g.* P, As, Sb) and trivalent acceptor atoms are from group III (*e.g.* B, Ga, In). In absence of doping a semiconductor is called intrinsic. Free electrical charges still exist because of intrinsic thermal excitation.

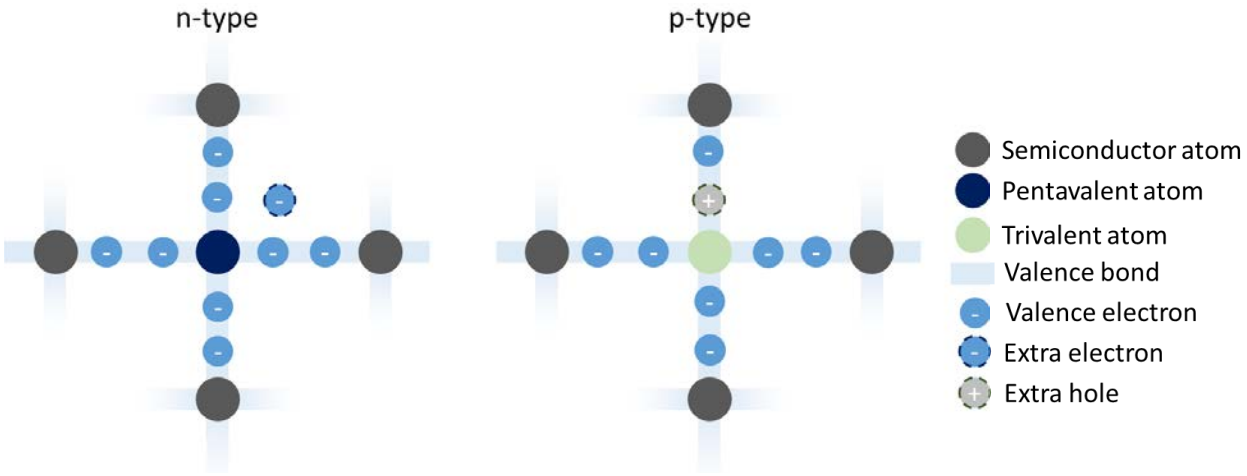

Figure V.3: Schematic of n-type and p-type doping for tetravalent semiconductor atoms

V.3.3 Intrinsic carrier concentration

Free carrier concentration n_i in an intrinsic semiconductor depends on temperature and energy bandgap:

$$n_i(T) = \sqrt{N_c(T)N_v(T)}e^{\frac{-E_g(T)}{2k_BT}}, \quad (V.1)$$

$$N_c(T) = \frac{1}{4\pi^3}\left(\frac{2\pi k_B T m_e^*}{\hbar^2}\right)^{3/2}, \quad (V.2)$$

$$N_v(T) = \frac{1}{4\pi^3}\left(\frac{2\pi k_B T m_h^*}{\hbar^2}\right)^{3/2}, \quad (V.3)$$

where N_c and N_v are the effective densities of states in the conduction and valence bands, k_B the Boltzmann constant, T the temperature, m_e^* and m_h^* the effective masses of electrons and holes. For calculation of densities of states, respectively Eq. (V.2) and (V.3) can be simplified as

$$N_{c,v}(T) = N_{c,v}^{T=300\,K}\left(\frac{T}{300}\right)^{3/2}, \quad (V.4)$$

where $N_{c,v}^{T=300\,K}$ are densities of states at 300 K. In Eq. (V.1) it appears that temperature has a direct effect on the intrinsic carrier concentration, and also affects N_c, N_v and E_g. Since n_i depends on E_g, low-energy bandgap semiconductors are expected to have a higher intrinsic carrier concentration compared to high energy bandgap semiconductors. Energy bandgap is generally expressed as a function of temperature by Varshni's empirical equation[119]:

$$E_g(T) = E_g^{T=0} - \frac{\alpha_e T^2}{T\beta}, \quad (V.5)$$

where $E_g^{T=0}$ is the energy bandgap at $T = 0$, and α_e and β are fitting parameters. When temperature increases, the amplitude of atomic vibrations increases and leads to larger lattice parameters that tend to decrease the bandgap.

In order to illustrate the intrinsic carrier concentration dependence on temperature and energy bandgap, Figure V.4 shows n_i as a function of temperature for Si and InSb. Parameters used for calculations, in inset of the figure, were found in the literature[74,120]. At room temperature, intrinsic carrier concentration is 6 orders of magnitude higher for InSb ($E_g^{T=0}$ = 0.235 eV) than that for Si

($E_g^{T=0}$ = 1.166 eV). For doped semiconductors, equilibrium concentrations of electrons and holes depend on the intrinsic carrier concentration as[71]:

$$n_0 = \frac{n_i^2}{N_A}, \tag{V.6}$$

$$p_0 = \frac{n_i^2}{N_D}, \tag{V.7}$$

for respectively a n-doped and a p-doped semiconductor. Here N_D and N_A are the donor and acceptor extrinsic concentrations. In the case of a low energy bandgap semiconductor such as InSb, a high intrinsic carrier concentration implies either that a high doping level is required or working at low temperatures in order to decrease the density of thermally-generated carriers.

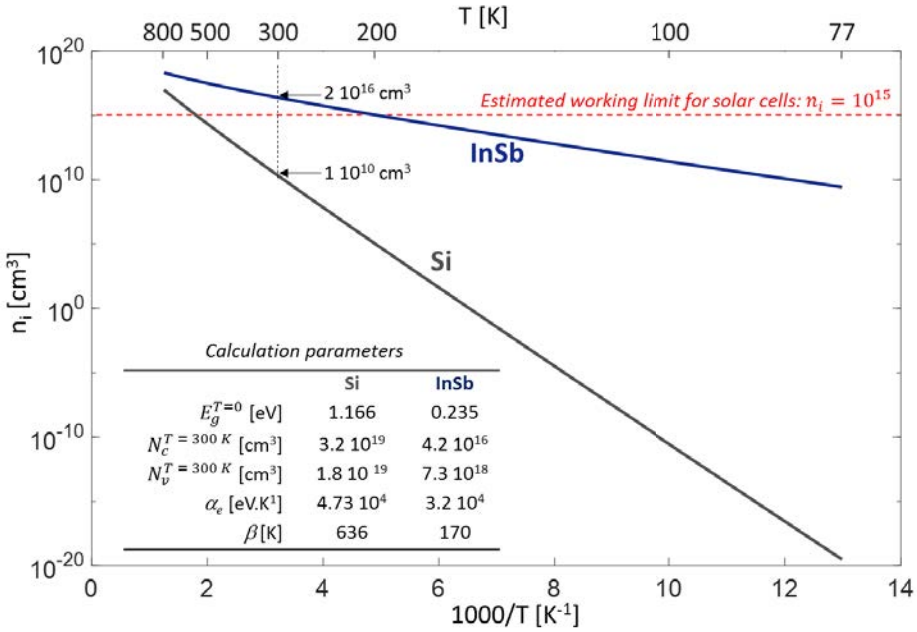

Figure V.4: Intrinsic carrier concentration for Si and InSb, as a function of temperature

V.3.4 p-n junction

A p-n junction is commonly used to separate and collect photogenerated electrical charge carriers. The junction is formed by the contact of two regions of the semiconductor with a different doping type (Figure V.5). One region is n-doped, while the other is p-doped. In the p-type region, there are excess holes coming from the acceptor atoms while there are excess free electrons in the n-type region as described in Figure V.3. When the two regions are in contact, free electrons from the n-type region diffuse across the junction into the p-type region where they fill holes. This electron displacement leaves donor atoms as positive ions in the n-type region and creates negative ions from acceptor atoms in the p-type region. The region where removed electrons and filled holes leave no free charge is called the depletion region. The charge density changes across the depletion region due to the displacement of charges. This generates an electrostatic potential between both sides of the depletion region thus inducing a drift current. Motion of electrons and holes is ruled both by the drift current and the diffusion current. The diffusion current is caused by diffusion of charges from regions where their concentration is high to less concentrated regions.
Motion of charges is described by transport equations for a 1D configuration written as:

$$J_n(z) = en(z)\mu_n E(z) + eD_n \frac{dn(z)}{dz}, \tag{V.8}$$

$$J_p(z) = ep(z)\mu_p E(z) - eD_p \frac{dp(z)}{dz}, \tag{V.9}$$

$$D_{n,p} = \frac{k_B T \mu_{n,p}}{e}, \tag{V.10}$$

where J_n and J_p are electron and hole current densities, e the elementary charge of the electron. Densities of free electrons and holes as a function of position z are represented by $n(z)$ and $p(z)$. D_n and D_p, and μ_n and μ_p, are respectively diffusion coefficients and mobilities of electrons and holes. Diffusion coefficients are given by Einstein's relation (equation (V.10)). When a photon is absorbed, photogenerated electrons and holes are put into motion by drift and diffusion. The charges are separated and migrate towards their respective electrical contacts in order to be collected in an external electrical circuit before recombination happens.

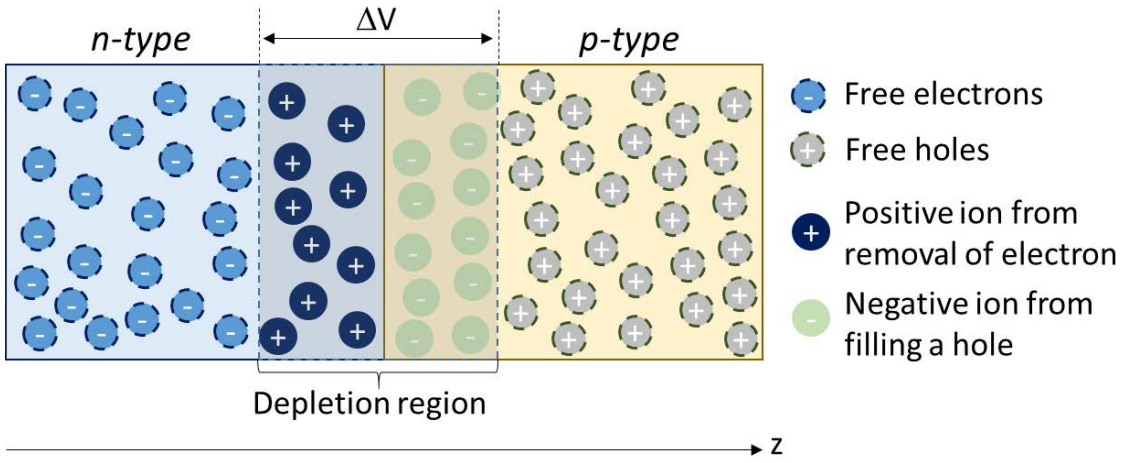

Figure V.5: Schematic of a p-n junction

V.4 Low energy bandgap semiconductors

Conversion of a radiative power carried by a photon into electrical power via electron-hole pair generation requires a semiconductor material with an appropriate energy bandgap. For TPV applications, the energy of a photon is relatively low and corresponds to the infrared spectrum region. Photons that can be converted must have an energy higher than the bandgap energy of the semiconductor. Figure V.6 shows the hemispherical radiative heat flux emitted by a blackbody, at either 900 or 1500 K, as a function of photon energy. Several semiconductors, and their associated energy bandgap, are superimposed on the curves. For silicon, which is the most commonly used material for solar PV applications, only 2.4 % of the power emitted by a blackbody at 1500 K is from photons with an energy $E > E_g^{Si}$.

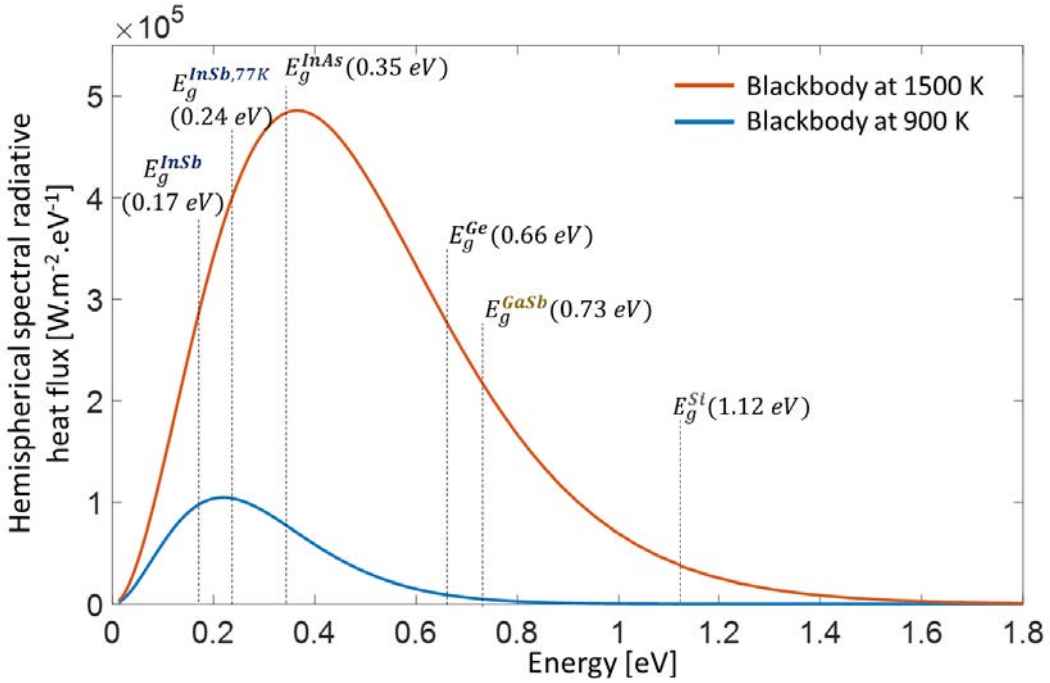

Figure V.6: Hemispherical spectral radiative heat flux emitted by a blackbody at 900 and 1500 K, as a function of photon energy

For a medium-grade temperature of 900 K, the fraction of convertible power drops to 0.03 %. It appears clearly that a semiconductor with an energy bandgap matching the blackbody emission spectrum is a key parameter for TPV conversion. Because the emission spectrum of a blackbody depends on temperature, the semiconductor material has to be selected considering the emitter temperature. For example, InAs is well suited for an emitter at 1500 K because its energy bandgap is close to the wavelength of maximum thermal radiation λ_{Wien}. In this case, 67 % of the emitted power comes from photons with an energy $E > E_g^{InAs}$.

For emitter temperatures lower than 1000 K, a semiconductor with a lower energy bandgap is required such as InSb. At 300 K, InSb has an energy bandgap of 0.17 eV. Combined with a blackbody emitter at 900 K, 78 % of the emitted power is at $E > E_g^{InSb,300K}$. However, InSb TPV cells are not expected to work at room temperature due to the high concentration of thermally generated carriers (Figure V.4). InSb can be cooled down to cryogenic temperatures, 77 K for instance, to lower the intrinsic carrier concentration. At 77 K, the energy bandgap of InSb remains very low: $E_g^{InSb,77K}$= 0.24 eV. For a blackbody emitter at 900 K, 61 % of the emitted power comes from photons with energy larger than $E_g^{InSb,77K}$.

Figure V.7 shows the energy (and wavelength) bandgap of III-V semiconductors as a function of the lattice parameter reported from the thesis work of Caro[121]. The lattice parameter has to be considered in the choice of materials for PV cell fabrication. Indeed, similar lattice parameters are required between the different layers of material composing a PV cell in order to maximize its performance. For instance, lattice mismatch may lead to dislocations, rough surfaces or cracking[122]. III-V semiconductors cover a wide range of energy bandgap from 0.17 eV for InSb to above 6 eV for AlN at 300 K. For AlN, GaN and InN, the crystalline structure has an influence on the energy bandgap. In Figure V.7, it appears that InSb is the III-V semiconductor having the lowest energy bandgap. Based on this property, it was decided to fabricate TPV cells made of InSb in order to

potentially convert as much thermal radiation as possible emitted by moderate temperature (< 1000 K) sources.

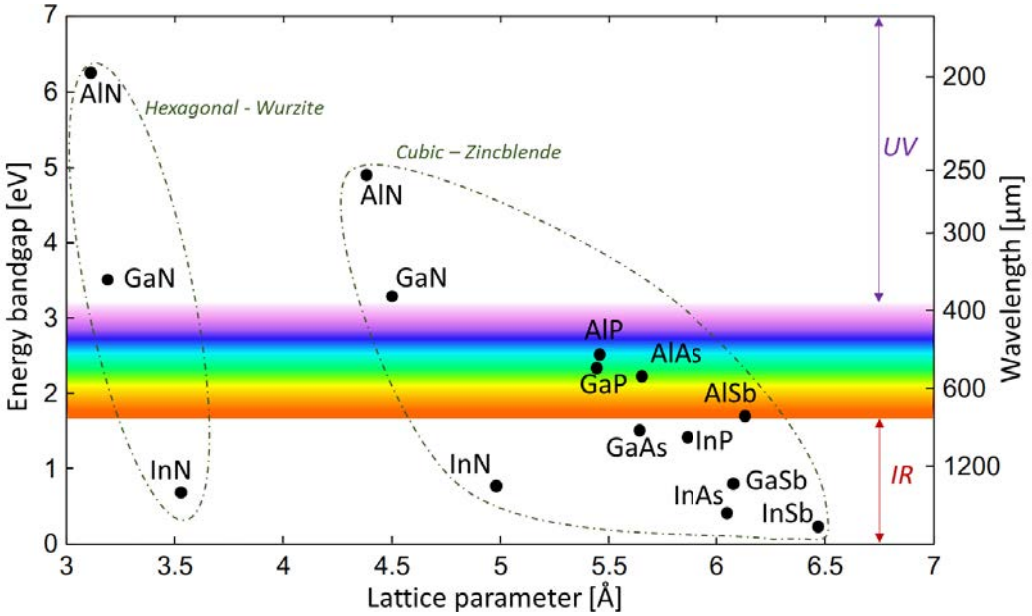

Figure V.7: Energy bandgap at 300 K of III-V semiconductors as a function of lattice parameter. Figure inspired from the work of Caro et al[121].

V.5 I-V characteristics

The current-voltage (I-V) characteristic of a PV cell is obtained by measuring the electrical current passing through a cell while the voltage is scanned. Under illumination, the measured I-V curve is usually equal to the addition of the curve in the dark and the photogenerated current[123] and is written with the following diode equation:

$$I = I_0 \left[\exp\left(\frac{eV}{n_f k_B T} \right) - 1 \right] - I_L \,, \qquad (V.11)$$

where I is the current, I_0 the reverse saturation current (or dark current), e the elementary charge, V the applied voltage, n_f the ideality factor, and I_L the photogenerated current. The reverse saturation current I_0 is caused by diffusion of charge carriers to the depletion region and depends on intrinsic carrier concentration n_i which depends on temperature. Therefore, I_0 increases with temperature.

Figure V.8 shows the calculated current I as a function of voltage. The blue curve corresponds to the dark condition meaning $I_L = 0$. The red curve considers a condition with illumination resulting in a photogenerated current $I_L = 0.4$ A. The subtraction of a photogenerated current lowers the dark I-V curve down to negative currents. Two notable parameters can be highlighted: the short-circuit current I_{SC} and the open-circuit voltage V_{OC}. I_{SC} is equal to the electrical current at a voltage $V = 0$. V_{OC} is the voltage where the electrical current is equal to 0. The light-yellow area, where the current is negative and the voltage is positive, is called the photogeneration quadrant.

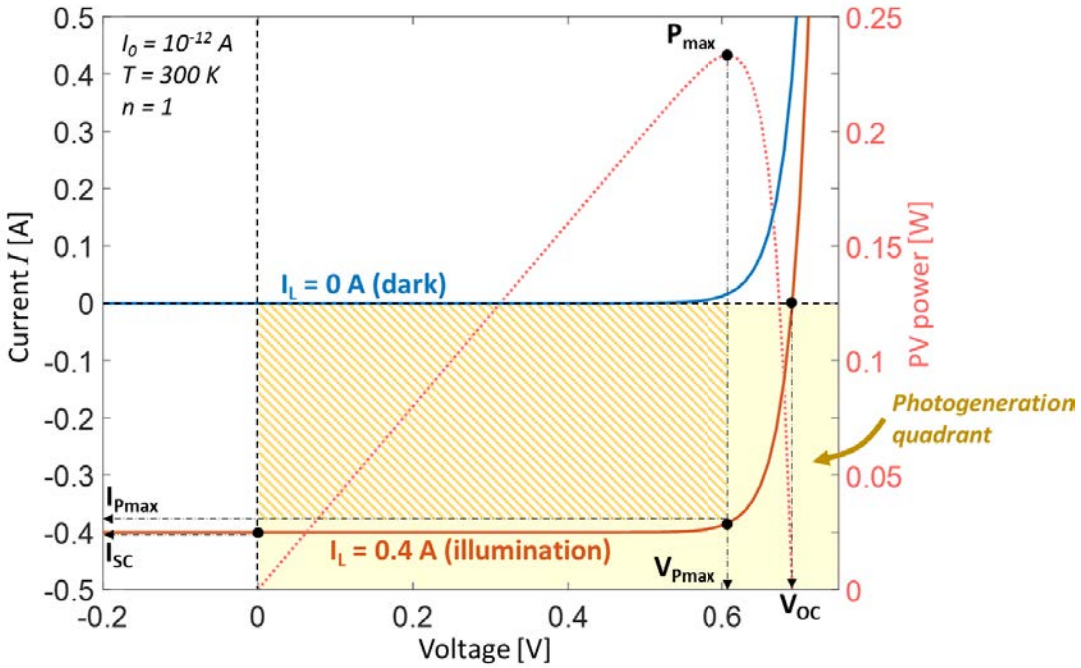

Figure V.8: Calculated I-V characteristics of a PV cell under dark and illuminated conditions. Dotted curve is the PV generated electrical power as a function of voltage

In the photogeneration quadrant, the PV cell is an active device generating an electrical power P_{PV}, calculated as:

$$P_{PV} = -I \times V \,, \qquad (V.12)$$

where I is the current and V the voltage. P_{PV} is represented by the dotted curve as a function of voltage in Figure V.8 for the case of an illumination I_L = 0.4 A. The $P_{PV}(V)$ curve reveals a maximum value P_{max} corresponding to a voltage V_{Pmax} and a current I_{Pmax}. The maximum generated power P_{max} is also visualized in the figure by the hatched area. To characterize performances of PV cells, a dimensionless parameter called fill factor (*FF*) can be calculated as:

$$FF = \frac{P_{max}}{-I_{SC} \times V_{OC}} \qquad (V.13)$$

An ideal PV cell would work at the Shockley-Queisser[124] limit reaching a fill factor $FF = FF_0$ which depends on various parameters such as energy bandgap, temperature and V_{OC}[125].
The I-V characteristic of a PV cell is a way to obtain key performances parameters such as I_{SC}, V_{OC}, P_{max} and *FF*. Experiments, detailed in chapter VI, are performed in order to measure I-V characteristics of a cooled InSb TPV cell as a function of distance with an infrared emitter. As distance decreases, the I-V curve is expected to be shifted to larger negative currents because of the increasing illumination.

V.6 Experimental thermophotovoltaic devices

Experimental characterization of TPV cells were performed in the past using various cells and emitters. In this section, published experimental works are reported differentiating classical far-field illumination and recent near-field illumination works.
The first use of TPV conversion device was initiated in 1956 by Kolm[126]. He held a Si solar cell close to the flame of a lantern and measured the generated electrical power. It is interesting to note

that the first practical Si solar cells had been reported only two years before by Chapin *et al*.[127] in 1954. It has been shown in previous sections that Si has an energy bandgap of 1.12 eV, which is too high for TPV applications. Many TPV conversion devices were investigated experimentally combining different sorts of heat sources, emitters, and cells made of various energy bandgap semiconductors. First, several experimental results using far-field infrared illuminations are highlighted. Then, near-field TPV devices are detailed in order to find emerging fields of study and paths of improvements.

V.6.1 Far-field illumination

Far-field TPV devices are using infrared radiation separated by relatively large distances (above ~ 1 mm) from the cell. One application of such device is solar energy conversion referred to as solar TPV (STPV).

V.6.1.1 Solar TPV devices

STPV devices are composed of three major parts (Figure V.9). First, an absorber converts concentrated solar radiation into heat. Then, heat is conducted to a thermal emitter radiating towards a TPV cell. Finally, a TPV cell converts thermal radiation power into electrical power. Emitters above 1000 K are desirable in order to provide an emission spectrum matching the usual energy bandgap of TPV cells. Achieving such an emitter temperature requires concentration of solar radiation. Recently, research groups have demonstrated the potential of STPV systems for solar energy harvesting (Table V.1). For instance, Lenert *et al*.[128] used carbon nanotubes as absorber deposited on an emitter made of a Si/SiO_2 multilayer structure expected to improve the spectral matching with an InGaAsSb cell (E_g = 0.55 eV at 300 K). Radiative power incident on the absorber was provided by a xenon-arc light source simulating the solar spectrum. Illumination was concentrated to be equivalent to 750 suns (75 $W.cm^{-2}$). This illumination level allowed to heat the emitter up to 1285 K. A chilled-water cooling system was used in order to keep the TPV cell at room temperature. They measured an overall efficiency of 3.2 % corresponding to the output electrical power from the cell divided by the radiative power incident on the absorber surface. Bierman *et al.*[129] performed the same kind of measurements with a Si/SiO_2 multilayer emitter and a cooled InGaAsSb TPV cell. The incident radiative power corresponded to the AM1.5D solar spectrum with 100x concentration. They obtained an overall conversion efficiency of 6.8 %. Both Lenert *et al.* and Bierman *et al.* reached similar output electrical power densities of 0.4-0.45 $W.cm^{-2}$. The same power densities were also obtained by Kohiyama *et al.*[130] using a cooled GaSb TPV cell (E_g = 0.67 eV at 300 K) and a Mo/HfO_2 nanostructured absorber/emitter. Under a solar radiation concentration factor of 1020, they reached an overall efficiency of 5.1%. The highest output electrical power densities were reached by Ungaro *et al.*[131] and Bhatt *et al.*[132]. They used concentration factors higher than 2000 and W/Si_3N_4 thin films emitters associated to GaSb TPV cells. The TPV cells were mounted on water cooled copper heat sinks to prevent excess heating. Ungaro *et al.* reached an overall efficiency of 6.2 % with a 1700 K emitter. Bhatt *et al.* reached a record overall efficiency of 8.4 % with a 1676 K emitter generating an electrical power density of 1.71 $W.cm^{-2}$. In the latter experiments, the TPV cell was heated from room temperature up to 315 K by thermal radiation despite being in contact with a water-cooled heat sink. The advantage of STPV devices is their ability to convert concentrated sunlight radiation generating large output electrical power. Depending on the TPV cell material, temperature of the emitter must be in the

range where the emission spectrum matches the energy bandgap of the cell. On Table V.1, GaSb cells (E_g = 0.67 eV at 300 K) are associated with 1640-1700 K emitters while InGaAsSb cells (E_g = 0.55 eV at 300 K) are ideal with 1273-1285 K emitters. A drawback of STPV devices is that they require temperature management of the TPV cell, usually by means of a water-cooled heat sink, in order to prevent excess heating from the emitter.
In the next section, TPV devices with other cell and absorber/emitter materials are highlighted, along with state-of-the art TPV conversion efficiencies.

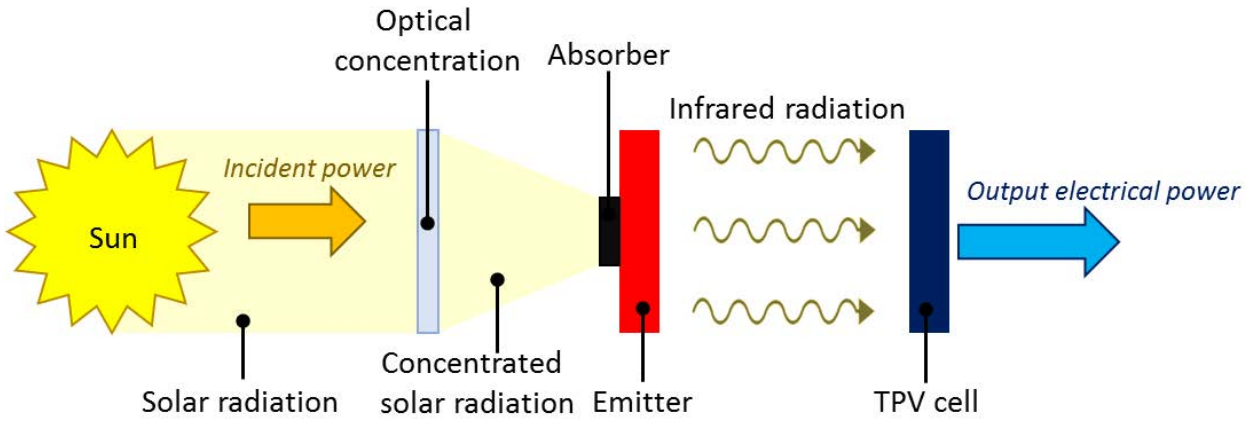

Figure V.9: Schematic of the STPV energy conversion principle

Table V.1: Selected recent experimental STPV devices

Source	Emitter	Emitter T [K]	Concentration factor	TPV cell	E_g [eV]	Output electrical power density [W.cm^{-2}| W.m^{-2}K^{-1}]	Overall efficiency [%]
Lenert *et al.*, 2014[128]	Si/SiO_2 multilayer	1285	750x	InGaAsSb	0.55	0.45 | 4.6	3.2
Kohiyama *et al.*, 2016[130]	Mo/HfO_2 nanostructure	1640	1020x	GaSb	0.67	0.42 | 3.1	5.1
Ungaro *et al.*, 2015[131]	W with Si_3N_4 thin film	1700	2483x	GaSb	0.67	1.56 | 11.1	6.2
Bierman *et al.*, 2016[129]	Si/SiO_2 multilayer	1273	100x	InGaAsSb	0.55	0.40 | 4.1	6.8
Bhatt *et al.*, 2020[132]	W with Si_3N_4 thin film	1676	2100x	GaSb	0.67	1.71 | 12.4	8.4

V.6.1.2 Emitters for TPV conversion

A wide diversity of thermal emitters and absorbers were studied in the literature. One of the advantages of TPV is that the emitter radiation spectrum can be tuned, contrary to solar PV where radiation is coming from the sun. Table V.2 lists thermal emitters used in TPV conversion devices. A more complete analysis is provided by Sakakibara et al.[12] where fabricated (but non-included in TPV devices) and simulated emitters are summarized. The interest of using non-bulk emitters is for tailoring the emission spectra. In order to get a better conversion efficiency, emitted thermal radiation spectra must match the energy bandgap of the TPV cell with a wavelength of maximum thermal radiation λ_{wien} (see Sec. I.2.2) close to the bandgap wavelength of the cell. All radiative power absorbed at wavelengths above the bandgap wavelength of the cell cannot be converted into electrical power and generates only heat inside the cell. Emission spectra can be controlled using different kinds of materials. For instance, naturally selective emitters exist and are based on rare-earth materials such as Er or Yb. In addition, 1D and 2D photonic crystals, which are periodic structures, are able to suppress electromagnetic radiation in a desired spectral band[133] usually at $E < E_g$. Multilayer structures are also used to control emission spectra via coherence effects[130].

Table V.2: List of emitters used in TPV conversion devices.

Bulk emitters with or without anti-reflection (ARC) coating			**Naturally selective emitters**				
	Metals						
Grey and blackbodies	*With ARC*	*Without ARC*					
Si_xN_y on Si[134]	ARC on W[135]	W[136,137]	Gas mantle in Coleman lantern[126]	Er-doped yttrium aluminum garnet[138]	Al_2O_3/ $Er_3Al_5O_{12}$ composite[139]	Yb_2O_3 mantle[140–143]	Yb_2O_3-coated SiC or Al_2O_3 foam[142]
Bulk Si[144]	ARC on Pt[145]	Metal alloy[146]					
Bulk SiC[116,147–151]	HfO_2 on W[152]	Pt[151]					
Graphite[153]	Si_3N_4 on W[131,132]						
Blackbody[154]							

1D photonic crystal	**2D photonic crystal**			**Multilayer stack**	
Si and SiO_2 on Si[128,129,144]	Ta with HfO_2 coating[155,156]	Ta-W alloy with HfO_2 coating[157,158]	Pt plucks with Al_2O_3 layers[159]	W and yttria-stabilized zirconia[160]	Mo and HfO_2[130]

V.6.1.3 Conversion efficiency and optimal emitter temperature

In terms of TPV conversion efficiency, the best result so far was obtained by Omair *et al*.[153]. They used a 1482 K graphite emitter located at 2.12 mm above an InGaAs TPV cell having an energy bandgap of 0.75 eV at 300 K. The cell was in contact with a copper heat sink, cooled by a 20°C water flow. Their TPV cell had a rear gold layer used both as holes collector and radiation reflector. Thermal radiation with photon energy $E < E_g$ which is not absorbed by the cell is reflected back to the emitter. This principle is called photon recycling. They claimed 29.1% TPV conversion efficiency.

Most of experimental works are focusing on emitter temperatures higher than 1000 °C (1273 K). For harvesting heat from lower temperature sources, lower energy bandgap TPV cells must be used. The work of Lu *et al.*[154] demonstrated TPV conversion with InAs cells having an energy bandgap of 0.35 eV. They used a blackbody source at temperatures up to 800 °C (1073 K) and a cell at 300 or 100 K. With the cell at 300 K, conversion efficiency was very low (0.35%) because the I-V curve of the cell is almost linear: a fill-factor of 0.25 was measured. As described in previous sections, thermally generated carrier concentration in low energy bandgap semiconductors is very high leading to a high dark current. They demonstrated that the dark current decreases by ~ 4 orders of magnitude when the cell was cooled from 300 to 100 K by means of a liquid nitrogen cryostat. When cooled at 100 K, the shape of the I-V curve of the cell became comparable to that presented in Figure V.8, and V_{OC} rose from 18 mV to 252 mV. With the cell at 100 K and a blackbody source at 1073 K, they measured a TPV conversion efficiency of 10 % that is 28 times larger than that with the cell at 300 K. In such case, cooling the cell appears essential for harvesting thermal radiation from emitters below 1000 °C using low energy bandgap TPV cells.

To illustrate the relation between the emitter temperature and the cell properties (spectral matching), Figure V.10 shows the emitter temperature as a function of the energy bandgap of TPV cells used in selected published experimental works. When cells with a larger energy bandgap are used, higher emitter temperatures are required to efficiently convert thermal photons. The black line is the temperature T_{Wien} where the energy of a photon emitted at λ_{Wien} is the same as the energy bandgap of the cell. Wien's law (see Eq. (I.3)) can also be written as:

$$\lambda_{Wien} = \frac{hc}{4.96 k_B T}. \qquad (V.14)$$

In Eq. (V.4), h is the Planck constant, k_B the Boltzmann constant ant T the temperature. Then knowing the energy of a photon being $E = hc/\lambda$, T_{Wien} can be expressed as :

$$T_{Wien} = \frac{E_g}{4.96\ k_B}, \qquad (V.15)$$

where E_g is the energy bandgap. It appears in the figure that experimental works are following the trend of the $T_{Wien}(E_g)$ curve. This demonstrates that the importance of spectral matching between emitter radiation and TPV cell energy bandgap was captured by the different groups. It is interesting to remark that, in terms of efficiency, the two recent performances of Woolf *et al*.[159] (24.1 %) and Omair *et al.*[153] (29.1 %) were obtained with emitter temperatures below T_{Wien}. This may result from the metamaterial selective emitter used by Woolf *et al*, and the reusing of unabsorbed sub-bandgap photons for Omair *et al*. Harvesting heat from emitters below 800 K would require TPV cells with energy bandgap lower than that of InAs (0.35 eV). InSb is therefore a suitable material because it has the lowest energy bandgap of III-V semiconductors (Figure V.7) with 0.17 eV at 300 K and 0.24 eV at 77 K. It is reasonable to state that TPV conversion with InSb at 300 K would not be possible due to the high density of thermally-generated carriers. However,

cooled InSb TPV cells at liquid nitrogen temperature should provide efficient energy conversion from emitters around 600 K[74].
Except for STPV devices under large concentration factors (> 2000), output electrical power densities provided by TPV devices are relatively small (lower than 1 W.cm^{-2}). To compete with thermoelectric devices[161], the enhancement of electrical power generation must be obtained in TPV devices. A solution consists in using near-field thermal radiation to increase radiative heat transfer between the hot emitter and the cell and improve the generated electrical power.

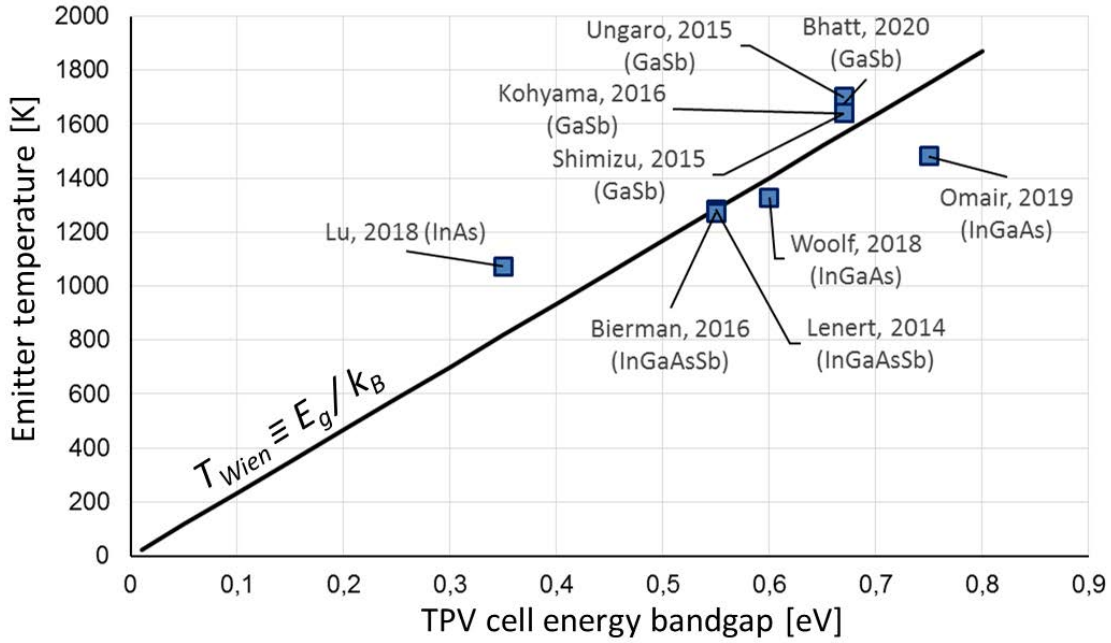

Figure V.10: Emitter temperature versus TPV cell energy bandgap at 300 K for several published works.

V.6.2 Near-field illumination

The idea of using near-field thermal radiation in a TPV cell to enhance the generated power was theoretically proposed more than two decades ago[18,19,162,163]. The first attempt to experimentally demonstrate near-field enhancement of TPV generated power was performed in 2001 by DiMatteo *et al.*[164]. They used an InAs cell mounted on a brass block, which was in contact with a thermoelectric cooler, located on a liquid cooling system. The planar emitter was made of silicon with 1 µm high SiO_2 spacers. The gap distance between the emitter and the cell was monitored using a piezo actuator applying a force on a quartz clamp in contact with the emitter back surface. Variations of gap distance were drawn from capacitance measurements between the emitter and the cell. The experimental device was placed in a vacuum chamber where the pressure was lowered to 5 10^{-2} mbar. At an emitter temperature of 408 K, they measured an increase in the short-circuit current by a factor 5 reaching 1.7 mA when the gap was decreased to an unknown distance below one micron. However, they performed only qualitative measurements and the increase in short-circuit current might have been caused by other energy transfer mechanisms.
Another attempt was made by Hanamura *et al.*[165] in 2007. In a vacuum chamber, they used a GaSb TPV cell mounted on a water-cooled copper block pasted on an *x-y-z-θ* micro-stage. The suspended planar emitter was made of tungsten and heated up to 1000 K by a CO_2 laser. The gap distance was

measured by an optical microscope. They could precisely measure the gap from 1 mm down to 14.6 µm. These distances are larger than the distance where evanescent waves starts to contribute to radiative heat transfer. Therefore, they concluded that the electrical power enhancement, from 1.8 to 2.6 mW, was due to the increase of view factor when distance decreases. They tried to perform measurements for gap distances below 5 µm and might have measured the effect of evanescent waves below 3 µm. However, large uncertainties on gap distance could not allow to conclude on an experimental observation of generated electrical power enhanced by near-field effects.

The first successful experiment demonstrating near-field enhancement of photocurrent generation was performed by Fiorino *et al.*[20] in 2018. They used two different InAsSb/InAs TPV cells: one with an energy bandgap of 0.345 eV and another with E_g = 0.303 eV at 300 K. They fabricated a thermal emitter made of silicon with a 15 µm tall and 80 µm in diameter circular mesa structures suspended by two 550 µm long beams (Figure V.11). A platinum serpentine heater was located next to the circular structure used to rise the temperature up to 655 K. The cell, at room temperature, was square-shaped with a 300x300 µm^2 active area. The emitter and the cell could be moved and tilted along *x* and *y* axes, enabling parallelism control between the emitter and the cell. Piezoelectric actuation along the vertical axis was used to move the cell and monitor the vacuum gap distance with the emitter. The smallest distances (60 and 75 nm for the 0.345 eV and 0.303 eV cells respectively) were limited by peak-to-peak roughness of the emitter and the cells. They reached a maximum TPV output electrical power of 31 nW with the cell having an energy bandgap of 0.345 eV, and 10 nW for the cell having an energy bandgap of 0.303 eV.

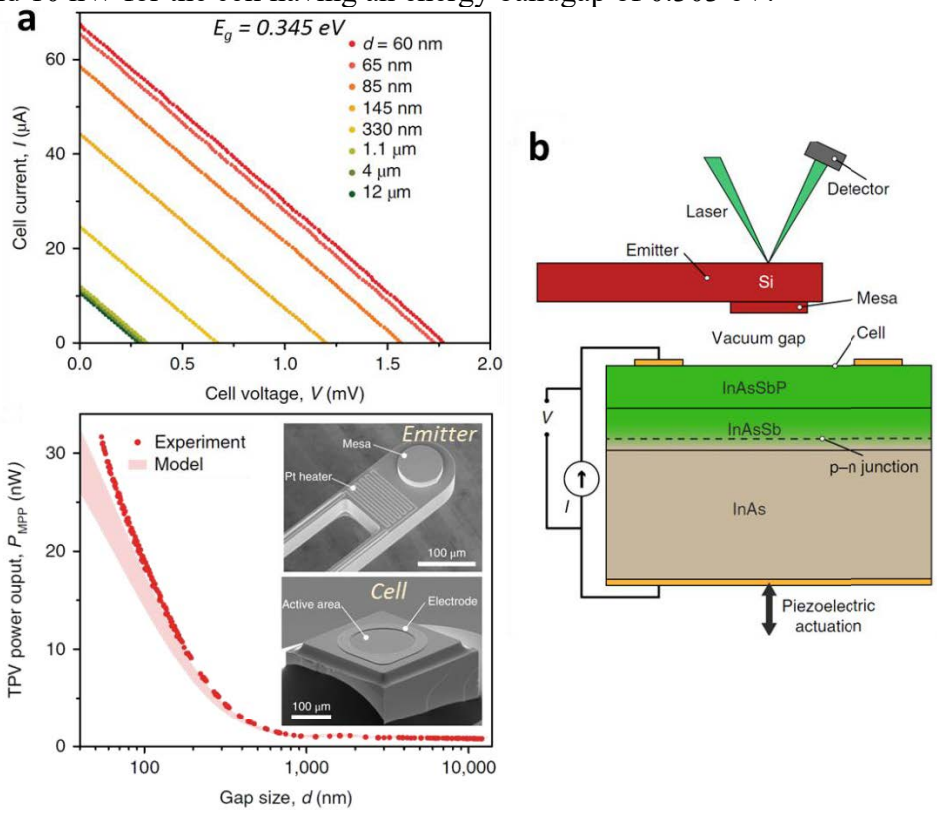

Figure V.11: (a) I-V curves and TPV generated power as a function of distance between Si circular mesa having a 80 µm diameter and an InAsSb/InAs TPV cell at room temperature having an energy bandgap of 0.345 eV and a size of 300x300 µm². (b) Schematic of the experimental device. Figures reported from the work of Fiorino et al.[20]

Because the cells were at room temperature, low energy bandgap induced large thermally generated carriers and poor performances of the cells (V_{OC} = 1.8 mV, FF = 0.25, Figure V.11). Considering the active area of the cell, the highest measured electrical power density was 0.34 W.m^{-2} (3.4 10^{-5} W.cm^{-2}), which is 4 orders of magnitude lower than measurements performed with classical TPV devices (Table V.1).

They estimated the conversion efficiency by computing radiative power exchanged between the emitter and the cell for photon energies above the energy bandgap since a direct measurement was not possible with their setup. They estimated a low conversion efficiency η_{TPV} ~ 0.015 % for the cell with E_g = 0.345 eV. They ascribed low performances to the small illuminated cell area (5% of the surface), and the relatively low temperature of the emitter. Despite the low generated electrical power, they demonstrated the feasibility of enhancing generated electrical power using the contribution of evanescent waves to radiative heat transfer. Indeed, they measured a ~40-fold enhancement in generated power compared to a far-field illumination. As distance decreases, enhancement of radiative power exchanged between the emitter and the cell is observed with a larger effect at low frequencies (*e.g.* low energies) (Figure V.12). This property is well suited for near-field TPV applications because a larger portion of thermal radiation is exchanged in the near field with photons having lower energies, thus potentially converted by a TPV cell. After this first successful demonstration of Fiorino *et al.*, two other groups published experimental works in 2019 (see Table V.3).

Inoue *et al.*[21] fabricated one-chip devices coupling suspended Si emitters, heated up to 1065 K, and an InGaAs TPV cell at room temperature having an energy bandgap of 0.73 eV (Figure V.13a). This one-chip planar design has the advantage of being upscalable but the small gap distance is fixed. Two devices were made with gap distances of 140 and 1160 nm between the planar emitter and a 50 µm-thick undoped Si intermediate substrate in contact with the top surface of the cell. This intermediate substrate extracts frustrated modes of the evanescent waves from the surface of the emitter and transfers them to the TPV cell. This technique allows also to prevent excess heating of the cell caused by the contribution of surface modes to radiative heat transfer because they stated that their undoped Si substrate did not support any surface modes. They measured I-V curves for both devices (Figure V.13b) and found relatively good performances, with a 0.56 fill factor and V_{OC} equal to 188 and 238 mV for the 1160 and 140 nm gap distance devices, respectively.

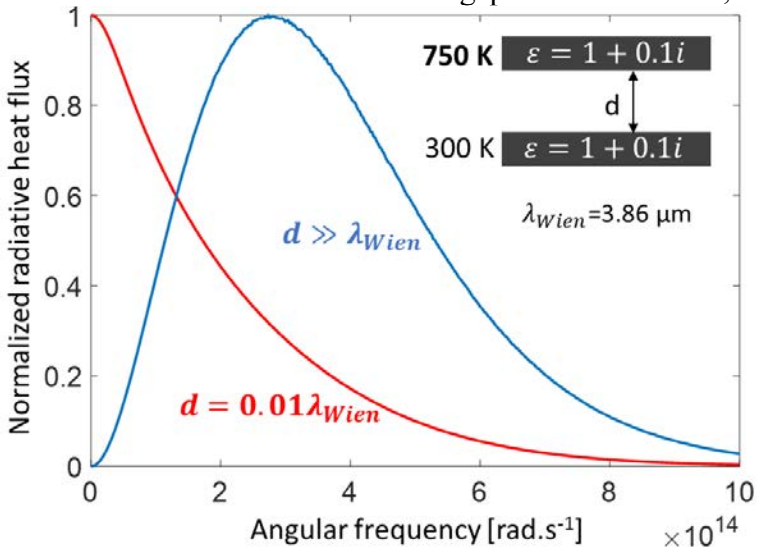

Figure V.12: Normalized radiative heat flux exchanged between two bodies at 750 and 300 K as a function of angular frequency

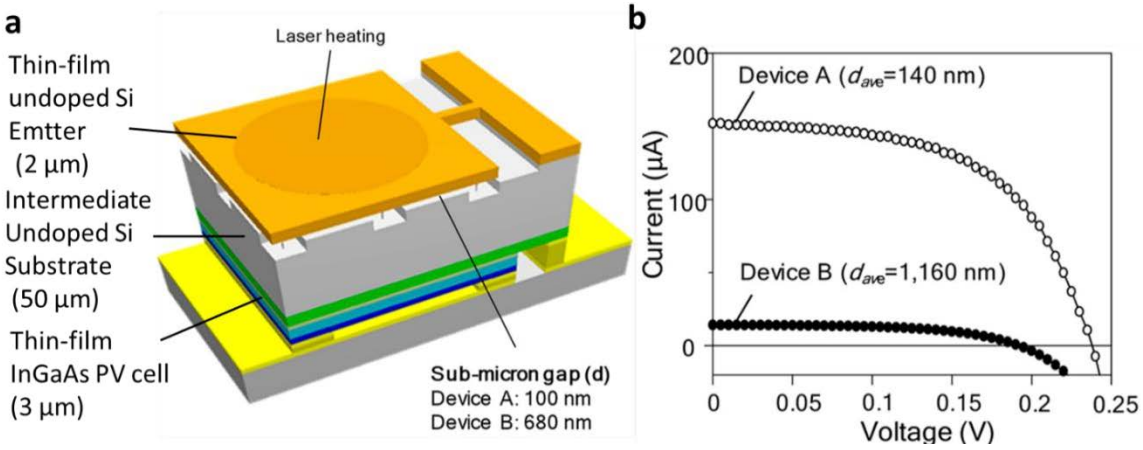

Figure V.13: (a) Schematic of the experimental device from Inoue et al. (b) I-V for two devices having different sub-micron gaps. Figures reported from the work of Inoue et al.[21]

For the device with an emitter-cell gap distance d = 140 nm, they measured a generated electrical power density equal to 7.5 W.m^{-2} (7.5 10^{-4} W.cm^{-2}). This value is one order of magnitude higher than the previous work of Fiorino *et al*. but is still significantly lower than classical TPV devices. They also could not directly measure the efficiency but estimated it to be equal to 0.98 %.

Bhatt *et al.*[22] made a near-field TPV conversion device using a germanium photodetector with E_g = 0.67 eV at 300 K. Above the photodetector, they integrated a nano-electromechanical system (NEMS) for monitoring the position of a planar emitter made of Cr-W-Cr layers on amorphous silicon (Figure V.14a). The gap distance between the emitter and the photodetector was regulated by applying a potential to the NEMS actuation electrode leading to electrostatic attraction of the emitter. However, this system did not allow to study a large range of gap distances. The emitter (80x15 µm size) was heated up to 880 K by an electrical current while the photodetector remained at room temperature (301 K). The gap distance was reduced from 500 to 180 nm while I-V curves were measured. They obtained straight curves (Figure V.14b), similar to Fiorino *et al.*, with a fill factor equal to 0.25. Generated electrical power reached a maximum value of 23.6 pW corresponding to a generated electrical power density equal to 0.0125 W.m^{-2} (1.25 10^{-6} W.cm^{-2}). These low values can be explained by the low emitter temperature compared to the energy bandgap of the germanium photodetector. From Figure V.10, one finds an emitter temperature of ~ 1600 K would be more suitable for applications with a germanium photodetector having E_g = 0.67 eV. They also indicated that performances of their device were limited by the low estimated efficiency (0.003 %) of their germanium photodetector.

Experimental near-field TPV devices were developed only very recently. So far, enhancement of generated TPV power by evanescent wave contribution to radiative heat transfer was demonstrated but with low efficiencies and electrical power densities. Conversion efficiencies could not be measured directly and were estimated using near-field radiative heat transfer calculations. Published experimental works were reported with a maximum temperature difference between the emitter and the cell of 765 K[21], where spectral matching between emitted thermal photons and the cell energy bandgap was not optimal. In addition, the selected low energy bandgap TPV cells have poor performances at room temperature with fill factors equal to 0.25. All these issues have to be overcome if one wants to harvest thermal photons in the near field with high efficiencies and electrical power densities. In our experimental work, InSb cells cooled down to 77 K (E_g = 0.24 eV) are paired with a graphite emitter heated to temperatures comprised between 732 and 1200 K. Details of experimental measurements are reported in chapter VI.

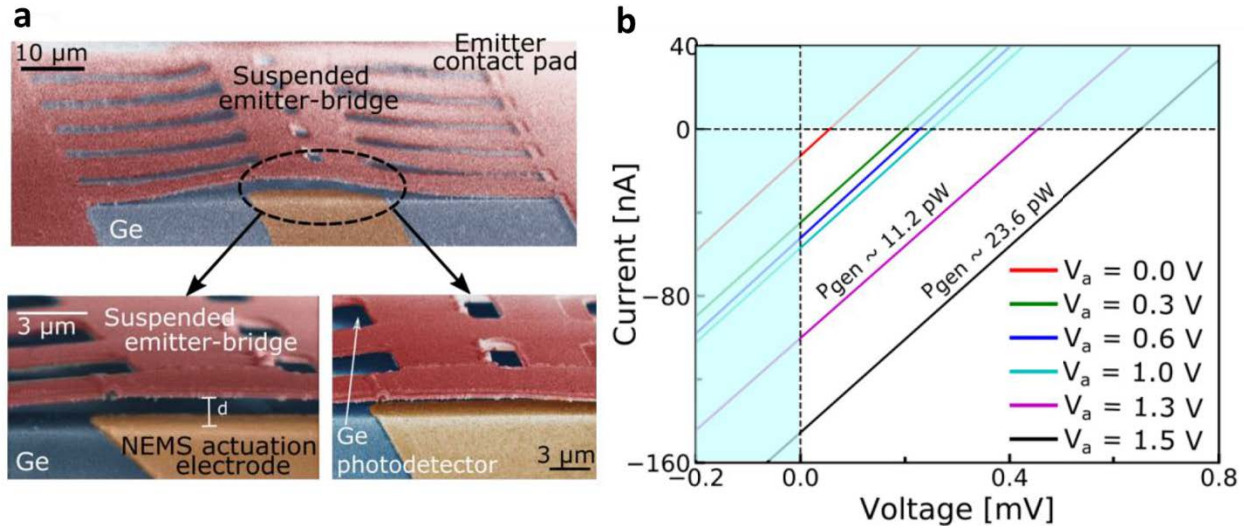

Figure V.14: (a) Schematic of the experimental device from Bhatt et al. (b) I-V for two devices having different sub-micron gaps. Figures reported from Bhatt et al.[22]

Table V.3: List of experimental near-field TPV devices and their associated parameters

Source	Year	η_{TPV} estimated [%]	P_{TPV} [W] [W.cm^{-2}|W.m^{-2}.K^{-1}]	Cell	E_g at 300 K [eV]	Emitter	Emitter T [K]	ΔT [K]	FF	d_{min}
DiMatteo *et al.*[164]	2001	-	-	InAs	0.35	Si	408	110	-	~1 µm
Hanamura *et al.*[165]	2007	-	$2.5.10^{-3}$ $1.6.10^{-3}$ | $2.2.10^{-2}$	GaSb	0.67	W	1000	702	-	< 10 µm
Fiorino *et al.*[20]	2018	0.015	$3.4.10^{-8}$ $3.4.10^{-5}$ | $9.7.10^{-4}$	InAsSb	0.35	Si	655	360	0.26	60 nm
		0.008	$1.0.10^{-8}$ $1.1.10^{-5}$ | $3.1.10^{-4}$		0.3				0.25	75 nm
Inoue *et al.*[21]	2019	0.98	$3.0.10^{-5}$ $7.5\ 10^{-4}$ | $9.8.10^{-3}$	InGaAs	0.73	Si	1065	765	0.56	140 nm
		?	$2.5.10^{-6}$ $6.3\ 10^{-5}$ | $8.2.10^{-4}$						0.57	1160 nm
Bhatt *et al.*[22]	2019	0.003	$2.4.10^{-11}$ $1.3\ 10^{-6}$ | $2.2.10^{-5}$	Ge	0.67	Cr-W-Cr on a-Si	880	579	0.25	180 nm

V.7 Conclusion

Fundamentals of photovoltaics have been presented in this chapter where doping and p-n junction principles have been reminded. Direct conversion of thermal radiation into electrical power can be achieved using thermophotovoltaic devices. Typically, TPV cells are made of low energy bandgap III-V semiconductors able to convert infrared thermal radiation. A diversity of semiconductors allows power harvesting from heat sources covering a large temperature range. In any case, heat sources should be combined with TPV cells having an energy bandgap matching their emission

spectrum. Therefore, low-temperature emitters require low energy bandgap TPV cells. However, such TPV cells are not performing well at room temperature resulting in low efficiencies and generated electrical power densities. TPV cells can be coupled with infrared emitters in the near field with the aim of enhancing the generated electrical power through the contribution of evanescent waves to radiative heat transfer. Up to now, low performances were reported for near-field thermophotovoltaic devices. As a conclusion, converting thermal photons in the near field with high efficiencies and electrical power densities should be achieved by using a cooled low energy bandgap TPV cell matching the emission spectrum of the infrared thermal emitter.

Chapter VI

VI Near-field thermophotovoltaic measurements with InSb TPV cells

VI.1 Introduction

The main objective of the work presented in this chapter is to demonstrate the enhancement of the electrical power photogenerated by the TPV cell (P_{TPV}) when the distance between the cell and the emitter decreases, achieved with high photoconversion efficiency and high generated electrical power density. The fabrication process of the InSb TPV cells is briefly described. Characterizations of the cells are performed as a function of temperature and for different illumination conditions, with the aim of assessing their performances. Integration of the cells in the experimental setup is detailed, along with methods for performing near-field thermophotovoltaic (NF-TPV) experiments. Then, measurements are done with the same spherical emitters as those used for radiative heat transfer measurements (see chapter IV). A parametric study investigating the cell diameter, substrate thickness, p-doping level, emitter material and growth conditions allows to determine the best configuration to maximize P_{TPV} in the near field. The main objectives of the work are shown to be fulfilled, by using a graphite emitter and the TPV cells specifically designed for near-field thermophotovoltaics.

VI.2 InSb TPV cells

Fabrication of the InSb TPV cells was performed at *Institut d'Électronique et des Systèmes* (*IES, UMR 5214, Montpellier, France*) by Jean-Philippe Perez and Dilek Cakiroglu. Design of the cells was made in the work of Vaillon *et al*.[74], and the complete technological process is provided in the work of Cakiroglu *et al*.[166]. In this section, an overview of the design and the fabrication process is presented highlighting key parameters.

VI.2.1 Design of the cells

Most of InSb TPV cells were fabricated using the optimum growth parameters formerly established. Near-field radiation heat transfer and low-injection charge transport simulations were used to find the optimum architecture of the p-n junction layers. Various cases combing different doping levels and thicknesses of the p- and n-doped layers were investigated in order to find those maximizing the output electrical power. In most of the case, the p-n junction was grown on a 500 µm thick n-doped InSb substrate with $N_D = 10^{17}$ cm^{-3} (Figure VI.1). According to simulations, the top p-doped layer must be 0.5 µm thick with $N_A = 10^{17}$ cm^{-3} or 10^{18} cm^{-3}, and the bottom n-doped layer must be 2.5 µm thick with $N_D = 10^{15}$ cm^{-3} corresponding to a growth with no intentional doping. High p-doping levels allow to increase the potential barrier of the junction, thus enhancing the performances of the cell. In addition, the thickness of the substrate can be decreased in order to further enhance the performances by lowering the parasitic absorption in the substrate and allowing more thermal radiation to be reflected on the back surface passing a second time through the p-n junction. The fabrication process implies that the cells can have an active area (*AA*) diameter of 20, 40, 80 or 160 µm. The active area is the portion of the p-doped layer of the cell exposed to incident radiation from the environment. Photons collected in this area are possibly absorbed and their energy may be converted into electrical energy. Micron-sized photovoltaic cells allow low series resistance. However, the series resistance losses raise with current, which would become huge in large area photovoltaic cells. Smart designs of the front electrode have been recently discussed in this respect[167,168] and could help in upscaling, a step which is not addressed in this thesis.

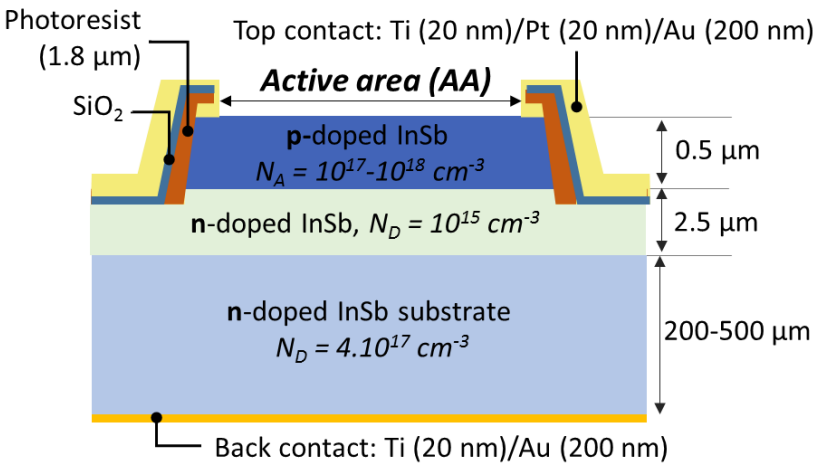

Figure VI.1: Cross-sectional schematic view of the InSb TPV cell design

VI.2.2 Fabrication process

VI.2.2.1 Molecular beam epitaxy

The p-n junction of the InSb TPV cell is formed by molecular beam epitaxy (MBE). The cells were grown on InSb n-doped substrates in a RIBER 412 reactor. Beryllium was used as the p-type dopant. First, native oxide on the surface of InSb substrates was removed using a low-temperature (673 K) hydrogen plasma process imposed by the relatively low melting temperature of InSb (800 K). This technique resulted in a flat surface ready for epitaxy. Optimum growth conditions were determined using InSb test samples. Then, the best incorporation rate ratio $IRR = R_{Sb}/R_{In}$, with R_{Sb} and R_{In} respectively the antimony and indium growth rate (in monolayer per second ML.s^{-1}), was determined using X-ray diffraction and AFM for assessing the crystalline and structural quality. Figure VI.2a shows that the best result was obtained with IRR = 4 for a growth temperature T_G = 713 K leading to the smallest full-widths at half-maximum of the diffraction peak of 19 arcsec. The optimum growth temperature was determined by photoluminescence measurements using a Brucker Vertex 70 FTIR and an InSb test sample at 80 K. In Figure VI.2b, the photoluminescence peak centered at 0.234 eV, corresponding to the energy bandgap of InSb was the most intense with a sample grown at T_G = 713 K. Some cells were fabricated with a substrate thinned down to 200 µm. To do so, mechanical polishing was performed on several samples in order to reduce the substrate thickness down to 200 µm. In the end, five types of InSb TPV cells were fabricated, with either a 200 or 500 µm thick substrate and a p-doped top layer with $N_A = 10^{17}$ cm^{-3} or 10^{18} cm^{-3}. In order to evaluate how detrimental it is for the performances of the cell, an additional sample was made using non-optimal growth parameters that may impact the crystalline structure of the cell. As described in the work of DeSutter *et al.*[169], cells with large density of non-radiative recombinations should lead to a stronger enhancement of the photogenerated power in the near field relative to the far field, because of the increase of the external luminescence caused by radiative heat transfer with evanescent waves

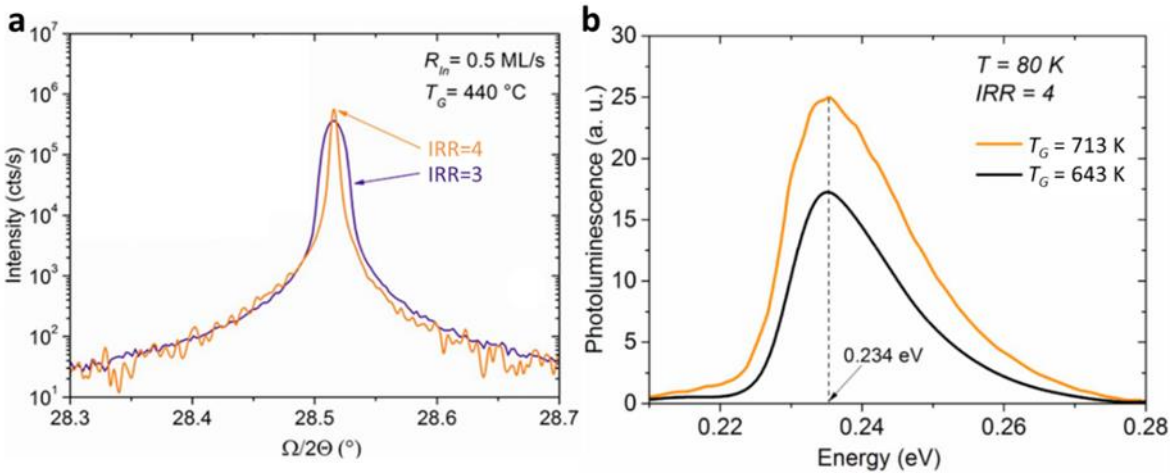

Figure VI.2: Determination of the optimum MBE growth parameters.
(a) High resolution X-ray diffraction (004) reflection spectra of InSb layers grown by MBE. (b) Photoluminescence spectra measurements performed at a substrate temperature of 80 K for InSb layers grown by MBE. Figures from Cakiroglu et al.

VI.2.2.2 Processing of the InSb TPV cells

InSb cells were processed using a classical UV photolithography technique in order to create circular mesa structures with diameters of 70, 90, 130 and 210 µm and a depth of 1.8 µm. The passivation of the cells was performed straight after mesa etching in order to avoid parallel current surface leakages. This issue is seen in the dark I-V characteristics for a reverse voltage polarization. An organic passivation technique was selected using the AZ1518 photoresist deposited by spin-coating. This material was chosen among SiO_2 and ZnS during a previous study, as it was the one minimizing the reverse polarization current of the cell ($V < 0$ in the I-V curve). A SiO_2 layer was added in order to prevent damages of the cells during the wire bonding process. Finally, Ti/Pt/Au ohmic contacts with thicknesses of 20/20/200 nm were added using e-beam evaporation, on top of the SiO_2 layer, and 20/200 nm of Ti/Au contacts were deposited at the back of the InSb substrate (Figure VI.3). In the end, the circular mesa diameters of 70, 90, 130 and 210 µm correspond to active areas (*AA*) with diameters of 20, 40, 80 and 160 µm.

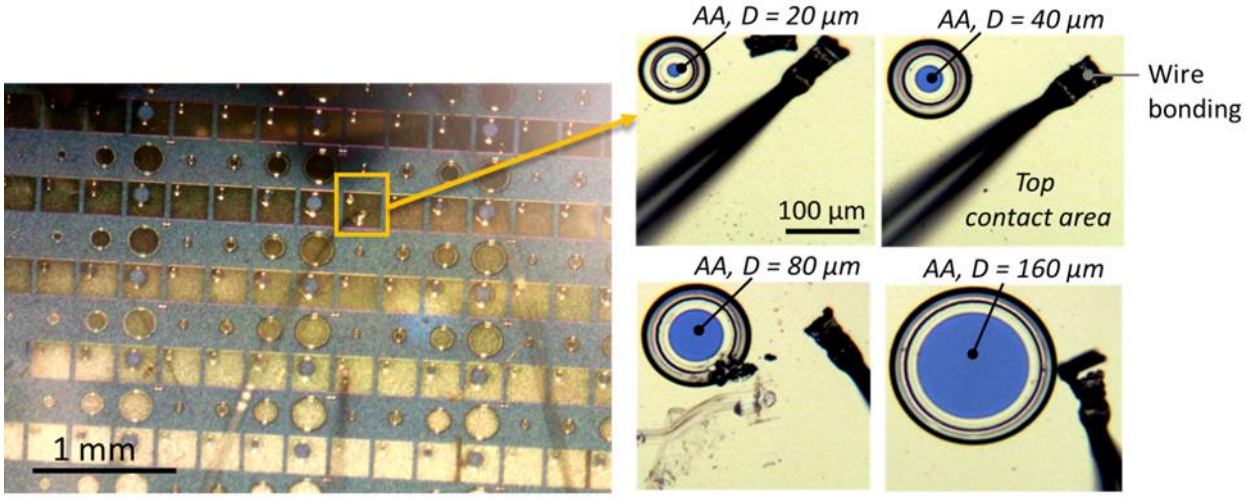

Figure VI.3: Top view of a cell sample and optical microscope top view of InSb TPV cells

InSb cell samples (~ 1x1 cm^2) were glued with silver paste on a chip holder, partially coated with gold in order to provide an electrical contact with the back of the cells. Electrical contacts on the top contact areas were provided by wire bonding. At this point, InSb TPV cells were ready to be integrated in the experimental setup in order to be characterized and for performing NF-TPV measurements.

VI.2.3 Integration of the TPV cells in the experimental setup

The chip holder, where the cells were glued, was additionally glued on the cold finger with silver paste acting as adhesive and thermal contact (Figure VI.4). It is reminded that the cold finger is the part of the experimental setup located in the vacuum chamber that is cooled down to cryogenic temperatures (see Sec. III.3.2 for details on the cooling system). The cooling system is necessary because the cells are expected to work properly only at cryogenic temperatures (see Sec. V.4). A good thermal conduction is needed between the chip holder and the cold finger in order to efficiently cool the cells down to 77 K. Electrical contacts on top of the cells are individual for each cell (3 cells are connected in the figure), while the back contact is common for all cells. Electrical wires were welded on the contact areas of the chip holder, which were linked to the top contacts of the cells via wire bonding. Outside the vacuum chamber, these electrical connections were made by means of BNC coaxial connectors (see Figure III.17). Top and back contacts were connected to a remotely controlled Keithley 2400 source measurement unit. I-V characteristic measurements of the InSb TPV cells were performed by applying a voltage scan to the cell while the resulting current is measured. Prior to performing NF-TPV experiments, InSb TPV cells were tested in order to observe their behaviour as a function of temperature.

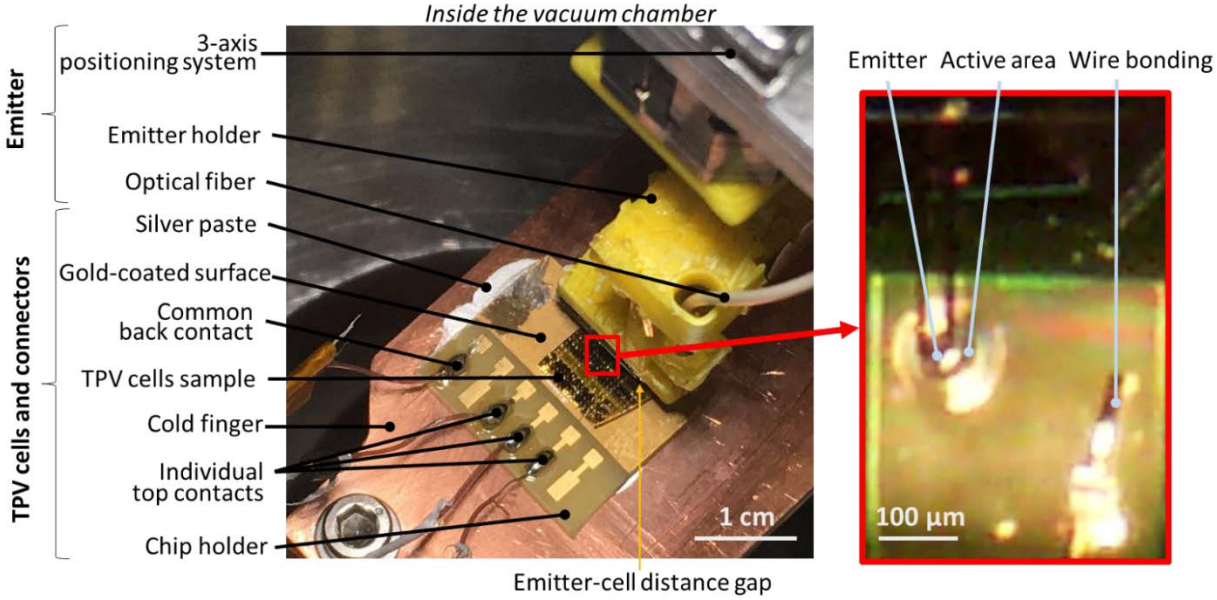

Figure VI.4: View of a TPV cell sample on its chip holder glued on the cold finger, inside the vacuum chamber, with the emitter positioned above the cells

VI.2.3.1 Current-voltage characteristics in the far field at different temperatures

In Figure VI.5, performances of the TPV cells are assessed as a function of temperature, from 250 K down to 30 K, by analyzing the measured I-V curves. In this configuration, thermal radiation illuminating the cell comes only from the ambient-temperature environment. Above ~ 110 K, I-V

characteristics are linear. They do not correspond to a diode behavior anymore but are those of a passive resistive device. In this case, the thermally-generated carrier concentration is high and the p-n junction effect does not exist anymore. When temperature decreases, the exponential shape of the curve progressively appears. The reverse bias current decreases while the forward bias current rises. It is observed in the semi-logarithmic scale (Figure VI.5b) that for $T \leq 90$ K the open circuit voltage (V_{OC}) becomes positive and keeps increasing when the cell temperature is decreasing. The presence of a positive V_{OC} means that the cell is generating power due to the ~ 300 K ambient illumination. Thus, according to expectations, the cell needs to be cooled to work properly. For NF-TPV experiments, a working temperature of 77 K is chosen as it corresponds to the commonly used boiling point of liquid nitrogen. In addition, the illumination level in the experiments with the spherical emitter is higher (see Sec. IV.3.8.2) so the generated current is large enough to be detected at this temperature, indicating that a lower temperature cooling to reduce the dark current is not required. I-V characteristics indicate low series resistance in the devices with a fill factor $FF = 0.69$ under ambient illumination. All these results demonstrate that InSb TPV cells showed good performances at 77 K while illuminated only by thermal radiation coming from the ambient temperature environment. Additional measurements performed in the far field with higher illumination levels confirmed these good performances[166]. In the following, we assess near-field measurements.

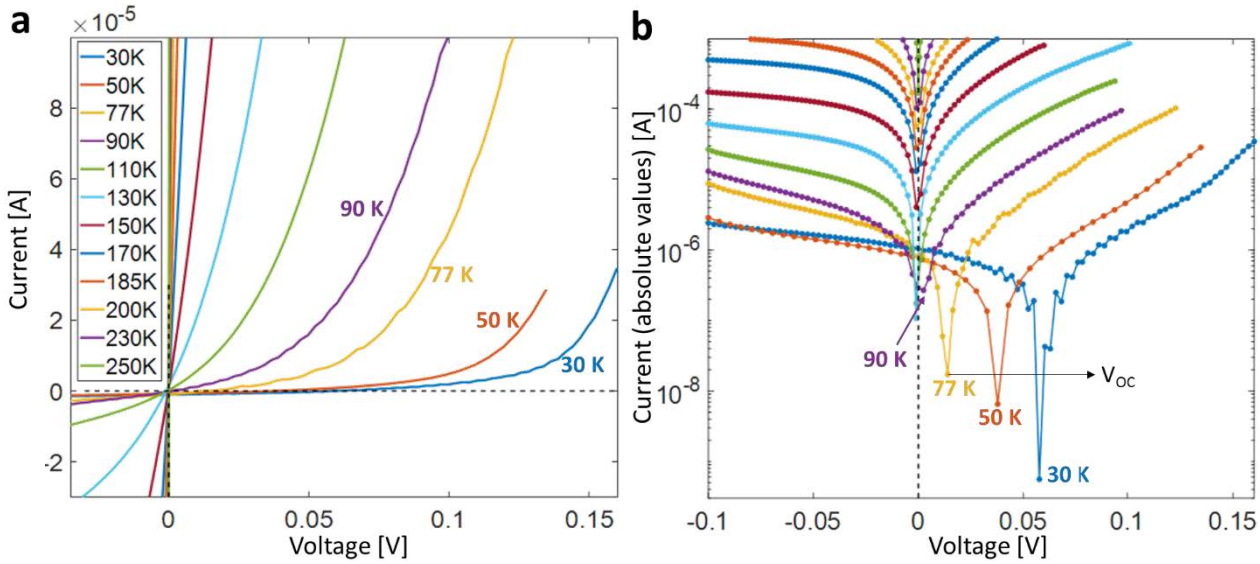

Figure VI.5: I-V characteristics of an InSb TPV cell as a function of temperature, under ambient-temperature illumination condition.
(a) Linear scale. (b) Semi-logarithmic scale with the current in absolute values.

VI.2.3.2 Positioning of the emitter

It is reminded that the position of the cells was fixed in the experiment, and the moving part was the emitter. The emitter was initially placed at approximately 2 mm above the surface of the cell and could be moved in *x*-, *y*- and *z*-axis directions by the custom piezoelectric positioning system. Positioning of the emitter above the centre of the active area of the cell was done in three steps.
First, the position of the emitter was controlled using piezoelectric positioners and the long working distance microscope camera (see details of the general experimental setup in Sec. III.3.1). The emitter, often heated above 730 K, was brought into contact with the chip at an arbitrary location

then retracted at a safe distance of around 100 µm and moved over the cell (see Figure VI.4 for a top view). The contact was detected by measuring electrical resistance variations of the emitter, as shown in Figure III.14. In a second step, the emitter was brought into contact with the cell and retracted at a distance smaller than 5 µm. There, the last step consisted in measuring the short-circuit current (I_{SC}) of the cell according to the emitter displacement along the x and y axes. Once the maximum current was reached along one axis, the maximum current position along the other axis corresponded to the centre of the active area. It is reminded that parallelization of the emitter and cell surfaces was not required due to the sphere-plane configuration, chosen on purpose in place of the plane-plane configuration.

In Figure VI.6, the hot emitter was placed at $d \approx 10$ µm from the cell surface and was moved laterally from approximately -120 µm to +120 µm relative to the center of the cell, while the short-circuit current was measured. As expected, a maximum is observed for the current when the emitter is above the center, which first decreases rapidly and then more smoothly as the emitter goes away from the center. Measurements are compared with the theoretical model using the view factor, with a normalization applied at the maximum value. A very good agreement is found between measurements and the view factor predictions. It can be noted that measurements are slightly non-symmetrical. This issue is mainly due to the motion of the x and y positioners, which is not always perfectly smooth and linear and can vary slightly over large displacements (larger than 100 µm). Most importantly, performing this kind of measurement along both x and y directions for a lower displacement range (approximately the size of the active area) provides a precise positioning of the emitter above the center of the cell. This was performed at vertical distances lower than 5 µm.

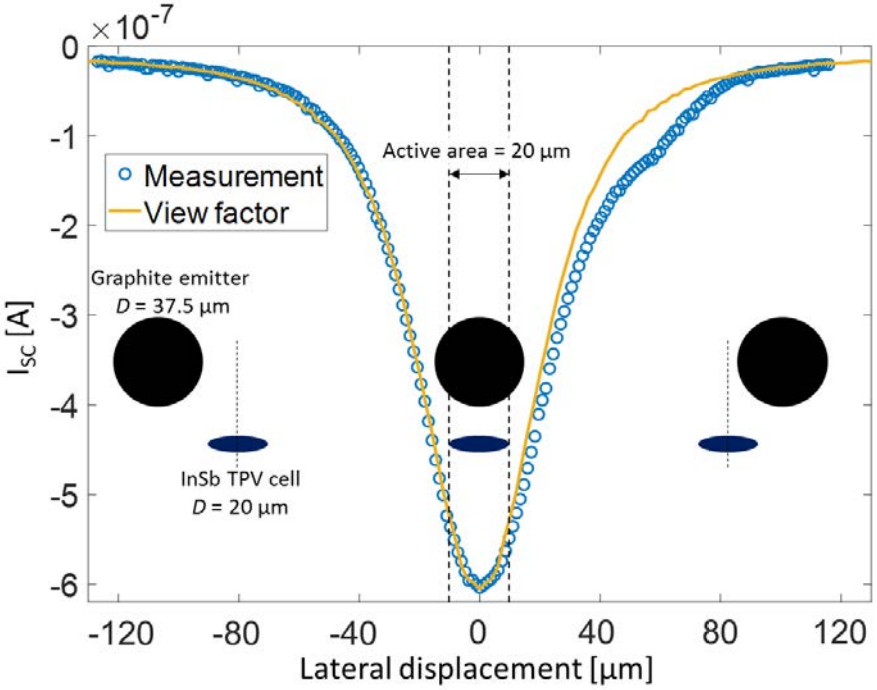

Figure VI.6: Short-circuit current as a function of the lateral displacement of the emitter and comparison with the view factor

VI.2.4 Superposition principle and performances of the cells

In order to characterize the cells under illumination, I-V curves were measured for various emitter temperatures and emitter-cell distances. Theoretically, as the illumination level increases, the I-V

characteristic of the cells should keep the same shape while being shifted to lower currents into the photogeneration quadrant (see Sec. V.5). This property is referred to as the superposition principle. It tells that the measured photocurrent is equal to the sum of the current generated in dark conditions and the short-circuit current under illumination[170] in low-injection conditions[162]. This principle is very interesting experimentally because the entire I-V curve can be retrieved by measuring only the curve in the dark, and then measuring I_{SC} as a function of illumination. In order to verify the superposition principle, a first I-V curve measurement was performed with a cell cooled down to 77 K, having an active area diameter of 20 µm, under dark conditions. A cooled radiative shield located over the active area of the cell was used to block ambient radiation coming from the environment. It was verified that the emitter provides different levels of illumination to the cell by either changing the emitter-cell distance or the emitter temperature (Figure VI.7a). It can be noticed that the I-V characteristics in the dark exhibits a slightly positive value for the short-circuit current (~ 3 nA) due to a slight offset of the electronics. As expected, it is observed that when illumination increases, the I-V curves are lowered into the photogeneration quadrant corresponding to larger I_{SC} and V_{OC} (see Table VI.1).

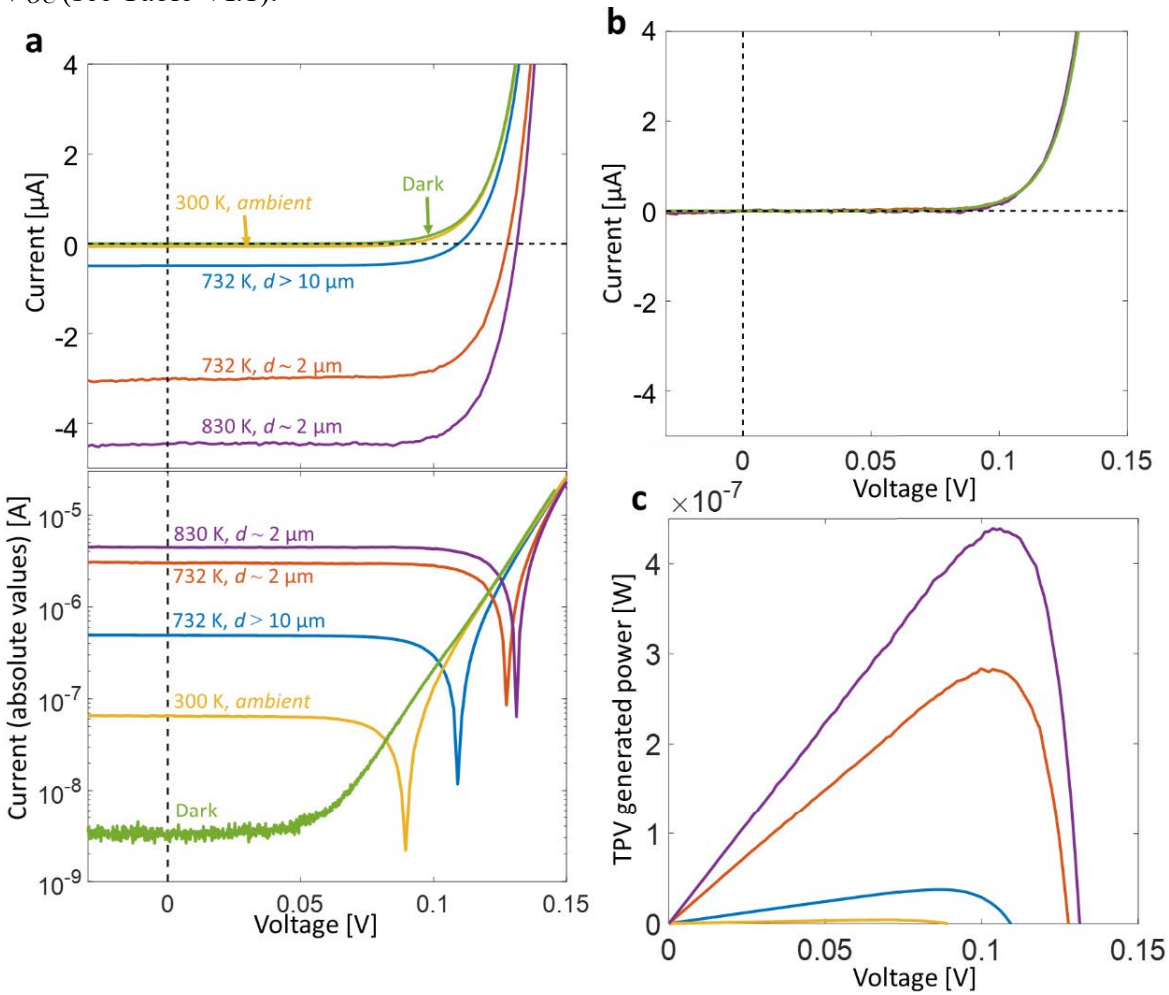

Figure VI.7: I-V curves for an InSb TPV cell at 77 K, having an active area diameter of 20 µm in the dark and under different illumination conditions.
(a) I-V curves under illumination for different distances and emitter temperatures, with a linear (top) and semi-logarithmic scale (bottom). (b) Curves shifted in current: the short-circuit current of each curve is set equal to zero. (c) Generated electrical power as a function of voltage

From 300 K (ambient) to 830 K illuminations at $d \sim 2$ µm, I_{SC} increases by ~ 2 orders of magnitude, from 65 nA up to 4.46 µA. V_{OC} increases from 89 mV to 131 mV. Figure VI.7c shows the photogenerated electrical power P_{TPV} as a function of voltage for different illuminations. The maximum power increases from 4 nW up to 439 nW. It is worth noticing that the fill factors range from 0.69 to 0.75 at the highest illumination, which is remarkable for a cell with a low energy bandgap.

In Figure VI.7b, all curves are shifted in current only so their I_{SC} are all set equal to 0. It appears that all curves are well superimposed, meaning that the superposition principle is valid for this kind of TPV cell and illumination levels. The fact that the superposition principle is valid is a proof that the temperature of the cell remains the same (77 K). Since the shape of I-V curves strongly depends on temperature (see Figure VI.5), the curves would not be superimposed if the cell temperature was modified.

An estimation of the radiative power incident on the cell Q_{rad} was made (Table VI.1). A 300 K blackbody illumination from the environment was considered in the absence of emitter, while contributions of propagative and evanescent waves were calculated from the hot emitter at $d \sim 2$ µm (see details of calculations in chapter II). The emitter-cell distance for these experiments was not well determined, with an uncertainty of ± 0.5 µm, leading to uncertainties on radiative heat flux calculations. For the ambient temperature illumination condition, the cell receives thermal radiation considered to be that of a blackbody at 300 K, calculated using Stefan-Boltzmann's law (Eq. (I.5)). When the emitter is close to the cell ($d \sim 2$ µm), it partially blocks thermal radiation coming from the environment but provides a significantly higher illumination level (> 10 kW.m^{-2}) because of its proximity and its high temperature. It was estimated that the efficiency of the cell increases from 2.8 % with ambient illumination, up to ~7–8 % under infrared illumination from a graphite emitter above 732 K. The rise in efficiency is explained by the shift of the wavelength of maximum thermal radiation λ_{Wien} as temperature increases. At 300 K, $\lambda_{Wien} \approx 10$ µm corresponds to an energy of photons of 0.128 eV, lower than the energy bandgap of InSb at 77 K (0.234 eV). At 732 and 830 K, energies of photons emitted at λ_{Wien} are respectively 0.313 and 0.355 eV, larger than E_g(InSb). Therefore, a larger portion of thermal radiation coming from the heated emitter is potentially converted into electrical power, compared with thermal radiation coming from the environment at 300 K. The measurement uncertainties do not allow to conclude if the estimated efficiency is affected when the emitter temperature rises from 732 to 830 K. This study demonstrates that the InSb TPV cells are functioning well under infrared thermal illumination, with a graphite emitter heated up to 830 K.

Table VI.1: Summary of the InSb TPV cell performances under different illuminations

Illumination	V_{OC} [mV]	I_{SC} [µA]	$P_{TPV,\,max}$ [nW]	$P_{TPV,\,max}$ [kW.m^{-2}]	*FF*	Q_{rad} *(estimated)* [kW.m^{-2}]	η_{TPV} *(estimated)* [%]
300 K, ambient	89	0.07	4	0.013	0.69	0.457	2.8
732 K, $d > 10$ µm	115	0.47	38	0.121	0.70	*Unknown distance*	
732 K, $d \sim 2$ µm	127	3.02	283	0.901	0.74	11.2 ± 1.0	8.0 ± 0.8
830 K, $d \sim 2$ µm	131	4.46	439	1.397	0.75	19.3 ± 1.6	7.2 ± 0.7

VI.3 Experimental protocol for near-field thermophotovoltaic measurements

In this section, the experimental protocol for near-field thermophotovoltaic measurements is described. The aim is to measure the maximum photogenerated electrical current, along with radiative heat transfer, as a function of distance between the emitter and the cell. When both measurements are combined, one can determine the near-field TPV conversion efficiency as the electrically generated power from contribution of evanescent waves divided by the radiative power received by the cell in the near field. Since near-field radiative heat transfer measurements are performed with the same method as that described in Sec. III.3.1.3, following sections focus on measurements of the electrical power generated by the cell as a function of distance.

VI.3.1 I-V and P_{TPV}-V curves as a function of distance

Measuring the maximum generated power as a function of distance can be achieved using different methods. First, a step-by-step approach can be performed while measuring the I-V curve of the cell at each step. A few seconds are necessary to acquire an I-V curve, but the measurement should be repeated at each nanometer-scale step leading to large durations of experiments. Performing quick experiments is preferable because it was observed that the cold finger is affected by mechanical drifts caused by thermal expansion (see Sec. III.3.2.2). Therefore, two other methods involving quick (~ 1 min) approaches are investigated.

VI.3.1.1 Method using the superposition principle

This method uses the superposition principle, whose validity has been demonstrated in Sec. VI.2.4.

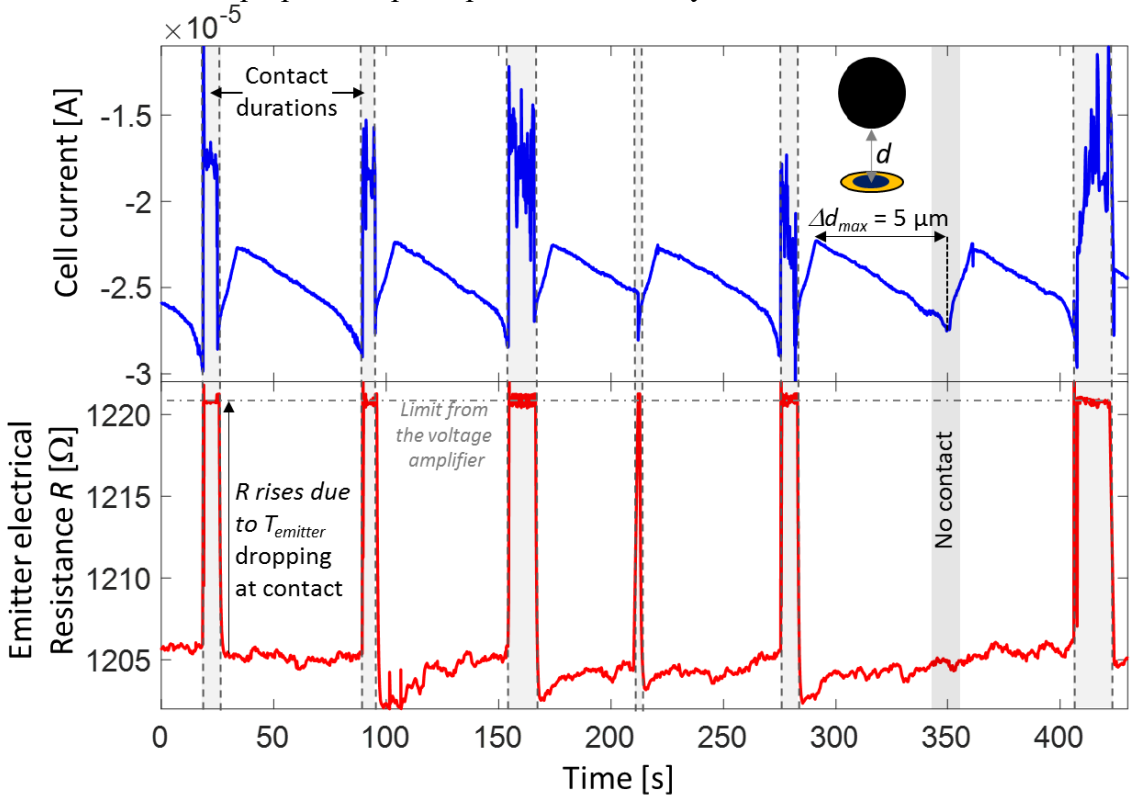

Figure VI.8: Cell current and emitter electrical resistance as a function of time, during a series of approaches between a 732 K graphite emitter and a 77 K InSb TPV cell

First, a reference I-V curve is measured under ambient illumination. The small short-circuit current I_{SC} of the reference curve is subtracted in order to obtain the curve corresponding to dark conditions: $I_{TPV}^{ref}(V = 0) = 0$. Then, series of approach curves are performed with the hot emitter, where only I_{SC} is measured (at $V = 0$) as a function of distance, from ~ 5 µm down to contact. The contact point is observed as usual on the thermal signal of the emitter but also on I_{SC} measurements. Figure VI.8 shows simultaneous measurements of the electrical current of the cell and the electrical resistance of the emitter as a function of time. Contact durations are highlighted where the electrical resistance of the emitter rises, corresponding to a temperature drop (see Figure III.8) due to thermal conduction with the cold cell. At contact, the electrical current of the cell increases due to the heating of the cell by the emitter. When temperature of the cell increases, performances of the cell are lowered as observed in Figure VI.5. Due to mechanical drift of the cold finger, contact may not be reached at each approach. In the figure, the highlighted area near t = 350 s represents the transition between an approach (duration of 60 s) and a withdrawal (duration of 10 s) of the emitter, when the maximum distance displacement Δd_{max} = 5 µm is reached. In this area, there is no contact so the electrical resistance signal does not rise. When contact is reached, both signals are recorded in order to calculate the average curve for getting a better signal-to-noise ratio.
In Figure VI.9a, I_{SC} is plotted as a function of z-piezo position between a 830 K graphite emitter (diameter of 37.5 µm) and an InSb TPV cell at 77 K with an active area diameter of 20 µm. The red curve corresponds to an average of 19 curves, and the uncertainty (standard deviation) is represented by the pink area. Relative uncertainty on I_{SC} measurements is ~1 % only, therefore it is barely visible in the figure. It is observed that I_{SC} increases from 2.7 to 10.1 µA as distance decreases. This increase is explained by the enhancement of radiative power incident onto the cell, both due to the contributions of propagative (view factor) and evanescent waves. The two contributions are separated by comparing the evolution as a function of distance of the output electrical power with that predicted by the view factor, representative of the propagative waves (see details in Sec. VI.3.2). Finally, I-V curves for different distances are calculated by shifting the reference I-V curve plotting $\left(I_{TPV}^{ref} + I_{SC}(d)\right)$-V curves at each distance (Figure VI.9b).

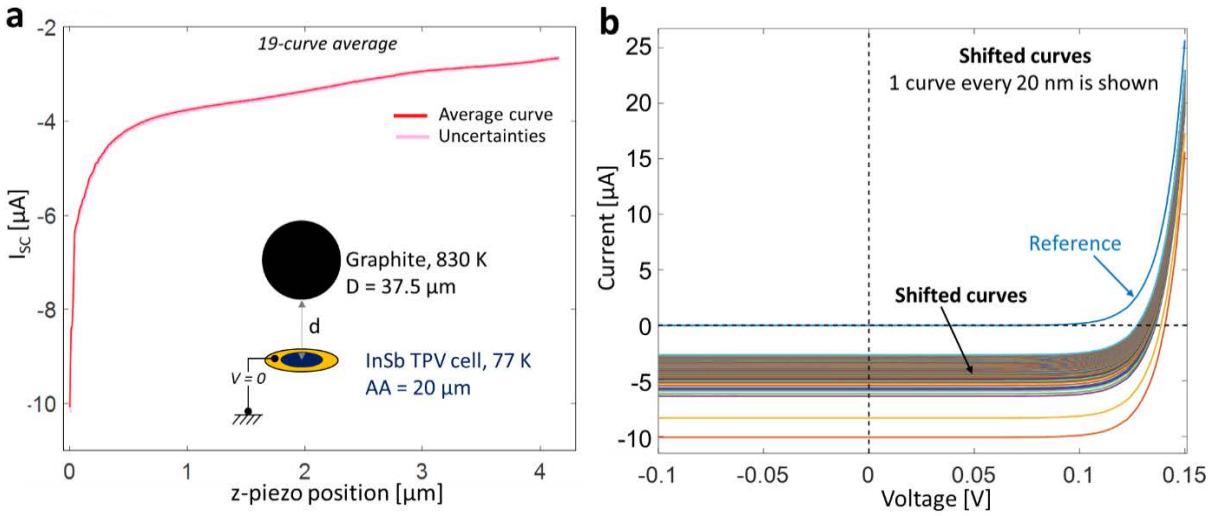

Figure VI.9: I-V curves determination as a function of z-piezo position, using the superposition principle
(a) I_{SC} as a function of distance for a 77 K InSb cell with a 20 µm diameter active area, illuminated by a 37.5 µm diameter graphite emitter at 830 K. (b) Reference and I-V curves shifted by $I_{SC}(d)$

The reference I-V curve is plotted in blue and has an I_{SC} equal to 0. Shifted curves have the same shape as the reference curve but are shifted in I_{SC}, following the $I_{SC}(d)$ curve shown in Figure VI.9a. For clarity, shifted curves are shown with a distance step of 20 nm. Shifting the curves in I_{SC} also has an influence on V_{OC}, increasing it from 127 to 140 mV. From these curves, one can infer the electrical power generated by the cell P_{TPV} and its maximum $P_{TPV,max}$ as a function of distance.
Figure VI.10a shows P_{TPV} as a function of voltage for different distances, still with a 20 nm step. Similarly to I_{SC}, P_{TPV} increases as distance decreases. It is interesting to remark that the voltage where P_{TPV} is maximum, represented by the black dashed line, increases from 101 up to 115 mV as distance decreases. $P_{TPV,max}$ is shown in Figure VI.10b as a function of distance. It increases from 0.251 up to 1.071 µW. The fact that this enhancement (x4.3) is larger than that of I_{SC} (x3.7) is explained by the increase of the voltage V_{max} where $P_{TPV,max}$ is reached. Similarly to I_{SC}, the total enhancement of P_{TPV} is due to both evanescent and propagative wave contributions. The effect of evanescent waves is observed in the near field, especially where the enhancement is sharp (d < 500 nm in the figure). Above 3 µm, the evanescent wave contribution is very small, making propagative waves the main source of thermal radiation incident on the cell. The method for differentiating the effects of the two contributions on the electrical power is provided in Sec. VI.3.2.
Using the superposition principle for measuring P_{TPV} as a function of distance does not provide a direct measurement of the electrical power because it is inferred from a reference I-V curve and an $I_{SC}(d)$ measurement. The method described in the next section requires more time to be performed experimentally but is more reliable because it allows to directly measure I-V curves as a function of distance, and thus to the generated electrical power.

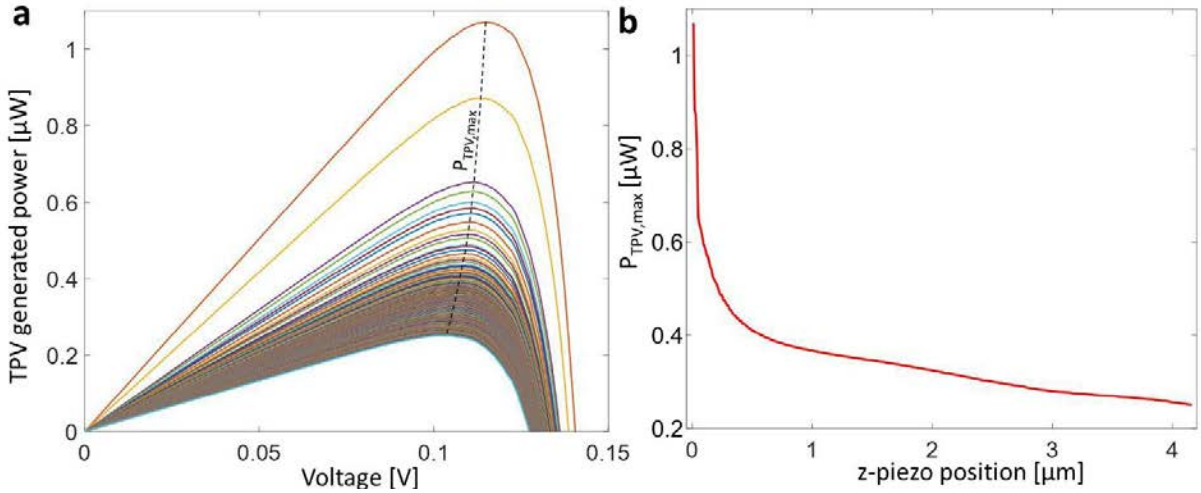

Figure VI.10: Determination of the electrical power generated by the cell as a function of z-piezo position.
(a) P_{TPV} as a function of voltage for different distances. (b) $P_{TPV,max}$ as a function of z-piezo position

VI.3.1.2 Series of approaches at different voltages

This method consists in measuring the current generated by the cell as a function of distance for a given voltage, then repeat the process for other voltages. Selected results are shown in Figure VI.11a, where the current generated by the cell at different voltages is measured as a function of distance. Approaches of the emitter are performed with a voltage applied to the cell, ranging from 102 to 122 mV. This voltage range does not allow to recover the entire I-V curve but focus on the interesting part where P_{TPV} is maximum. Experiments with a wider range of voltages are possible but take much more time to be performed.

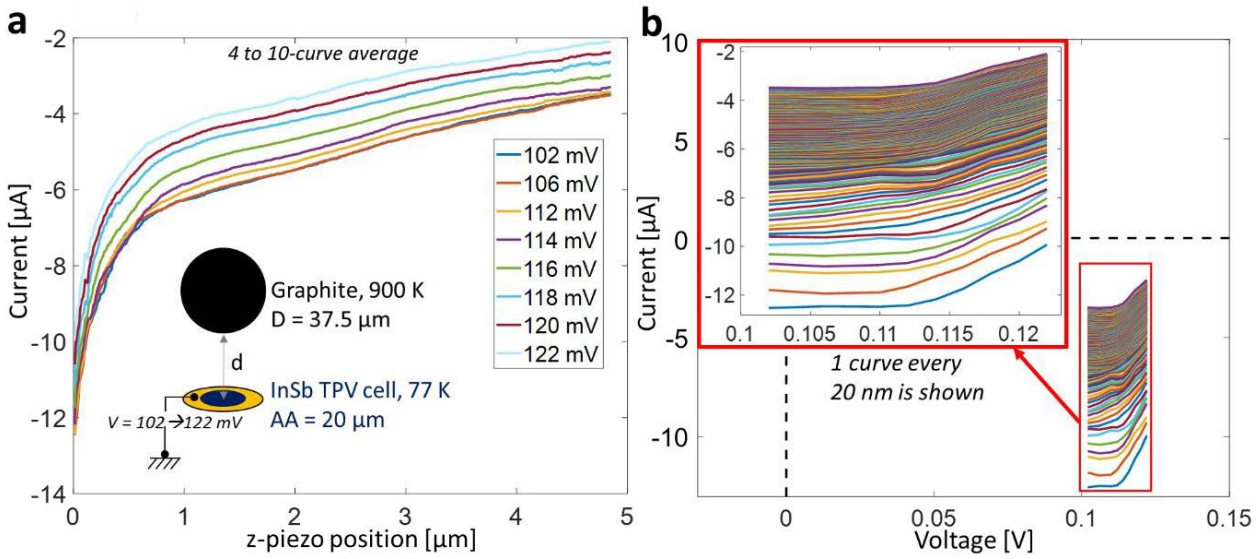

Figure VI.11: I-V curves determination as a function of z-piezo position, using approaches at different voltages
(a) Current as a function of z-piezo position for a 77 K InSb cell with a 20 µm diameter active area, illuminated by a 37.5 µm diameter graphite emitter at 900 K. (b) Measured I-V curves in the voltage range where P_{TPV} is maximum

It is observed in the figure that the curves are superimposed below a cell voltage of 112 mV. This voltage range corresponds to the flat portion of the I-V curve (see Figure VI.9b), where the current does not depends on voltage. At larger voltages, the current is larger corresponding to the exponentially growing portion of the I-V curve. From the current-distance curves at different voltages shown in Figure VI.11a, current-voltage curves at different distances are reconstructed and plotted in Figure VI.11b. Each curve represents an I-V curve measured at one distance, at voltages between 102 and 122 mV. The figure is at the scale of the entire photogeneration quadrant, while the inset is a closer view of the curves. As expected, the curves are lowered into the photogeneration quadrant as distance decreases. From these measurements, the electrical power generated by the cell is determined and provided in Figure VI.12a. In the figure, one can recognize the top shape of P_{TPV}-V curves like those plotted in Figure VI.10a. The maximum generated power increases from 0.383 up to 1.392 µW. From each curve, $P_{TPV,max}$ is extracted and plotted as a function of distance in Figure VI.12b. The behavior of the curve is similar to that of the curve determined using the superposition principle (Figure VI.10b). Above d = 1 µm, the variations of $P_{TPV,max}$ are gradual and expected to be caused by the view factor between the spherical emitter and the cell only due to propagative waves. Below 1 µm, the effect of evanescent waves becomes significant, leading to a sharper increase.
Contrarily to the previous method based on the superposition principle, this method allows direct measurements of P_{TPV} as a function of distance but requires more time to be performed. In the end, both methods give P_{TPV} as a function of distance.

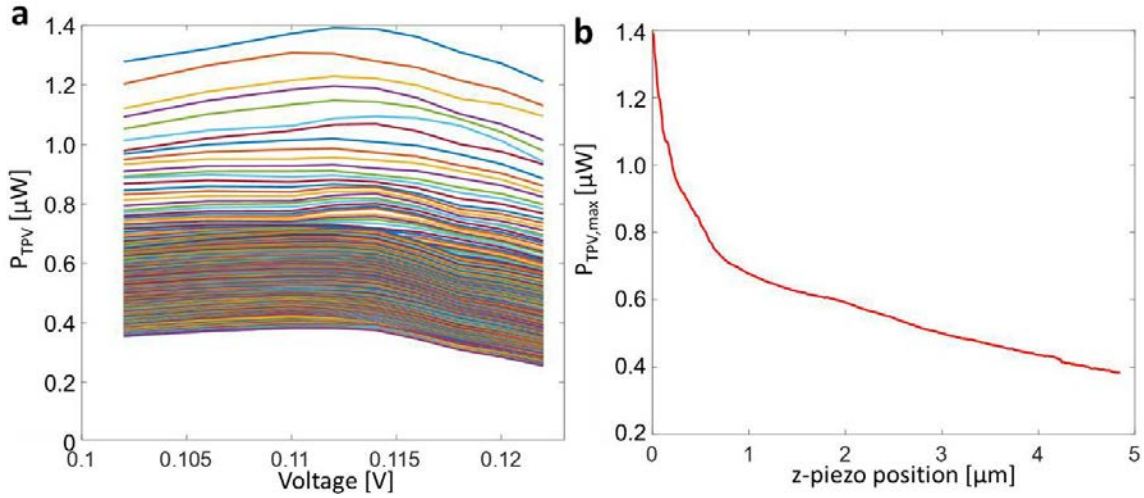

Figure VI.12: Measurement of the electrical power generated by the cell as a function of distance. (a) P_{TPV} as a function of voltage for different distances. (b) $P_{TPV,max}$ as a function of distance

VI.3.2 Determination of the near-field contribution

Determining the contribution of evanescent waves on radiative heat transfer between the emitter and the cell is a key step to assess the electrical power generated by converting near-field (evanescent) or far-field (propagative) thermal radiation. The experimental setup allows the measurement of the short-circuit current of the cell for distances up to 2 mm. In order to analyze the contribution of propagative waves to the photocurrent generation, the short-circuit current I_{SC} of a cell having an active area diameter of 20 µm was measured with the emitter moving from the contact up to d > 150 µm. The increase in I_{SC} as distance decreases can be compared with the evolution of the view factor if the variation of V_{OC} is small enough to be neglected. Table VI.1 indicates that for illumination levels leading to short-circuit currents I_{SC} between 0.5 and 4 mA the variation of V_{OC} for a similar cell is lower than 15%. At the largest distances, the current started to level off due to the low illumination. In this case, the *z*-piezo positioner was used in slip-stick mode with 80 nm steps. Then, measurements were compared to the evolution predicted by the analytic expression of the sphere-disc view factor given in Eq. (II.11). Figure VI.13 shows that the evolution of I_{SC} matches well the prediction of the view factor, from a few micrometers up to more than 150 µm. Below 2-3 µm, the measured data and the view factor prediction are not in agreement because the evanescent waves are contributing to the radiative heat transfer, in addition to the propagative wave contribution predicted by the view factor. The fact that the photocurrent generation depends on the propagative wave contribution, for distances larger than 3 µm, is useful to single out the evanescent wave contribution from NF-TPV experiments, when measurements are performed for distances up to 5 µm.

In Figure VI.14, the electrical generated power measured at the largest distance (for a different cell than that used in Figure VI.13) is used as the fitting parameter to the view factor evolution, assuming that $P_{TPV,max}$ results only from the contribution of propagative waves. The difference between the power $P_{TPV,max}^{vf}$ calculated with the view factor and the total measured power corresponds to the near-field electrical power at the maximum power point: $P_{TPV,max}^{NF} = P_{TPV,max} - P_{TPV,max}^{vf}$. Note that, in this case, the definition of the far-field contribution is that related to the view-factor theory, and that it can depart from an exact calculation of the contribution of propagative waves in the selected geometry by means of fluctuational electrodynamics.

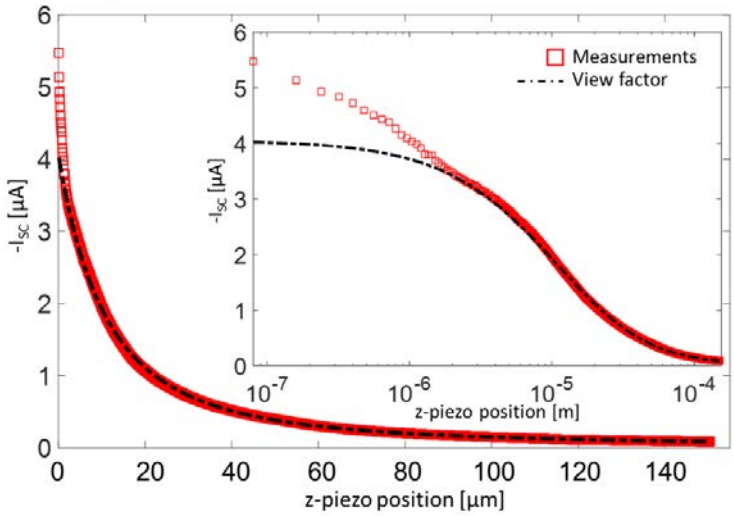

Figure VI.13: Short-circuit current as a function of the vertical displacement of the emitter and comparison with the view factor

In case of a slight error on the identification of the far-field contribution from the experimental data, the estimation of $P_{TPV,max}^{NF}$ is a lower bound to the actual near-field contribution. The contribution of propagative waves $P_{TPV,max}^{vf}$ increases almost linearly in the last 5 µm, from 0.33 up to 0.49 µW, whereas evanescent wave contribution increases sharply below 1 µm. The linear behavior of the contribution of propagative waves below 5 µm is expected because a series expansion of the analytic expression of the view factor (Eq. (II.11)) leads to a linear evolution. At the last distance before contact, the total generated electrical power reaches a maximum of 1.90 µW (6.05 kW.m^{-2}), including a contribution of 1.41 µW (4.49 kW.m^{-2}) from evanescent waves.

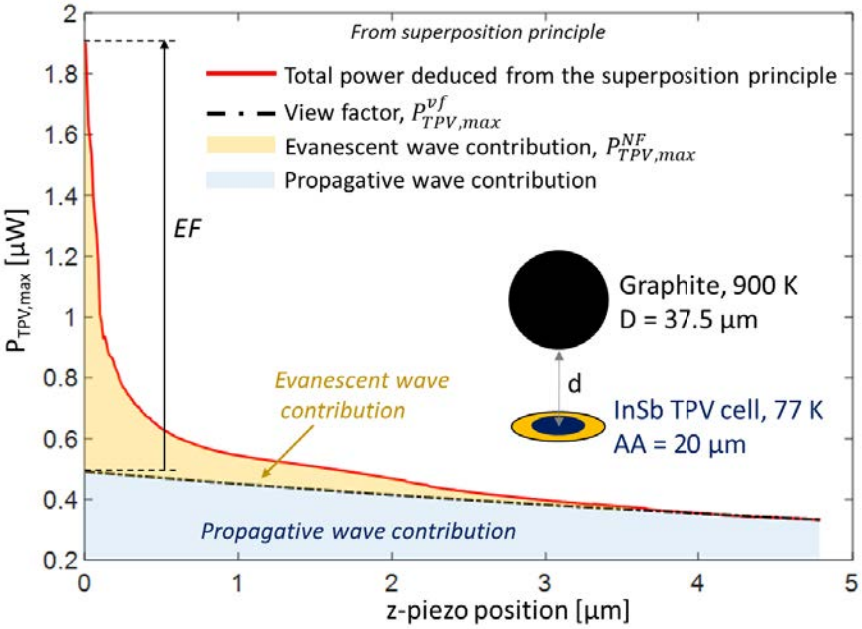

Figure VI.14: Electrical power at the maximum power point as a function of z-piezo position generated by an InSb cell at 77 K, having a 20 µm diameter active area, illuminated by a graphite emitter at 900 K

The near-field enhancement factor *EF* is calculated as:

$$EF = \frac{\max\left(P_{TPV,max}\right)}{\max\left(P_{TPV,max}^{vf}\right)}, \qquad (VI.1)$$

where $\max\left(P_{TPV,max}\right)$ is the maximum electrical generated power as a function of distance, $\max\left(P_{TPV,max}^{vf}\right)$ is the maximum generated power predicted by the evolution of the view factor. In the figure, the near-field enhancement factor *EF* is equal to 4.

Finally in Figure VI.15, the near-field generated electrical power $P_{TPV,max}^{NF}$ is plotted as a function of distance. This curve is representative of the electrical power generated by the conversion of radiative thermal power carried through evanescent waves. The inset in the figure is a representation using a logarithmic scale in order to observe $1/d^n$ behaviors. The grey area is representative of the 100 nm range where there is strong uncertainty on the distance determination induced mainly by mechanical vibrations of the cold finger (see Sec. III.4.2). Between 2 µm and 50 nm the evolution of $P_{TPV,max}^{NF}$ follows a $1/d^{0.8}$ behavior close to the $1/d^1$ asymptotic behavior expected for near-field radiative heat transfer considering the sphere-plane geometry (see Figure II.17). At small distances $P_{TPV,max}^{NF}$ levels off and its evolution tends to a $1/d^{0.2}$ behavior. This phenomenon may be explained by the uncertainty on distance determination close to contact, similarly observed during the near-field radiative heat transfer experiments reported in Chapter IV. At the largest distances $P_{TPV,max}^{NF}$ is expected to tend to 0 because of the decreasing contribution of the evanescent waves. With a logarithmic scale this behavior is observed as a sharp evolution following approximately a $1/d^4$ law.

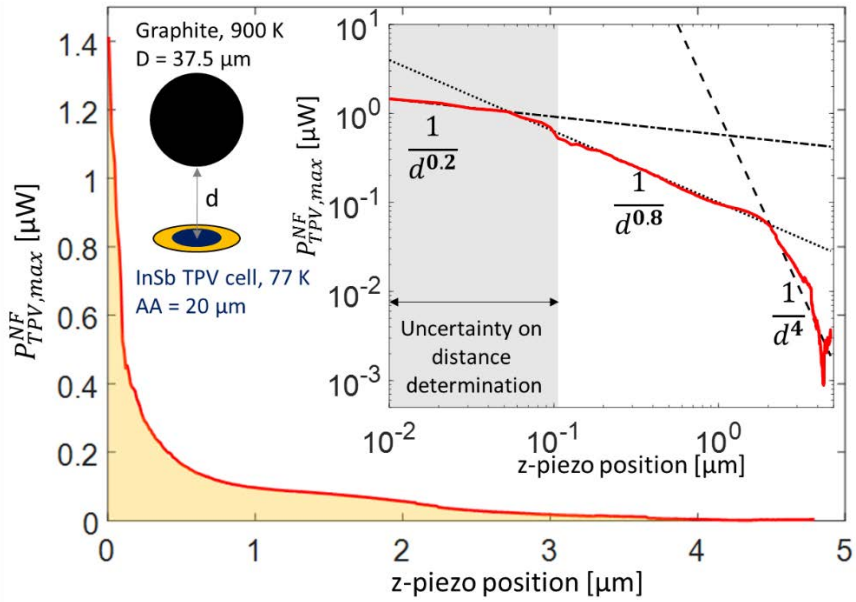

Figure VI.15: Near-field generated electrical power as a function of distance, by an InSb TPV cell at 77 K having a 20 µm active area diameter, illuminated by a graphite emitter at 900 K

VI.3.3 Near-field thermophotovoltaic conversion efficiency

Because near-field radiative heat transfer between the emitter and the cell is measured simultaneously with $P_{TPV,max}^{NF}$, one can deduce the near-field conversion efficiency from the

measurements. Near-field conversion efficiency η_{TPV}^{NF} is the electrical power generated by the cell $P_{TPV,max}^{NF}$, considering the contribution of evanescent waves, divided by the near-field exchanged radiative power Q_{NF}, also representative of evanescent waves:

$$\eta_{TPV}^{NF} = \frac{P_{TPV,max}^{NF}}{Q_{NF}}. \qquad (VI.2)$$

In Figure VI.16a, Q_{NF} is shown as a function of distance between a 900 K graphite emitter and a 77 K InSb TPV cell, having an active area diameter of 20 µm. This curve is the same as the one presented in Sec. IV.3.8.2, but plotted in power instead of conductance. At the closest distance to contact, Q_{NF} reaches 14.1 µW corresponding to a near-field illumination on the active area of 45 kW.m^{-2}.

Simultaneously with Q_{NF} measurements, $P_{TPV,max}$ is measured as a function of distance and shown in Figure VI.16b. The near-field contribution to the generated electrical power $P_{TPV,max}^{NF}$ is determined as explained in Sec. VI.3.2 from the comparison with the theoretical evolution predicted by the view factor. Finally, Figure VI.16c shows the near-field conversion efficiency η_{TPV}^{NF} as a function of distance, with uncertainties caused by Q_{NF} measurements

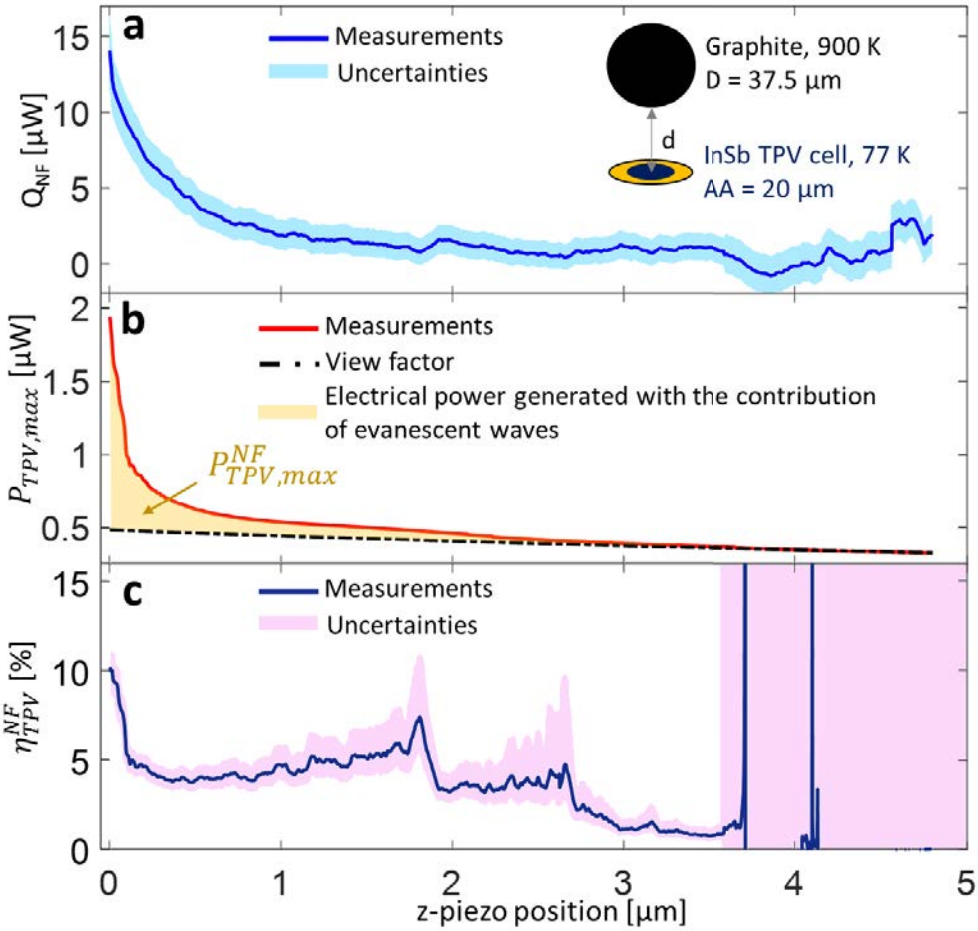

Figure VI.16: Near-field exchanged radiative power, maximum generated electrical power obtained using the superposition principle and near-field conversion efficiency obtained simultaneously as a function of the emitter-cell distance.
(a) Near-field radiative power according to distance. (b) Generated electrical power as a function of distance. (c) Near-field conversion efficiency determined from measurements.

Above ~ 3.5 µm, the relative uncertainty of Q_{NF} is very large because Q_{NF} is close to 0. Therefore, η_{TPV}^{NF} cannot be determined in this distance range. As distance decreases, η_{TPV}^{NF} increases, reaching (10.0 ± 1.8) % at the smallest distance, estimated to be in the range of d_{min} ~ 53 nm (see Sec. IV.3.8.2). This measured value is representative of the conversion of thermal radiation considering the contribution of evanescent waves only. The uncertainty results from the accuracy of the near-field radiative heat flux measurement affected mainly by the systematic error on the emitter calibration of ~20% (see Sec. III.4.3). Since the propagative wave contribution to radiative heat transfer cannot be measured with this experimental setup, it is calculated in order to estimate the total conversion efficiency. For the configuration presented in Figure VI.16, the far-field contribution is estimated to Q_{FF} = 7.8 µW. Therefore, $Q_{FF} + Q_{NF}$ = 21.9 µW, leading to a total conversion efficiency η_{TPV} = (8.7 ± 0.9) % (Table VI.2) calculated using:

$$\eta_{TPV} = \frac{P_{TPV,max}}{Q_{NF} + Q_{FF}}. \qquad (VI.3)$$

The contribution of far-field radiative heat transfer to the TPV output power is almost half that of the near field. The relative uncertainty provided here for the total conversion efficiency is lower than that of the near-field efficiency because the calculation of η_{TPV} involves the calculated term Q_{FF}, the uncertainty of which is set to 0 in absence of precise evaluation. The real uncertainty for the total conversion is probably higher in reality.

The experimental procedure allows direct measurements of near-field thermophotovoltaic conversion efficiency, via simultaneous measurements of near-field radiative heat transfer and electrical power generated by the TPV cell.

Table VI.2: Summary of parameters for near-field thermophotovoltaic conversion calculation

$max(P_{TPV,max})$		$max(P_{TPV,max}^{vf})$		$max(P_{TPV,max}^{NF})$		$max(Q_{NF})$	η_{TPV}^{NF}	Q_{FF} *(estimated)*	η_{TPV} *(estimated)*
[µW]	[kW.m^{-2}]	[µW]	[kW.m^{-2}]	[µW]	[kW.m^{-2}]	[µW]	[%]	[µW]	[%]
1.90	6.05	0.49	1.56	1.41	4.49	14.1 ± 2.2	10.0 ± 1.8	7.8	8.7 ± 0.9

VI.4 Parametric study for enhancing the electrical power density and conversion efficiency

The objective of this study is to find the optimal parameters maximizing the electrical power density generated by the TPV cell and conversion efficiency. The diameter of the active area, MBE growth parameters (temperature), substrate thickness and p-doping level are investigated. Experiments with a SiO_2 emitter, in place of the graphite one, is performed in order to verify theoretical calculations, predicting that graphite should provide a better enhancement of photogenerated power in the near field. Six classes of TPV cells are investigated, including some of them with the same parameters but from two different fabrication batches. Figure VI.17a shows I-V curves under ambient illumination, for TPV cells having active area diameters of 20 µm. In the linear scale plot, all the curves are almost superimposed except the one fabricated using non-optimal MBE growth parameters. For this cell the growth of the p-n junction layers was performed at a temperature 30 K lower than the optimal growth temperature. However the quality of the crystalline structure might not have been affected by the non-optimal growth because there was no effect observed on the X-ray diffraction analysis.

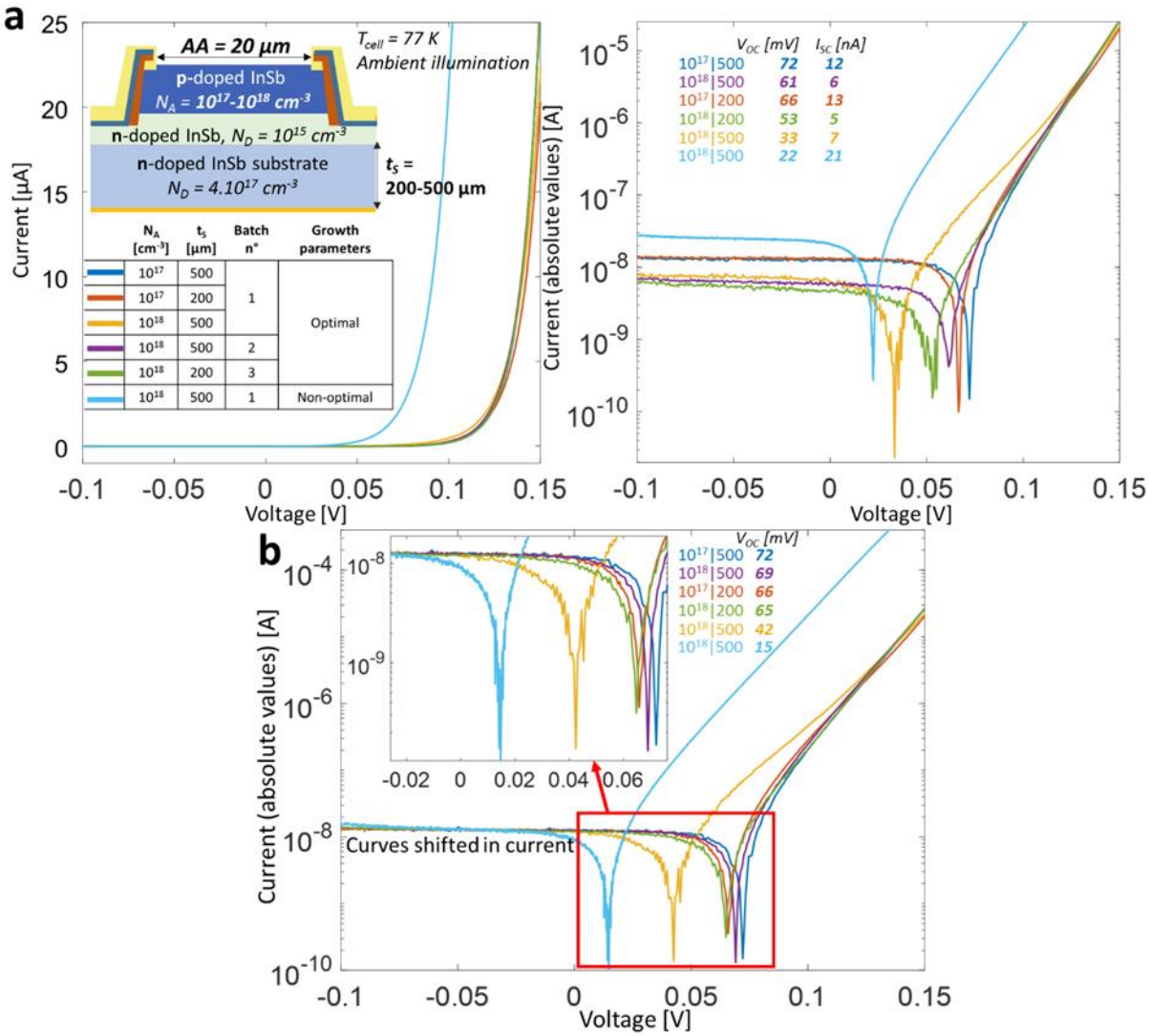

Figure VI.17: I-V curves of the different cells at 77 K under ambient illumination.
(a) I-V with a linear (left) and semi-logarithmic (right) scale. (b) I-V curves shifted in current

In the logarithmic scale plot, differences in I_{SC} appears but are very small (< 21 nA). The curves were not measured at the same time, thus ambient illumination may have changed between measurements leading to different I_{SC} and V_{OC}. In order to compare V_{OC} values among the cells, curves shifted in I_{SC} are presented in Figure VI.17b where they are ascribed a similar photogenerated current. Three cells having $N_A = 10^{18}$ cm^{-3} and $t_S = 500$ µm were fabricated. One of those cells shows an I-V curve with a shape that seems to be in-between those of the cells with optimized growth parameters, and that of the cell with non-optimal growth parameters. Therefore, this characteristics with a significantly smaller V_{OC} might be caused by an issue during the fabrication process. For the cells with optimal growth parameters, the I-V curves are very similar considering the same I_{SC}, with differences in V_{OC} smaller than 7 mV. However, a trend may appear with thick substrates and low doping levels increasing V_{OC}. It has to be mentioned that only three different batches of TPV cell samples were fabricated. This small number of samples is not sufficient to ensure full stability and repeatability of the measurements. Therefore, the comparison

of I-V curves among cells with different parameters has to be considered with care, having in mind that the fabrication process appears to have a large impact on the TPV cell characteristics.

VI.4.1 Cell diameter

InSb TPV cells were fabricated with an active area ranging from 20 to 160 µm in diameter (see Figure VI.3). NF-TPV measurements were performed with cells having active area diameters of 20, 80 and 160 µm in diameter, in order to find the best size maximizing the generated electrical power density. Figure VI.18 shows the output thermophotovoltaic power at the maximum power point $P_{TPV,max}$ as a function of distance for the three cells at 77 K, with an emitter at 732 K. The minimum z-piezo position is 10 nm, which corresponds to the step between two measurements. No distance correction was applied because the method for estimating the minimum distance used in Chapter IV (see IV.3.1) provides a qualitative estimation only. Furthermore, the uncertainty on near-field radiative conductance measurements observed when the cooling system is operating should strongly impact the estimation of the minimum distance. Based on the study reported in Sec. III.4.2, the distance determination close to contact during NF-TPV experiments should be considered with high uncertainties below 100 nm. Measurements were performed using the method with approaches at different cell voltages. During these experiments, cells with the same p-doping level $N_A = 10^{17}$ cm^{-3} and substrate thickness $t_S = 500$ µm were studied. The total generated power $P_{TPV,max}$ is represented, along with theoretical predictions from the view factor.

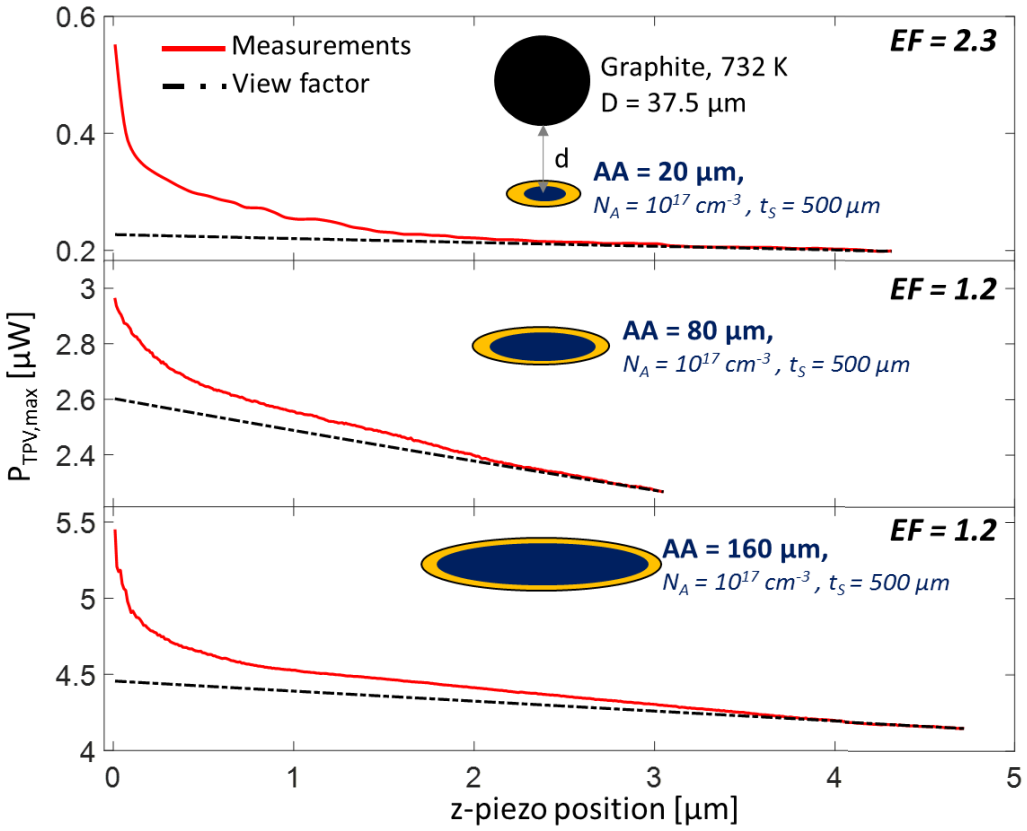

Figure VI.18: Output thermophotovoltaic power at the maximum power point as a function of distance between a 732 K graphite emitter and InSb cell at 77 K (N_A=10^{17} cm^{-3}, t_S = 500 µm, batch n°1) having active areas of 20, 80 and 160 µm in diameter

At the largest distance, which may slightly vary from one experiment to another, a larger electrical power is measured for larger cells. This is explained by the large area illuminated by the emitter with the contribution of propagative waves in the far field. As expected from calculations (see Figure II.29), small cells are collecting and converting only a small fraction of far-field thermal radiation. However, a larger share of the exchanged power comes from the near field for the smallest cell. This results in a larger near-field enhancement factor *EF*, above 2, for the smallest cell. In Figure VI.18 for the cell having an active area diameter of 80 µm, view factor predictions were based on the value of $P_{TPV,max}$ at the largest distance of ~3 µm, which is smaller than that for the two other cells. At such a distance, evanescent waves contribute to $P_{TPV,max}$. Therefore, the view factor might overestimate the evolution of the contribution of propagative waves for the cell having an active area diameter of 80 µm, thus underestimating the enhancement factor.

Figure VI.19 shows the maximum electrical power and power density as a function of the active area diameter. Areas with a darker color on the top are representative of the evanescent wave contribution to $P_{TPV,max}$ while areas with a lighter color show the propagative wave contribution. The electrical power decreases with the cell diameter, from 5.45 down to 0.55 µW, because less illumination especially from propagative waves is collected, resulting in a larger ratio of the evanescent wave contribution. However, electrical power density increases from 0.27 up to 1.80 kW.m^{-2}, because the area where near-field radiative heat transfer takes place is localized close to the point where the emitter-cell distance is the smallest. Away from this point, the increasing distance between the sphere and the active area of the cell leads to a decrease of the evanescent wave contribution to radiative heat transfer.

For instance, Figure VI.20 shows calculations of the fraction of the near-field radiative power exchanged between the sphere and the active area of the cell $Q_{NF}^{sphere \to AA} / Q_{NF}^{sphere \to semi-infinite\ plane}$. It is observed that an active area diameter of 20 µm allows to collect 93 % of the total available radiative power considering the contribution of evanescent waves. Because evanescent waves are considered to interact only with the closest parts of the other body, all near-field radiative power coming from the sphere would be received by an active area of the size equal to that of the sphere (see details in Sec. II.3.2).

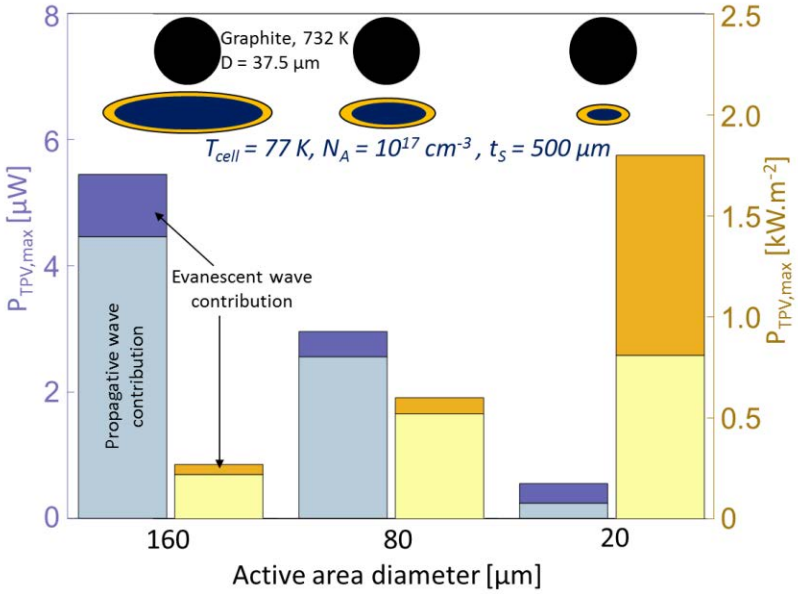

Figure VI.19: Maximum electrical power and power density generated by InSb TPV cells at 77 K from batch n°1 having different active area diameters, illuminated by a 732 K graphite emitter

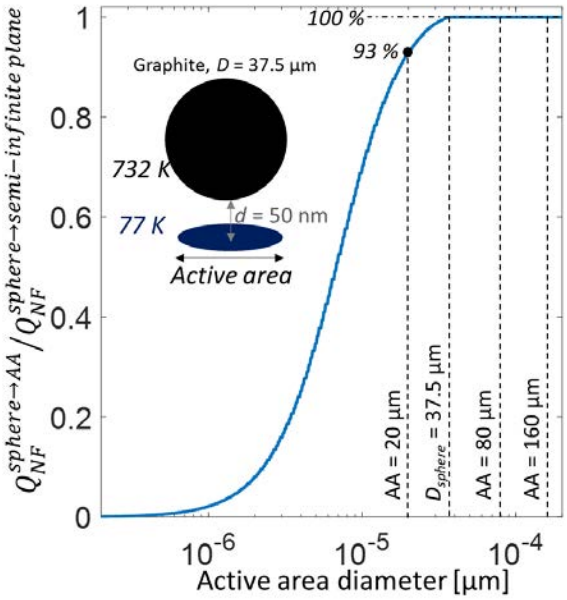

Figure VI.20: Fraction of the near-field radiative power exchanged between the sphere and a plane substrate, exchanged with the active area of the cell as a function of the active area diameter of the cell

The study of the effect of the cell active area diameter has demonstrated that the smallest cell generates the lowest electrical power but the highest electrical power density. Reducing the size of the active area increases the share of radiative power from the contribution of evanescent waves, over that from the contribution of propagative waves. Therefore in the next sections, the other parameters will be investigated using cells having active areas with a diameter of 20 µm.

VI.4.2 Substrate thickness and p-doping level

Cells with substrate thicknesses of 200 and 500 µm were fabricated in order to measure the impact of the substrate thickness on the electrical power density generated by the cell. By reducing the thickness from 500 to 200 µm, part of the parasitic absorption of photons in the substrate is mitigated, and an additional passage of these photons across the p-n junction is possible after reflection by the bottom gold contact layer which acts as a mirror[171]. Note that the near-field contribution in the sphere-plane geometry is mostly related to frustrated modes (see Figure II.27), which are evanescent in the gap but propagative in the substrate. In addition, two doping levels of the p-doped layer ($N_A = 10^{17}$ and 10^{18} cm^{-3}) were investigated, knowing that they have an influence on the potential barrier of the p-n junction[74]. When the p-doping level increases from 10^{17} to 10^{18} cm^{-3} the absorption coefficient at energies larger than the energy bandgap of the cell is not modified but the potential barrier is increased leading to a larger V_{OC} for the same photocurrent, thus enhancing the electrical power generation and the conversion efficiency. However, the absorption coefficient for energies below the energy bandgap is larger with $N_A = 10^{18}$ cm^{-3} and negatively impact the efficiency. In the end the photogenerated electrical power should be enhanced by increasing the p-doping level, which is not necessarily the case for the efficiency.
Because the cells were fabricated from three different batches (see Figure VI.17), comparison of the performances among the cells may be possible only between cells fabricated from the same batch. For instance, Figure VI.21 shows the electrical power generated by two cells from different

batches having the same parameters ($N_A = 10^{18}$ cm^{-3} and $t_S = 500$ µm) and illuminated by a graphite emitter at 732 K. Two very disparate behaviors appear, with differences of generated electrical power at small as well as at large distances. The behaviors appear also very different with a logarithmic scale in inset of the figure. These differences may be expected because the I-V characteristics of these two cells measured under ambient illumination are different (see Figure VI.17). This comparative analysis is based only on the output electrical power because near-field radiative heat transfer could not be measured for the cell fabricated from the batch n°1, due to a strong random noise on the temperature signal of the emitter during the experiments. The noise may indicate that the emitter was polluted and that its temperature was not stable during the experiment. As a consequence, determination of the near-field efficiency is not possible. This comparative study shows that the measurements performed during this work should be compared for cells fabricated from the same batch only. Comparisons with cells from different batches might be possible if a better characterization of the cells was provided, for instance by measuring the I-V characteristics under dark conditions as well as under illumination for all cells. In addition, assessing the spectral response of the cells by means of external quantum efficiency (EQE) measurements should also provide key information for determining the characteristics of the cells.

Figure VI.22 shows the electrical power generated at the maximum power point $P_{TPV,max}$ by InSb TPV cells at 77 K, the near-field radiative heat flux Q_{NF}, and the near-field conversion efficiency η_{TPV}^{NF}. Experiments were performed with the method involving measurements at different voltages. All the cells of the figure have the same active area diameter of 20 µm, but different substrate thicknesses and p-doping levels. Plots on top of the figure are representative of cells having a substrate thickness $t_S = 500$ µm, while bottom plots are for cells having $t_S = 200$ µm. For cells with a p-doping level of 10^{18} cm^{-3}, measurements were performed with the emitter at 732 and 900 K. Efficiency measurements exhibit large uncertainties when Q_{NF} is close to 0. In addition, large variations of the efficiency may appear as a function of distance due to the small number of curves averaged for determining Q_{NF}, resulting in irrelevant high efficiency values above a distance of 1 µm.

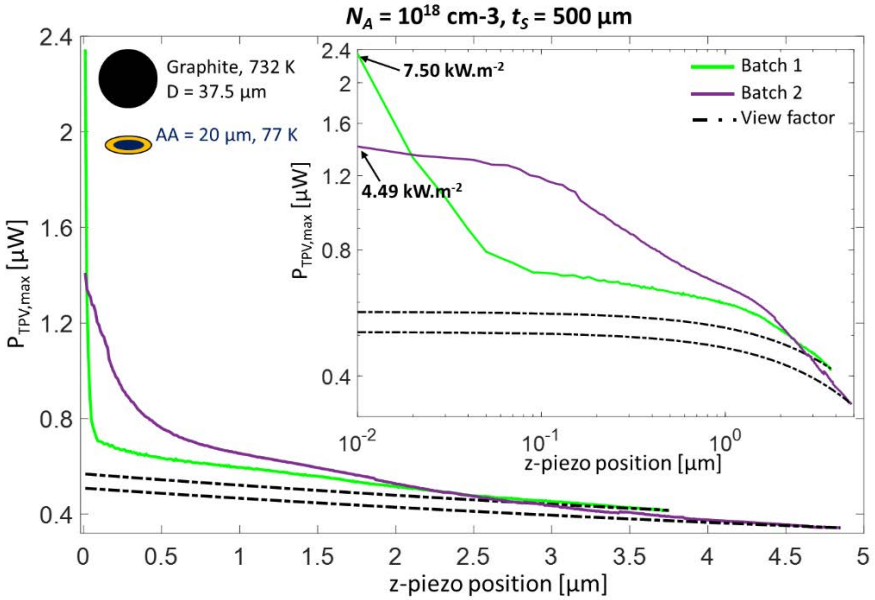

Figure VI.21: Electrical power generated by InSb TPV cells at 77 K, fabricated from two different batches, having $N_A = 10^{18}$ cm^{-3}, $t_S = 500$ µm and an active area diameter of 20 µm, illuminated by a 732 K graphite emitter

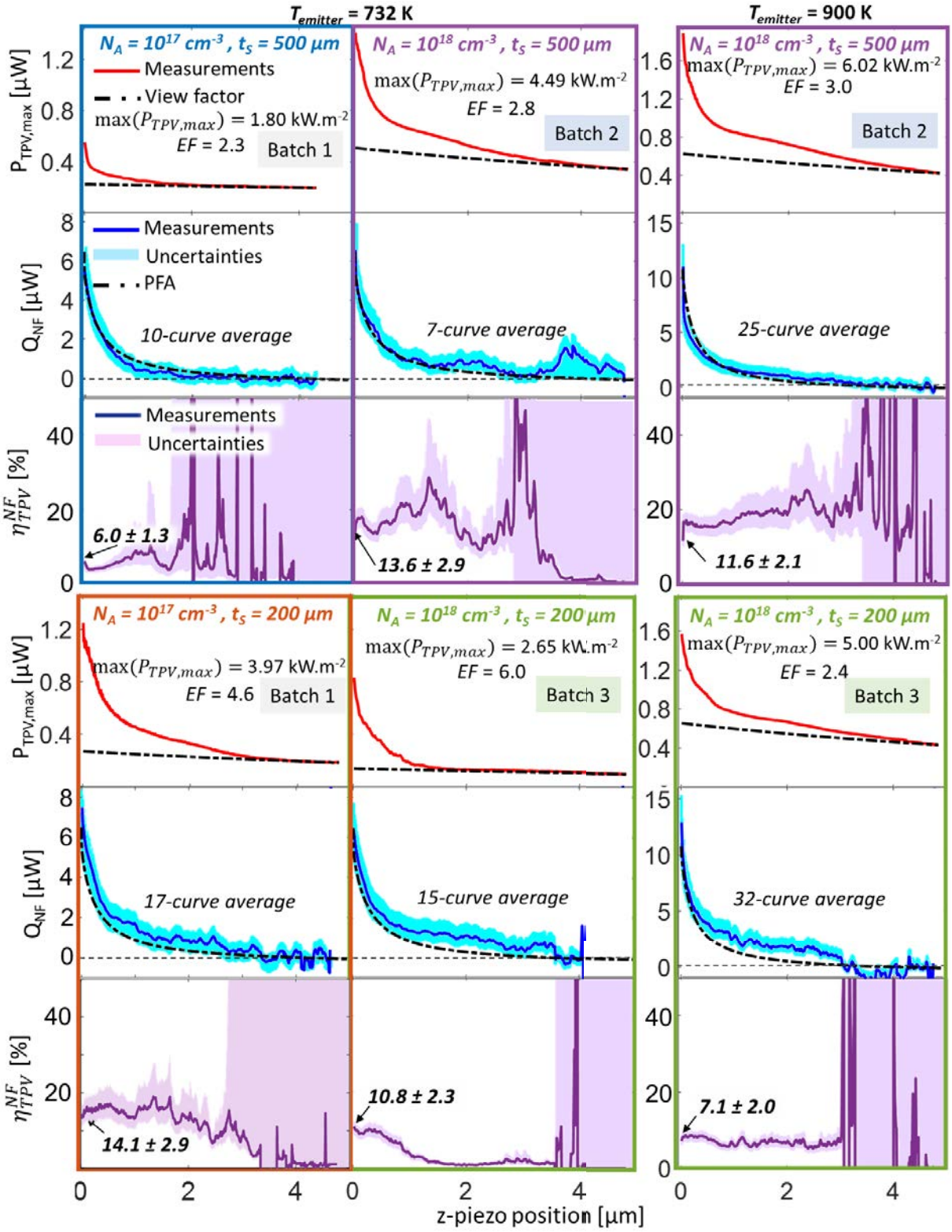

Figure VI.22: Generated electrical power, near-field radiative heat flux and near-field conversion efficiency as a function of distance between a graphite emitter at 732 or 900 K and InSb TPV cells at 77 K, having an active area diameter of 20 µm, for different substrate thicknesses and p-doping levels.

Table VI.3: Summary of the performances of the cells

$T_{emitter}$	Batch n°	Cell N_A [cm^{-3}]	Cell t_S [µm]	max ($P_{TPV,\max}$) [µW | kW.m^{-2}]	$max(P^{NF}_{TPV,max})$ [µW | kW.m^{-2}]	$max(Q_{NF})$ [µW]	η^{NF}_{TPV} [%]
732 K	1	10^{17}	500	0.55 | 1.80	0.31 | 0.99	5.3 ± 1.0	6.0 ± 1.3
		10^{17}	200	1.25 | 3.97	1.04 | 3.31	7.4 ± 1.4	14.1 ± 2.9
		10^{18}	500	2.36 | 7.50	1.79 | 5.70	-	
	2	10^{18}	500	1.41 | 4.49	0.90 | 2.87	6.6 ± 1.2	13.6 ± 2.9
	3	10^{18}	200	0.83 | 2.65	0.69 | 2.21	6.4 ± 1.2	10.8 ± 2.3
900 K	2	10^{18}	500	1.89 | 6.02	1.27 | 4.03	11.0 ± 1.8	11.6 ± 2.1
	3	10^{18}	200	1.57 | 5.00	0.92 | 2.92	12.9 ± 2.0	7.1 ± 2.0

However, a stable evolution of the efficiency as a function of distance is observed when the number of averaged curve is large. In order to compare efficiencies between experiments, the last point before contact is considered where the signal-to-noise ratio is the highest. However, this point may not represent the same emitter-cell distance from one experiment to another. Indeed the large uncertainty on distance determination close to contact probably affects the measurements because the electrical power generated by the cell is expected to strongly vary in the sub-100 nm distance range. Because of the different fabrication batches, only a limited number of meaningful comparisons can be made between the experiments:

- The two cells from the batch n°1 having a p-doping level $N_A = 10^{17}$ cm^{-3} are represented in the left column in Figure VI.22. For these cells, thinning the substrate from 500 down to 200 µm increases the near-field enhancement factor *EF* by a factor of ~2. The maximum values of $P_{TPV,max}$ and η^{NF}_{TPV} increase from 1.80 up to 3.97 kW.m^{-2}, and from 6.0 up to 14.1 % (see Table VI.3 for a summary of performances). The best efficiency measured for this cell is explained by the increase in power conversion for photon energies above the bandgap when the substrate is thinned down, and by the reflection of near-field thermal photons below the bandgap, reducing the parasitic absorption that does not lead to photoconversion[74,172].
- The cells having $N_A = 10^{18}$ cm^{-3} were fabricated from two different batches. Figure VI.21 shows that cells having the same p-doping and substrate thickness, but fabricated in two different batches (1 and 2) don't have the same performances. As a consequence, comparison of performances between these cells when the substrate is thinned down has to be made with caution, since the cells are from two different batches (2 & 3). As a matter of fact, thinning down the substrate does not provide the expected results because the cell having $t_S = 200$ µm has lower performances than the cell having $t_S = 500$ µm. This observation can be made on measurements with an emitter temperature of 732 and 900 K.
- The influence of the p-doping level can be estimated by comparing the output electrical power measured with the cells fabricated from the batch n°1 (see Figure VI.23) with $t_S = 500$ µm. It appears that increasing the p-doping level from 10^{17} to 10^{18} cm^{-3} leads to a large enhancement of the output electrical power at the last distance before contact from 1.80 up to 7.50 kW.m^{-2}, which is the highest value measured for all cells. At $d = 3.7$ µm, the electrical power generated by the cell having $N_A = 10^{18}$ cm^{-3} is twice that generated by the other cell, meaning that the

conversion of photons is enhanced in the near field and in the far field. Observing the I-V curve of the cell having $N_A = 10^{18}$ cm^{-3}, we conclude that the characteristics of this cell probably differs from those of other cells. Thus, the high electrical power density may be induced by other parameters than the p-doping level. As mentioned previously, the near-field radiative power, and the near-field efficiency as a consequence, could not be measured for the cell with the highest doping level.

The impact of the substrate thickness and p-doping level may be observed by studying the cells fabricated from the first batch, with better performances measured with t_S = 200 µm or $N_A = 10^{18}$ cm^{-3}. However, more cells from a same batch should be fabricated and studied in order to conclude with assurance on the effect of the doping level and the substrate thickness.
For a better visualization, the performances summarized in Table VI.3 are plotted in Figure VI.24 for the cells where Q_{NF} and η_{TPV}^{NF} could be measured. It is observed that rising the emitter temperature from 732 up to 900 K increases the electrical power density generated by the cell. This is expected because of the increase in radiative power density received by the cell induced by a higher emitter temperature. However, increasing $T_{emitter}$ leads to a lower near-field conversion efficiency. It was suggested in Figure V.10 that TPV cells may perform better when paired with an emitter heated at a certain temperature, providing spectral matching between the emitter and the cell. For InSb at 77 K, Eg = 0.234 eV corresponds to the energy of a photon emitted at the maximum of the emission spectrum of a blackbody at T_{Wien} = 547 K (Eq. (V.15)). Therefore, InSb TPV cells at 77 K may be more efficient with an emitter heated at 732 K than one at 900 K, because it corresponds to a temperature closer to T_{Wien}. The variations of near-field radiative power absorbed by cells having different parameters are smaller than the measurement uncertainty. Therefore, it cannot be established if the substrate thickness and the p-doping level have any influence on the power absorbed by the cell.

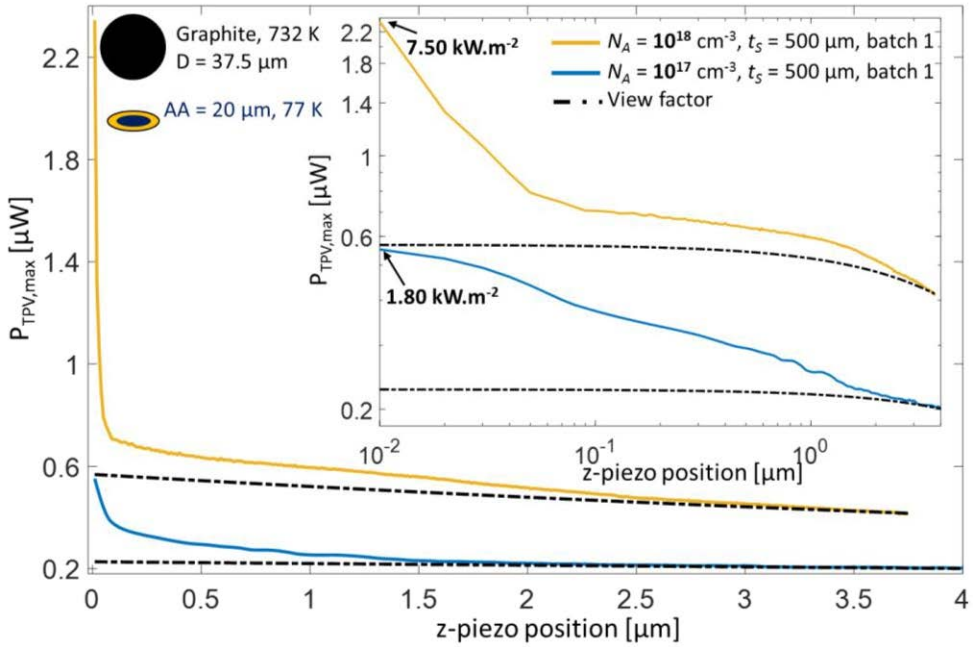

Figure VI.23: Electrical power generated by InSb TPV cells at 77 K, fabricated from the same batch, having $N_A = 10^{18}$ or 10^{17} cm^{-3}and t_S = 500 µm with an active area diameter of 20 µm, illuminated by a 732 K graphite emitter

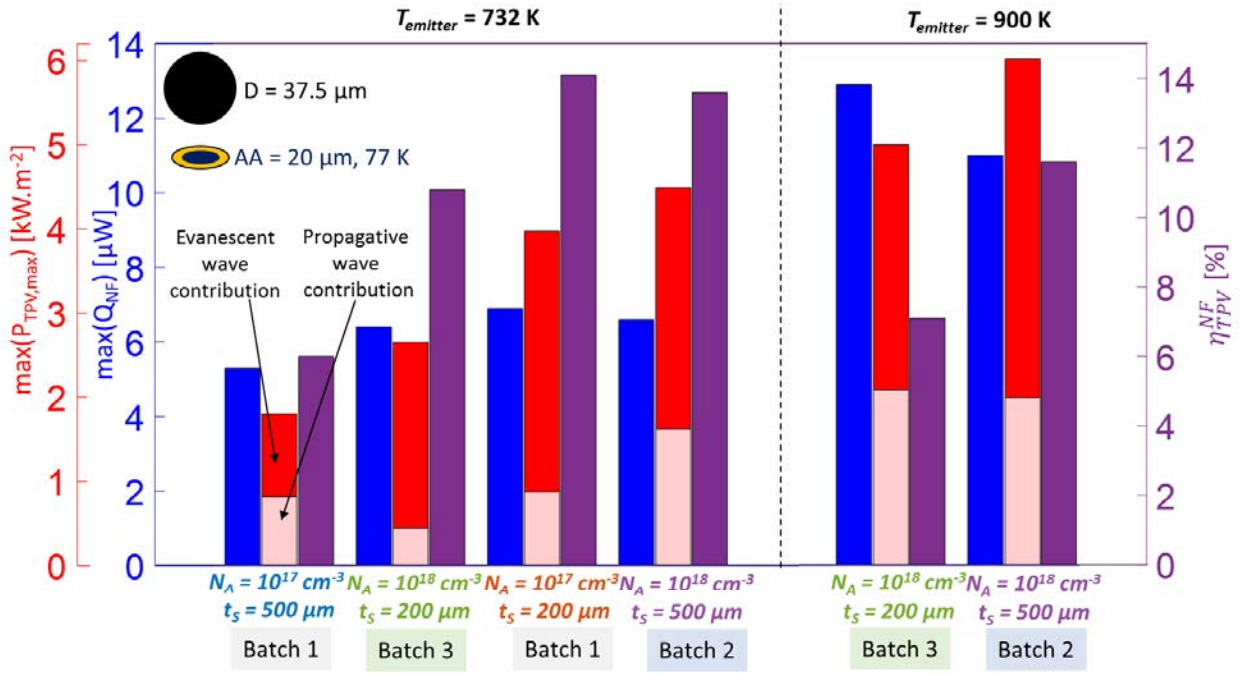

Figure VI.24: Maximum electrical power density, maximum near-field radiative power and near-field conversion efficiency measured for the different configurations

For energy harvesting applications it is useful to study the electrical power generated by the cell normalized by the surface of the active area and the temperature difference between the emitter and the cell $G_{TPV,max}$ expressed as

$$G_{TPV,max} = \frac{P_{TPV,max}}{S_{active\ area}(T_{emitter} - T_{cell})}. \qquad (VI.4)$$

Figure VI.25 shows the maximum value of $G_{TPV,max}$ for the different cells. It is interesting to compare the cells having a p-doping level of 10^{18} cm^{-3} because measurements were performed with the emitter at 732 and 900 K. For the cell having $N_A = 10^{18}$ cm^{-3} and $t_S = 200$ µm, $G_{TPV,max}$ increases with the emitter temperature but mainly because of the enhancement of the contribution of the propagative waves. This may be due to the temperature power law of the exchange power having a higher exponent in the far field than in the near field as predicted in Figure II.27. This hypothesis cannot be verified because significantly more measurements should be performed in order to rely on a sufficient amount of experimental data. In addition, the cell having $N_A = 10^{18}$ cm^{-3} and $t_S = 500$ µm keeps almost the same value of $G_{TPV,max} = 7.32$ W.m^{-2}.K^{-1} whether the emitter temperature is 732 or 900 K.

This study of the thickness and p-doping level shows that the measured performances of TPV cells are better with cells fabricated from batch n°1 either having $N_A = 10^{18}$ cm^{-3} and $t_S = 500$ µm or $N_A = 10^{17}$ cm^{-3} with $t_S = 200$ µm. The best measured near-field efficiency is 14.1 %, while the best power density reached 7.50 kW.m^{-2}. A larger number of experiments with cells from the same batch in addition of a more reliable process for determining the minimum distance should be performed in order to fully conclude on the effect of the doping level and substrate thickness on the performances of the cells. A summary of all of the NF-TPV experiments, including estimations of the total conversion efficiency (considering the evanescent and propagative wave contributions), is provided in Appendix 5. Considering uncertainties, measured near-field η_{TPV}^{NF} and estimated total efficiency η_{TPV} have similar values for a given cell, implying that the conversion efficiency does

not depend on whether absorbed photons are coming from the propagative or the evanescent contribution. This may be in agreement with the fact that most of thermal radiation from the contribution of evanescent waves are supported by frustrated modes, which are propagative in the cell.

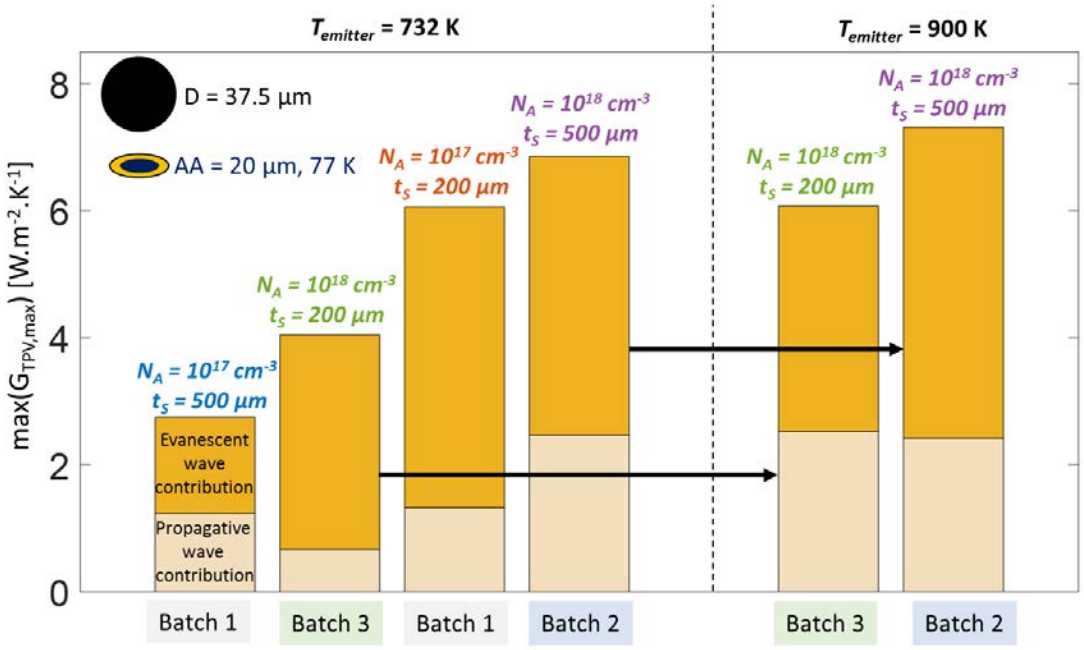

Figure VI.25: Maximum electrical power density normalized by the temperature difference between the emitter and the cell for the different configurations

VI.4.3 Growth parameters

An InSb TPV cell was fabricated from the first batch using non-optimized MBE growth parameters (see Sec. VI.2.2.1 for details on the MBE growth process). The aim was to study the influence of the growth parameters on the performances of a cell. In Figure VI.17, this cell has an I-V characteristic very different from that of the other cell with the same p-doping level and substrate thickness. For the same photogenerated current, the non-optimized cell has a V_{OC} of 15 mV, compared to 69 mV for the one with optimized growth parameters. A lower V_{OC} is expected because non-optimized growth parameters may impact the crystalline structure of the cell, creating defects and leading to electron-hole pair recombinations. However, the X-ray diffraction analysis did not reveal any issue compared with the observations for the other cells, implying that the crystalline structure was not significantly affected by the non-optimized growth parameters (Figure VI.26).

In order to investigate the performances of this cell in the near field, NF-TPV experiments were performed with a graphite emitter at 732 K, using the method requiring approaches at different cell voltages. In Figure VI.27, measurements are compared with those of cells having the same p-doping level and substrate thickness fabricated from batches n°1 and 2, and illuminated by an emitter at the same temperature. At the largest distance, the cell with non-optimized growth parameters generates less than half of the electrical power produced by the other cell which is mainly due to the lower voltage. However at the last point before contact, the current is larger for cell with non-optimal growth parameters (24.9 compared with 12.6 and 20.5 µA), compensating the lower voltage.

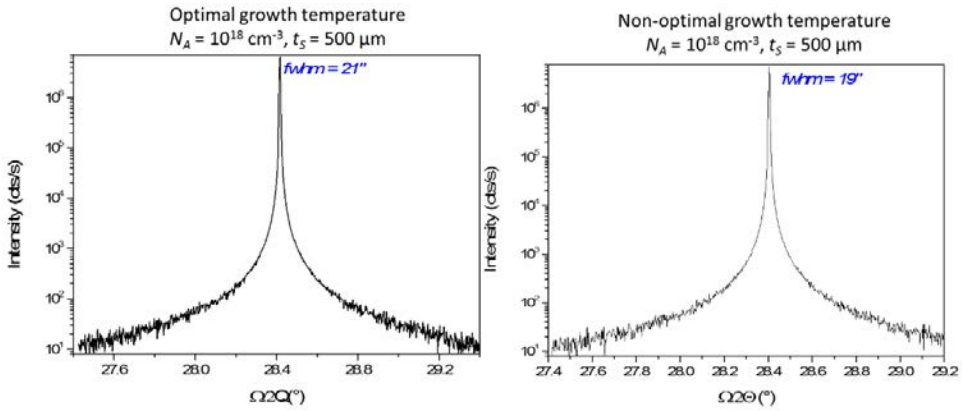

Figure VI.26: X-ray diffraction spectra performed on a cell with optimal growth parameters (left) and non-optimal parameters (right) for a 30 K lower growth temperature. Spectra provided by Jean-Philippe Perez (IES, Montpellier)

This cell generates a maximum electrical power of 5.70 kW.m^{-2}, leading to the largest enhancement factor of 7.4. In terms of near-field efficiency, this cell reached a record value of 21.5 %. Such a high efficiency is surprising because its non-optimized growth parameters are expected to negatively impact performances of the cell.

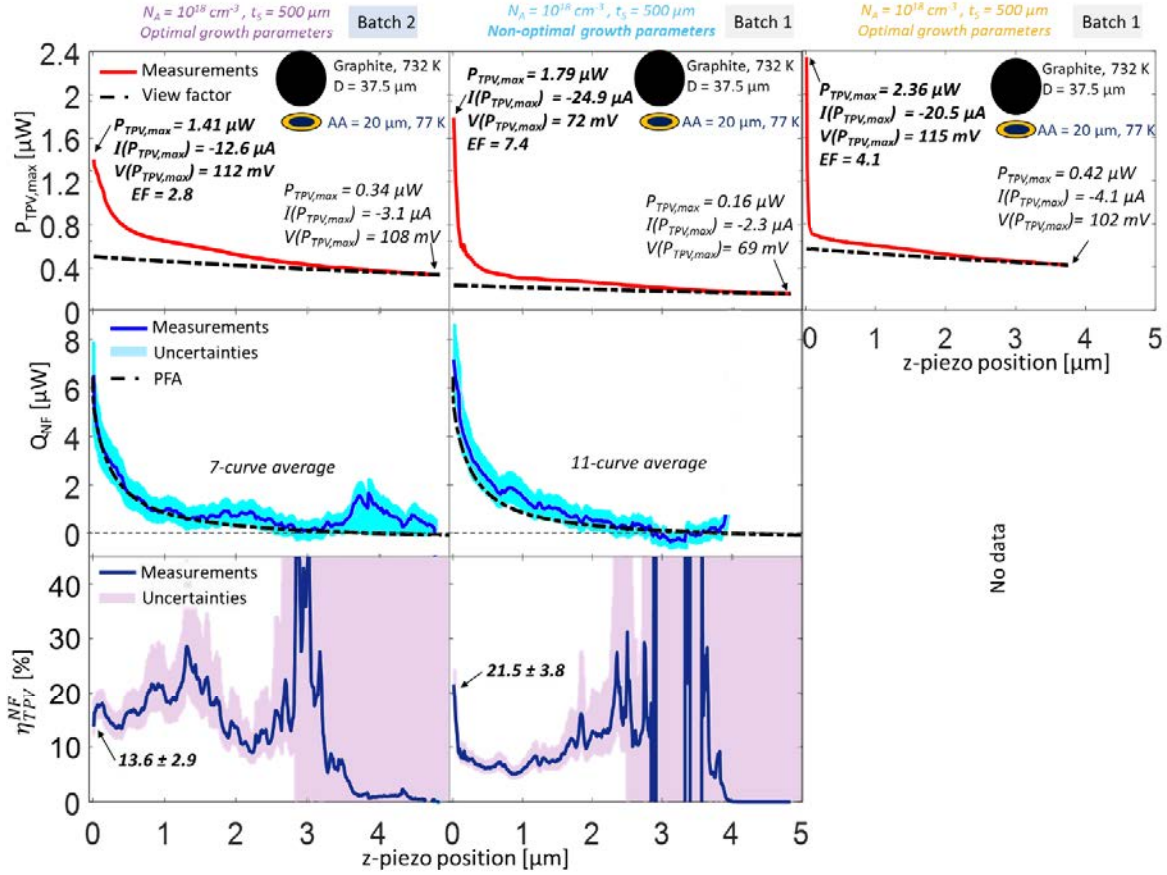

Figure VI.27: Generated electrical power, near-field radiative heat flux and near-field conversion efficiency as a function of distance for a graphite emitter at 732 K and InSb TPV cells at 77 K, having active areas of 20 µm in diameter, $N_A = 10^{18}$ cm^{-3}and t_S = 500 µm, with optimal or non-optimal growth parameters

Good performances may agree with the X-ray diffraction analysis suggesting that the structure of the cell was not impacted by the non-optimized growth temperature. These unexpected results may be provided by the uncertainty on distance determination close to contact which could be different between the two experiments especially in the sub-100 nm regime. However, larger electrical currents generated for smaller voltages remain unexplained. Further analyses, for instance with external (EQE) and internal quantum efficiency (IQE), would be necessary to better characterize this cell and understand the causes of its peculiar I-V curve and performances. Unfortunately, such analyses were not possible to perform in the timeframe of this thesis.

VI.4.4 Emitter material

Experiments were performed with a SiO_2 emitter at 732 K in order to verify if graphite is a better choice for the emitting material according to calculations (see Sec. II.4.1). NF-TPV measurements using the cell having $N_A = 10^{17}$ cm^{-3} and $t_S = 200$ µm are reported in Figure VI.28. For the graphite emitter, results are the same as those already shown in Figure VI.22. Measurements with the SiO_2 emitter were performed using a sphere having a diameter of 44 µm, which is slightly larger than the graphite sphere. Because of differences of diameter and optical properties between graphite and SiO_2, calculations of the contribution of propagative waves give 3.2 µW for graphite, and 5.2 µW for SiO_2, corresponding to a difference of a factor of 1.63. Measured electrical power generated by the cell at the largest distance are 0.18 µW for graphite, and 0.30 µW for SiO_2, representing a difference of a factor of 1.66, close to the one obtained by calculations.

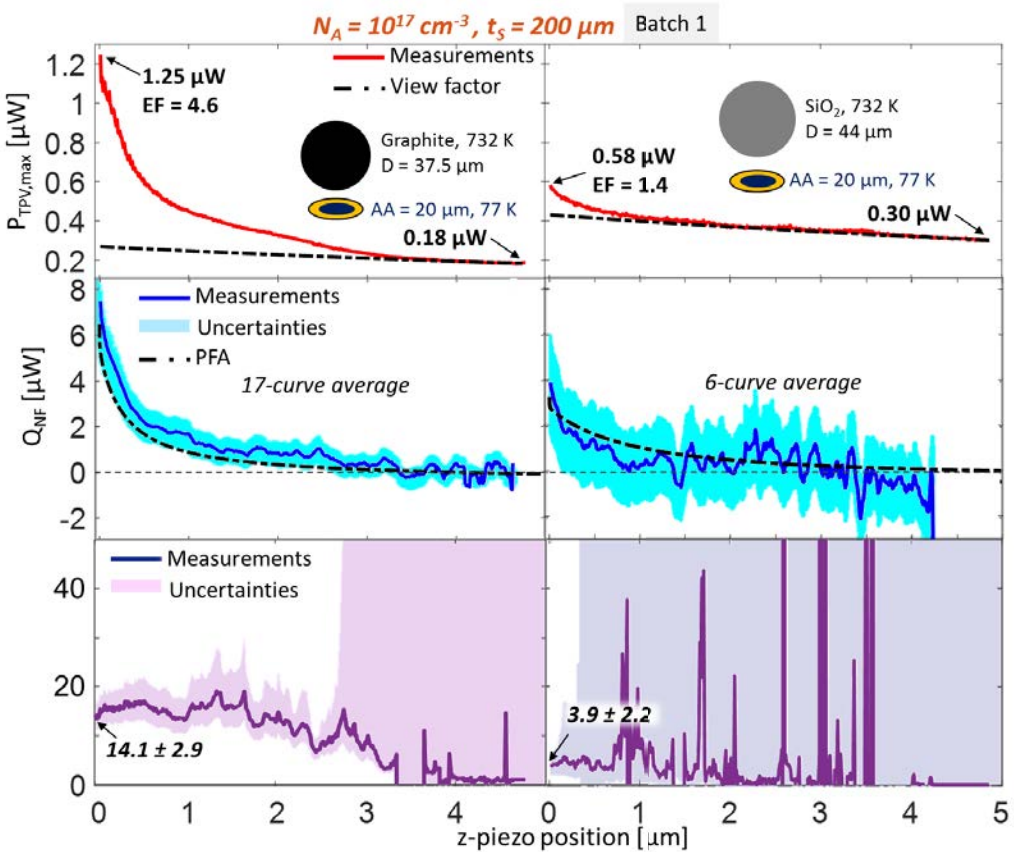

Figure VI.28: Generated electrical power, near-field radiative heat flux and near-field conversion efficiency as a function of distance for a graphite or SiO_2 emitter at 732 K and an InSb TPV cell at 77 K, having an active area diameter of 20 µm, $N_A = 10^{17}$ cm^{-3} and $t_S = 200$ µm.

In the near field, electrical power generated by the cell is significantly larger with the graphite emitter, corresponding to a larger enhancement (*EF* = 4.6) than with SiO_2 (*EF*=1.4). In terms of near-field efficiency, 14.1 % is reached with a graphite emitter, compared to 3.9 % with one made of SiO_2. This is explained because most of the radiative power exchanged between the SiO_2 emitter and the cell in the near field occurs at wavelengths larger than the gap wavelength of InSb at 77 K (see Figure II.16). Therefore, most of the radiative power absorbed by the cell cannot be potentially converted into electrical power.
This study demonstrates the importance of the selection of the emitter material for near-field thermophotvoltaics. For instance, choosing graphite over SiO_2 as emitter material leads to a maximum generated electrical power larger by a factor of ~2.2, and a better near-field conversion efficiency by a factor of ~3.6.

VI.5 Electrical power as a function of temperature

This section reports on a study of the evolution of the electrical power generated by a TPV cell as a function of emitter temperature. The graphite emitter was placed at a fixed distance $d \sim 5$ µm above a cell at 77 K having an active area diameter of 20 µm. A reference I-V curve is measured under ambient illumination. Then, the emitter is heated from room temperature up to ~1100 K, while the short-circuit current of the cell is measured. The electrical power generated by the cell is determined using the superposition principle (see Sec VI.3.1.1). Figure VI.29a shows the electrical power generated by an InSb TPV cell at 77 K as a function of emitter temperature, compared with Monte Carlo calculations of far-field radiative power absorbed by the cell (see Sec. II.3.3). At low emitter temperature, thermal radiation coming from the environment considered at 300 K is taken into account. The estimation is made considering that the sphere, located at 5 µm above the cell, is screening a part of thermal radiation coming from the environment. The cell-environment view factor $F_{c\to env}$ was estimated using the reciprocity of view factors[30] ($S_i F_{i\to j} = S_j F_{j\to i}$) as:

$$F_{cell\to sphere} = \frac{S_{sphere}}{S_{cell}} F_{sphere\to cell}\,, \qquad (VI.5)$$

$$F_{cell\to env} = 1 - F_{cell\to sphere}\,, \qquad (VI.6)$$

based on the sphere-cell analytical view factor $F_{sphere\to cell}$ (Eq. (II.11)), and S_{sphere} and S_{cell} respectively the sphere and the cell active area. Estimation of the radiative power coming from the environment is considered to be that of a blackbody and is written as:

$$Q_{env} = \sigma S_{cell} T_{env}^4 F_{cell\to env}\,, \qquad (VI.7)$$

with σ the Stefan-Boltzmann constant and T_{env} the environment temperature. At d = 5 µm, $F_{sphere\to cell}$= 0.0392 so $F_{cell\to sphere}$= 0.551 and $F_{cell\to env}$= 0.449, giving an estimated power from the 300 K environment Q_{env} = 64 nW including 1.2 nW at $\lambda < \lambda_{gap}^{InSb,\,77\,K}$. Considering the blackbody spectrum for the radiative power from the environment corresponds to an upper bound of the thermal radiative power received by the cell without being illuminated by an external source. In the figure, different contributions of the radiative power absorbed by the cell are calculated and represented:

- The black curve represents the total radiative power absorbed by the cell.
- The grey dashed curve represents the share of the radiative power absorbed at $\lambda > \lambda_{gap}^{InSb,\,77\,K}$ which cannot be photoconverted into electrical power by the cell.

- The yellow-dotted curve represents the radiative power absorbed at $\lambda < \lambda_{gap}^{InSb,\,77\,K}$ of interest for the conversion into electrical power.
- In Figure VI.29c, the purple curve represents the electrical charge generation and collection ratio per absorbed photon at $\lambda < \lambda_{gap}^{InSb,\,77\,K}$ for an InSb TPV cell at 77 K. The number of electrical charges generated and collected by the cell $\frac{P_{TPV,max}}{qV_{max}}$ is divided by the number of photons absorbed at $\lambda < \lambda_{gap}^{InSb,\,77\,K}$ calculated as $\int_0^{\lambda_{gap}^{InSb,\,77\,K}} \frac{q(\lambda)}{\hbar\omega} d\lambda$.

In the linear scale plot, the measured electrical power is very small compared to estimations of absorbed radiative power. In the logarithmic scale plot, it is observed that $P_{TPV,max}$ increases steeply up to 700 K, then at a slower rate above 700 K.

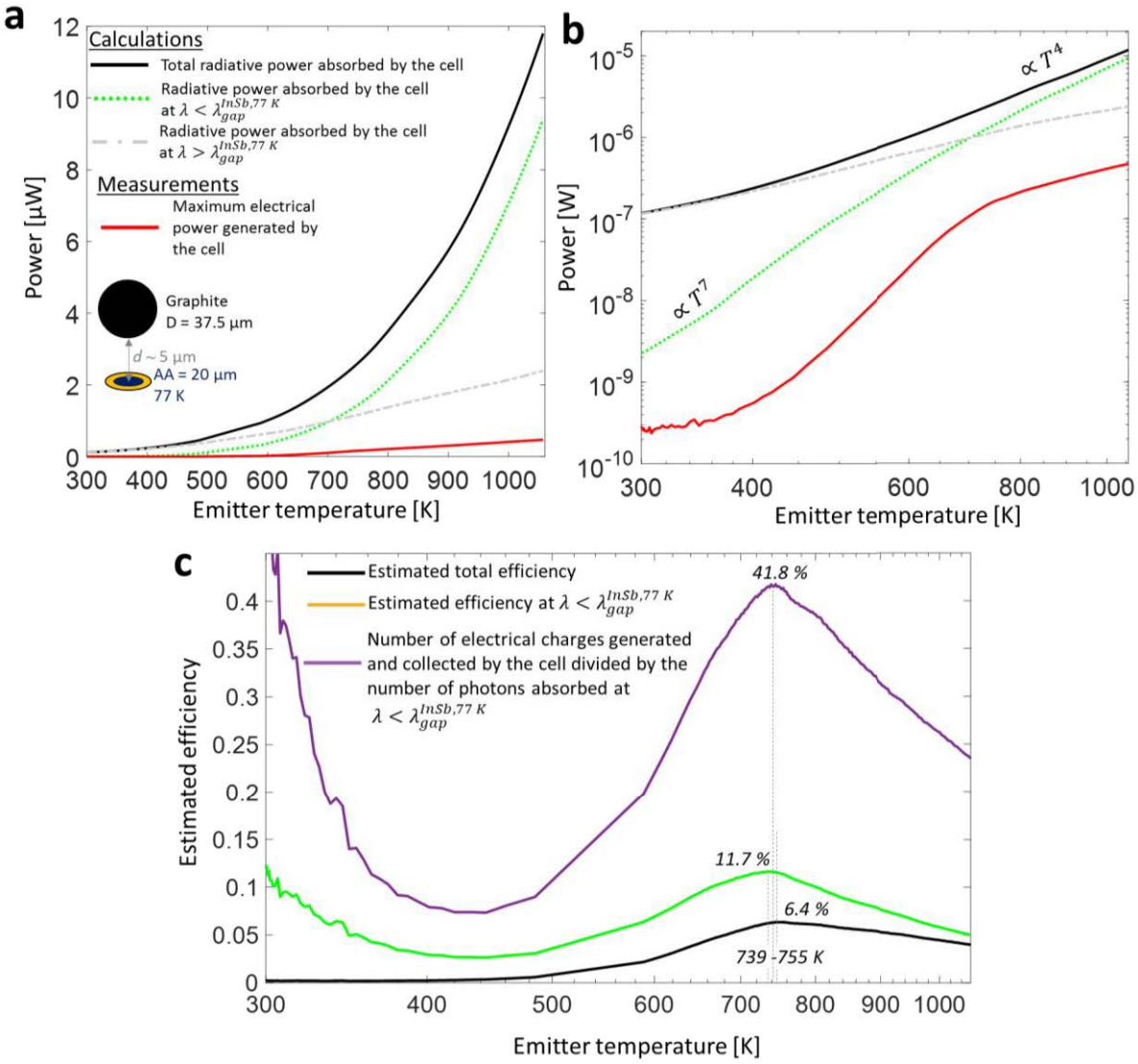

Figure VI.29: Electrical power generated by an InSb TPV cell at 77 K as a function of emitter temperature.
(a) Linear and (b) logarithmic scale plot of the measured electrical power generated by the cell, compared to calculations of far-field radiative power absorbed by the cell. (c) Estimated efficiencies of the InSb TPV cell

The measured photogenerated and calculated radiative powers have all different behaviors. By dividing the electrical power generated by the cell by the absorbed radiative power, one can estimate the efficiency of the cell (Figure VI.29b). For the total efficiency, the curve increases and reaches a maximum of 6.4 % at 755 K, which is closer to efficiencies reported in Table VI.1. Considering thermal radiation at $\lambda < \lambda_{gap}^{InSb,\,77\,K}$, the efficiency reaches 11.7 % at 739 K and 41.8 % at 745 K considering the charge generation and collection ratio. Below 400 K, large uncertainties are expected given the very low electrical power and the approximate estimation of Q_{env}. Above 739-755 K, the efficiency decreases, which agrees with the lower efficiencies measured at $T_{emitter}$ = 900 K compared to those at $T_{emitter}$ = 732 K (Figure VI.22). However, this is not at the cost of the output power, which still increases with temperature.

This experiment demonstrates the ability of the experimental setup to maintain large temperature differences (> 1000 K) across a small gap distance. Therefore, NF-TPV measurements were attempted with an emitter at 1200 K. It is reminded that, despite InSb having a melting temperature of 800 K, NF-TPV experiments were possible to perform using an emitter at 900 K, most probably because the thermal contact resistance between the emitter and the cell limits the cell heating at contact. However, the attempt with the emitter heated at 1200 K resulted in the destruction of the cell. Figure VI.30 shows I-V characteristics under ambient illumination, and optical microscope images of a clean active area (no NF-TPV experiments) and the damaged active area of the cell brought into contact with the emitter heated at 1200 K. The surface of the damaged active area exhibits a lot of dark spots, which may represent partially melted areas. After contact with the hot emitter, the I-V curve under ambient illumination changed drastically, exhibiting a V_{OC} of ~1 mV, compared with 66 mV before contact.

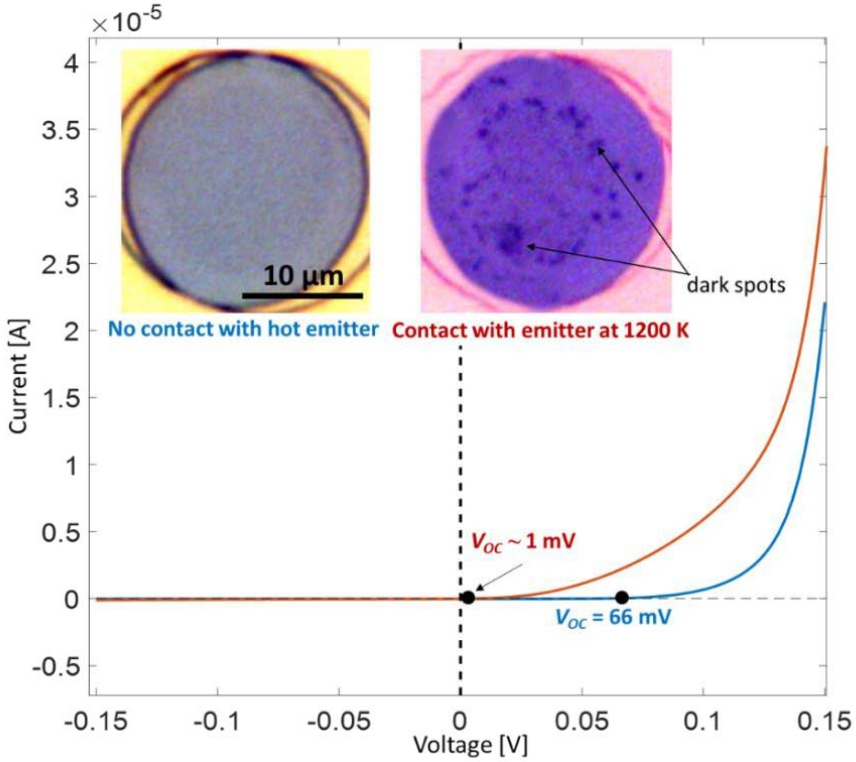

Figure VI.30: I-V curves under ambient illumination and optical microscope images of an InSb TPV cell having an active area diameter of 20 µm, before and after contact with a graphite emitter at 1200 K. Color differences between the images come from the parameters of the optical microscope

Such a low V_{OC} indicates that the cell was severely damaged due to the contact with the emitter at 1200 K. Performing NF-TPV experiments with InSb cells at such high emitter temperature would require thermal protection of the active area, with a layer of a material stable at high temperature and transparent in the infrared region. Moreover, this material should be able to transfer near-field thermal radiation, from frustrated mode contribution, to the InSb TPV cell in order to keep a near-field enhancement of the photogenerated power. Such intermediate substrate has been experimentally tested in an NF-TPV device in the work of Inoue *et al.*[21], where they used a 50 µm-thick undoped Si substrate placed between the emitter and the cell (see Sec.V.6.2 for more details).

VI.6 Conclusion

In this chapter, near-field thermophotovoltaic experiments between a spherical emitter and InSb TPV cells have been performed (see Appendix 5 for a summary of the performances). In order to maximize the electrical power generated by the cell, both the emitter and the cell have been specifically designed. Optimum cell characteristics, such as doping levels and substrate thickness, previously established with calculations have been applied in the fabrication process. Performances of the TPV cells fabricated for this work have been measured without and with infrared illumination as a function of the active area diameter, substrate thickness, p-doping level, operating temperature of the cell and emitter material. The cells have been found to be fully functional at cryogenic temperatures below 77 K, with remarkably good I-V characteristics, even generating electrical power under ambient-temperature illumination. This study has demonstrated that near-field thermal energy can be exploited efficiently, when optical properties of the emitter are best matching those of the cell. Thermophotovoltaic conversion of thermal photons in the near field was measured using a graphite emitter with efficiency reaching 20% and electrical power density reaching 7.50 $kW.m^{-2}$, orders of magnitude larger than previous works[20–22]. Such an electrical power density is close to the ~1 $W.cm^{-2}$ threshold typical for powerful thermoelectric energy harvesting devices[102], and close to the best far-field thermophotovoltaic performances despite much lower emitter temperatures[116,153]. However, the limited statistics from the experiments has not allowed to conclude fully on the parametric study. The reliability of the measurement setup should be improved in terms of distance uncertainty. In addition, further characterizations with *e.g.* EQE measurements could provide a better understanding of the characteristics of the cells.

This proof of principle for efficient near-field thermophotovoltaic conversion paves the way for fabrication of devices in different fields. For energy harvesting it is also required to upscale the sizes, implying flat surfaces, and to avoid cooling the cell. Recent strategies for designing efficient cells illuminated in the far field with narrow energy bandgap III-V materials operating at room temperature[173] could also be applied in the near field, with frustrated photon modes and would be particularly useful for harnessing energy of medium-grade heat sources. For high-grade heat sources, this study has demonstrated the possibility to maintain a temperature difference larger than 1000 K across a small gap distance, so larger energy gap materials used in cells operating at room temperature could also be considered with a careful design for the near field following the highlighted paths. Finally, it is reminded that further enhancement of the performances is predicted for materials with polariton resonances above the energy bandgap[163,174].

General conclusion and prospects

Radiative heat transfer at the nanoscale is very different from that at the macroscale, in terms of spectral distribution and power amplitude. In this work, experimental demonstrations of the contribution of evanescent waves to radiative heat transfer at the nanoscale between two bodies have been achieved. A review of the state of the art based on experimental works of many research groups has been made and some trends have been highlighted. We have found that all of the published experimental works could be classified into three categories with respect to their near-field radiative exchange area. Each category has advantages and drawbacks in terms of minimum emitter-sample distance and radiative conductance level and accuracy. Uninvestigated fields of study have emerged, in particular concerning the influence of materials and temperature differences larger than 420 K. Large temperature differences are essential in order to use near-field radiative heat transfer in energy harvesting applications such as TPV systems. This review has led to the definition of some of the objectives of this work. It has appeared that using a microsphere as the radiative emitter, instead of a planar or tip-shaped one, is the best compromise between large radiative heat fluxes and a small emitter-sample distance.

Numerical calculations have allowed to calculate radiative heat transfer between several pairs of materials made of either SiO_2, graphite or InSb at different temperatures. The evolution of the near-field radiative conductance as a function of temperature has been observed to be very different from one pair of materials to the other because of the differences of optical properties. In addition, the exponent of the temperature power law of the exchanged radiative power has appeared to be different from that calculated in the far field due to the modification of the spectrum when evanescent waves contribute. Furthermore, calculations have shown that graphite was a promising emitter material to be paired with an InSb TPV cell. The aim has been to maximize radiative heat transfer in the near field for photons having energies larger than the energy bandgap of the cell. The optimization of the dimensions of the emitter-cell system has shown that the smallest cell available, having an active area diameter of 20 µm, should be paired with a graphite sphere having a diameter 1.5 times larger.

The design and development of an experimental setup has permitted near-field radiative heat transfer and near-field TPV measurements between a microsphere and a planar substrate. A key advance of our experimental setup has been the integration of a liquid helium cryostat for cryogenic cooling of the substrate especially needed for our near-field TPV measurements. Large emitter-substrate temperature differences above 900 K, more than twice the maximum reported in the literature for near-field radiative heat transfer measurements, have been reached by fabricating the emitters based on SThM doped-silicon probes. The minimum distance between the emitter and the substrate has been determined to be around 30-40 nm without the cooling system and 100 nm with it because of larger mechanical vibrations. The typical accuracy of the near-field radiative conductance measurements has been found to be a relative uncertainty of 20 % with a 30 $pW.K^{-1}$ ($0.67\ pW.K^{-1}/\sqrt{Hz}$) sensitivity by considering the random electrical noise and the systematic error from the emitter calibration. The performances of the setup in terms of minimum distance and measurement accuracy have been found to be of the same order as similar published experimental works.

During near-field radiative heat transfer experiments, the emitter has been heated up to 1200 K representing a significant advance compared to the state of the art. The cantilever and the tip of the SThM probe have been found to have a negligible contribution to near-field radiative heat transfer with conductances below ~ 200 $pW.K^{-1}$. Such conductances are one to two orders of magnitude

lower than those measured during sphere-plane experiments. With a spherical emitter, a near-field radiative conductance of 68.9 $nW.K^{-1}$ has been measured for the graphite-graphite configuration with the emitter at 1200 K, which is the highest reported to date for the sphere-plane configuration[16,24,40,41,44,47,67,68]. The temperature dependence of the near-field conductance has been characterized as a function of distance for six pairs of materials by determining the exponent of the temperature power law of the measured conductance. The exponent has been found to be lower than the values above 4 in the far field and to vary as a function of distance and materials, from 2.58 ± 0.22 for the SiO_2-InSb configuration up to 3.58 ± 0.34 for the graphite-InSb configuration at a distance of 100 nm. These values are higher than the $\propto T^2$ behavior expected in the near field for a greybody. This result demonstrates that the radiative power exchanged in the near field increases with temperature but differently according to the materials. Therefore, material pairs presenting a temperature power law with a large exponent may be expected to be more suitable for applications where a large radiative heat flux is needed at high temperatures, such as TPV energy harvesting.

A theoretical study has suggested that good performances could be achieved for a near-field TPV device coupling a cooled InSb TPV cell matching the emission spectrum of a graphite infrared thermal emitter. This strategy is based on the idea of using a low-energy bandgap material, but therefore requires to cool down the cell. The TPV cells, designed and fabricated specifically for this work, have appeared to be functioning well at cryogenic temperatures near 77 K, even generating power under ambient-temperature illumination. Good performances have been observed with a fill factor up to 0.75 and an open-circuit voltage above 130 mV for cells generating an electrical power of a few microwatts. The best results with a near-field illumination have been obtained with cells having the same active areas of 20 µm in diameter but different characteristics. An electrical power density of 7.5 $kW.m^{-2}$ (or 11.5 $W.m^{-2}.K^{-1}$ considering the temperature difference between the emitter and the cell) and near-field conversion efficiencies up to ~20 % have been measured, representing a remarkable performance improvement compared to state-of-the-art devices (Table VI.4). The near-field conversion efficiency has been measured for the first time, with a 20-fold enhancement compared to the previous best estimated total efficiency reported in the literature. The electrical power density measured during this work is three orders of magnitude larger that the best one previously reported. The large electrical power densities in the near field are due to an electrical power enhancement up to a factor of 6 compared to a far field illumination. Such good performances prove that NF-TPV devices may compete with thermoelectric generators reaching power densities of 1 $W.cm^{-2}$ for a similar medium-grade hot body temperature[8].

This work has also demonstrated the possibility of maintaining temperature differences above 1100 K between the emitter and the substrate, opening the door to near-field energy harvesting from high-grade heat sources. The main contribution of this work is the experimental demonstration of the near-field enhancement of the electrical power generated by a TPV cell, achieved with large output electrical power densities and measured near-field conversion efficiencies. However, the influence of the parameters of the cell has not been well established because of the limited number of cells that were fabricated. Further study should be performed with more TPV cells in order to observe the expected influence of the different cell designs, independently from the repeatability issues of the fabrication-measurement process. This work suggests that further near-field radiative heat transfer experiments should be performed with various configurations, especially with materials interesting for energy harvesting applications.

Table VI.4: Comparison of performances between state-of-the-art NF-TPV experiments and measurements performed during this work

Source	Year	Efficiency [%]	$max(P_{TPV,max})$ [W.cm^{-2}]	[W.m^{-2}.K^{-1}]	Cell	E_g [eV]	Emitter	Emitter T [K]	ΔT [K]	FF	d_{min} [nm]
Fiorino *et al.*[20]	2018	0.015 *estimated*	3.4.10^{-5}	9.7.10^{-4}	InAsSb	0.35 *at 300 K*	Si	655	360	0.26	60
Inoue *et al.*[21]	2019	0.98 *estimated*	7.5 10^{-4}	9.8.10^{-3}	InGaAs	0.73 *at 300 K*	Si	1065 *(estimated)*	765	0.56	140
Bhatt *et al.*[22]	2019	0.003 *estimated*	1.3 10^{-6}	2.2.10^{-5}	Ge	0.67 *at 300 K*	Cr-W-Cr on a-Si	880	579	0.25	180
This work[175]	2020	21.5 ± 3.8 ***measured*** *(near-field contribution)*	7.5.**10^{-1}**	1.2.**10^{1}**	InSb	0.23 *at 77 K*	Graphite	732-900	655-823	0.75	~100

Near-field radiative heat transfer experiments using microstructured substrates made of either SiO_2 or InSb were considered but could not be performed during the timeframe of this work. In addition, experiments using the tip-plane configuration could be made with various substrate materials and an analysis on the temperature dependence could be worth in order to compare to the measurements obtained with the sphere-plane configuration. The possibility of cooling the substrate down to 10 K could offer the possibility of studying materials exhibiting changing properties at cryogenic temperatures such as superconductors[176]. For TPV energy harvesting applications, it would be worth studying innovative pairs of materials in order to find behaviors maximizing the radiative heat flux for photons with energies higher than the energy bandgap of the cell. For instance, a wide diversity of thermal emitters such as selective emitters, photonic crystals or multilayers have already been used experimentally for TPV conversion devices[12] and may have an interest for NF-TPV devices. Future research should focus on materials with polariton resonances above the energy bandgap of the cell[163,174]. During this work an emitter material supporting polariton resonances at an energy close to the energy bandgap of the cell (0.234 eV at 77 K) could not be found, resonances appearing at lower energies. However, promising materials such as zinc oxides[177] or rare-earth alloys[178] seem to have surface polariton resonance frequencies that can be tuned in the mid-infrared range. Lanthanum-lutetium-arsenide ($La_{1-x}Lu_xAs$) alloys seem promising with surface plasmon resonance frequencies corresponding to photon energies ranging from 0.146 up to 0.413 eV depending on the composition[178].

Following thermal energy harvesting applications, upscaling the sizes of the emitter and the cell appears essential in order to create NF-TPV devices that could supply valuable levels of electrical power. This could be achieved by replacing the spherical emitter by a planar one providing a larger area for radiative heat transfer in the near field. However, a large planar emitter leads to parallelization issues between the emitter and the cell. In addition, a practical NF-TPV device should involve an integrated TPV cell placed at a fixed position close to the emitter. The parallelization and fixed position requirements could be fulfilled by using an interface material between the emitter and the cell, providing durability and reliability to the device. The interface

material should be selected with care because it should reflect photons with energies lower than the bandgap of the cell while being transparent for photons having high energies. These characteristics could avoid excess heating of the cell due to sub-bandgap absorption simultaneously increasing the conversion efficiency. However, thermal conduction between the emitter and the substrate induced by the interface material could drastically lower the temperature difference and affects consequently the output power and conversion efficiency. Materials such as silicon were investigated experimentally[21] but appeared to absorb a portion of photons with energies higher than the bandgap of the cell. It may also be possible to use an interface material with thermoelectric properties for fabricating a hybrid TPV-thermoelectric energy conversion device. In addition to the upscaling, a solution to avoid cooling the cell must be found. Recently, strategies have emerged for the design of TPV cells operating at room temperature with narrow energy bandgap III-V semiconductor materials. For instance, these strategies may involve multiple-stage absorbers[173], or optimization of the characteristics of the cell and the front contact grid parameters[179]. Furthermore, the enhancement of the electrical power generated by a NF-TPV device could be achieved by coupling it with a thermionic energy conversion system[168].

There are still ways of improving the characterization and fabrication of the InSb TPV cells developed during this work. For instance, external quantum efficiency (EQE) measurements could not be performed but should provide key information on the spectral response of the cells. I-V characteristics under dark conditions have been performed for one cell only but should ideally be measured systematically for every cell, assessing dark current densities that should help evaluating the influence of the fabrication parameters. In addition, it may be worth fabricating a second generation of InSb TPV cells with an anti-reflection coating (ARC). Integrating an ARC in the design of a NF-TPV device has been suggested to enhance radiative heat transfer between the emitter and the cell for photons with energy higher than the energy bandgap of the cell, while decreasing the sub-bandgap transmission[180]. The minimum emitter-cell distance reached during NF-TPV experiments have been of the order of 100 nm but could be lower by further improving the experimental setup, thus allowing the cell to generate larger electrical power densities.

Each of these improvement paths leads to exciting scientific challenges that should be overtaken in the future in order to create NF-TPV devices with performances competing, or even exceeding, those of thermoelectric generators for harvesting energy from medium-grade heat sources.

Appendices

1. List of the main parameters of the experimental works found in the literature

Source	Date	d_{min} [m]	ΔT_{max}	Materials	Emitter	Exchange area	Exchange area [m²]	G [W.K⁻¹]	Resolution [W.K⁻¹]	G [W.m⁻²K⁻¹]	Resolution [W.m⁻²K⁻¹]
Feng, 2012	2012	$5.5\ 10^{-7}$	100	SiO_2	Plane	80 x 80 µm	$6.40\ 10^{-9}$			-	
Feng, 2013	2013	$1.0\ 10^{-6}$	100	SiO_2	Plane	80 x 80 µm	$6.40\ 10^{-9}$	$3.8\ 10^{-7}$	-	$5.9\ 10^{1}$	-
Kutateladze, 1979	1979	$1.0\ 10^{-5}$		Cu	Plane	107 mm disc	$8.99\ 10^{-3}$			-	
Hargreaves, 1969	1969	$1.5\ 10^{-6}$	23	Cr	Plane	25 mm disc	$4.91\ 10^{-4}$	$1.1\ 10^{-3}$		2.2	
Domoto, 1970	1970	$1.0\ 10^{-5}$	10	Cu	Plane	8.5 cm disc	$5.67\ 10^{-3}$	$5.7\ 10^{-8}$	-	$1.0\ 10^{-5}$	-
Hu, 2008	2008	$1.6\ 10^{-6}$	80	SiO_2	Plane	1.27 cm disc	$1.27\ 10^{-4}$	$1.6\ 10^{-3}$		$1.3\ 10^{1}$	
Ottens, 2011	2011	$3.6\ 10^{-6}$	30	Sapphire	Plane	5 x 5 cm	$2.50\ 10^{-3}$	$4.6\ 10^{-3}$	$3.3\ 10^{-4}$	1.8	$1.3\ 10^{-1}$
Kralik, 2011	2011	$1.0\ 10^{-6}$	95	W	Plane	3.5 cm disc	$9.62\ 10^{-4}$	$3.1\ 10^{-6}$		$3.2\ 10^{-3}$	
St-Gelais, 2014	2014	$2.5\ 10^{-7}$	135	SiO_2	Plane	200 µm x 500 nm	$1.00\ 10^{-10}$	$1.3\ 10^{-8}$	-	$1.3\ 10^{2}$	-
Ijiro, 2015	2015	$1.0\ 10^{-6}$	20	SiO_2, Au	Plane	2.5 cm disc	$4.91\ 10^{-4}$	$4.8\ 10^{-3}$	$1.2\ 10^{-4}$	9.8	$2.5\ 10^{-1}$
St-Gelais, 2016	2016	$5.0\ 10^{-8}$	420	SiO_2	Plane	200 µm x 500 nm	$1.00\ 10^{-10}$	$1.4\ 10^{-9}$	-	$1.4\ 10^{1}$	-
Song, 2016	2016	$6.0\ 10^{-8}$	10	SiO_2	Plane	40 x 40 µm	$1.60\ 10^{-9}$	$9.4\ 10^{-7}$	$2.0\ 10^{-9}$	$5.9\ 10^{2}$	1.3
Lang, 2017	2017	$1.5\ 10^{-7}$	7	SiO_2	Plane	2 cm disc	$3.14\ 10^{-4}$	$2.9\ 10^{-2}$	$3.8\ 10^{-3}$	$9.2\ 10^{1}$	$1.2\ 10^{1}$
Ito, 2017	2017	$3.7\ 10^{-7}$	60	SiO_2,VO_2	Plane	1.26 x 1.26 cm	$1.59\ 10^{-4}$	$3.2\ 10^{-3}$	$2.1\ 10^{-5}$	$2.0\ 10^{1}$	$1.3\ 10^{-1}$
Ghashami, 2018	2018	$2.0\ 10^{-7}$	156	SiO_2	Plane	5 x 5 mm	$2.50\ 10^{-5}$	$1.2\ 10^{-2}$	$2.6\ 10^{-3}$	$4.6\ 10^{2}$	$1.0\ 10^{2}$
Fiorino, 2018	2018	$3.0\ 10^{-8}$	13	SiO_2	Plane	50 x 50 µm	$2.50\ 10^{-9}$	$1.2\ 10^{-5}$	$5.3\ 10^{-7}$	$4.6\ 10^{3}$	$2.1\ 10^{2}$
Fiorino, 2018	2018	$1.4\ 10^{-7}$	70	Si, VO_2	Plane	80 µm disc	$5.03\ 10^{-9}$	$2.6\ 10^{-7}$	$7.1\ 10^{-9}$	$5.3\ 10^{1}$	1.4
DeSutter, 2019	2019	$1.1\ 10^{-7}$	100	Doped Si	Plane	5x5 mm	$2.50\ 10^{-5}$	$4.3\ 10^{-3}$	$6.3\ 10^{-4}$	$2.5\ 10^{2}$	$2.5\ 10^{1}$
Ying, 2019	2019	$1.9\ 10^{-7}$	85	Doped Si	Plane	1 x 1 cm	$1.00\ 10^{-4}$	$8.5\ 10^{-3}$	$2.1\ 10^{-3}$	$8.5\ 10^{1}$	$2.1\ 10^{1}$
Lim, 2019	2019	$3.8\ 10^{-7}$	130	Doped Si, SiO_2, Ti	Plane	540 µm x 14 mm	$7.56\ 10^{-6}$	$1.3\ 10^{-4}$	$3.5\ 10^{-5}$	$1.7\ 10^{1}$	4.6
Shi, 2019	2019	$1.7\ 10^{-7}$	35	Graphene, SiO_2	Plane	5 x 5mm	$2.50\ 10^{-5}$	$6.7\ 10^{-3}$	$1.4\ 10^{-4}$	$2.7\ 10^{2}$	5.7
Musilova, 2019	2019	$5.4\ 10^{-6}$	40	NbN	Plane	3.5 cm disc	$9.62\ 10^{-4}$	$7.5\ 10^{-6}$	$3.0\ 10^{-6}$	$7.8\ 10^{-3}$	$3.1\ 10^{-3}$
Thompson, 2019	2019	$2.5\ 10^{-7}$	9	SiN	Plane	60 x 180 µm	$1.08\ 10^{-8}$	$5.0\ 10^{-10}$	$7.5\ 10^{-11}$	$4.6\ 10^{-2}$	$6.9\ 10^{-3}$
Kralik, 2012	2012	$1.0\ 10^{-6}$	35	W	Plane	35 mm disc	$9.62\ 10^{-4}$	$1.9\ 10^{-5}$	-	$2.0\ 10^{-2}$	-
Lim, 2018	2018	$1.6\ 10^{-7}$	100	Ti/MgF2 multi-layers	Plane	540 µm x 14 mm	$7.56\ 10^{-6}$	$5.3\ 10^{-4}$	$3.8\ 10^{-5}$	$7.0\ 10^{1}$	5.0
Narayanaswamy, 2008	2008	$1.0\ 10^{-7}$	47	SiO_2	Sphere	50 µm diameter	$1.96\ 10^{-9}$	$6.4\ 10^{-9}$	$4.3\ 10^{-10}$	3.3	$2.2\ 10^{-1}$
Rousseau, 2009	2009	$3.0\ 10^{-8}$	21	SiO_2	Sphere	40 µm diameter	$1.26\ 10^{-9}$	$1.9\ 10^{-8}$	$1.9\ 10^{-9}$	$1.5\ 10^{1}$	1.5
Shen, 2009	2009	$3.0\ 10^{-8}$	17	SiO_2, Si, Au	Sphere	50 µm diameter	$1.96\ 10^{-9}$	$1.8\ 10^{-8}$	$4.1\ 10^{-10}$	9.0	$2.1\ 10^{-1}$
Shen, 2012	2012	$3.0\ 10^{-8}$	34	Au	Sphere	50 µm diameter	$1.96\ 10^{-9}$	$1.5\ 10^{-9}$	$3.8\ 10^{-10}$	$7.5\ 10^{-1}$	$1.9\ 10^{-1}$
Song, 2015	2015	$2.0\ 10^{-8}$	10	SiO_2	Sphere	53 µm diameter	$2.21\ 10^{-9}$	$1.2\ 10^{-8}$	$5.0\ 10^{-10}$	5.4	$2.3\ 10^{-1}$
Menges, 2016	2016	$1.5\ 10^{-8}$	159	SiO_2	Sphere	17 µm diameter	$2.27\ 10^{-10}$	$6.3\ 10^{-9}$	$6.3\ 10^{-11}$	$2.8\ 10^{1}$	$2.8\ 10^{-1}$
van Zwol, 2012	2012 (108)	$8.0\ 10^{-8}$	75	SiO_2, VO_2	Sphere	40 µm diameter	$1.26\ 10^{-9}$	$1.0\ 10^{-8}$	$2.0\ 10^{-9}$	8.0	1.6
van Zwol, 2012	2012 (109)	$8.0\ 10^{-8}$	60	SiO_2, SiC	Sphere	40 µm diameter	$1.26\ 10^{-9}$	$2.7\ 10^{-9}$	$1.9\ 10^{-9}$	2.2	1.5
Müller-Hirsch, 1999	1999	$1.0\ 10^{-10}$	200	Au, Ni	Tip	1 µm R_C	$7.85\ 10^{-13}$			-	
Kittel, 2005	2005	$1.0\ 10^{-9}$	200	Au, GaN	Tip	60 nm R_C	$1.13\ 10^{-14}$	$5.0\ 10^{-8}$	$5.0\ 10^{-11}$	$4.4\ 10^{6}$	$4.4\ 10^{3}$
Kim, 2015	2015	$2.0\ 10^{-9}$	115	SiO_2, SiN, Au	Tip	225 nm R_C	$1.59\ 10^{-13}$	$1.7\ 10^{-9}$	$4.3\ 10^{-11}$	$1.1\ 10^{4}$	$2.7\ 10^{2}$
Cui, 2017	2017	$3.0\ 10^{-10}$	130	Au	Tip	150 nm R_C	$7.07\ 10^{-14}$	$5.0\ 10^{-10}$	$2.5\ 10^{-9}$	$7.1\ 10^{3}$	$3.5\ 10^{4}$
Kloppstech, 2017	2017	$5.0\ 10^{-10}$	160	Au	Tip	30 nm R_C	$2.83\ 10^{-15}$	$3.1\ 10^{-9}$	$9.4\ 10^{-10}$	$1.1\ 10^{6}$	$3.3\ 10^{5}$
Xu, 1994	1994	$5.0\ 10^{-08}$	40	In. AgCuCr	Tip	100 µm disc	$7.85\ 10^{-9}$	-	$9.8\ 10^{-09}$	-	1.3
Guha, 2012	2012	$4.0\ 10^{-07}$	162	SiO_2	Tip	15 µm R_C	$2.83\ 10^{-9}$	$1.2\ 10^{-9}$	$9.3\ 10^{-11}$	$4.4\ 10^{-1}$	$3.3\ 10^{-2}$
Worbes, 2013	2013	$1.0\ 10^{-10}$	160	Au, NaCl	Tip	50 nm R_C	$7.85\ 10^{-15}$			-	

2. Details on conductance uncertainties calculations

In this section, details on the different steps for the calculation of the conductance uncertainty are provided.
The relative uncertainty of the emitter current is expressed as a function of the total current I_{heat} and the electrical resistances of the circuit R_1, R_2, R_V and R the resistance of the emitter:

$$\frac{\delta I}{I} = \frac{\delta I_{heat}}{I_{heat}} + \frac{\delta\left[1-\left(1+\frac{R_1+R_V}{R_2+R}\right)^{-1}\right]}{1-\left(1+\frac{R_1+R_V}{R_2+R}\right)^{-1}} \quad (1)$$

The numerator of the second term of the previous equation can be written and developed as:

$$\delta\left[1-\left(1+\frac{R_1+R_V}{R_2+R}\right)^{-1}\right] = \delta\frac{1}{1+\frac{R_1+R_V}{R_2+R}} = \frac{1}{1+\frac{R_1+R_V}{R_2+R}}\left[\frac{\delta\left(1+\frac{R_1+R_V}{R_2+R}\right)}{1+\frac{R_1+R_V}{R_2+R}}\right] \quad (2)$$

$$\delta\left[1-\left(1+\frac{R_1+R_V}{R_2+R}\right)^{-1}\right] = \frac{\frac{R_1+R_V}{R_2+R}\left[\frac{\delta R_1+\delta R_V}{R_1+R_V}+\frac{\delta R_2+\delta R}{R_2+R}\right]}{\left(1+\frac{R_1+R_V}{R_2+R}\right)^2} \quad (3)$$

The final expression of the relative uncertainty of the emitter current is given in the main text by Eq. (III.16).
Development of the second term of Eq. (III.12) is presented with the following equations:

$$\delta\left[\Delta\theta\left(\alpha-\frac{1}{\theta}\right)+2\frac{\Delta I}{I}\right] = \delta\left[\Delta\theta\left(\alpha-\frac{1}{\theta}\right)\right]+2\delta\left[\frac{\Delta I}{I}\right] \quad (4)$$

$$\delta\left[\Delta\theta\left(\alpha-\frac{1}{\theta}\right)\right] = \delta\left[\alpha\Delta\theta-\frac{\Delta\theta}{\theta}\right] \quad (5)$$

$$\delta\left[\alpha\Delta\theta-\frac{\Delta\theta}{\theta}\right] = \delta[\alpha\Delta\theta]+\delta\left[\frac{\Delta\theta}{\theta}\right] = \alpha\Delta\theta\left[\frac{\delta\alpha}{\alpha}+\frac{\delta\Delta\theta}{\Delta\theta}\right]+\frac{\Delta\theta}{\theta}\left[\frac{\delta\Delta\theta}{\Delta\theta}+\frac{\delta\theta}{\theta}\right] \quad (6)$$

$$\delta\left[\Delta\theta\left(\alpha-\frac{1}{\theta}\right)+2\frac{\Delta I}{I}\right] = \alpha\Delta\theta\left[\frac{\delta\alpha}{\alpha}+\frac{\delta\Delta\theta}{\Delta\theta}\right]+\frac{\Delta\theta}{\theta}\left[\frac{\delta\Delta\theta}{\Delta\theta}+\frac{\delta\theta}{\theta}\right]+2\delta\left[\frac{\Delta I}{I}\right] \quad (7)$$

New terms appear as the difference of temperature elevation $\delta\Delta\theta$ and the current variation $\delta\Delta I$. They can all be expressed as the following equations considering that $\Delta\theta = T - T_{ref}$:

$$\delta\Delta\theta = err_T\Delta\theta + 2\delta T \quad (8)$$

$$\delta\left[\frac{\Delta I}{I}\right] = \frac{\Delta I}{I}\left[\frac{\delta\Delta I}{\Delta I}+\frac{\delta I}{I}\right] = \frac{\Delta I}{I}\left[\frac{2\delta I}{\Delta I}+\frac{\delta I}{I}\right] = \frac{\delta I}{I}\left[2+\frac{\Delta I}{I}\right] \quad (9)$$

Combination of Eq. (7) and (9) gives the final expression of the second term of Eq. (III.12), which is written in the main text as Eq. (III.19).

3. Microsphere semi-transparency coefficient calculation

Microsphere have an emissivity different from that of the bulk material due to semi-transparency effect. A semi-transparency emissivity coefficient taking this effect into account can be calculated as a function of the frequency, sphere radius and emission angle[30]. One writes:

$$q_\omega^i = q_\omega^{i-1} T_\omega(l) + \int_{s=0}^{l} \kappa_\omega(s) q_\omega^{BB}\big(T(s)\big) T_\omega(s,l) \tag{10}$$

$$l = 2R_{sphere}\cos\,\theta' \tag{11}$$

$$\sin\theta' = \left(\frac{\sqrt{2}\sin\,\theta}{\sqrt{n^2-\kappa^2+\sin(\theta)^2+\sqrt{(n^2-\kappa^2-\sin(\theta)^2)^2+4n^2\kappa^2}}} \right) \tag{12}$$

$$l = 2R_{sphere}\cos\left(\sin^{-1}\left(\frac{\sqrt{2}\sin\,\theta}{\sqrt{n^2-\kappa^2+\sin(\theta)^2+\sqrt{(n^2-\kappa^2-\sin(\theta)^2)^2+4n^2\kappa^2}}} \right) \right) \tag{13}$$

where, q_ω^i is the spectral radiative hemispherical heat flux at point *i* (Figure A.1), q_ω^{i-1} is the spectral radiative hemispherical heat flux at the point *i-1*, $T_\omega(l)$ is the transmittance of the path with a length *l*, $\kappa_\omega(s) q_\omega^{BB}(T(s))$ is the local emission reinforcement term with the extinction index $\kappa_\omega = \frac{2\omega\kappa}{c}$ (κ is the extinction coefficient) and $q_\omega^{BB}(T(s))$ the blackbody radiative hemispherical heat flux at a temperature *T*(s). The last term $T_\omega(s,l) = e^{-\kappa_\omega l}$ is the transmittance of the path from point *s* to point *l*.

The length *l* is calculated using Eq. (11), depending on the angle θ' and the sphere radius R_{sphere}. θ' is calculated using Eq. (12), corresponding to the Descartes-Snell's law of refraction in an absorbing medium, reported from the work of Kovalenko *et al.*[181]. Finally, the length *l* (Eq. (13)) depends on R_{sphere}, the emission angle θ and the complex refractive index of the media $n+i\kappa$. The spectral radiative hemispherical heat flux at the point *n* of the sphere (Fig. A.1a) can be expressed as:

$$q_\omega^n = \left[q_\omega^{n-1} T_\omega(l) + \int_{s=0}^{l} \kappa_\omega(s) q_\omega^{BB}\big(T(s)\big) T_\omega(s,l) \right] (1 - re_\omega) \tag{14}$$

Here, re_ω is the reflection coefficient at the interface so the spectral radiative hemispherical heat flux at the point *n* is the spectral radiative hemispherical heat flux coming from the point *n-1* reinforced along the path *l* that is not internally reflected at the interface. Then, the spectral radiative hemispherical heat flux at the point *n-1* can be expressed as:

$$q_\omega^{n-1} = \left[q_\omega^{n-2} T_\omega(l) + \int_{s=0}^{l} \kappa_\omega(s) q_\omega^{BB}\big(T(s)\big) T_\omega(s,l) \right] re_\omega \tag{15}$$

For point *n-1*, the spectral radiative hemispherical heat flux is the one coming from the point *n-2* that is not internally reflected at the interface. Eq. (15) can be used for the other points *n-2*, *n-3* and so on. The spectral radiative hemispherical heat flux at the point *n* can be written as:

$$q_\omega^n = (1 - re_\omega)[1 + re_\omega T_\omega(d) + (re_\omega T_\omega(d))^2 + \cdots] \int_{s=0}^{l} \kappa_\omega(s) q_\omega^{BB}\big(T(s)\big) T_\omega(s,l)\, ds \tag{16}$$

$$q_\omega^n = (1 - re_\omega) \sum_{j=0}^{\infty} \left(re_\omega T_\omega(d)\right)^j \int_{s=0}^{l} \kappa_\omega(s) q_\omega^{BB}\left(T(s)\right) T_\omega(s,l)\, ds \qquad (17)$$

Eq. (17) has a term being the infinite sum of a geometrical series. Such a term has an analytical solution so the final expression of the spectral radiative hemispherical heat flux at point *n* can be expressed as:

$$q_\omega^n = \frac{1 - re_\omega}{1 - re_\omega T_\omega(d)} \int_{s=0}^{l} \kappa_\omega(s) q_\omega^{BB}\left(T(s)\right) T_\omega(s,l)\, ds \qquad (18)$$

The semi-transparency coefficient is the ratio of q_ω^n and the radiative hemispherical heat flux of the bulk material (here SiO_2):

$$st = \frac{q_\omega^n}{q_\omega^{BB} \epsilon_{SiO_2}^{bulk}(\omega, \theta)} \qquad (19)$$

Study of the influence of the sphere radius indicates that, for large spheres, st tends to large values close to 1, corresponding to an opaque bulk material. In Figure A.1b, st is plotted as a function of wavelength for different sphere radii and different emission angles. When θ increases, the spectral radiative hemispherical heat flux decreases, leading to a smaller st. As expected, the spectral radiative heat flux calculated for a large sphere tends to that of the bulk material, as seen in Figure A.1c. For R = 10^{-3} m, the curves representative of the sphere and the bulk material are superimposed. It has to be noticed that for small spheres, when R_{sphere} is smaller or of the order of λ_{Wien}, the accuracy of this calculation method is questionable because of coherence effects[84].

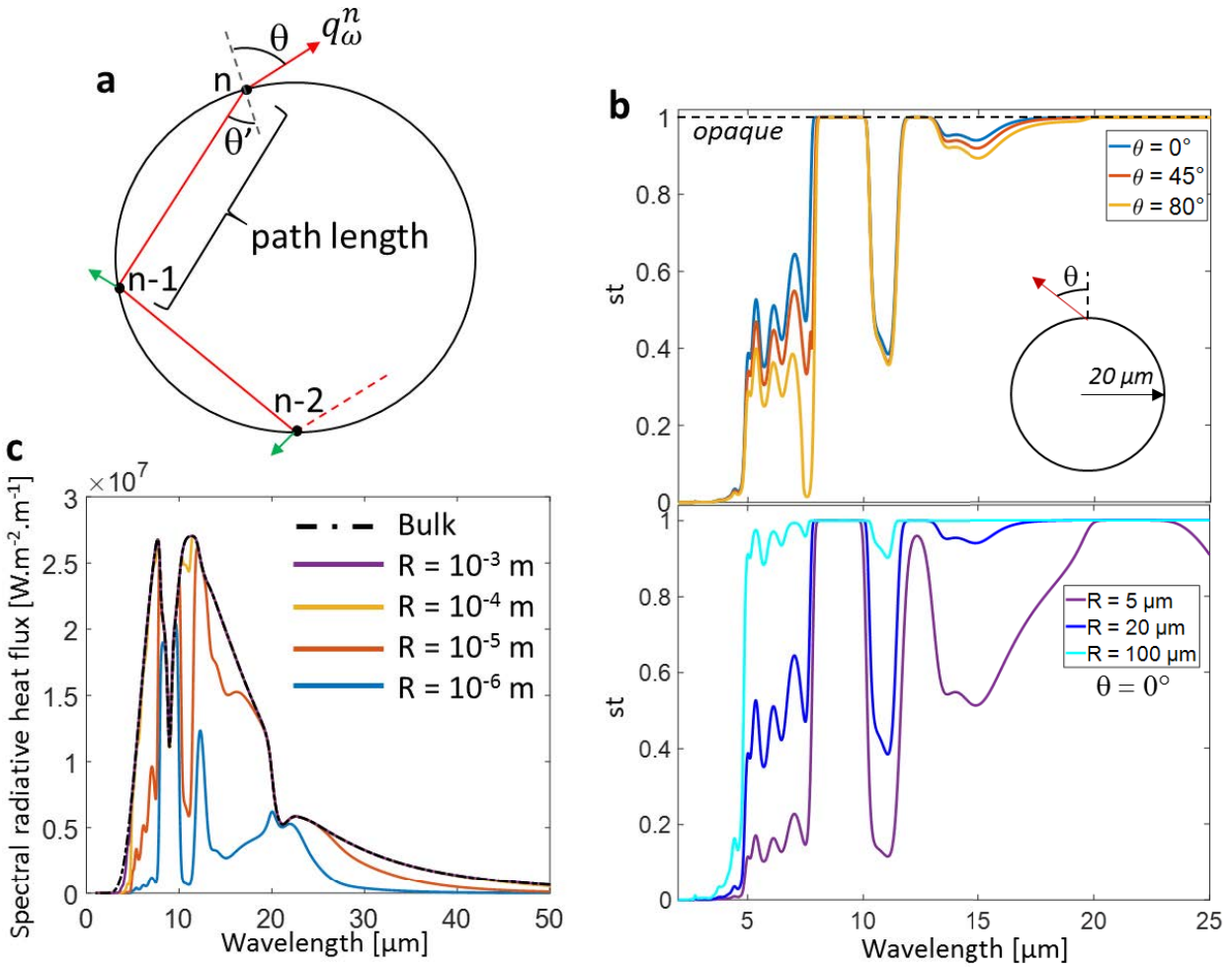

Figure A.1: (a) Schematic of the emissivity of a semi-transparent sphere. (b) Semi-transparency coefficient calculations for a 20 µm radius SiO_2 sphere at 300 K as a function of wavelength for three emission angles (top) and for three different sphere radii at a normal emission angle (bottom). (c) Spectral radiative heat flux at $\theta = 0$ and at 300 K for different sphere radii

4. Influence of air in emitter-substrate heat transfer

The experimental setup allows to perform approach curves while measuring thermal conductance of the emitter in air. In this configuration, heat transfer through conduction in air between the emitter and the substrate is expected to be dominant over radiative heat transfer. Therefore, the temperature drop of the emitter as a function of distance is expected to be larger than that observed in vacuum. Experiments are performed in two steps, in order to study a larger distance range than the usual 5 µm. First, the z piezoelectric positioner is used in slip-stick mode (see Sec. III.3.1.2 for details) during an approach from ~ 2 mm until contact, with a step size of 300 nm. Then, another approach is made during the last 5 µm using the fine positioning mode. The two approach curves are gathered to obtain a complete approach curve, from ~ 2 mm down to a few nanometers close to contact.

Sphere-plane configuration

Figure A.2a shows the temperature of a SiO_2 sphere, initially heated at 584 K, as a function of distance from 2 mm down to close to contact. In air, the observed temperature drop is of the order of tens of kelvins, which is much larger than ~ 0.1-1 K in vacuum.

Thermal conductance of the emitter as a function of distance is deduced from temperature measurements and shown in Figure A.2b. The global conductance increase during the approach is 1.894 $\mu W.K^{-1}$, more than two orders of magnitude higher than previously measured near-field radiative thermal conductances (*Table IV.1*). The part of the curve where near-field radiative heat transfer occurs corresponds to the part measured using the z piezoelectric positioner in fine positioning mode. In the corresponding distance range, the conductance increase is 550 $nW.K^{-1}$ which is still one order of magnitude higher than the highest measured near-field conductance value. This large difference proves that heat transfer through conduction in air is largely dominant over near-field radiative heat transfer. Figure A.2c shows the thermal conductance as a function of distance using a semi-logarithmic scale. This representation allows clearly to observe the different regimes of heat transfer between the sphere and the substrate. At distances around one millimeter, the sphere and the substrate are out of thermal interaction. Therefore, heat dissipation from the sphere is driven by heat convection between the emitter and the air, which does not depend on distance. When the distance starts decreasing, heat transfer increases between the sphere and the substrate due to the contribution of heat conduction in the diffusive regime. In this regime, heat carriers are gas molecules interacting between each other. When distance decreases below a certain value, gas molecules do not interact between each other anymore. This distance range corresponds to the ballistic regime, where heat carriers interact directly between the hot and cold bodies areas. In this regime, heat transfer does not depend on distance. Transition from convective to diffusive, then to ballistic regime are clearly seen on Figure A.2c, near respectively d = 0.5 mm and d = 200 nm. Studying heat transfer between a spherical emitter and a bulk substrate in air confirms that heat conduction is largely dominant over near-field radiative heat transfer. This work also shows that the experimental setup allows to study heat transfer in both air and vacuum. Performing experiments under atmospheric pressure with other gases than air can be easily considered, since no major modification of the experimental setup is needed. In addition, measuring heat transfer as a function of pressure might also be performed[182].

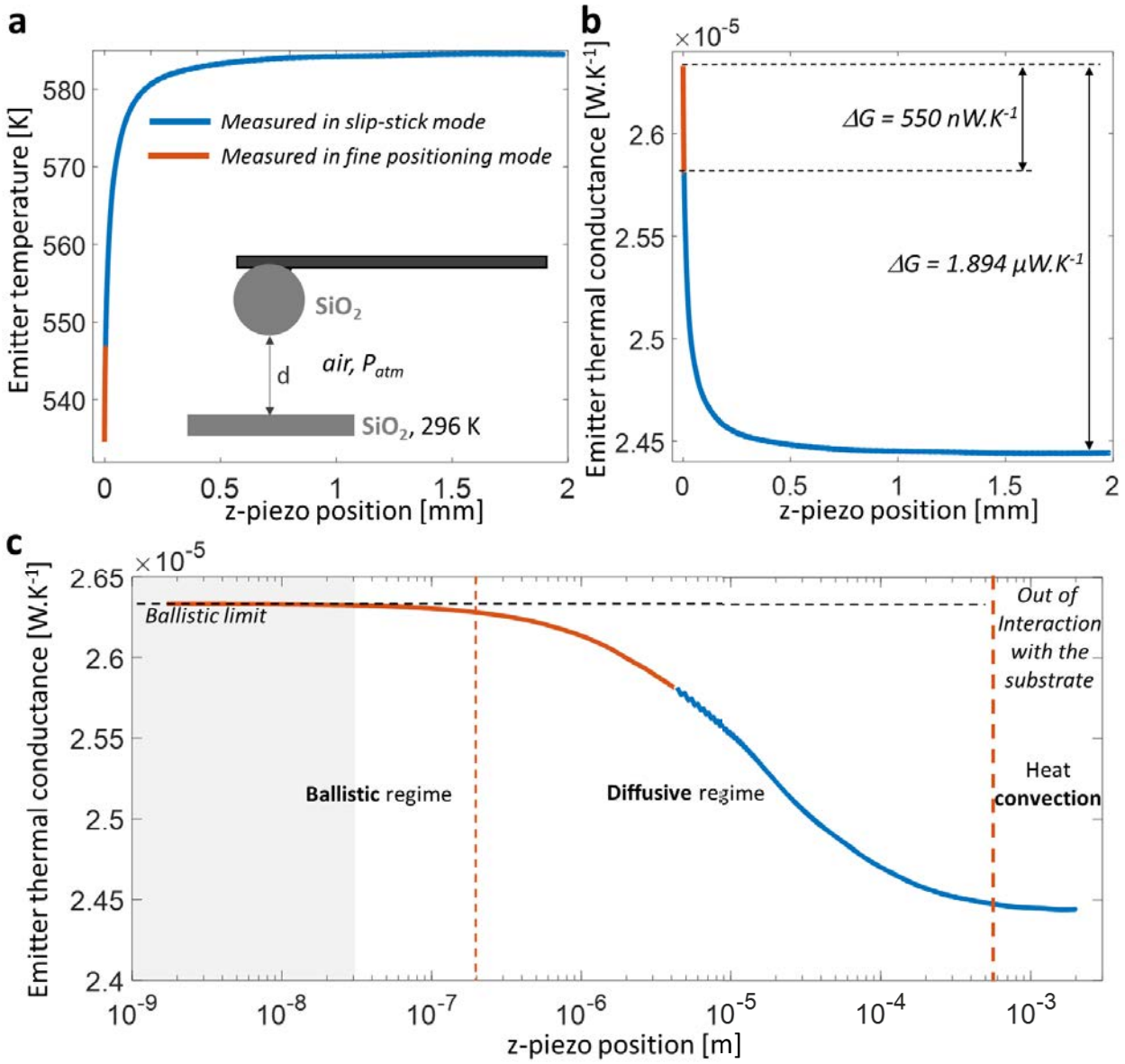

Figure A.2: Heat transfer in air at atmospheric pressure between a heated 40µm SiO_2 sphere and a flat bulk SiO_2 substrate as a function of distance.
(a) Emitter temperature as a function of distance. (b) Emitter thermal conductance as a function of distance. (c) Semi-logarithmic plot of emitter thermal conductance as a function of distance

Tip-plane configuration

Following the same experimental protocol as that for the sphere-plane configuration, measurements of heat transfer in air is performed for the tip-plane geometry, using a doped-Si SThM probe. Figure A.3a shows the temperature of a doped-Si tip, initially heated at 671 K, as a function of distance ranging from 2.3 mm to close to contact. The observed temperature drop of ~ 40 K is of the same order as the one measured for the sphere-plane configuration, despite using a tip hotter than the sphere. This may be due to the difference of heated area between the two geometrical configurations. The sphere represents a larger heated area compared to the area around the tip. Because of the higher temperature, the measured conductance enhancement at low distances for

the tip (Figure A.3b) is twice that measured with a sphere. In the semi-logarithmic scale plot (Figure A.3c), transitions between convective, diffusive and ballistic regimes are observed.
In order to compare measurements between sphere-plane and tip-plane geometries, normalized thermal conductance variations are plotted as a function of distance in Figure A.4. Thermal conductance for the sphere-plane configuration starts to increase at larger distances compared to the tip-plane configuration. However, the linear plot in inset shows that the increase occurs at a faster rate without sphere. At low distances, below 2 µm, behaviors become similar for the two configurations. Different observed general behaviors between the two configurations demonstrate that heat transfer in air depends on geometry, such as near-field radiative heat transfer. Further experiments and simulation of heat transfer between a SThM tip and a substrate are presented in the PhD thesis of E. Guen[90].

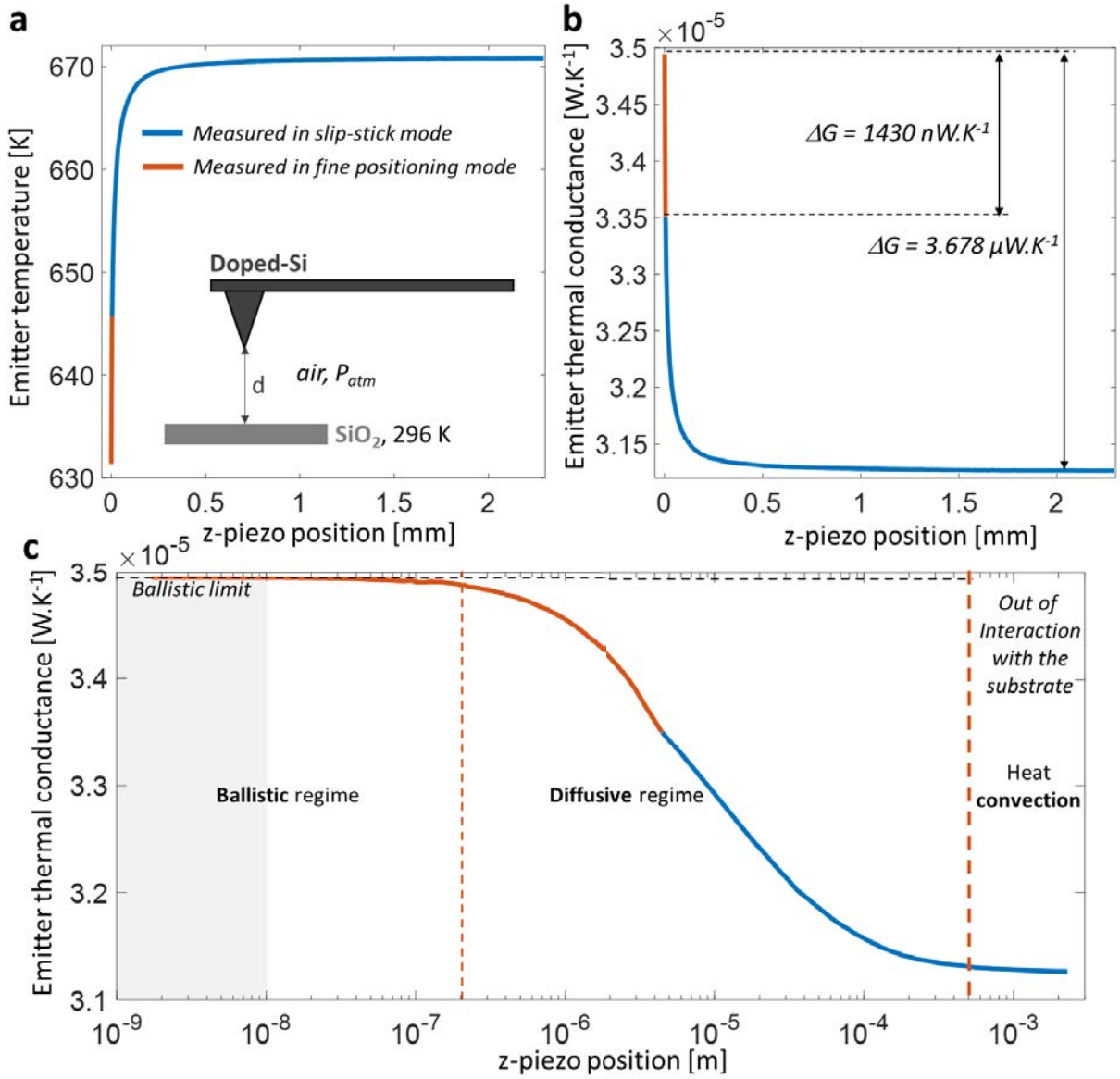

Figure A.3: Heat transfer in air at atmospheric pressure between a heated doped-Si SThM tip and a flat bulk SiO_2 substrate as a function of distance.
(a) Emitter temperature as a function of distance. (b) Emitter thermal conductance as a function of distance. (c) Semi-logarithmic plot of emitter thermal conductance as a function of distance

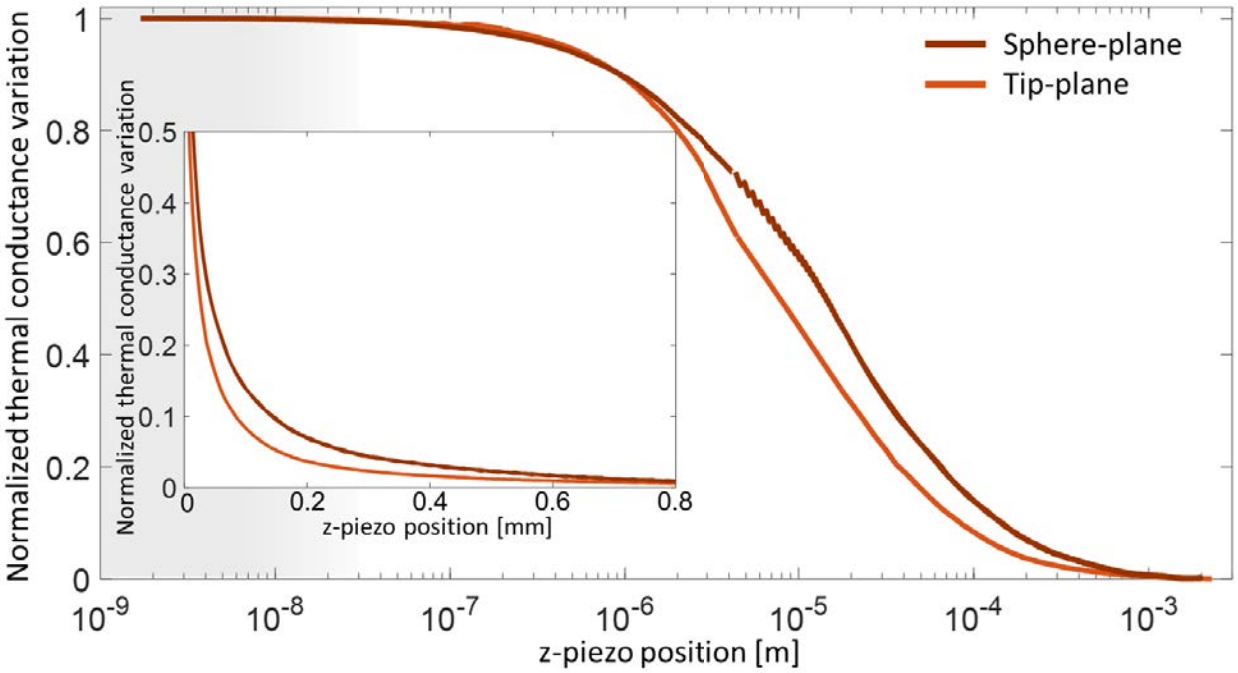

Figure A.4: Normalized thermal conductance variation for the sphere-plan and tip-plane configurations

5. Summary of NF-TPV measurements

Growth parameters	Batch n°	Method	$T_{emitter}$ [K]	N_A [cm^{-3}]	t_S [µm]	ΔT [K]	AA [µm]	$max(P_{TPV,max})$ [µW]	$max(P_{TPV,max})$ [kW.m^{-2}]	$max(P_{TPV,max})$ [W.m^{-2}.K^{-1}]	$max(P^{NF}_{TPV,max})$ [µW]	$max(P^{NF}_{TPV,max})$ [kW.m^{-2}]	$max(P^{NF}_{TPV,max})$ [W.m^{-2}.K^{-1}]	$Q_{NF,max}$ [µW]	η^{NF}_{TPV} [%]	EF	$Q_{FF,max}$ (estimated) [µW]	η_{TPV} (estimated) [%]
Optimal	1	≠ V	732	10^{17}	500	655	80	2.96	0.60	0.92	0.40	0.08	0.12		-	1.2	16.8	-
		≠ V	732	10^{17}	500	655	20	0.55	1.80	2.75	0.31	0.99	1.51	5.3 ± 1.0	5.9 ± 1.3	2.3	3.39	6.3 ± 0.7
		Sup. pr.	732	10^{17}	500	655	20	0.55	1.80	2.75	0.32	1.02	1.56	5.3 ± 1.0	6.0 ± 1.3	2.4	3.39	6.3 ± 0.7
		Sup. pr.	830	10^{17}	500	753	20	1.08	3.40	4.52	0.70	2.24	2.97	8.8 ± 1.6	7.9 ± 1.2	2.8	6.12	7.2 ± 0.7
		Sup. pr.	732	10^{17}	500	655	160	4.82	0.24	0.37	1.11	0.06	0.09		-	1.3	22.2	-
		≠ V	732	10^{17}	500	655	160	5.45	0.27	0.41	0.99	0.05	0.08	7.6 ± 1.4	13.0 ± 2.0	1.2	22.2	18.3 ± 0.9
		Sup. pr.	732	10^{17}	200	655	20	1.28	4.10	6.26	1.05	3.20	4.89	6.5 ± 1.1	16.2 ± 2.4	5.6	3.20	13.2 ± 1.4
		Sup. pr.	900	10^{17}	200	823	20	1.90	6.05	7.35	1.41	4.49	5.46	14.1 ± 2.2	10.0 ± 1.8	4.0	7.84	8.7 ± 0.9
		≠ V	732	10^{17}	200	655	20	1.25	3.97	6.06	1.04	3.31	4.73	7.4 ± 1.4	14.1 ± 2.9	4.6	3.20	12.4 ± 1.3
		≠ V SiO_2	732	10^{17}	200	655	20	0.58	1.85	2.82	0.15	0.48	0.73	3.9 ± 2.1	3.2 ± 2.2	1.4	5.23	6.4 ± 1.2
		Sup. pr.	732	10^{18}	500	655	20	2.35	7.48	11.42	1.96	6.25	9.54		-	5.9	3.44	-
		≠ V	732	10^{18}	500	655	20	2.36	7.50	11.45	1.79	5.70	8.70		-	4.1	3.44	-
	3	≠ V	900	10^{18}	200	823	20	1.57	5.00	6.08	0.92	2.92	3.55	12.9 ± 2.0	7.1 ± 2.0	2.4	7.99	7.5 ± 0.7
		≠ V	732	10^{18}	200	655	20	0.83	2.65	4.05	0.69	2.21	3.37	6.4 ± 1.2	10.8 ± 2.3	6.0	3.26	8.6 ± 1.0
	2	≠ V	732	10^{18}	500	655	20	1.41	4.49	6.85	0.90	2.87	4.38	6.6 ± 1.2	13.6 ± 2.9	2.8	3.44	14.0 ± 1.5
		≠ V	900	10^{18}	500	823	20	1.89	6.02	7.31	1.27	4.03	4.90	11.0 ± 1.8	11.6 ± 2.1	3.0	8.93	9.5 ± 0.8
Non-optimal	1	≠ V	732	10^{18}	500	655	20	1.79	5.70	8.70	1.55	4.94	7.54	7.2 ± 1.1	21.5 ± 3.8	7.4	3.39	16.9 ± 1.6

In the table, "≠ V" refers to the NF-TPV measurement method requiring series of approaches at different cell voltages, while "Sup. pr." refers to superposition principle.

Bibliography

1. Lawrence Livermore National Laboratory. 2019 energy flow chart. (2019).
2. Kishore, R. & Priya, S. A Review on Low-Grade Thermal Energy Harvesting: Materials, Methods and Devices. *Materials* **11**, 1433 (2018).
3. Thekdi, A. & Nimbalkar, S. U. *Industrial Waste Heat Recovery - Potential Applications, Available Technologies and Crosscutting R&D Opportunities*. ORNL/TM--2014/622, 1185778 http://www.osti.gov/servlets/purl/1185778/ (2015) doi:10.2172/1185778.
4. Datas, A. & Martí, A. Thermophotovoltaic energy in space applications: Review and future potential. *Solar Energy Materials and Solar Cells* **161**, 285–296 (2017).
5. Lolos, P. & Rogdakis, E. Thermodynamic analysis of a Kalina power unit driven by low temperature heat sources. *Therm. sci.* **13**, 21–31 (2009).
6. Knudsen, T., Clausen, L. R., Haglind, F. & Modi, A. Energy and Exergy Analysis of the Kalina Cycle for Use in Concentrated Solar Power Plants with Direct Steam Generation. *Energy Procedia* **57**, 361–370 (2014).
7. Go, D. B. *et al.* Thermionic Energy Conversion in the Twenty-first Century: Advances and Opportunities for Space and Terrestrial Applications. *Front. Mech. Eng.* **3**, 13 (2017).
8. Okanimba Tedah, I. A., Maculewicz, F., Wolf, D. E. & Schmechel, R. Thermoelectrics versus thermophotovoltaics: two approaches to convert heat fluxes into electricity. *J. Phys. D: Appl. Phys.* **52**, 275501 (2019).
9. Coutts, T. J. & Fitzgerald, M. C. Thermophotovoltaics. *Scientific American* **279**, 90–95 (1998).
10. Bauer, T. *Thermophotovoltaics: basic principles and critical aspects of system design*. (Springer, 2011).
11. Pfiester, N. A. & Vandervelde, T. E. Selective emitters for thermophotovoltaic applications: Selective emitters for TPV applications. *Phys. Status Solidi A* **214**, 1600410 (2017).
12. Sakakibara, R. *et al.* Practical emitters for thermophotovoltaics: a review. *J. Photon. Energy* **9**, 1 (2019).
13. Baranov, D. G. *et al.* Nanophotonic engineering of far-field thermal emitters. *Nat. Mater.* **18**, 920–930 (2019).
14. Polder, D. & Van Hove, M. Theory of radiative heat transfer between closely spaced bodies. *Physical Review B* **4**, 3303 (1971).
15. St-Gelais, R., Guha, B., Zhu, L., Fan, S. & Lipson, M. Demonstration of Strong Near-Field Radiative Heat Transfer between Integrated Nanostructures. *Nano Letters* **14**, 6971–6975 (2014).
16. Narayanaswamy, A., Shen, S. & Chen, G. Near-field radiative heat transfer between a sphere and a substrate. *Physical Review B* **78**, (2008).
17. Kittel, A. *et al.* Near-Field Heat Transfer in a Scanning Thermal Microscope. *Physical Review Letters* **95**, (2005).
18. Pan, J., Choy, H. & Jr, C. Very large radiative transfer over small distances from a black body for thermophotovoltaic applications. *Electron Devices, IEEE Transactions on* **47**, 241–249 (2000).

19. Whale, M. D. & Cravalho, E. G. Modeling and performance of microscale thermophotovoltaic energy conversion devices. *IEEE Transactions on Energy Conversion* **17**, 130–142 (2002).

20. Fiorino, A. *et al.* Nanogap near-field thermophotovoltaics. *Nature Nanotechnology* **13**, 806–811 (2018).

21. Inoue, T. *et al.* One-Chip Near-Field Thermophotovoltaic Device Integrating a Thin-Film Thermal Emitter and Photovoltaic Cell. *Nano Letters* **19**, 3948–3952 (2019).

22. Bhatt, G. R. *et al.* Integrated near-field thermo-photovoltaics for on-demand heat recycling. *arXiv e-prints* **1911**, arXiv:1911.11137 (2019).

23. DeSutter, J., Tang, L. & Francoeur, M. A near-field radiative heat transfer device. *Nat. Nanotechnol.* **14**, 751–755 (2019).

24. Menges, F. *et al.* Thermal radiative near field transport between vanadium dioxide and silicon oxide across the metal insulator transition. *Applied Physics Letters* **108**, 171904 (2016).

25. Kloppstech, K. *et al.* Giant heat transfer in the crossover regime between conduction and radiation. *Nature Communications* **8**, 1–5 (2017).

26. Planck, M. Zur Theorie des Gesetzes der Energieverteilung im Normalspectrum. *Verhandl. Dtsc. Phys. Ges.* **2**, 237 (1900).

27. Siegel, R. & Howell, J. R. *Thermal radiation heat transfer*. (Taylor & Francis, 2002).

28. Tsurimaki, Y. *et al.* Coherent regime and far-to-near-field transition for radiative heat transfer. *Journal of Quantitative Spectroscopy and Radiative Transfer* **187**, 310–321 (2017).

29. Rytov, S. M. Theory of electric fluctuations and thermal radiation. *Air Force Cambridge Research Center, Bedford, Mass.* AFCRC-TB-59-162 (1959).

30. Sacadura, J.-F. *Transferts thermiques: initiation et approfondissement*. (Lavoisier : Tec & Doc, 2015).

31. Loomis, J. J. & Maris, H. J. Theory of heat transfer by evanescent electromagnetic waves. *Physical Review B* **50**, 18517 (1994).

32. Mulet, J.-P. Modélisation du rayonnement thermique par une approche électromagnétique. Rôle des ondes de surface dans le transfert d'énergie aux courtes échelles et dans les forces de Casimir. (Université Paris Sud - Paris XI, 2003).

33. Joulain, K., Mulet, J.-P., Marquier, F., Carminati, R. & Greffet, J.-J. Surface electromagnetic waves thermally excited: Radiative heat transfer, coherence properties and Casimir forces revisited in the near field. *Surface Science Reports* **57**, 59–112 (2005).

34. Hargreaves, C. M. Anomalous radiative transfer between closely-spaced bodies. *Physics Letters A* **30**, 491–492 (1969).

35. Domoto, G. A., Boehm, R. F. & Tien, C. L. Experimental Investigation of Radiative Transfer Between Metallic Surfaces at Cryogenic Temperatures. *Journal of Heat Transfer* **92**, 412 (1970).

36. Xu, J. -B., Läuger, K., Möller, R., Dransfeld, K. & Wilson, I. H. Heat transfer between two metallic surfaces at small distances. *Journal of Applied Physics* **76**, 7209–7216 (1994).

37. Müller-Hirsch, W., Kraft, A., Hirsch, M. T., Parisi, J. & Kittel, A. Heat transfer in ultrahigh vacuum scanning thermal microscopy. *Journal of Vacuum Science & Technology A: Vacuum, Surfaces, and Films* **17**, 1205–1210 (1999).

38. Narayanaswamy, A. Investigation of Nanoscale Thermal Radiation: Theory and Experiments. 145 (2007).

39. Hu, L., Narayanaswamy, A., Chen, X. & Chen, G. Near-field thermal radiation between two closely spaced glass plates exceeding Planck's blackbody radiation law. *Applied Physics Letters* **92**, 133106 (2008).

40. Rousseau, E. *et al.* Radiative heat transfer at the nanoscale. *Nature Photonics* **3**, 514–517 (2009).

41. Shen, S., Narayanaswamy, A. & Chen, G. Surface Phonon Polaritons Mediated Energy Transfer between Nanoscale Gaps. *Nano Letters* **9**, 2909–2913 (2009).

42. Ottens, R. *et al.* Near-field radiative heat transfer between macroscopic planar surfaces. *Physical Review Letters* **107**, (2011).

43. Kralik, T., Hanzelka, P., Musilova, V., Srnka, A. & Zobac, M. Cryogenic apparatus for study of near-field heat transfer. *Review of Scientific Instruments* **82**, 055106 (2011).

44. Shen, S., Mavrokefalos, A., Sambegoro, P. & Chen, G. Nanoscale thermal radiation between two gold surfaces. *Applied Physics Letters* **100**, 233114 (2012).

45. Guha, B., Otey, C., Poitras, C. B., Fan, S. & Lipson, M. Near-Field Radiative Cooling of Nanostructures. *Nano Letters* **12**, 4546–4550 (2012).

46. Ijiro, T. & Yamada, N. Near-field radiative heat transfer between two parallel SiO_2 plates with and without microcavities. *Applied Physics Letters* **106**, 023103 (2015).

47. Song, B. *et al.* Enhancement of near-field radiative heat transfer using polar dielectric thin films. *Nature Nanotechnology* **10**, 253–258 (2015).

48. Kim, K. *et al.* Radiative heat transfer in the extreme near field. *Nature* **528**, 387–391 (2015).

49. St-Gelais, R., Zhu, L., Fan, S. & Lipson, M. Near-field radiative heat transfer between parallel structures in the deep subwavelength regime. *Nature Nanotech* **11**, 515–519 (2016).

50. Song, B. *et al.* Radiative heat conductances between dielectric and metallic parallel plates with nanoscale gaps. *Nature Nanotechnology* **11**, 509–514 (2016).

51. Lang, S. *et al.* Dynamic measurement of near-field radiative heat transfer. *Scientific Reports* **7**, (2017).

52. Ito, K., Nishikawa, K., Miura, A., Toshiyoshi, H. & Iizuka, H. Dynamic Modulation of Radiative Heat Transfer beyond the Blackbody Limit. *Nano Letters* **17**, 4347–4353 (2017).

53. Cui, L. *et al.* Study of radiative heat transfer in Ångström- and nanometre-sized gaps. *Nature Communications* **8**, (2017).

54. Ghashami, M. *et al.* Precision Measurement of Phonon-Polaritonic Near-Field Energy Transfer between Macroscale Planar Structures Under Large Thermal Gradients. *Physical Review Letters* **120**, (2018).

55. Fiorino, A. *et al.* A Thermal Diode Based on Nanoscale Thermal Radiation. *ACS Nano* **12**, 5774–5779 (2018).

56. Fiorino, A. *et al.* Giant Enhancement in Radiative Heat Transfer in Sub-30 nm Gaps of Plane Parallel Surfaces. *Nano Letters* **18**, 3711–3715 (2018).

57. Ying, X., Sabbaghi, P., Sluder, N. & Wang, L. Super-Planckian Radiative Heat Transfer between Macroscale Surfaces with Vacuum Gaps Down to 190 nm Directly Created by SU-8 Posts and Characterized by Capacitance Method. *ACS Photonics* **7**, 190–196 (2019).

58. Lim, M., Song, J., Lee, S. S., Lee, J. & Lee, B. J. Surface-plasmon-enhanced near-field radiative heat transfer between planar surfaces with a thin-film plasmonic coupler. *arXiv:1911.10315 [physics]* (2019).

59. Shi, K. *et al.* Colossal Enhancement of Near-Field Thermal Radiation Across Hundreds of Nanometers between Millimeter-Scale Plates through Surface Plasmon and Phonon Polaritons Coupling. *Nano Lett.* **19**, 8082–8088 (2019).

60. Musilová, V., Králík, T., Fořt, T. & Macek, M. Strong suppression of near-field radiative heat transfer by superconductivity in NbN. *Physical Review B* **99**, (2019).

61. Thompson, D., Zhu, L., Meyhofer, E. & Reddy, P. Nanoscale radiative thermal switching via multi-body effects. *Nat. Nanotechnol.* **15**, 99–104 (2020).

62. Lim, M., Song, J., Lee, S. S. & Lee, B. J. Tailoring near-field thermal radiation between metallo-dielectric multilayers using coupled surface plasmon polaritons. *Nat Commun* **9**, 4302 (2018).

63. Kutateladze, S. S., Robtsov, N. A. & Baltsevich, Y. Effect of magnitude of gap between metal plates on their thermal interaction at cryogenic temperatures. *Soviet Physics Doklady* **23**, 577–578 (1979).

64. Worbes, L., Hellmann, D. & Kittel, A. Enhanced Near-Field Heat Flow of a Monolayer Dielectric Island. *Phys. Rev. Lett.* **110**, 134302 (2013).

65. Feng, C., Tang, Z.-A. & Yu, J. A Novel CMOS Device Capable of Measuring Near-Field Thermal Radiation. *Chinese Phys. Lett.* **29**, 038502 (2012).

66. Feng, C., Tang, Z., Yu, J. & Sun, C. A MEMS Device Capable of Measuring Near-Field Thermal Radiation between Membranes. *Sensors* **13**, 1998–2010 (2013).

67. van Zwol, P. J., Ranno, L. & Chevrier, J. Tuning Near Field Radiative Heat Flux through Surface Excitations with a Metal Insulator Transition. *Phys. Rev. Lett.* **108**, 234301 (2012).

68. van Zwol, P. J., Thiele, S., Berger, C., de Heer, W. A. & Chevrier, J. Nanoscale Radiative Heat Flow due to Surface Plasmons in Graphene and Doped Silicon. *Phys. Rev. Lett.* **109**, 264301 (2012).

69. Kralik, T. *et al.* Strong Near-Field Enhancement of Radiative Heat Transfer between Metallic Surfaces. *Phys. Rev. Lett.* **109**, 224302 (2012).

70. Carnot, S. *Réflexions sur la puissance motrice du feu et sur les machines propres à développer cette puissance*. (Gauthier-Villars, 1824).

71. Blandre, É. Thermal radiation at the nanoscale: near-field and interference effects in few-layer structures and on the electrical performances of thermophotovoltaic devices. (INSA Lyon, 2016).

72. Joulain, K., Ezzahri, Y., Drevillon, J., Rousseau, B. & De Sousa Meneses, D. Radiative thermal rectification between SiC and SiO_2. *Optics Express* **23**, A1388 (2015).

73. Kitamura, R., Pilon, L. & Jonasz, M. Optical constants of silica glass from extreme ultraviolet to far infrared at near room temperature. *Appl. Opt.* **46**, 8118 (2007).

74. Vaillon, R. *et al.* Micron-sized liquid nitrogen-cooled indium antimonide photovoltaic cell for near-field thermophotovoltaics. *Opt. Express* **27**, A11 (2019).

75. Querry, M. R. Optical constants. *Contractor Report, Sep. 1982 - May 1984 Missouri Univ., Kansas City.* (1985).

76. Xiao, L. *et al.* Origins of high visible light transparency and solar heat-shielding performance in LaB $_6$. *Appl. Phys. Lett.* **101**, 041913 (2012).

77. Sato, Y., Terauchi, M., Mukai, M., Kaneyama, T. & Adachi, K. High energy-resolution electron energy-loss spectroscopy study of the dielectric properties of bulk and nanoparticle LaB_6 in the near-infrared region. *Ultramicroscopy* **111**, 1381–1387 (2011).

78. Ung, B. & Sheng, Y. Interference of surface waves in a metallic nanoslit. *Opt. Express* **15**, 1182 (2007).

79. Rakić, A. D., Djurišić, A. B., Elazar, J. M. & Majewski, M. L. Optical properties of metallic films for vertical-cavity optoelectronic devices. *Appl. Opt.* **37**, 5271 (1998).

80. Fu, C. J. & Zhang, Z. M. Nanoscale radiation heat transfer for silicon at different doping levels. *International Journal of Heat and Mass Transfer* **49**, 1703–1718 (2006).

81. Derjaguin, B. V., Abrikosova, I. I. & Lifshitz, E. M. Direct measurement of molecular attraction between solids separated by a narrow gap. *Quarterly Reviews, Chemical Society* **10**, 295–329 (1956).

82. Nguyen, K. L., Merchiers, O. & Chapuis, P.-O. Near-field radiative heat transfer in scanning thermal microscopy computed with the boundary element method. *Journal of Quantitative Spectroscopy and Radiative Transfer* **202**, 154–167 (2017).

83. Otey, C. & Fan, S. Numerically exact calculation of electromagnetic heat transfer between a dielectric sphere and plate. *Physical Review B* **84**, (2011).

84. Nguyen, K. L., Merchiers, O. & Chapuis, P.-O. Temperature-dependent and optimized thermal emission by spheres. *Appl. Phys. Lett.* **112**, 111906 (2018).

85. Feingold, A. & Gupta, K. G. New Analytical Approach to the Evaluation of Configuration Factors in Radiation From Spheres and Infinitely Long Cylinders. *Journal of Heat Transfer* **92**, 69–76 (1970).

86. Roberts, N. A. & Walker, D. G. A review of thermal rectification observations and models in solid materials. *International Journal of Thermal Sciences* **50**, 648–662 (2011).

87. Ito, K., Nishikawa, K., Iizuka, H. & Toshiyoshi, H. Experimental investigation of radiative thermal rectifier using vanadium dioxide. *Applied Physics Letters* **105**, 253503 (2014).

88. Spieser, M., Rawlings, C., Lörtscher, E., Duerig, U. & Knoll, A. W. Comprehensive modeling of Joule heated cantilever probes. *Journal of Applied Physics* **121**, 174503 (2017).

89. Dürig, U. Fundamentals of micromechanical thermoelectric sensors. *Journal of Applied Physics* **98**, 044906 (2005).

90. Guen, É. Microscopie thermique à sonde locale : étalonnage, protocoles de mesure et applications quantitatives sur des matériaux nanostructurés. (INSA Lyon, 2020).

91. Eickhoff, T., Grosse, P. & Theiss, W. Diffuse reflectance spectroscopy of powders. *Vibrational Spectroscopy* **1**, 229–233 (1990).

92. Christiansen, C. Untersuchungen über die optischen Eigenschaften von fein vertheilten Körpern. *Ann. Phys.* **259**, 298–306 (1884).

93. Kubelka, P. & Munk, F. Ein Beitrag Zur Optik Der Farbanstriche. *Zeitschrift für Technische Physik* **12**, 593–601 (1931).

94. Mie, G. Beiträge zur Optik trüber Medien, speziell kolloidaler Metallösungen. *Ann. Phys.* **330**, 377–445 (1908).

95. Bohren, C. F. & Huffman, D. R. *Absorption and Scattering of Light by Small Particles*. (Wiley, 1998). doi:10.1002/9783527618156.

96. Hassan, U. & Anwar, M. S. Reducing noise by repetition: introduction to signal averaging. *Eur. J. Phys.* **31**, 453–465 (2010).

97. Mosso, N. *et al.* Thermal Transport through Single-Molecule Junctions. *Nano Lett.* **19**, 7614–7622 (2019).

98. Cui, L. *et al.* Thermal conductance of single-molecule junctions. *Nature* **572**, 628–633 (2019).

99. Properties: Silica - Silicon Dioxide (SiO_2). *AZoM.com* https://www.azom.com/properties.aspx?ArticleID=1114.

100. Graphite (C) - Classifications, Properties & Applications. *AZoM.com* https://www.azom.com/article.aspx?ArticleID=1630 (2002).

101. Beeby, S. P., Cao, Z. & Almussallam, A. 11 - Kinetic, thermoelectric and solar energy harvesting technologies for smart textiles. in *Multidisciplinary Know-How for Smart-Textiles Developers* (ed. Kirstein, T.) 306–328 (Woodhead Publishing, 2013). doi:10.1533/9780857093530.2.306.

102. Shirvanimoghaddam, M. *et al.* Towards a Green and Self-Powered Internet of Things Using Piezoelectric Energy Harvesting. *IEEE Access* **7**, 94533–94556 (2019).

103. Coddington, O., Lean, J. L., Pilewskie, P., Snow, M. & Lindholm, D. A Solar Irradiance Climate Data Record. *Bull. Amer. Meteor. Soc.* **97**, 1265–1282 (2015).

104. *Clean energy for sustainable development: comparisons and contrasts of new approaches*. (Academic Press is an imprint of Elsevier, 2017).

105. Sil, I., Mukherjee, S. & Biswas, K. A review of energy harvesting technology and its potential applications. *EESRJ* **4**, 33–38 (2017).

106. Tervo, J., Manninen, A., Ilola, R. & Hänninen, H. State-of-the-art of Thermoelectric Materials. Processing, Properties and Applications. 31.

107. Zhao, Y., Dyck, J. S., Hernandez, B. M. & Burda, C. Enhancing thermoelectric performance of ternary nanocrystals through adjusting carrier concentration. *J. Am. Chem. Soc.* **132**, 4982–4983 (2010).

108. Madan, D., Chen, A., Wright, P. K. & Evans, J. W. Printed Se-Doped MA n-Type Bi2Te3 Thick-Film Thermoelectric Generators. *Journal of Elec Materi* **41**, 1481–1486 (2012).

109. Harder, N.-P. & rfel, P. W. Theoretical limits of thermophotovoltaic solar energy conversion. *Semicond. Sci. Technol.* **18**, S151–S157 (2003).

110. Tests results and performance comparisons of coated and un-coated skutterudite based segmented unicouples. *Energy Conversion and Management* **47**, 174–200 (2006).

111. Zhang, Q. *et al.* Realizing a thermoelectric conversion efficiency of 12% in bismuth telluride/skutterudite segmented modules through full-parameter optimization and energy-loss minimized integration. *Energy Environ. Sci.* **10**, 956–963 (2017).

112. Kraemer, D. *et al.* Concentrating solar thermoelectric generators with a peak efficiency of 7.4%. *Nat Energy* **1**, 1–8 (2016).

113. Enhanced performance thermoelectric module having asymmetrical legs. *Energy Conversion and Management* **148**, 1372–1381 (2017).

114. Direct thermal to electrical energy conversion using very low bandgap TPV cells in a gas-fired furnace system. *Energy Conversion and Management* **79**, 54–58 (2014).

115. Bermel, P. *et al.* Design and global optimization of high-efficiency thermophotovoltaic systems. *Opt. Express, OE* **18**, A314–A334 (2010).

116. Wernsman, B. *et al.* Greater Than 20% Radiant Heat Conversion Efficiency of a Thermophotovoltaic Radiator/Module System Using Reflective Spectral Control. *IEEE Trans. Electron Devices* **51**, 512–515 (2004).

117. Würfel, P. & Würfel, U. *Physics of solar cells: from basic principles to advanced concepts*. (Wiley-VCH, 2009).

118. Wurfel, U., Cuevas, A. & Wurfel, P. Charge Carrier Separation in Solar Cells. *IEEE J. Photovoltaics* **5**, 461–469 (2015).

119. Varshni, Y. P. Temperature dependence of the energy gap in semiconductors. *Physica* **34**, 149–154 (1967).

120. Levinshtein, M., Rumyantsev, S. & Shur, M. *Handbook Series on Semiconductor Parameters: Volume 1: Si, Ge, C (Diamond), GaAs, GaP, GaSb, InAs, InP, InSb*. vol. 1 (WORLD SCIENTIFIC, 1996).

121. Caro, M. A. Theory of elasticity and electric polarization effects in the group III-nitrides. (University College Cork, 2013).

122. Wanlass, M. W. *et al.* Lattice-mismatched approaches for high-performance, III-V photovoltaic energy converters. in *Conference Record of the Thirty-first IEEE Photovoltaic Specialists Conference, 2005.* 530–535 (IEEE, 2005). doi:10.1109/PVSC.2005.1488186.

123. Lindholm, F. A., Fossum, J. G. & Burgess, E. L. Application of the superposition principle to solar-cell analysis. *IEEE Trans. Electron Devices* **26**, 165–171 (1979).

124. Shockley, W. & Queisser, H. J. Detailed Balance Limit of Efficiency of *p-n* Junction Solar Cells. *Journal of Applied Physics* **32**, 510–519 (1961).

125. Guillemoles, J.-F., Kirchartz, T., Cahen, D. & Rau, U. Guide for the perplexed to the Shockley–Queisser model for solar cells. *Nat. Photonics* **13**, 501–505 (2019).

126. Kolm, H. Solar-Battery Power Source Quarterly Progress Report Solid State Research, Group 35. *Lexington, MA: MIT Lincoln Laboratory* (1956).

127. Chapin, D. M., Fuller, C. S. & Pearson, G. L. A New Silicon p-n Junction Photocell for Converting Solar Radiation into Electrical Power. *Journal of Applied Physics* **25**, 676–677 (1954).

128. Lenert, A. *et al.* A nanophotonic solar thermophotovoltaic device. *Nature Nanotech* **9**, 126–130 (2014).

129. Bierman, D. M. *et al.* Enhanced photovoltaic energy conversion using thermally based spectral shaping. *Nat Energy* **1**, 16068 (2016).

130. Kohiyama, A., Shimizu, M. & Yugami, H. Unidirectional radiative heat transfer with a spectrally selective planar absorber/emitter for high-efficiency solar thermophotovoltaic systems. *Appl. Phys. Express* **9**, 112302 (2016).

131. Ungaro, C., Gray, S. K. & Gupta, M. C. Solar thermophotovoltaic system using nanostructures. *Opt. Express* **23**, A1149 (2015).

132. Bhatt, R., Kravchenko, I. & Gupta, M. High-efficiency solar thermophotovoltaic system using a nanostructure-based selective emitter. *Solar Energy* **197**, 538–545 (2020).

133. Maka, T., Chigrin, D. N., Romanov, S. G. & Sotomayor-Torres, C. M. Three dimensional photonic crystals in the visible regime. *Progress In Electromagnetics Research,PIER 41* 307–335 (2003).

134. Nielsen, O. M., Arana, L. R., Baertsch, C. D., Jensen, K. F. & Schmidt, M. A. A thermophotovoltaic micro-generator for portable power applications. in *TRANSDUCERS '03. 12th International Conference on Solid-State Sensors, Actuators and Microsystems. Digest of Technical Papers (Cat. No.03TH8664)* vol. 1 714–717 vol.1 (2003).

135. Fraas, L., Samaras, J., Avery, J. & Minkin, L. Antireflection coated refractory metal matched emitters for use with GaSb thermophotovoltaic generators. in *Conference Record of the Twenty-Eighth IEEE Photovoltaic Specialists Conference - 2000 (Cat. No.00CH37036)* 1020–1023 (2000). doi:10.1109/PVSC.2000.916059.

136. Aicher, T. *et al.* Development of a Novel TPV Power Generator. *AIP Conference Proceedings* **738**, 71–78 (2004).

137. Andreev, V. M. *et al.* Solar Thermophotovoltaic Converters Based on Tungsten Emitters. *J. Sol. Energy Eng* **129**, 298–303 (2007).

138. Stone, K. W., Chubb, D. L., Wilt, D. M. & Wanlass, M. W. Testing and modeling of a solar thermophotovoltaic power system. *AIP Conference Proceedings* **358**, 199–209 (1996).

139. Yugami, H., Sai, H., Nakamura, K., Nakagawa, N. & Ohtsubo, H. Solar thermophotovoltaic using $Al_2O_3/Er_3/Al_5O_{12}$ eutectic composite selective emitter. *Conference Record of the Twenty-Eighth IEEE Photovoltaic Specialists Conference - 2000 (Cat. No.00CH37036)* 1214–1217 (2000). doi:10.1109/PVSC.2000.916107.

140. Chen, K. Small, efficient thermophotovoltaic power supply. *Technical Report DAAG55-97-C-0003, U.S. Army Research Office* (1999).

141. Bitnar, B., Durisch, W., Mayor, J.-C., Sigg, H. & Tschudi, H. R. Characterisation of rare earth selective emitters for thermophotovoltaic applications. *Solar Energy Materials and Solar Cells* **73**, 221–234 (2002).

142. Bitnar, S. *et al.* Practical thermophotovoltaic generators. *Semiconductors* **38**, 941–945 (2004).

143. Nelson, R. E. TPV Systems and State-of-Art Development. *AIP Conference Proceedings* **653**, 3–17 (2003).

144. Chan, W. R. *et al.* Toward high-energy-density, high-efficiency, and moderate-temperature chip-scale thermophotovoltaics. *PNAS* **110**, 5309–5314 (2013).

145. Doyle, E. Development and demonstration of a 25 watt thermophotovoltaic power source for a hybrid power system. *Technical Report TR04-2001, National Aeronautics and Space Administration* (2001).

146. Qiu, K., Hayden, A. C. S. & Entchev, E. TPV Power Generation System Using a High Temperature Metal Radiant Burner. *AIP Conference Proceedings* **890**, 27–36 (2007).

147. Fraas, L. Small efficient thermophotovoltaic power supply using infrared-sensitive gallium antimonide cells. *Tech. Rep. DAAG55-97-C-0002, U.S. Army Research Office* (1996).

148. Horne, E. Hybrid thermophotovoltaic power systems. *Technical Report, EDTEK, Inc.* (2002).

149. Astle, C. Design and preliminary testing of a prototype thermophotovoltaic system. *Proc. IMECE* (2003).

150. Astle, C. J., Kovacik, G. J. & Heidrick, T. R. Design and Performance of a Prototype Thermophotovoltaic System. *J. Sol. Energy Eng* **129**, 340–342 (2007).

151. Wenming, Y., Siawkiang, C., Chang, S., Hong, X. & Zhiwang, L. Research on micro-thermophotovoltaic power generators with different emitting materials. *J. Micromech. Microeng.* **15**, S239–S242 (2005).

152. Datas, A. & Algora, C. Development and experimental evaluation of a complete solar thermophotovoltaic system. *Progress in Photovoltaics: Research and Applications* **21**, 1025–1039 (2013).

153. Omair, Z. *et al.* Ultraefficient thermophotovoltaic power conversion by band-edge spectral filtering. *Proc Natl Acad Sci USA* **116**, 15356–15361 (2019).

154. Lu, Q. *et al.* InAs thermophotovoltaic cells with high quantum efficiency for waste heat recovery applications below 1000 °C. *Solar Energy Materials and Solar Cells* **179**, 334–338 (2018).

155. Rinnerbauer, V. *et al.* Metallic Photonic Crystal Absorber-Emitter for Efficient Spectral Control in High-Temperature Solar Thermophotovoltaics. *Advanced Energy Materials* **4**, 1400334 (2014).

156. Chan, W. R. *et al.* Enabling efficient heat-to-electricity generation at the mesoscale. *Energy Environ. Sci.* **10**, 1367–1371 (2017).

157. Wang, X. *et al.* Prototype of radioisotope thermophotovoltaic system using photonic crystal spectral control. *J. Phys.: Conf. Ser.* **660**, 012034 (2015).

158. Wang, X. Toward high efficiency radioisotope thermophotovoltaic system by spectral control,. (Massachusetts Institute of Technology, 2017).

159. Woolf, D. N. *et al.* High-efficiency thermophotovoltaic energy conversion enabled by a metamaterial selective emitter. *Optica* **5**, 213 (2018).

160. Shimizu, M., Kohiyama, A. & Yugami, H. High-efficiency solar-thermophotovoltaic system equipped with a monolithic planar selective absorber/emitter. *J. Photon. Energy* **5**, 053099 (2015).

161. Jaziri, N. *et al.* A comprehensive review of Thermoelectric Generators: Technologies and common applications. *Energy Reports* S2352484719306997 (2019) doi:10.1016/j.egyr.2019.12.011.

162. Blandre, E., Chapuis, P.-O. & Vaillon, R. High-injection effects in near-field thermophotovoltaic devices. *Scientific Reports* **7**, (2017).

163. Laroche, M., Carminati, R. & Greffet, J.-J. Near-field thermophotovoltaic energy conversion. *Journal of Applied Physics* **100**, 063704 (2006).

164. DiMatteo, R. S. *et al.* Enhanced photogeneration of carriers in a semiconductor via coupling across a nonisothermal nanoscale vacuum gap. *Applied Physics Letters* **79**, 1894–1896 (2001).

165. Hanamura, K. & Mori, K. Nano-gap TPV Generation of Electricity through Evanescent Wave in Near-field Above Emitter Surface. in vol. 890 291–296 (AIP, 2007).

166. Cakiroglu, D. *et al.* Indium antimonide photovoltaic cells for near-field thermophotovoltaics. *Solar Energy Materials and Solar Cells* **203**, 110190 (2019).

167. Karalis, A. & Joannopoulos, J. D. Transparent and 'opaque' conducting electrodes for ultra-thin highly-efficient near-field thermophotovoltaic cells. *Sci Rep* **7**, 14046 (2017).

168. Datas, A. & Vaillon, R. Thermionic-enhanced near-field thermophotovoltaics. *Nano Energy* **61**, 10–17 (2019).

169. DeSutter, J., Vaillon, R. & Francoeur, M. External Luminescence and Photon Recycling in Near-Field Thermophotovoltaics. *Phys. Rev. Applied* **8**, 014030 (2017).

170. Tarr, N. G. & Pulfrey, D. L. The superposition principle for homojunction solar cells. *IEEE Transactions on Electron Devices* **27**, 771–776 (1980).

171. Bright, T. J., Wang, L. P. & Zhang, Z. M. Performance of Near-Field Thermophotovoltaic Cells Enhanced With a Backside Reflector. *J. Heat Transfer* **136**, (2014).

172. Chen, K., Santhanam, P. & Fan, S. Suppressing sub-bandgap phonon-polariton heat transfer in near-field thermophotovoltaic devices for waste heat recovery. *Appl. Phys. Lett.* **107**, 091106 (2015).

173. Huang, W. *et al.* Enhanced collection efficiencies and performance of interband cascade structures for narrow bandgap semiconductor thermophotovoltaic devices. *Journal of Applied Physics* **124**, 023101 (2018).

174. Narayanaswamy, A. & Chen, G. Surface modes for near field thermophotovoltaics. *Appl. Phys. Lett.* **82**, 3544–3546 (2003).

175. Lucchesi, C. *et al.* Harnessing near-field thermal photons with efficient photovoltaic conversion. *arXiv:1912.09394 [physics]* **1912**, arXiv:1912.09394 (2019).

176. Sharma, R. G. *Superconductivity*. (Springer International PU, 2016).

177. Calzolari, A., Ruini, A. & Catellani, A. Transparent Conductive Oxides as Near-IR Plasmonic Materials: The Case of Al-Doped ZnO Derivatives. *ACS Photonics* **1**, 703–709 (2014).

178. Krivoy, E. M. *et al.* Rare-Earth Monopnictide Alloys for Tunable, Epitaxial, Designer Plasmonics. *ACS Photonics* **5**, 3051–3056 (2018).

179. Milovich, D. *et al.* Design of an indium arsenide cell for near-field thermophotovoltaic devices. *arXiv:2001.02663 [physics]* (2020).

180. Yu, H., Liu, D., Yang, Z. & Duan, Y. Simple Rectangular Gratings as a Near-Field "Anti-Reflection" Pattern for GaSb TPV Cells. *Sci Rep* **7**, 1026 (2017).

181. Kovalenko, S. A. Descartes-Snell law of refraction with absorption. *Semiconductor Physics, Quantum Electronics & Optoelectronics* **4**, 214–218 (2001).

182. Chapuis, P.-O. Contribution à l'étude des transferts thermiques à l'échelle nanométrique : interaction pointe-surface. (Ecole Centrale Paris, 2007).

FOLIO ADMINISTRATIF
THESE DE L'UNIVERSITE DE LYON OPEREE AU SEIN DE L'INSA LYON

NOM : LUCCHESI
Prénoms : Christophe

DATE de SOUTENANCE : 15/07/2020

TITRE : Conception et développement d'un convertisseur thermophotovoltaïque en champ proche

NATURE : Doctorat

Numéro d'ordre : 2020LYSEI053

Ecole doctorale : MEGA de Lyon

Spécialité : Thermique et énergétique

RESUMÉ : Une cellule thermophotovoltaïque (TPV) convertit l'énergie de photons émis par des corps chauds en énergie électrique. Lorsque la distance séparant deux corps rayonnants devient inférieure à la longueur d'onde caractéristique du rayonnement thermique (~10 µm à température ambiante, ~2,3 µm vers 1000°C), le transfert de chaleur radiatif peut s'accroître de plusieurs ordres de grandeur grâce à la contribution des ondes évanescentes. Cette propriété a un intérêt pour la récupération d'énergie en promettant une augmentation de la puissance électrique générée par une cellule TPV lorsqu'elle est placée en champ proche d'un émetteur thermique radiatif. Dans le but de vérifier cette prédiction, cette thèse a consisté à développer un banc expérimental de mesures TPV en champ proche. Le dispositif est basé sur un montage de microscopie thermique avec actuateurs piézo-électriques (SThM). L'émetteur est une sphère micrométrique de graphite attachée sur un levier SThM chauffé de manière thermorésistive jusqu'à 1200 K et la cellule TPV en antimoniure d'indium (InSb), qui ne peut fonctionner au-delà de 100 K, est placée sur le doigt froid d'un cryostat. Le flux radiatif en champ proche transféré par l'émetteur peut être mesuré indépendamment de la puissance électrique générée par la cellule. La preuve expérimentale de l'accroissement de la densité de puissance électrique générée en champ proche, par rapport à la prédiction de la théorie macroscopique du rayonnement, a été apportée avec un facteur jusqu'à 6. L'étude de différents paramètres a permis d'atteindre des puissances TPV de 7.5 $kW.m^{-2}$ et des rendements de conversion mesurés de ~20 %. Des expériences de transfert radiatif en champ proche dans diverses configurations (matériaux, géométries, températures) ont également été menées. La puissance radiative transférée en champ proche suit des lois de puissance très différentes de celles du champ lointain. Ces résultats démontrent expérimentalement l'intérêt applicatif des effets de champ proche pour le rayonnement thermique.

MOTS-CLÉS : Transfert thermique, rayonnement, champ proche, thermophotovoltaïque, SThM, cryogénie, InSb, conversion d'énergie

Laboratoire (s) de recherche : Centre d'Énergétique et de thermique de Lyon (CETHIL, UMR 5008)

Directeur de thèse: VAILLON Rodolphe

Président de jury : DE WILDE Yannick

Composition du jury :

KITTEL Achim	Professeur	Universität Oldenburg	Rapporteur
MARTI VEGA Antonio	Professeur	UPM, Madrid	Rapporteur
DELMAS Agnès	Maitre de conférences	INSA de Lyon	Examinatrice
DE WILDE Yannick	Directeur de recherches	Institut Langevin, Paris	Examinateur
GUILLEMOLES Jean-François	Directeur de recherches	IPVF, Palaiseau	Examinateur
KAMINSKI-CACHOPO Anne	Professeur	Grenoble INP - Phelma	Examinatrice
VAILLON Rodolphe	Directeur de recherches	IES, Montpellier	Directeur de thèse
CHAPUIS Pierre-Olivier	Chargé de recherche	CETHIL, Lyon	Co-directeur de thèse
PEREZ Jean-Philippe	Maitre de conférences	IES, Montpellier	Membre invité